

An Investigation into Ambulatory Blood Pressure Measurement

by

Hai Lan

**A Thesis Submitted to
Auckland University of Technology
in Fulfilment of the Requirements for the Degree of
Doctor of Philosophy (PhD)**



Institute of Biomedical Technologies

March 2012

dedicated to

My wife Qiusong Liu and my daughter Oliver Jianing Lan

ACKNOWLEDGEMENT

There are many people I wish to formally thank for their contribution to this thesis. First of all, I would like to express my appreciations and gratitude to my supervisor, Professor Ahmed Al-Jumaily. He is such knowledgeable, patient and helpful. Without his invaluable support, consistently encouragement and push, I will not finish the research like this.

I am grateful to thank my second supervisor Dr. Andrew Lowe for his generous technical guidance, constructive criticism and contiguous support throughout my endeavour. I wish to thank Assoc. Professor Wayne Hing for training and technical support for ultrasound measurement.

Warmest thanks to Dr. David Parker and Meha Mathur for revising this thesis. They gave me lots of help and valuable suggestions about writing. To my colleagues and friends at IBtec, they made everyone feel like in a family here. To Prasika, Gijs, Thomas, Mohammad and Maggie, thank you for your help and advice.

I wish to give my most sincere appreciation to my family Binqi Lan, Wenxian Tong, Yanjun Liu, and Jie Hong. They always stay behind me and support me. Without their support and encouragement, the thesis would not have been possible.

I would like to acknowledge Institute of Biomedical Technologies for financial support.

Finally, I would also like to acknowledge ethical approval from the Auckland University of Technology Ethics Committee approval number 08/232 approved on 8 December 2008.

ABSTRACT

Hypertension is one of the most common cardiovascular diseases threatening people's health worldwide. Although, hypertension itself is rarely an acute problem, it increases the risk of cardiovascular events and kidney diseases. Recent studies have shown that the end-organ damage associated with hypertension is more strongly correlated with ambulatory blood pressure monitoring (ABPM) than with traditional clinic BP measurements. Currently, the ambulatory, cuff-based devices are predominantly based on automatic techniques which are inherently motion-sensitive. The other devices which claim to compensate for motion artefacts measure the arterial pressure at the wrist and are less accurate than cuff-based measurement.

This research aims to develop a cuff-based ABPM technique which can measure BP accurately during their daily lives. The primary objective of this research is to investigate two major issues related to ABPM technique: (1) the theory of oscillometric BP measurement method used in most of ABPM device; (2) the method to compensate for the noises during the measurement.

This thesis introduces for the first time a 3D finite element (FE) model which simulates the entire oscillometric BP measurement process. The model is validated by both arm simulator and clinical results. The brachial artery closure process and the factors of arm material properties in BP measurement are discussed. The model indicates that the nonlinearity of brachial artery plays the key role in oscillometric BP measurement. It also offers a new explanation of the common phenomenon: overestimation in the elderly and underestimation in the younger.

Since BP pulse, arm motion and environmental tremors all lead to the upper arm skin stretches, it is anticipated that the strain distribution due to these causes is unique for different arm motion. This thesis also describes the design of a piezoelectric strain sensor array and the relevant method for eliminating the noises and determining the subject's BP. A FE model, whose geometry is obtained from Visible Human Body dataset, is established to study surface strain distribution during different arm motions. Referring to its results, the piezoelectric sensor array is designed and used in the clinical experiments. Using the obtained signals, a generalized input-output configuration of the designed measurement system is developed. The transfer functions of the system are determined through empirical equations. Using the developed method, the device is able to detect the arm motions, compensate for the noises and determine patients' BP. The results can be used as a guide for developing a new type of ABPM device insensitive to artefacts.

TABLE OF CONTENTS

| | |
|--|------------|
| ACKNOWLEDGEMENT | ii |
| ABSTRACT | iii |
| TABLE OF CONTENTS..... | v |
| LIST OF FIGURES | ix |
| LIST OF TABLES | xiv |
| STATEMENT OF ORIGINALITY | xv |
| LIST OF UNIT, SYMBOLS AND ABBREVIATIONS | xvi |
| Chapter 1 Background..... | 1 |
| 1.1 Introduction | 1 |
| 1.2 Clinical factors of BP | 1 |
| 1.3 BP measurement..... | 4 |
| 1.3.1 Auscultatory method..... | 6 |
| 1.3.2 Oscillometric method | 8 |
| 1.3.3 Ambulatory BP measurement..... | 10 |
| 1.4 Thesis overview | 11 |
| Chapter 2 Literature Review..... | 12 |
| 2.1 Introduction | 12 |
| 2.2 Mechanical analysis of oscillometric measurement process..... | 12 |
| 2.2.1 CP transmission | 13 |
| 2.2.2 BP transmission | 14 |
| 2.3 Theoretical analysis of non-invasive oscillometric BP measurement..... | 14 |
| 2.3.1 Artery models | 15 |
| 2.3.2 Arm model | 15 |
| 2.4 Finite element analysis | 16 |
| 2.4.1 Model geometry..... | 17 |
| 2.4.2 Material properties of human tissue | 19 |
| 2.4.3 Other conditions..... | 20 |
| 2.4.4 Current models..... | 21 |

| | | |
|------------------|---|-----------|
| 2.5 | Closure | 24 |
| 2.6 | Objectives..... | 24 |
| Chapter 3 | Numerical Formulation | 26 |
| 3.1 | Introduction | 26 |
| 3.2 | Continuum model..... | 26 |
| 3.2.1 | <i>Material</i> | 26 |
| 3.2.2 | <i>Element</i> | 31 |
| 3.2.3 | <i>Equilibrium Equations of the Model</i> | 34 |
| 3.2.4 | <i>Contact Problem</i> | 38 |
| 3.3 | Summary | 40 |
| Chapter 4 | Finite Element Models | 41 |
| 4.1 | Introduction | 41 |
| 4.2 | Model selection | 41 |
| 4.2.1 | <i>Material properties</i> | 42 |
| 4.2.2 | <i>Geometry</i> | 48 |
| 4.2.3 | <i>Interactive properties</i> | 49 |
| 4.2.4 | <i>Boundary conditions</i> | 50 |
| 4.2.5 | <i>Model loading</i> | 52 |
| 4.2.6 | <i>Model mesh</i> | 56 |
| 4.3 | Refined model | 58 |
| 4.3.1 | <i>Material properties</i> | 58 |
| 4.3.2 | <i>Geometry of the model</i> | 61 |
| 4.3.3 | <i>Boundary conditions</i> | 67 |
| 4.3.4 | <i>Interactive properties</i> | 68 |
| 4.3.5 | <i>Model loading</i> | 69 |
| 4.3.6 | <i>Model mesh</i> | 69 |
| 4.4 | Summary | 71 |
| Chapter 5 | EXPERIMENT INVESTIGATION..... | 72 |
| 5.1 | Introduction | 72 |
| 5.2 | Arm simulator | 72 |
| 5.2.1 | <i>Upper arm system</i> | 73 |
| 5.2.1.1 | <i>Model geometry</i> | 73 |
| 5.2.1.2 | <i>Materials</i> | 74 |
| 5.2.1.3 | <i>Mould Development</i> | 76 |






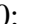







| | | |
|------------------|---|------------|
| 5.2.1.4 | <i>Model fabrication</i> | 77 |
| 5.2.2 | <i>Circulation System</i> | 82 |
| 5.2.3 | <i>Ultrasound Measurement</i> | 89 |
| 5.3 | <i>FE Model Validation</i> | 92 |
| 5.4 | <i>Clinical Trial</i> | 93 |
| 5.4.1 | <i>Oscillometric BP Measurement</i> | 93 |
| 5.4.2 | <i>Experimental Protocol</i> | 94 |
| 5.4.3 | <i>Experimental Procedures</i> | 96 |
| 5.5 | <i>Summary</i> | 97 |
| Chapter 6 | FE Model Results and Discussion | 98 |
| 6.1 | <i>Introduction</i> | 98 |
| 6.2 | <i>FE model with cylindrical geometry</i> | 98 |
| 6.2.1 | <i>Validation of simplified cylindrical FE model</i> | 99 |
| 6.2.1.1 | <i>Artery closure process</i> | 99 |
| 6.2.1.2 | <i>CP oscillation during BP measuring process</i> | 101 |
| 6.2.2 | <i>Variability of the arm tissue mechanical properties</i> | 105 |
| 6.2.2.1 | <i>Soft tissue materials</i> | 105 |
| 6.2.2.2 | <i>Theory of oscillometric BP measurement method and brachial artery</i> 110 | |
| 6.3 | <i>Realistic FE model</i> | 115 |
| 6.3.1 | <i>Piezoelectric film sensor array</i> | 115 |
| 6.3.1.1 | <i>Strain distribution with BP</i> | 115 |
| 6.3.1.2 | <i>Strain distribution with arm motion</i> | 117 |
| 6.3.2 | <i>Components of piezoelectric film sensor signals</i> | 120 |
| 6.4 | <i>Summary</i> | 122 |
| Chapter 7 | Experimental results and Signal Post-Processing | 123 |
| 7.1 | <i>Introduction</i> | 123 |
| 7.2 | <i>Clinical experiment</i> | 123 |
| 7.2.1 | <i>Oscillometric BP measurement</i> | 124 |
| 7.2.2 | <i>Constant CP</i> | 127 |
| 7.2.2.1 | <i>CP at supra-systolic pressure</i> | 127 |
| 7.2.2.2 | <i>CP at SP</i> | 129 |
| 7.2.2.3 | <i>CP at MP</i> | 131 |

| | | |
|-------------------|--|------------|
| 7.2.2.4 | <i>CP at DP</i> | 133 |
| 7.2.2.5 | <i>CP at sub-diastolic pressure</i> | 135 |
| 7.2.3 | <i>Arm motion</i> | 137 |
| 7.3 | Signal relationship..... | 138 |
| 7.3.1 | <i>Without arm motion</i> | 139 |
| 7.3.2 | <i>With arm motion</i> | 141 |
| 7.3.2.1 | <i>Without BP</i> | 141 |
| 7.3.2.2 | <i>With BP and arm motion</i> | 144 |
| 7.4 | Waveform rebuild | 145 |
| 7.5 | Summary | 148 |
| Chapter 8 | Conclusion and Future work | 149 |
| 8.1 | Conclusion | 149 |
| 8.1.1 | <i>Theory of oscillometric BP measurement method</i> | 149 |
| 8.1.2 | <i>Compensate the noises during the measurement</i> | 150 |
| 8.2 | Future work | 150 |
| 8.2.1 | <i>BP measurement technique</i> | 151 |
| 8.2.2 | <i>Detecting BP waveform</i> | 151 |
| 8.2.3 | <i>Noise compensation</i> | 151 |
| REFERENCES | | 153 |
| APPENDIX | | 160 |
| APPENDIX I | | 161 |
| APPENDIX II | | 169 |
| APPENDIX III | | 176 |
| APPENDIX IV | | 184 |

LIST OF FIGURES

| | |
|---|----|
| Figure 1.1 Identified high BP in adults, by age group and sex [4]. | 3 |
| Figure 1.2 Auscultatory BP measurement process [12]. | 7 |
| Figure 1.3 Typical clinical data in oscillometric BP measuring process: — measured CP, — pressure oscillation after filtering. | 9 |
| Figure 2.1 Flow chart of signal transmission in the oscillometric BP measurement. | 13 |
| Figure 2.2 MR image of the right wrist [52]. | 18 |
| Figure 2.3 A sample of upper arm from VHB dataset [53]. | 18 |
| Figure 2.4 (a) MR image of the right wrist; (b) MR image of the same wrist under inflated cuff; (c) 2D FE model of right wrist: the light grey, dark grey and black shades represent skin and connective tissue, muscle, and tendons, respectively; (d) 3D model of right wrist [constructed by extending the 2-D finite-element model at site L in the longitudinal (z) direction] [52, 66]. | 23 |
| Figure 3.1 Model deformation function in continuum model. | 27 |
| Figure 3.2 A tetrahedral element is shown in the co-ordinate system. | 32 |
| Figure 3.3 Typical steps for solving the contact problem. | 39 |
| Figure 4.1 Brachial artery pressure vs. area under three experimental conditions: baseline, norepinephrine (NE, 1.2 μ g), and nitroglycerin (NTG, 100 μ g). [82] | 45 |
| Figure 4.2 The stress-strain relationship of the artery wall used in the finite element model. | 47 |
| Figure 4.3 The stress-strain relationship of the artery wall is calculated from experimental results [81]. — normal artery, — soft artery, — hard artery. | 48 |
| Figure 4.4 Transverse section of the arm model [36, 75]. | 49 |
| Figure 4.5 Boundary conditions of the simplified model. | 51 |
| Figure 4.6 Load and boundary conditions of the simplified model. | 52 |
| Figure 4.7 The artery is at normal open status at position 1 and compressed at position 2 by external CP. | 53 |
| Figure 4.8 BP waveform obtained from clinical experiment. | 55 |
| Figure 4.9 CP changes in the finite element model. | 55 |
| Figure 4.10 (a) the fine mesh with four layers; (b) the used mesh with two layers. | 57 |

| | |
|---|----|
| Figure 4.11 Cross section view of the meshed model..... | 57 |
| Figure 4.12 (a) one sample (No.0417) of the selected images from VHB dataset [75] (b) the image between pixel (1335, 530) and pixel (1713, 1033) of the original image is selected from the original image for further analysis. | 60 |
| Figure 4.13 (a) Anterior and posterior view of upper arm muscles, (b) the positions of selected slices in VHB Dataset [75, 86]..... | 62 |
| Figure 4.14 (a) The edges between different materials are highlighted after colour processing. (b) The boundaries of different parts are defined by smoothed spin lines which are guided by the highlighted edges..... | 63 |
| Figure 4.15 The 3D models of the simulated parts are shown above: (a) the biceps, (b) the triceps, (c) other muscles, (d) integrated muscles, (e) the soft tissue, (f) the bone, (g) the brachial artery. | 64 |
| Figure 4.16 3D structure of the upper arm model: (a) biceps, triceps, other muscles and artery; (b) soft tissue and bone, (c) the assembled model. | 66 |
| Figure 4.17 Boundary condition and loading in the 3D model..... | 67 |
| Figure 4.18 Mesh of different parts in the finite element model: (a) brachial artery, (b) biceps (c) soft tissue, (d) other muscles (e) triceps | 70 |
| Figure 5.1 Transverse section of the arm simulator | 73 |
| Figure 5.2 Custom designed jigs and fixtures for testing the elasticity of the selected silicone | 75 |
| Figure 5.3 The assembled silicone mould..... | 77 |
| Figure 5.4 Moulding process: a. the pouring process of moulding; b. the entire setup for simulator moulding | 79 |
| Figure 5.5 The assembled arm simulator. | 80 |
| Figure 5.6 (a) The silver steel bar is fitted into the lathe. (b) The parting tool is set to control the wall thickness..... | 81 |
| Figure 5.7 The schedule structure of the arm simulator..... | 83 |
| Figure 5.8 The open loop DC pump control system | 85 |
| Figure 5.9 The Labview® program for generating pressure pulse waves: (a) front panel, (b) block diagram. | 86 |
| Figure 5.10 (a) Front panel of the Labview® program for recording pressure sensor readings (b) Block diagram of the Labview® program for recording pressure sensor readings..... | 88 |
| Figure 5.11 Ultrasound image in transverse plane..... | 89 |

| | |
|---|-----|
| Figure 5.12 Ultrasound image in coronal plane | 90 |
| Figure 5.13 Ultrasound image of the silicone arm simulator..... | 90 |
| Figure 5.14 The relationship between transmural pressure and artery diameter obtained from arm simulator by ultrasound device. | 93 |
| Figure 5.15 The CP oscillation measured in oscillometric BP measurement | 94 |
| Figure 5.16 The differential charge amplifier is designed to connect the piezoelectric film sensor with data acquisition card..... | 95 |
| Figure 6.1 The relationship between TP and artery diameter obtained from arm simulator and FE model respectively.  FE model results;  Ultrasound measurement..... | 100 |
| Figure 6.2 Pressure oscillations vs. CP: (a) clinical result, (b) FE model results. | 102 |
| Figure 6.3 The relationship between CP oscillation amplitude and applied CP. \times shows the characteristic ratios range of diastolic pressure and $*$ shows the characteristic ratios range of the systolic pressure reported in the literature [38]. | 105 |
| Figure 6.4 Pressure distribution of FE model under CP in longitudinal direction, when CP=100mmHg..... | 107 |
| Figure 6.5 FE pressure transmission ratio for soft tissue material properties at CP= 100 mmHg; (a) $E = 40$ kPa, γ :  , 0.40;  , 0.45;  0.49. (b) $\gamma = 0.45$, E (kPa):  , 30;  , 40;  , 60 | 109 |
| Figure 6.6 Brachial artery buckling pressure was TP = -5.6 mmHg when it was isolated from the surrounding tissues. | 110 |
| Figure 6.7 Brachial artery closure process with increasing TP..... | 111 |
| Figure 6.8 Relationship between artery buckling pressure and soft tissue elasticity E | 112 |
| Figure 6.9 CP oscillations trend when linear elastic artery wall was used in the model | 113 |
| Figure 6.10 FE artery lumen area vs. CP of the mid section predicted:  normal artery;  soft artery;  hard artery. | 114 |
| Figure 6.11 Arm surface strain distribution driven by the BP in the brachial artery without any external pressure..... | 116 |
| Figure 6.12 Comparison between the applied intravascular pressure and obtained surface strain changes. :  Surface strain change,  intravascular pressure..... | 117 |
| Figure 6.13 (a) Surface strain distribution during the biceps contraction; (b) Surface strain distribution during the triceps contraction..... | 118 |

| | |
|---|-----|
| Figure 6.14 The locations for the piezoelectric sensors to detect arm motion and BP pulses. Location 1: on the mid section of the model and above brachial artery; Location 2: over the mid section of the model and above the biceps belly; Location 3: on the mid section of the model and above triceps..... | 119 |
| Figure 6.15 Pressure distribution under CP | 121 |
| Figure 6.16 Strain distribution of the surface near the brachial artery..... | 121 |
| Figure 7.1 Sensor readings in the normal oscillometric BP measurement: (a) CP reading in the entire measuring process; (b) readings from the biceps sensor and the triceps sensor during normal oscillometric BP measurement; (c) artery CP reading during BP no motion; (d) FFT analysis of the obtained signals after normalizing: --- artery sensor, --- biceps sensor, - - triceps sensor, ---CP oscillation, — CP..... | 126 |
| Figure 7.2 Experiment results when CP was at supra-systolic pressure: (a) readings from the biceps sensor and the triceps sensor during normal oscillometric BP measurement; (b) artery CP reading during BP no motion; (c) FFT analysis of the obtained signals after normalizing: --- artery sensor, --- biceps sensor, - - triceps sensor, --- CP oscillation, — CP..... | 129 |
| Figure 7.3 Experiment results when CP was at SP: (a) readings from the biceps sensor and the triceps sensor during normal oscillometric BP measurement; (b) artery CP reading during BP no motion; (c) FFT analysis of the obtained signals after normalizing: --- artery sensor, --- biceps sensor, - - triceps sensor, --- CP oscillation, — CP..... | 131 |
| Figure 7.4 Experiment results when CP was at MP: (a) readings from the biceps sensor and the triceps sensor during normal oscillometric BP measurement; (b) artery CP reading during BP no motion; (c) FFT analysis of the obtained signals after normalizing: --- artery sensor, --- biceps sensor, - - triceps sensor, --- CP oscillation, — CP..... | 133 |
| Figure 7.5 Experiment results when CP was at DP: (a) readings from the biceps sensor and the triceps sensor during normal oscillometric BP measurement; (b) artery CP reading during BP no motion; (c) FFT analysis of the obtained signals after normalizing: --- artery sensor, --- biceps sensor, - - triceps sensor, --- CP oscillation, — CP..... | 135 |
| Figure 7.6 Experiment results when CP was at sub-diastolic pressure: (a) readings from the biceps sensor and the triceps sensor during normal oscillometric BP measurement; (b) artery CP reading during BP no motion: --- artery sensor, --- biceps sensor, - - triceps sensor, ---CP oscillation, — CP. | 136 |
| Figure 7.7 CP in the oscillometric BP measurement process when arm motion was involved in the BP measurement process..... | 137 |
| Figure 7.8 Generalized input-output configuration of the designed BP measurement system..... | 138 |

| | |
|---|-----|
| Figure 7.9 Generalized input-output configuration of the measurement without any arm motion..... | 140 |
| Figure 7.10 The relationship between CP and piezoelectric sensors. — G_{bic} — G_{tri} — G_{art} | 141 |
| Figure 7.11 Generalized input-output configuration of the measurement without BP signals..... | 142 |
| Figure 7.12 (a) Readings from piezoelectric film sensors during passive lifting; (b) Readings from piezoelectric film sensors during passive twisting: — artery sensor — biceps sensor — triceps sensor | 143 |
| Figure 7.13 Experiment results when arm motion was involved in the BP measurement process: (a) rebuilt CP oscillations for BP analysis; (b) FFT analysis of the obtained signals after normalizing; (c) the measured oscillations signal from the artery sensor, the biceps sensor and the triceps sensor: — artery sensor, — biceps sensor, — triceps sensor, — measured CP oscillation, — CP, — rebuilt CP oscillation..... | 147 |

LIST OF TABLES

| | |
|--|----|
| Table 1-1 Classification of BP [3] | 2 |
| Table 1-2 The summary of the mostly used BP measurement methods. | 5 |
| Table 2-1 Commonly used material properties for human tissues..... | 20 |
| Table 5-1: Tensile test results of Proskin with different proportions of diluent. | 76 |

STATEMENT OF ORIGINALITY

‘I hereby declare that this submission is my own work and that, to the best of my knowledge and belief, it contains no material previously published or written by another person nor material which to a substantial extent has been accepted for the qualification of any other degree or diploma of a university or other institution of higher learning, except where due acknowledgment is made in the acknowledgments.’

..... (signed)

..... (date)

LIST OF UNIT, SYMBOLS AND ABBREVIATIONS

| Symbols | Unit |
|----------|---|
| F | Farad |
| Hz | Hertz |
| ml | Millilitre |
| mmHg | Millimeter of mercury, unit for pressure, 133 pascals |
| Pa | Pascal |
| S | Second |
| V | Volt |
| Ω | Ohm |

| | Description |
|---------------|---|
| C | Capacity |
| D | Distance |
| E | Young's modulus |
| E' | Young's modulus along the y axis |
| ε | Strain tensor |
| F | Force |
| f | Frequency |
| G | The gap normal to the contact surface |
| G' | The elastic shear modulus |
| G'' | The viscous shear modulus |
| $G_s(\omega)$ | The storage modulus |
| $G_l(\omega)$ | The loss modulus |
| N | The unit normal vector of the contact surface |
| η | The dynamic viscosity |
| ρ | Density |

| | |
|----------|---|
| σ | Stress |
| R | Resistance |
| S | Surface force |
| s | A shaping factor |
| T | The thickness of the vocal folds |
| τ | Shear stress |
| t | Time |
| U | The strain energy |
| μ | The shear modulus in the transverse plane |
| μ' | The shear modulus along the y axis |
| V | The volume of the element |
| ν | The Poisson's ratio in the transverse plane |
| ν' | The Poisson's ratio along the y axis |
| W_p | The virtual work |
| ω | The angular frequency |

Abbreviations

| | |
|-----|------------------------|
| A | Artery lumen area |
| BP | Blood pressure |
| CP | Cuff pressure |
| DP | Diastolic pressure |
| FE | Finite element |
| FFT | Fast Fourier transform |
| MP | Mean blood pressure |
| SP | Systolic pressure |
| TP | Transmural pressure |
| VHB | Visible human body |

Chapter 1 Background

1.1 Introduction

In the human body, blood is pumped into the arteries and then travels through the circulatory system. Blood pressure (BP) is the pressure exerted by the blood on the walls of the arteries [1]. The term BP as generally used in the medical area refers to arterial pressure. During each heartbeat, BP varies between systolic pressure (SP) and diastolic pressure (DP). SP is the peak pressure in the arteries, which occurs near the end of the cardiac cycle when the ventricles are contracting. DP is the minimum pressure in the arteries, which occurs near the beginning of the cardiac cycle when the ventricles are filled with blood. BP is not constant in the body, and it differs at various places. The pressure of the circulating blood decreases as blood passes through arteries, arterioles, capillaries, and veins. BP used in clinical practice is normally referred to the arterial pressure measured at the patient's upper arm without further specification. As BP is a powerful, consistent, and independent risk factor for cardiovascular and renal diseases [2]. It is one of the principal vital parameters and the most commonly clinically measured.

1.2 Clinical factors of BP

High BP, which is known as hypertension, is a medical condition in which the BP exceeds normal values. This disease is one of the most common ailments threatening people's health worldwide. It increases the risks of strokes, heart diseases, eye damage

and kidney failure. Systolic or diastolic BP measurements higher than accepted normal values for the age of individuals are classified as pre-hypertension or hypertension. Hypertension has several sub-classifications including, hypertension stage I, hypertension stage II, and isolated systolic hypertension [3]. The classification of hypertension is shown in Table 1-1.

Table 1-1 Classification of BP [3]

| Classification | SP | | DP | |
|--------------------------------|-------------|-------------|-------------|------------|
| | mmHg | kPa | mmHg | kPa |
| Normal | 90–119 | 12–15.9 | 60–79 | 8.0–10.5 |
| Prehypertension | 120–139 | 16.0–18.5 | 80–89 | 10.7–11.9 |
| Isolated systolic hypertension | ≥ 140 | ≥ 18.7 | < 90 | < 12.0 |
| Stage 1 (mild) | 140–159 | 18.7–21.2 | 90–99 | 12.0–13.2 |
| Stage 2 (moderate) | 160–179 | 21.3–23.9 | 100–109 | 13.3–14.5 |
| Stage 3 (severe) | 180–209 | 24–27.9 | 110–119 | 14.7–15.9 |
| Stage 4 (very severe) | ≥ 210 | ≥ 28 | ≥ 120 | ≥ 16 |

In New Zealand, one in five adults (males 18.0%, females 19.3%) has been reported suffering from hypertension [4]. Since there is no obvious cause in 90 ~ 95% of people who suffer from this disease, and there are often no obvious symptoms, many people have high BP for years without knowing it. The actual percentage of persons with hypertension might be higher than the reported value. As shown in Figure 1.1, hypertension is highly related to age. For people over 45 years of age, the number increases dramatically and reaches up to 50% for those are over 65 years of age. Therefore, all hypertension organizations recommend men over 50 and women over 55 years to check their BP regularly.

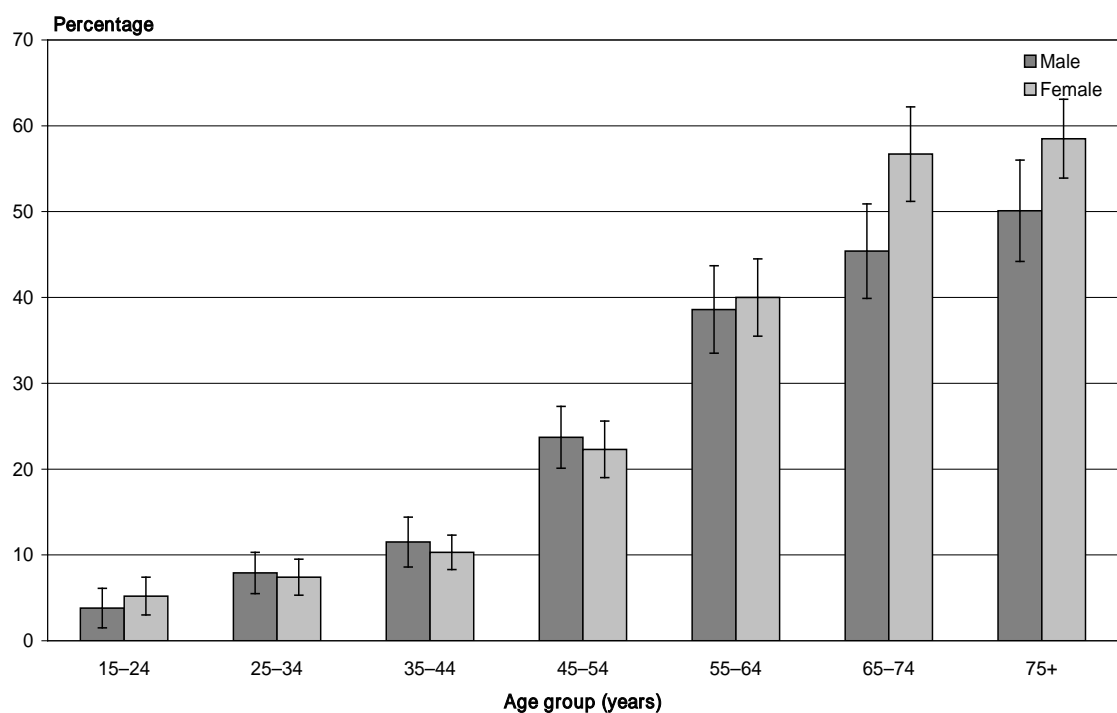


Figure 1.1 Identified high BP in adults, by age group and sex [4].

The level of BP is currently the main factor in hypertension diagnosis and the decision to start antihypertensive therapy. In normal healthy people, the desirable level of DP is about 75 mmHg. Any rise above that number is associated with an increase in adverse events: every 10 mm rise in DP will double the risk of heart attack, stroke, kidney

failure and heart failure. It has been shown that overestimation of DP by 5 mmHg would double the number of patients diagnosed with hypertension; conversely, underestimation by 5 mm Hg would reduce by around 60% the number of patients perceived as hypertensive [5, 6]. People who are identified incorrectly as having hypertension may experience adverse effects of medication and increase insurance and treatment costs. The underestimation of BP may cause misdiagnosis leading to delayed treatment and serious medical complications.

1.3 BP measurement

Accurate measurement of BP is essential in diagnosis and treatment of hypertension and ascertaining BP-related risk [2, 7]. BP is most accurately measured invasively by placing a catheter in the blood stream which has a high fidelity pressure transducer attached to its end. Since the invasive measurement method has a high associated risk, non-invasive methods for BP measurement are most commonly used in present clinical practice. They are simpler and quicker, produce less physical damage and require less expertise in fitting at the cost of slightly lower accuracy and small systematic differences in numerical results compared to invasive methods.

There are many kinds of non-invasive BP measurement methods available which include the auscultatory/Riva-Rocci/Korotkoff method, oscillometric method, volume clamp/vascular unloading method, tonometric method, and pressure pulse transit-time method [8]. Most of these methods are indirect and based mainly on measuring counter-pressure. The accuracy, popularity and suitable locations for these BP measurement methods are summarised in Table 1-2 and explained as follow.

Table 1-2 Summary of the mostly used BP measurement methods.

| Location | Method | Accuracy | Popularity |
|-----------|------------------------------------|--|--|
| Upper arm | Auscultatory method | SP: slight lower DP: slight higher | The most reliable non-invasive method in clinical practice |
| | Oscillometric method | Different from device to device, need to be validated first, average error at 1 ± 7 mmHg | Recently accepted and used in the clinical practice |
| Wrist | Oscillometric method | Different from device to device, not accurate enough for clinical using standard | Most of the wrist BP measurement device using this method |
| | Tonometric method | SP: 2.24 ± 8.7 mmHg, DP: 0.26 ± 8.88 mmHg, slight over the standard deviation of error | Some devices available for research purpose |
| | Pressure pulse transit-time method | Used to associate other BP measurement method | At research stage |
| Finger | Volume clamp method | SP: 3.1 ± 7.6 mmHg, DP: 4.0 ± 5.6 mmHg | At research stage |
| | Pressure pulse transit-time method | Used to associate other BP measurement method | At research stage |

The upper arm method required the use of inflatable cuff. Theoretically, this cuff can be placed on any part of the patient's limb using the auscultatory method or oscillometric method. Monitors that measure pressure at the wrist and fingers are becoming popular because they are smaller and can be easier to use in obese people [9]. However, they are less accurate and can only be used for domestic BP monitoring purpose. Since the upper arm measurements methods are the most commonly used, they will be elaborated as in following sections.

Clinical results show that SP and DP vary substantially in different parts of the arterial tree. In general, the SP increases in more distal arteries, whereas the DP decreases [10]. Experimental data have shown that upper arm non-invasive BP measurements at locations of the same vertical height as the heart give the most accurate readings [2, 8]. Table 1-2 shows that the auscultatory and oscillometric methods measured at the upper arm have the minimal errors among all of the non-invasive BP measurement methods and are well accepted in clinical practice.

1.3.1 Auscultatory method

Auscultatory method of BP measurement was firstly introduced by Riva-Rocci in 1896. In this method, firstly, air is pumped into the cuff thereby increasing the cuff pressure (CP) to a supra-systolic condition in which the artery is completely occluded (about 30 mmHg above SP). When the air pressure in the cuff is slowly released, a sound is detected by the stethoscope placed over the brachial artery in the antecubital fossa. This sound is known as the Korotkoff sound. SP and DP are then determined by the five phases of the Korotkoff sound [11]. Although this method has been used for more than 100 years, to date it is still the most accurate non-invasive BP measurement method. The diagrammatic presentation of this method is shown in Figure 1.2.

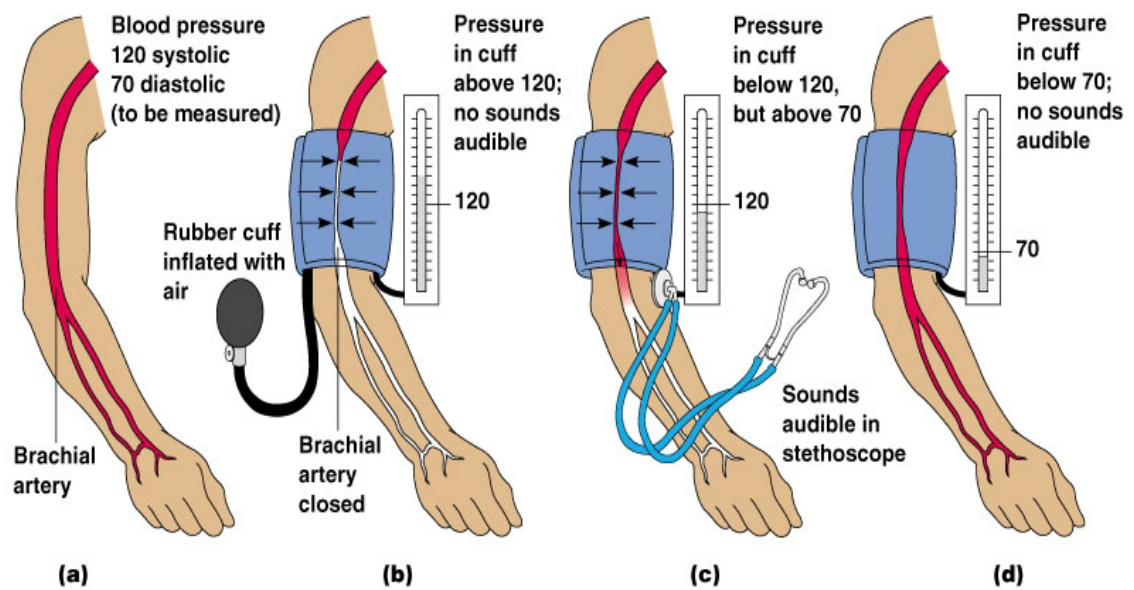


Figure 1.2 Auscultatory BP measurement process [12]

The auscultatory BP measurement consists of the following processes, see Figure 1.2.

- (a) selecting the proper cuff size for the patient, placing the cuff on the upper arm at roughly the same vertical height as the heart, and wrapping the cuff on the arm smoothly and snugly,
- (b) inflating cuff to about 30 mmHg above SP rapidly,
- (c) deflating at a rate of 2–3 mmHg per second and recording the auscultatory sounds,
- (d) finishing the measurement when the sound finally disappeared.

The observer then determines the patient's BP by the following five phases of auscultatory sounds in the measurement process [13].

Phase I: The first appearance of faint, repetitive, clear tapping sounds which gradually increase in intensity for at least two consecutive beats is the systolic BP

Phase II: A brief period may follow during which the sounds soften and acquire a swishing quality

Phase III: The return of sharper sounds, which become crisper to regain, or even exceed, the intensity of phase I sounds. The clinical significance, if any, to phases II and III has not been established

Phase IV: The distinct abrupt muffling of sounds, which become soft and blowing in quality

Phase V: The point at which all sounds finally disappear completely is the diastolic pressure

As described above, the auscultatory BP measurement technique is complicated and only suitable for clinic as assessment, which is normally conducted by professionally trained observers.

1.3.2 Oscillometric method

The measuring process of oscillometric method is similar to the auscultatory method. As shown in Figure 1.3, at the start of measurement, the cuff around a subject's limb is inflated to a pressure above SP and is then deflated in a controlled manner. During the process, the CP is monitored and recorded by the measuring device. The amplitude of pressure oscillations in the cuff increases gradually until maximum amplitude near the mean pressure (MP) is reached and then decreases until the end of the measurement. The SP and DP are then calculated by algorithms or characteristic ratio specific to the manufacturer [11]. Since the algorithm is different from manufacturer to manufacturer, the accuracy of the oscillometric devices are different.

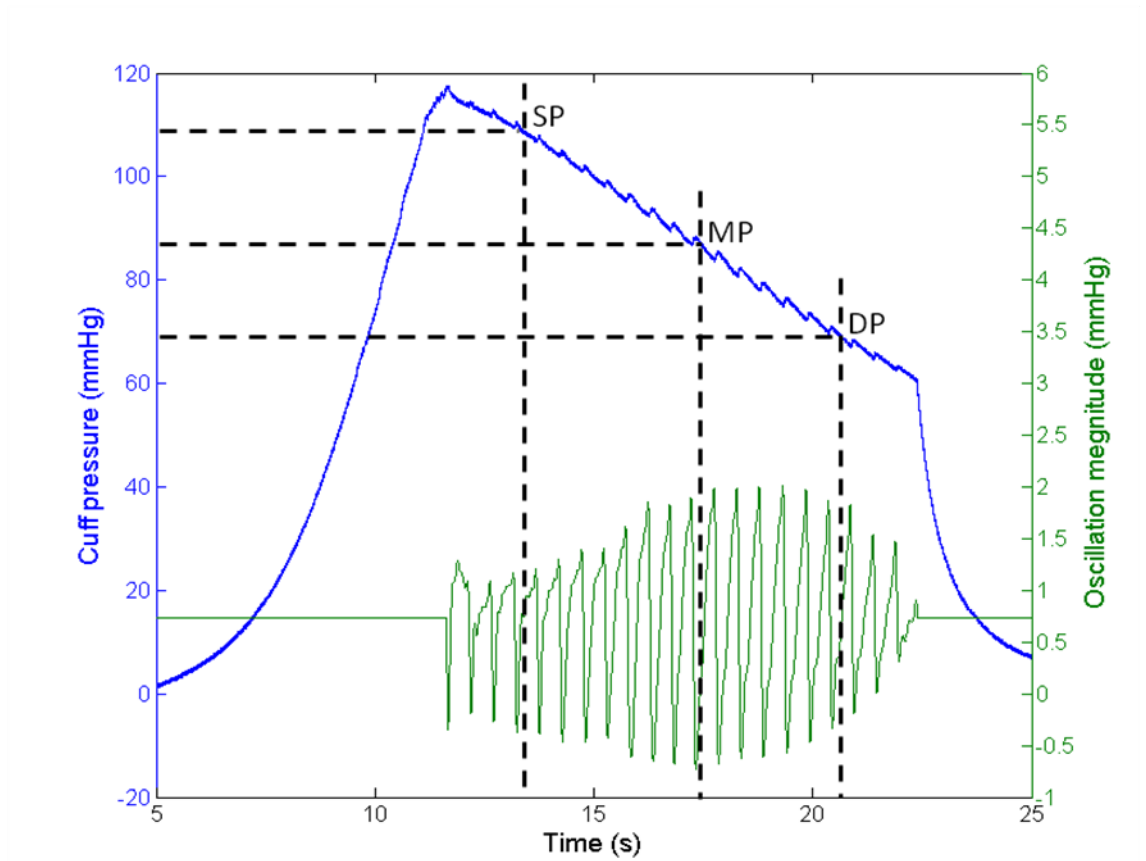


Figure 1.3 Typical clinical data in oscillometric BP measuring process:
— measured CP, — pressure oscillation after filtering

The overall accuracy of the oscillometric method is less than the auscultatory method and the main problem with this technique is that the amplitude of oscillations depends on several factors other than BP such as the stiffness of the arteries [14]. For example, in older people with stiff arteries and wide pulse pressures, MP identified by oscillometric method may be significantly underestimated and consequently the measured BP is underestimated [15]. However, this method is widely used in automated BP measurement devices, because it does not require professional training and gives reasonable measurement accuracy.

1.3.3 Ambulatory BP measurement

The control of BP requires appropriate diagnosis and antihypertensive therapy, which is based on accurate BP measurements. However, in-office BP measurements, which have been used for more than 50 years, have clinically shown relevant shortcomings, such as what is called the white coat hypertension. This can be explained by the fact that a patient's BP is elevated during the examination process due to nervousness and anxiety caused by being in a clinical setting [16]. Recent studies have shown that the end-organ damage associated with hypertension is more strongly correlated with Ambulatory BP monitoring than with traditional clinic BP measurements and useful for diagnosing white-coat hypertension [17-19]. Ambulatory monitoring is the BP measurement method which measures patients' BP at regular interval for 24 or 48 hours during their daily lives. Furthermore it is a more accurate way to detect a patient's BP and helpful in the evaluation of drug resistance and medication compliance [18].

Although the auscultatory method using the standard mercury sphygmomanometer is the most accurate device for non-invasive BP measurement [20], the oscillometric method is more suitable for self-monitoring using automatic devices, as it requires less professional training and is less susceptible to external noise. Therefore, most of the ambulatory BP monitoring devices use the oscillometric technique.

In comparison with typical measurements made under motionless conditions at the clinic or home, the ambulatory BP monitoring process sometimes needs to be conducted during activities such as working, talking, eating, walking and sports activities. During the measurement process, the current ambulatory BP monitoring devices require the patients to interrupt their activities and remain stationary until the process has completed.

There are some non-invasive BP devices which claim to compensate for motion artefacts [21-23]. However, most of these devices measure the arterial pressure at the wrist, which have been approved to be less accurate than the measurement at the upper arms. Also, they are not suitable for ambulatory BP monitoring [24]. Therefore, the need for ambulatory devices which are insensitive to arm motions and environmental tremors is essential for better accuracy.

1.4 Thesis overview

- Chapter 1 introduces the clinical factors of BP and the most popular BP measurement methods.
- Chapter 2 lists the mechanical analysis of oscillometric BP measurement and available model models of BP measurement in the literature.
- Chapter 3 states numerical implementation of finite element method.
- Chapter 4 describes the details of developed finite element models including the justifications of material properties, geometries, and etc.
- Chapter 5 illustrates the experiments for model validation and investigation.
- Chapter 6 shows theoretical analysis oscillometric BP measurement method and demonstrates proper sensor array to detect external tremors.
- Chapter 7 presents the clinical experiment results and shows the methodology of eliminating external noises.
- Chapter 8 gives conclusion and future work of this study.

Chapter 2 Literature Review

2.1 Introduction

As stated above, the oscillometric method is the most widely-used method in automatic BP measurement devices. In the measurement, CP oscillations and values obtained during the cuff deflating process are recorded and used to determine the subject's BP. The maximum amplitude pressure algorithm is one of the most commonly used techniques in the current available devices [25]. However there is still no specific standard procedure for this method such as the five-phase procedure in auscultatory method. Some theoretical analyses of oscillometric BP measurement have been developed to study the relationship between BP and pressure oscillation in the cuff. The literatures on these techniques are elaborated in the following sections.

2.2 Mechanical analysis of oscillometric measurement process

The basic principle for the oscillometric method is based on the fact that the subject's BP leads to artery deformation which transfers to the cuff in the form of CP oscillation. This deformation can be detected by pressure sensors connected to the cuffs, and then the subjects' BPs can be determined by the device [2, 14, 26, 27].

There many different types of oscillometric BP measuring devices available in the market nowadays. Different manufacturers claim that their devices have unique algorithms to determine BP. As all these devices share the same oscillometric

measurement process, their results are based on analyzing the relationship between BP in the brachial artery and pressure oscillations in the cuff as show in Figure 2.1.

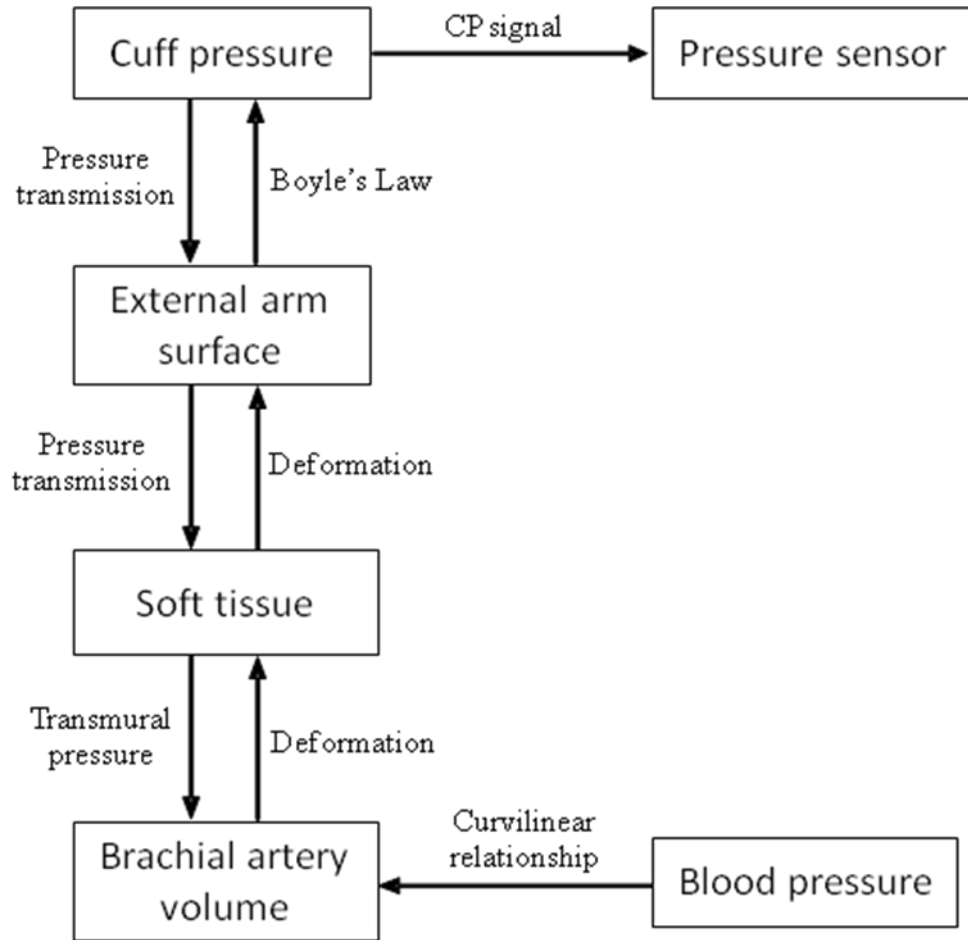


Figure 2.1 Flow chart of signal transmission in the oscillometric BP measurement

2.2.1 CP transmission

Since the cuff is wrapped on the arm smoothly and snugly, it is assumed that CP transfers to arm surface evenly without any pressure loss [28, 29]. Therefore, the pressure acting on the arm surface equals to CP which transfers through the soft tissue to the external surface of the brachial artery as an extra-vascular pressure. The brachial artery closure status is determined by the transmural pressure (TP), which is defined as BP in the brachial artery minus extra-vascular pressure on the external surface of the

brachial artery. Since the extra-vascular pressure is usually unknown, in practice it is replaced by CP and TP is then defined as the intra-artery pressure (BP) minus the external CP [30-32].

2.2.2 BP transmission

In the measurement process, CP variation is below 5 mmHg during each heart beat. Pulse pressure, which is the difference between SP and DP, is normally over 30 mmHg. Therefore, the TP changes over 25 mmHg and leads to a dramatic artery volume change under the cuff. As shown in Figure 2.1, the artery volume changes transfer through the arm soft tissue to the cuff which normally leads to pressure oscillations in the cuff. Therefore, several TP-volume models have been developed and used to study oscillometric method [33, 34]. Since artery deformation was assumed uniform along the longitudinal direction, brachial artery volume is normally replaced by lumen area (A). Therefore, CP oscillations are dominated by the brachial artery lumen area changes and thus the oscillometric method is associated with TP-A relationships [30, 35, 36].

2.3 Theoretical analysis of non-invasive oscillometric BP measurement

The maximum amplitude algorithm is the most popular algorithm in oscillometric BP measurement [37, 38]. There have been many studies on theoretical analysis of oscillometric algorithm in the last 40 years [30, 33, 34, 37-39]. These studies implement at various assumptions and different theoretical approaches as explained below.

2.3.1 Artery models

Some previous studies [30, 32, 39-41] considered that the maximum CP oscillation during the measurement is due to the bulking of the brachial artery under the cuff. Drzewiecki *et al* [30] developed a mathematical model to describe TP-A relationship in oscillometric BP measurement. They also conducted some clinical experiments on isolated canine arteries. Their theoretical results matched their experimental data quite well. Their results showed that the buckling of an artery under CP occurs near -2 to 0 mmHg transmural pressure. This result corresponds with a maximum arterial compliance and maximum CP oscillations when the CP is nearly equal to MP.

In 1997, Drzewiecki *et al* [41] expanded their model considering more artery mechanical properties and compared it with the experimental results on latex tubes and different arteries. Their results demonstrated that TP-A relationship was highly related to the mechanical properties of the artery such as the artery wall thickness and stiffness. Therefore, any condition that change the artery thickness or affects their elasticity will affect the accuracy of oscillometric BP measurement. Similar conclusions were confirmed in other studies [42-44].

All of these studies were conducted on isolated arteries. In reality, CP has to transmit through the soft tissues between the cuff and the brachial artery. Therefore, the TP-A relationship is also affected by the properties of these tissues.

2.3.2 Arm model

Several mathematical arm and cuff models have been developed to study the biomechanical factors which might affect the accuracy of oscillometric BP measurement.

The earliest and simplest arm model for non-invasive BP measurement was built in 1992 [45] which consisted of isotropic elastic tissues and a rigid bone. To keep the geometry of the model symmetrical, the artery was not presented in this model. The results indicated that the pressure transmission across the arm was significantly influenced by the elasticity of the arm tissue. In 1996, a more completed arm and cuff model was built [36]. This model included cuff compliance, pressure transmission from the cuff to the brachial artery through the soft tissue of the arm, and the biomechanics of the brachial artery. To simplify the model, the artery was replaced by a thin layer of volume uniformly distributed on the bone's external surface. Therefore, the calculated pressure on the bone surface was treated as the extra-vascular pressure. The artery deformation under the cuff was calculated using the tube law same as Drzewiecki's model. This model indicated that the alterations in the mechanical properties of the arm tissues may significantly affect the accuracy of BP estimation.

In all above mathematical models, there are some drawbacks. They are

- (1) The extra-vascular pressure was assumed uniform along the artery.
- (2) The artery was assumed isolated from the surrounding tissue and its deformation was calculated as a thick wall tube.
- (3) Cylindrical axisymmetric geometries were used in these models.

To overcome these drawbacks, some other modelling techniques were used.

2.4 Finite element analysis

There are many methods and software available for human body analysis. The finite element (FE) method is currently one of the best established numerical tools in the field of biomedical engineering and especially useful for estimating the biomechanical

performance of complex biological structures. All of FE models used in the literature were developed following similar process: (1) creating the geometry, (2) defining material properties, (3) determining boundary conditions and interactive properties, (4) applying loading.

2.4.1 Model geometry

In order to create anatomically accurate geometrical data for FE analysis, the magnetic resonance (MR) image or Visible Human Body (VHB) dataset were used in previous studies [46-49].

Most MR images use greyscales to identify the soft tissue. In an MR image, if an area is presented in the same grey grade, the tissue of this area can be considered as having similar mechanical properties [50]. In the analysis of human body's mechanical performance, tissue with similar mechanical properties can be considered to be the same material. The contour line of each area is defined as the edge between different tissues. Although there was a program developed for transferring MR images into input data for FE models [49], the obtained geometries were still required to be verified by experienced researchers with anatomic background. As shown in Figure 2.2, the contour line between ulna and surrounding tissue is clearly shown in this MR image. To get an accurate model, these contours have to be manually modified before exporting to FE software.

The VHB dataset gives much more details of the human anatomic structure and is becoming a common standard for researchers [51]. Since the VHB dataset includes coloured images as shown in Figure 2.3, it is easier to identify the tissue materials and boundaries.

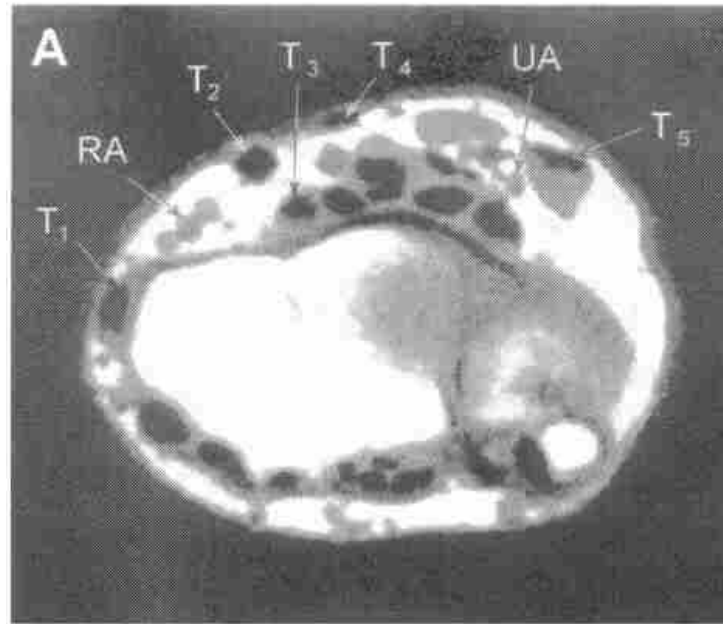


Figure 2.2 MR image of the right wrist [52]

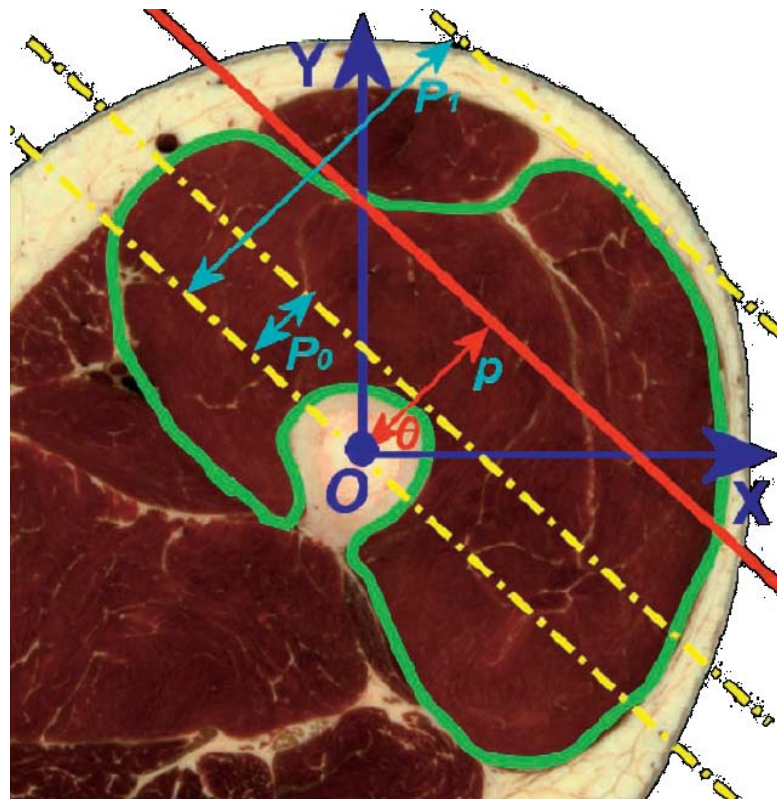


Figure 2.3 A sample of upper arm from VHB dataset [53]

Using the VHB dataset, many 3-D models of human limbs have been developed, including the lower limb [48], the upper arm [47], and the upper limb [46]. All of these models focus on creating and analysing the skeletal muscles rather than representing the entire limb. However, the VHB datasets are developed based on specific subjects and they are not suitable to simulate for general purpose applications.

2.4.2 Material properties of human tissue

Theoretically, the human tissue's property is nonlinear anisotropic viscoelastic material [54]. Referring to the image shown in Figure 2.3, the upper arm mainly consists of four types of materials: fat and skin, muscle, artery and bone. The bone is much stiffer than soft tissues and normally is considered rigid in most of previous researches [36, 45, 55, 56]. In all of the mathematical models of the human body, some simplifications of the tissue materials were made in order to achieve a balance between the computational cost and accuracy. Some simplifications of the soft tissue are summarized in Table 2-1.

Looking into the detailed structure of the four materials, while fat and skin tissues have no preferred direction and therefore are usually considered to be isotropic, muscle and artery tissues have a highly fibrous nature which presents anisotropic properties [54, 57]. The fibre direction in the muscle is closed to uniform, so, the muscle tissue is usually considered to be a transverse isotropic material. However, the artery is composed of an intima-media layer and an adventitial layer. Because the fibre directions in these two layers are quite different, artery materials have different properties in the three axes [54, 58], and it is an orthotropic material.

Table 2-1 Commonly used material properties for human tissues

| | Linear Isotropic | Nonlinear isotropic | Nonlinear transverse isotropic | Nonlinear anisotropic |
|-------------------------------|--|---|--|---|
| Required parameter | 1. Young's modulus, 2. Poisson's ratio | 1. Stress-strain (S - ϵ) relationship, 2. Poisson's ratio | 1. S - ϵ relationship on longitudinal direction, 2. S - ϵ relationship on transverse direction 3. Poisson's ratio on longitudinal direction, 4. Poisson's ratio on transverse direction | 1-3. S - ϵ relationship on each direction 4-6. Poisson's ratio on each direction, |
| Fat & skin | Mostly used [59, 60] | Used in the large deformation | Not used in the published literature | Not used in the published literature |
| Muscle | Used in simple models [61] or with small deformation | Used when just considering the transverse deformation [36] | Mostly used [48, 56, 62] | Seldom used |
| Artery | Seldom used | Usually used in the simplified model [36] | Seldom used | Used when investigating the artery's mechanical performance [58, 63] |

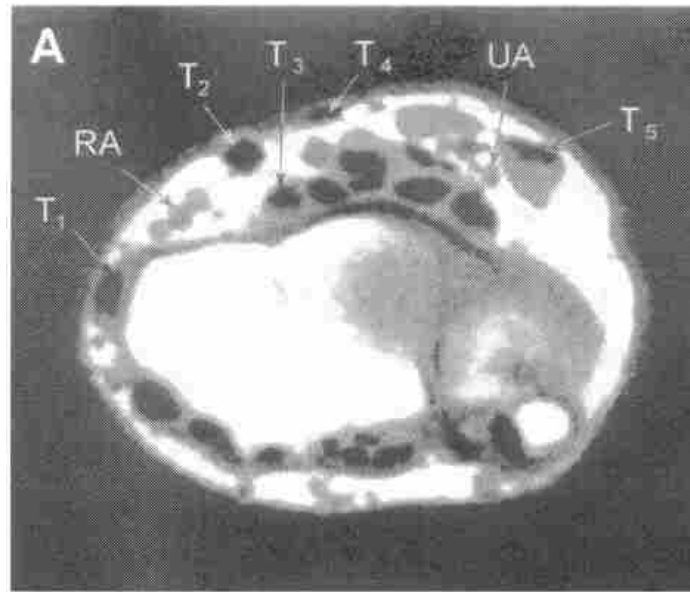
2.4.3 Other conditions

Since there is relatively no motion between the bone and soft tissues, the muscles are always assumed fixed to the bone [45, 55, 56]. The other conditions such as boundary and loading conditions are determined according to the particular simulating conditions.

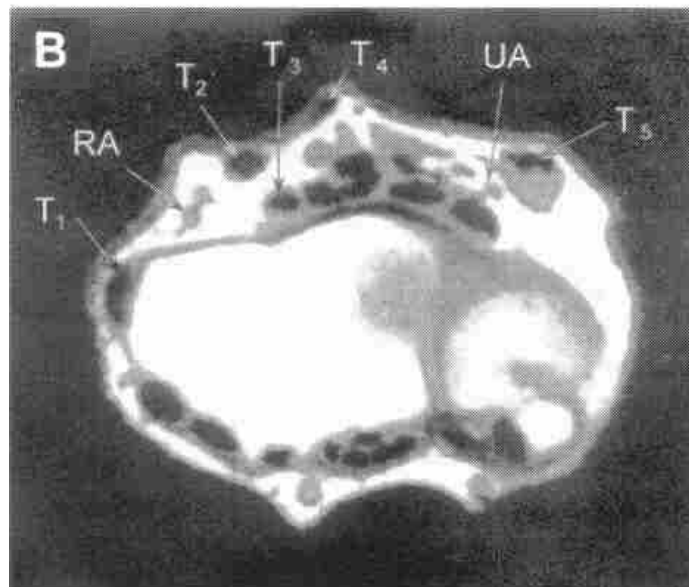
2.4.4 Current models

To the best of our knowledge, currently, there is no model with more realistic geometry of the upper arm available in the open literature. In contrast, some anatomically accurate FE models of other parts of the human's upper limb were built for analyzing the pressure transmission in the soft tissue during the oscillometric BP measurement process [52, 64]. The geometry of the model was established from the MR image of the cross-section scan of human's wrist as shown in Figure 2.4a. Although the wrist contains many different types of tissues, they were classified into four types of materials based on their mechanical properties. They were skin and connective tissue, muscle, tendon and bone. Therefore, the whole model consisted of four types of parts. As shown in Figure 2.4c, different parts of the wrist were represented by the coloured blocks in the model.

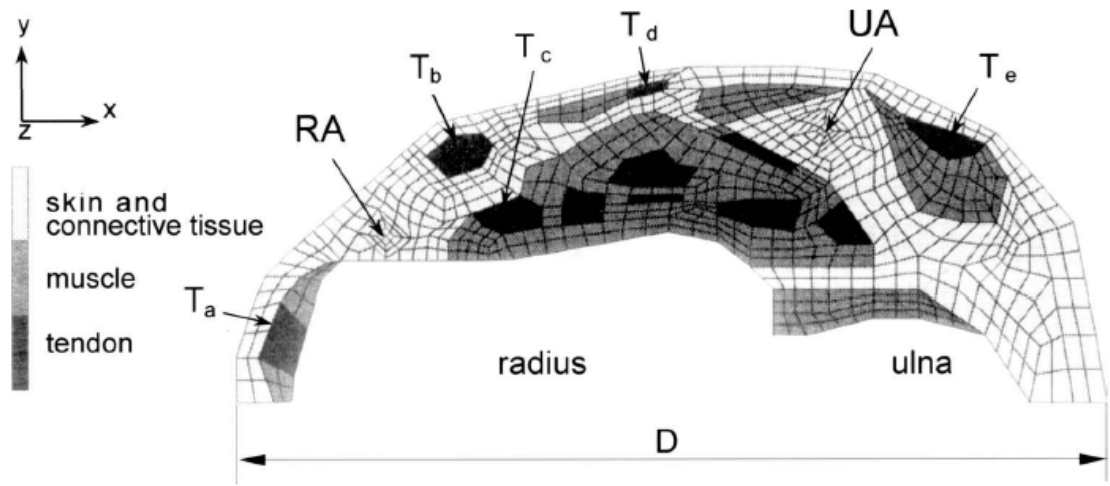
Since the bones are much stiffer than the soft tissues, in this work they were replaced by rigid boundary conditions in this model[52, 64]. Except for the bone parts, all of the soft materials were assumed linear elastic and isotropic. This linear elastic assumption is only reasonable for relatively small strains but must be modified if large displacements are applied [65]. Since most of the deformations under compression were small in the model as shown in Figure 2.4b, the material assumption was acceptable in this model. To get the volume change in the artery, a 3-D model of the wrist was constructed by extending the 2-D FE model in the longitudinal direction as shown in Figure 2.4d [66]. Some other parts of the human body were also built up using similar techniques [67-69].



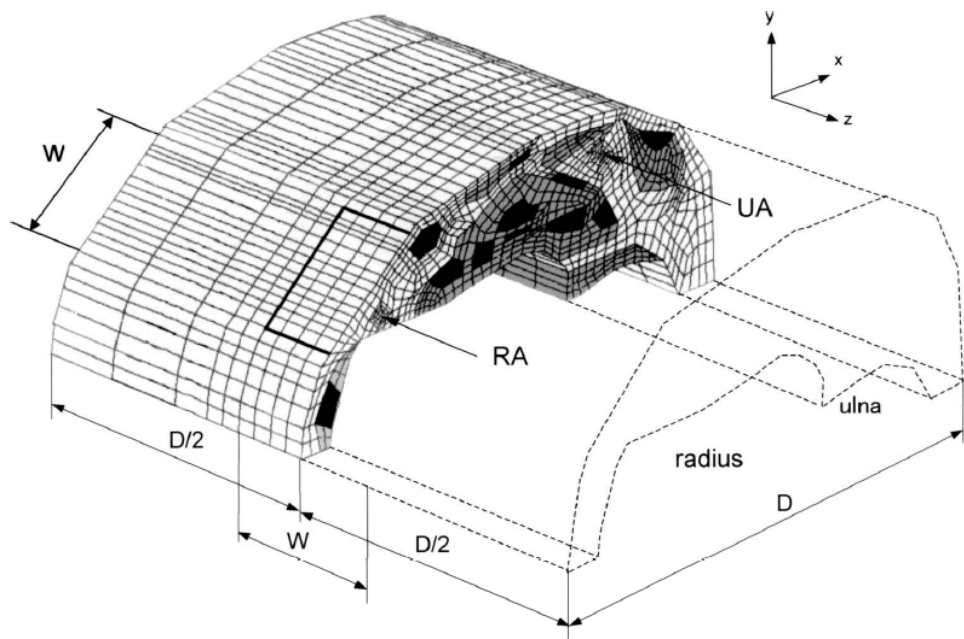
a



b



c



d

Figure 2.4 (a) MR image of the right wrist; (b) MR image of the same wrist under inflated cuff; (c) 2D FE model of right wrist: the light grey, dark grey and black shades represent skin and connective tissue, muscle, and tendons, respectively; (d) 3D model of right wrist [constructed by extending the 2-D . finite-element model at site L in the longitudinal (z) direction] [52, 66]

2.5 Closure

This chapter gives a thorough and comprehensive literature survey to summarise many different types of theoretical models which have been developed to investigate the oscillometric BP measurement. The material properties and classification stated in this chapter were obtained from the literature and already validated against the realistic tissue. The applied material classification and used material properties were proven valid. Among current available mathematical models on the oscillometric method, the following points are weakly treated in the available literature:

1. The brachial artery is assumed to be isolated from the arm in the available models. Brachial artery deformations are calculated following the tube law. The effects of surrounding tissue are ignored.
2. Only symmetrical cylindrical geometries are used.
3. Uniformly distributed pressure is applied on the external surface of the artery.
4. Lack of geometry accurate models.

With these assumptions and simplifications, available models are valid only for limited conditions. The main conclusion is that there is no model with more realistic geometry to investigate the oscillometric BP measurement.

2.6 Objectives

Since combining the oscillometric method with the arm in an accurate model form is complicated and it requires better understanding and knowledge of the overall system, the modelling process in this research is undertaken in two steps: first developing a simple model to give a good understating of the oscillometric method in the arm and to help setting the necessary conditions and assumptions of a more accurate model which

is developed in the second stage of this research. To overcome the weaknesses in the current available models, the main aims of this study are:

1. Develop a simplified FE model to study the effects of the following factors in oscillometric method: (a) brachial artery stiffness, (b) soft tissue stiffness and compressibility
2. Build a simulation rig to validate the established model.
3. Develop a more accurate FE model including more realistic geometry and material properties.
4. Conduct clinical trials to validate the model.
5. Investigate the effect of arm motions as disturbance to measurements and method of eliminating them.

Chapter 3 Numerical Formulation

3.1 Introduction

In the proposed model, fat, skin, connective tissues, muscle and artery are simulated. Since the active motion of the muscle will bring many uncertain changes such as large deformation and stiffness changes, it is not practical to simulate active motion in this research and only the passive muscle behaviour is considered in the model. Therefore, the following types of materials are assumed: isotropic linear material, transverse isotropic linear material and isotropic nonlinear material. In this chapter, the basic mechanical quantities of nonlinear continuum mechanics are introduced followed by discussion of FE implementation.

3.2 Continuum model

In the model, the following types of materials are considered: (1) isotropic linear material for fat, skin and connective tissues, (2) transverse isotropic linear material for muscle (3) nonlinear material for muscle with passive behaviour and artery. To mesh the model, tetrahedral element is used for the model with irregular geometry.

3.2.1 Material

In continuum model, the object consists of many points. To track the motion of the object, each material point is labelled by a position X in the initial object shape. The material point is mapped by function Φ to a new position x , which varies as time t .

$$x = \phi(X, t) \quad (3.1)$$

As shown in Figure 3.1, Φ determines the geometry of the subject. When relating initial material point X to its current point x through the deformation gradient F which is the key quantity in continuum model, their relationship is expressed by Equation (3.2).

$$\partial x_i = F_{ij} \partial X_j \quad (3.2)$$

where x_i is the i -th component of position vector in the deformed state and X_j is the j -th component of position vector in the undeformed state.

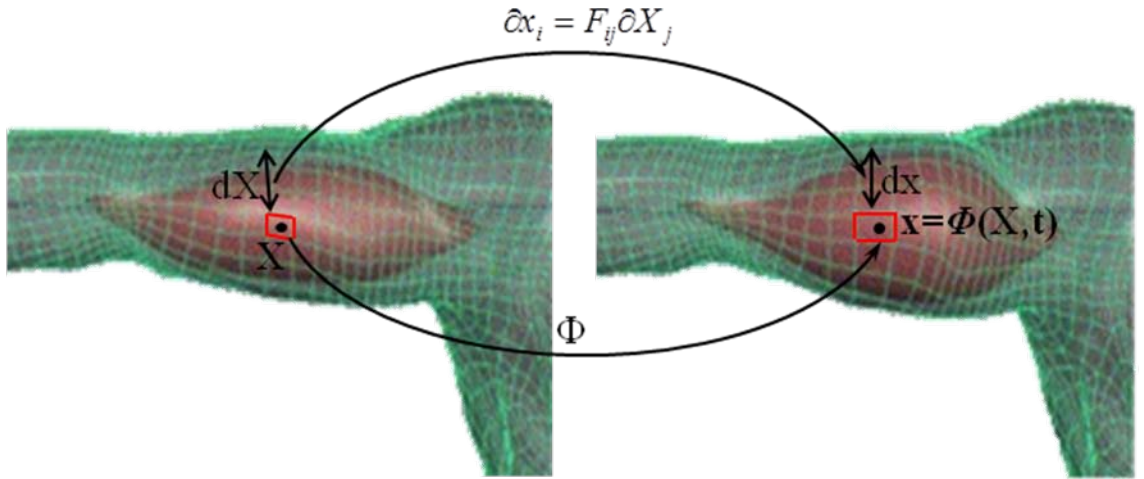


Figure 3.1 Model deformation function in continuum model

Then the total volume change at the point is expressed as

$$J = \det F \quad (3.3)$$

For simplicity, the modified deformation gradient is defined as

$$\bar{F} = J^{-1/3} F \quad (3.4)$$

The Right Cauchy-Green Deformation Tensor C is defined as

$$C = \bar{F}^T \bar{F} \quad (3.5)$$

Then, the Green-Lagrangian Strain Tensor E is written as

$$E = \frac{1}{2}(C - I) \quad (3.6)$$

where I is the identity tensor.

In linear continuum mechanics, the dominate quantities are the Cauchy stress tensor σ and the conjugated strain tensor ϵ ,

$$\sigma = [H]\epsilon \quad (3.7)$$

where $[H]$ is the stiffness of the material. Since the deformation is very slow during cuff based BP measurement process, viscosity of the tissue materials is not considered in this model. In anisotropic material, $[H]$ is a 6×6 symmetric matrix with 21 independent constants. For the case of transverse isotropic material about the y axis, the matrix of $[H]$ could be expressed in terms of five independent mechanical constants [70]. The stress tensor is expressed as,

$$\sigma = \left(\sigma_x \quad \sigma_y \quad \sigma_z \quad \sigma_{xy} \quad \sigma_{yz} \quad \sigma_{zx} \right)^T \quad (3.8)$$

the strain as,

$$\varepsilon = \begin{Bmatrix} \partial u / \partial x \\ \partial v / \partial y \\ \partial w / \partial z \\ \partial y / \partial x + \partial x / \partial y \\ \partial z / \partial y + \partial y / \partial z \\ \partial x / \partial z + \partial z / \partial x \end{Bmatrix} \quad (3.9)$$

and the material stiffness in ABAQUS is described by H_{ijkl} ,

$$[H] = \begin{pmatrix} E_{1111} & E_{1122} & E_{1133} & 0 & 0 & 0 \\ & E_{2222} & E_{2233} & 0 & 0 & 0 \\ & & E_{3333} & 0 & 0 & 0 \\ & & & E_{1212} & 0 & 0 \\ & \text{symm} & & & E_{2323} & 0 \\ & & & & & E_{3131} \end{pmatrix} \quad (3.10)$$

where i, j, k, l are the directions of the selected element. For the selected solid elements used in this simulation, the 1-, 2- and 3-directions are the same as default global spatial x-, y- and z-directions. For the case of isotropic material, the matrix of $[H]$ could be expressed in terms of two independent mechanical constants. Because there is standard expression of isotropic material in ABAQUS, the material matrix of isotropic materials is not introduced in details.

Since Cauchy stress tensors are defined in the deformed configuration, it is not practical to use for nonlinear continuum mechanics, whose quantities are varied to body deformations. To simulate the muscle passive behaviour, the second Piola-Kirchhoff stress tensor S is used in nonlinear continuum mechanics.

$$S = \frac{\partial W(E)}{\partial E} = 2 \frac{\partial W(C)}{\partial C} \quad (3.11)$$

For the nonlinear elastic strain energy function, W is written in terms of invariants

I_E, II_E, III_E of the Green-Lagrange Strain Tensor E as

$$W(E) = W(I_E, II_E, III_E) \quad (3.12)$$

where

$$\begin{aligned} I_E &\equiv \text{trace}(E) \\ II_E &\equiv \frac{1}{2}(I_E^2 - \text{trace}(EE)) \\ III_E &\equiv \det(E) \end{aligned} \quad (3.13)$$

Since the artery is almost incompressible, the New-Hookean hyperelastic material property is used in the description of the brachial artery. In New-Hookean hyperelastic material, the strain energy density function is

$$U = U(I_1, I_2, J) = C_{10}(I_1 - 3) + \frac{1}{D_1}(J - 1)^2 \quad (3.14)$$

where I_1 , I_2 and J are the three strain invariants, expressed in the terms of the left Cauchy-Green tensor,

$$\begin{aligned} J &\equiv \det(F) \\ \bar{B} &= \bar{F} \cdot \bar{F}^T \\ I_1 &\equiv \text{trace}(\bar{B}) \\ I_2 &\equiv \frac{1}{2}(I_1^2 - \text{trace}(\bar{B} \cdot \bar{B})) \end{aligned} \quad (3.15)$$

The relationship between Cauchy stress and deformation gradient is

$$\sigma_{ij} = \frac{2}{J} C_{10} (\bar{B}_{ij} - \frac{1}{3} \delta_{ij} \bar{B}_{kk}) + \frac{2}{D_1} (J - 1) \delta_{ij} \quad (3.16)$$

Since the Kirchhoff stress is defined as

$$\tau_{ij} = J\sigma_{ij} \quad (3.17)$$

the material Jacobian derives from the variation in Kirchhoff stress is

$$\delta\tau_{ij} = JC_{ijkl}\delta D_{kl} \quad (3.18)$$

where C_{ijkl} are the components of the Jacobian, and

$$\delta D_{ij} = \frac{1}{2}(\delta F_{im}F_{mj}^{-1} + F_{mi}^{-1}\delta F_{jm}) \quad (3.19)$$

Using the Neo-Hookean model, the Jacobian matrix of the artery material is defined.

$$\begin{aligned} C_{ijkl} = & \frac{2}{J}C_{10}\left(\frac{1}{2}(\delta_{ik}\bar{B}_{jl} + \bar{B}_{ik}\delta_{jl} + \delta_{il}\bar{B}_{jk} + \bar{B}_{il}\delta_{jk}) - \right. \\ & \left. \frac{2}{3}(\delta_{ij}\bar{B}_{kl} + \bar{B}_{ij}\delta_{kl} - \frac{1}{3}\delta_{ij}\delta_{kl}\bar{B}_{mm})) + \frac{2}{D_1}(2J-1)\delta_{ij}\delta_{kl} \right. \end{aligned} \quad (3.20)$$

3.2.2 Element

Since the model is designed to simulate the arm with anatomically accurate geometry, the tetrahedral element is used in the model which is one of the simplest and practical ways to mesh the complicated geometry.

The state of displacement of a point is defined by three displacement components, u , v , and w , in the directions of the three coordinates x , y , and z respectively. Thus

$$U = \begin{Bmatrix} u \\ v \\ w \end{Bmatrix} \quad (3.21)$$

Using the finite element concept, the displacements within an element have to be uniquely defined by these twelve values ($a_1 \sim a_{12}$). The simplest representation is clearly given by three linear polynomials

$$\begin{cases} u = a_1 + a_2x + a_3y + a_4z \\ v = a_5 + a_6x + a_7y + a_8z \\ w = a_9 + a_{10}x + a_{11}y + a_{12}z \end{cases} \quad (3.22)$$

As shown in Figure 3.2, i, j, m, p are four nodes on the tetrahedral element.

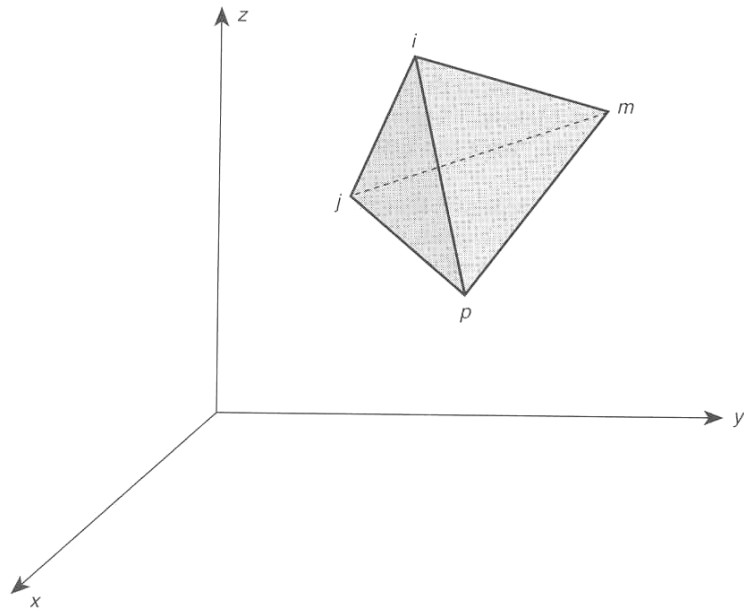


Figure 3.2 A tetrahedral element is shown in the co-ordinate system.

Equating the values of the displacements of the nodes in u direction in the default co-ordinate system, we have four equations of the type

$$\begin{cases} u_i = \alpha_1 + \alpha_2 x_i + \alpha_3 y_i + \alpha_4 z_i \\ u_j = \alpha_1 + \alpha_2 x_j + \alpha_3 y_j + \alpha_4 z_j \\ u_m = \alpha_1 + \alpha_2 x_m + \alpha_3 y_m + \alpha_4 z_m \\ u_p = \alpha_1 + \alpha_2 x_p + \alpha_3 y_p + \alpha_4 z_p \end{cases} \quad (3.23)$$

The displacement field can be written for each element as

$$\begin{cases} u = N_i u_i + N_j u_j + N_m u_m + N_p u_p \\ v = N_i v_i + N_j v_j + N_m v_m + N_p v_p \\ w = N_i w_i + N_j w_j + N_m w_m + N_p w_p \end{cases} \quad (3.24)$$

The interpolation function (shape function) N_i , N_j , N_m , N_p , consists of four linear polynomials, defining the shape of the displacement field for each tetrahedral element.

In this model the linear shape functions are assumed to be

$$\begin{cases} N_i = \frac{(a_i + b_i x + c_i y + d_i z)}{6V} \\ N_j = -\frac{(a_j + b_j x + c_j y + d_j z)}{6V} \\ N_m = \frac{(a_m + b_m x + c_m y + d_m z)}{6V} \\ N_p = -\frac{(a_p + b_p x + c_p y + d_p z)}{6V} \end{cases} \quad (3.25)$$

where V is the volume of the element which can be calculated by

$$V = \frac{1}{6} \det \begin{vmatrix} 1 & x_i & y_i & z_i \\ 1 & x_j & y_j & z_j \\ 1 & x_m & y_m & z_m \\ 1 & x_p & y_p & z_p \end{vmatrix} \quad (3.26)$$

and a_i , b_i , c_i , d_i are coefficients calculated from the nodal coordinates.

$$a_i = \det \begin{vmatrix} x_j & y_j & z_j \\ x_m & y_m & z_m \\ x_p & y_p & y_p \end{vmatrix} \quad b_i = -\det \begin{vmatrix} 1 & y_j & z_j \\ 1 & y_m & z_m \\ 1 & y_p & y_p \end{vmatrix} \quad (3.27)$$

$$c_i = -\det \begin{vmatrix} x_j & 1 & z_j \\ x_m & 1 & z_m \\ x_p & 1 & y_p \end{vmatrix} \quad d_i = -\det \begin{vmatrix} x_j & y_j & 1 \\ x_m & y_m & 1 \\ x_p & y_p & 1 \end{vmatrix}$$

The shape function can be determined by substituting Equation (3.27) into Equation (3.26). The stiffness and mass matrices will be defined in ABAQUS. The nodal force vector acting on each element is the aerodynamic pressure force, which can be calculated from Equation (3.7) by using the corresponding nodes.

3.2.3 Equilibrium Equations of the Model

The following sections state the equilibrium equations of motion and definitions to solve the finite element model. For infinitesimal displacements in an elastic continuum object, Newton's second law of motion is written as

$$\begin{cases} \frac{\partial \sigma_x}{\partial x} + \frac{\partial \tau_{xy}}{\partial y} + \frac{\partial \tau_{zx}}{\partial z} + F_x = \rho \frac{\partial^2 u}{\partial t^2} \\ \frac{\partial \tau_{xy}}{\partial x} + \frac{\partial \sigma_y}{\partial y} + \frac{\partial \tau_{yz}}{\partial z} + F_y = \rho \frac{\partial^2 v}{\partial t^2} \\ \frac{\partial \tau_{zx}}{\partial x} + \frac{\partial \tau_{yz}}{\partial y} + \frac{\partial \sigma_z}{\partial z} + F_z = \rho \frac{\partial^2 w}{\partial t^2} \end{cases} \quad (3.28)$$

where u , v and w are displacements in the x , y and z directions; ρ is the density of the material; σ_i are normal stresses; τ_{ij} are shear stresses ($i, j = x, y, z$); and F_x , F_y and F_z are the body forces. Consequently, the general tissue displacement vector about the equilibrium position is written as

$$\Psi(x, y, z, t) = u(x, y, z, t)i + v(x, y, z, t)j + w(x, y, z, t)k \quad (3.29)$$

Equations (3.28) and (3.29) contain both stresses and displacements as variables. To solve the equations, either stresses or displacements should be chosen and converted to the others. The model of upper arm needs spatial resolution that is capable of representing the tissue movement during the BP measurement process. Therefore, it is more appropriate to use displacements as variable in this research. The relationship between stresses and displacements depends on the nature of the material.

However, using stress-displacement equations are too involved and a bit complicated to solve explicitly. Another numerically oriented approach is normally used. Virtual work principle is the numerically oriented approach of motion. Problems of elasticity are intimately related to the energy principles which define equilibrium conditions. The concept of energy principles is very important in the solution of elasticity problems. The potential energy of the deformed vibrating continuum is

$$\pi = U - W_p \quad (3.30)$$

where U is the strain energy calculated from energy density as

$$U = \iiint_v \frac{1}{2} (\sigma_x \varepsilon_x + \sigma_y \varepsilon_y + \sigma_z \varepsilon_z + \tau_{xy} \gamma_{xy} + \tau_{yz} \gamma_{yz} + \tau_{zx} \gamma_{zx}) dV \quad (3.31)$$

and W_p is the virtual work defined as,

$$W_p = \iiint_v (F_x u + F_y v + F_z w) dV + \iint_A (S_x u + S_y v + S_z w) dA \quad (3.32)$$

In Equation (3.32), F_x, F_y, F_z are components of the body force (inertia) and S_x, S_y, S_z are components of the surface forces. The equations of motion are obtained by setting the variations of potential energy with respect to nodal displacement to zero. Principle of virtual work is an alternative formulation of Newton's law. It is entirely equivalent to Newton's first law. In this model, the virtual work principle is used to solve the equilibrium of motions.

The exponential form of the energy function as shown below is widely used for simulating passive behaviour of skeletal muscle [71, 72].

$$W(E) = a_0[\exp(a_1 I_E^2 + a_2 II_E + a_3 E_{11}^2 + a_4 (E_{12}^2 + E_{13}^2)) - 1] \quad (3.33)$$

And their constant values in the equation are $a_0 = 0.6$, $a_1 = 15.0$, $a_2 = 30.0$, $a_3 = -12$, $a_4 = -15$ [73].

Since the muscle is assumed transverse isotropic in this simulation, the reduced polynomial model available in ABAQUS is used instead. Similarly as Equation(3.12), the elastic strain energy function W can also be written in terms of the invariants of the Right Cauchy-Green Deformation Tensor C as

$$W(C) = W(I_C, II_C, III_C) \quad (3.34)$$

where

$$\begin{aligned} I_C &\equiv \text{trace}(C) \\ II_C &\equiv \frac{1}{2}(I_C^2 - \text{trace}(CC)) \\ III_C &\equiv \det(C) \end{aligned} \quad (3.35)$$

Since the stress-strain relationship must hold for all coordinate axis orientations, the equation is written in terms of the modified invariants \bar{I}_C, \bar{II}_C and \bar{III}_C in ABAQUS as

$$W(C) = W(\bar{I}_C, \bar{II}_C, \bar{III}_C) \quad (3.36)$$

where

$$\begin{aligned} \bar{I}_C &\equiv I_c III_C^{-1/3} \\ \bar{II}_C &\equiv II_c III_C^{-2/3} \\ \bar{III}_C &\equiv III_C^{1/2} \end{aligned} \quad (3.37)$$

In the reduced polynomial model, the strain energy function is written as

$$W(C) = \sum_{i=1}^N c_{io} (\bar{I}_C - 3)^i + \sum_{i=1}^N \frac{1}{2} (\bar{III}_C - 1)^{2i} \quad (3.38)$$

For $N = 3$ the third order reduced polynomial strain energy function is obtained from Equation (3.38) as

$$\begin{aligned} W(C) = & c_{10}(\bar{I}_C - 3) + c_{20}(\bar{I}_C - 3)^2 + c_{30}(\bar{I}_C - 3)^3 \\ & + \frac{1}{d_1}(\bar{III}_C - 1)^2 + \frac{1}{d_2}(\bar{III}_C - 1)^4 + \frac{1}{d_3}(\bar{III}_C - 1)^6 \end{aligned} \quad (3.39)$$

where $c_{10}, c_{20}, c_{30}, d_1, d_2, d_3$ are material parameters obtained from experiments. Since the muscle material is almost incompressible in the assumption, the volumetric change parameters d_1, d_2, d_3 are set to infinite in the model. The other three parameters are 0.01, 0.01, 0.0066667 [73].

Due to the transverse isotropic and linear assumptions, the parameters in $[H]$ can take the form of

$$\left\{ \begin{array}{l} E_{1111} = E_{3333} = E \\ E_{1122} = E_{2233} = E' \\ E_{1212} = E_{2323} = \mu' \\ E_{3131} = \frac{1}{2}(E_{3333} - E_{1133}) = \mu \end{array} \right. \quad (3.40)$$

Equation (3.40) is inversed in order to obtain the strains expressed by stresses,

$$\varepsilon = [H]^{-1} \sigma \quad (3.41)$$

$$\begin{pmatrix} \partial u / \partial x \\ \partial v / \partial y \\ \partial w / \partial z \\ \partial y / \partial x + \partial x / \partial y \\ \partial z / \partial y + \partial y / \partial z \\ \partial x / \partial z + \partial z / \partial x \end{pmatrix} = \begin{pmatrix} 1/E & -v'/E & -v/E & 0 & 0 & 0 \\ -v'/E & 1/E' & -v'/E & 0 & 0 & 0 \\ -v/E & -v'/E & 1/E & 0 & 0 & 0 \\ 0 & 0 & 0 & 1/\mu' & 0 & 0 \\ 0 & 0 & 0 & 0 & 1/\mu' & 0 \\ 0 & 0 & 0 & 0 & 0 & 1/\mu \end{pmatrix} \begin{pmatrix} \sigma_x \\ \sigma_y \\ \sigma_z \\ \tau_{xy} \\ \tau_{yz} \\ \tau_{zx} \end{pmatrix} \quad (3.42)$$

where E is the Young's modulus in the transverse plane, E' is the Young's modulus along the y axis, μ' is the shear modulus along the y axis, v is the Poisson's ratio in the transverse plane, and v' is the Poisson's ratio along the y axis.

Another constant μ (the shear modulus in the transverse plane), can be expressed by

$$\mu = \frac{E}{2(1+v)} \quad (3.43)$$

3.2.4 Contact Problem

The physical contact problem occurs when two or more bodies touch each other. There are two kinds of contact occurring in the model: (1) the soft tissues contact with each other, (2) the artery internal wall contacts itself under high cuff pressure.

In upper arm, every muscle is wrapped by a thin layer of fascia. Therefore, the surfaces between the different parts are assumed frictionless. On the contact surfaces, the traction

forces acting are called contact forces. The contact forces deform the objects. In this model, the simulation uses a contact algorithm (considering pure master-slave) to deal with the contact problem: all collided nodes (on the surface that interact with the other) are collected with the purpose of calculating the required forces to avoid body interpenetration. Such forces are calculated in terms of how deep one surface can enter into each other. A typical iterative algorithm repeats two operations until it finds a stable solution as shown in Figure 3.3:

- Find the section where two objects penetrate.
- Apply forces to push back the penetrating section.

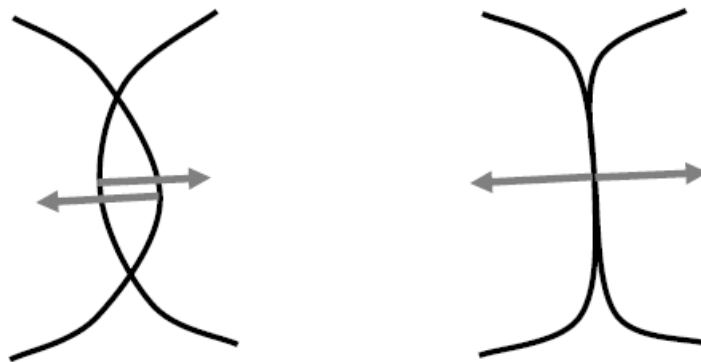


Figure 3.3 Typical steps for solving the contact problem.

The contact forces are the same as the push back forces in the final stable configuration. In conventional methods, the direction of a push back force, or the “normal”, is chosen as the direction from a penetrating surface point to the closest projection.

Mathematically, all the collided nodes follow the restriction:

$$\begin{aligned}
G &= (X - Y)^T * N \geq 0 \\
L &= F * N \geq 0 \\
G * L &= 0
\end{aligned}
\tag{3.44}$$

G = the gap normal to the contact surface

F = the collision force

N = the unit normal vector of the contact surface

L = the contact force normal to the contact surface

It means that the gap (G) between two nodes (X and Y are the spatial position of two nodes on master and slave surfaces) should be non-negative and that the collision force F should always take the bodies apart. Equation (3.44) points out that both the inequalities are exclusive: when one condition is achieved, the other one is automatically equal to zero.

3.3 Summary

The basic formulation of the finite element analysis used in ABAQUS is adopted in this work to link the relationship between the analytical and numerical modelling in the upper arm structure while searching for the dynamic response in application to BP measurement simulation. In the simulation, the continuum description of the muscle [71] is converted and applied in ABAQUS. Reduced polynomial strain energy function is adopted to provide the passive muscle characteristics.

Chapter 4 Finite Element Models

4.1 Introduction

The finite element method is currently one of the best established tools in the field of biomedical engineering and widely used in the computational analysis of complex biological structures. Anatomically, the human upper arm consists of different tissues with irregular geometries and various mechanical properties. In this research, some simplifications are made with the aim of achieving a balance between computational cost and accuracy. In this chapter, two finite element models are developed using the commercial software ABAQUS[®] which is widely used in biomedical engineering. The first one is a simplified cylindrical model, which is established to study the brachial artery closure process under external CP. It was used to compare with experimental results and give an initial assessment of the cuff based BP measurement. The second one is an anatomic accurate model, whose geometry is extracted from VHB dataset. This comprehensive model was able to simulate arm motion and used to map the strain distribution in different conditions.

4.2 Model selection

At the first stage of the investigation, the simplified model with cylindrical geometry is developed to simulate the entire BP measurement process and study the artery closure process during BP measurement. The simplified geometry was chosen for the following reasons:

- 1) The basic geometry of the simplified cylindrical model was widely used in previous studies [36, 61, 74], and the models were proven valid in studying cuff based non-invasive BP measurement in static status.
- 2) The location of the brachial artery was improved by using VHB Dataset [75]. The introduced model is able to give more accurate results.
- 3) Since the brachial artery will be fully closed under high CP, the clinical experiment with intra-vascular sensors is not valid. An arm simulator with simplified cylindrical geometry was developed to represent BP measurement and validate the mathematical model.

4.2.1 Material properties

The human arm consists mainly of five different types of nonlinear, anisotropic, viscoelastic and nearly incompressible tissues; namely, the skin, fat, muscle, bone and vessel. The following physical parameters play an important role in the modelling: viscosity, density, modulus of elasticity, and Poisson' ratio. To develop an appropriate and feasible theoretical model, some assumptions of tissue properties are made in this BP measurement process simulation:

- I. As the CP decreases slowly from supra-systolic to sub-DPs during the BP measurement process, the viscosities of these materials are neglected.
- II. Since the upper arm mainly consists of muscles, the density of the simulated soft tissues is assumed the same as the muscles 1.05g/cm^3 [54].
- III. The fat and skin tissues have no preferred direction and show evidence of isotropic properties, whereas the muscle and artery tissues are fibrous in nature

and present anisotropic properties [54, 57]. However, previous clinical experiments present that when the strain is under 10%, the muscle tissue exhibits linear isotropic elastic behaviour and its stiffness is similar to that of fat and skin [76]. Because the existing literature has confirmed that the arm tissue strain is less than 10% in normal BP measurements [77], the arm muscle tissue is considered as a linear isotropic elastic material. Consequently, the skin, fat and muscle tissues are integrated as one part and named soft tissue. The applied Young's modulus of the soft tissue is $E_{st} = 47.5$ kPa [36, 54].

- IV. Since the bone ($E_{bone} = 10$ GPa) is about two hundred thousand times stiffer than that of the arm soft tissues [78], the deformation of the bone is very little compared with soft tissues. In this simulation, the bone is assumed as a rigid undeformable material.
- V. In the oscillometric BP measurement method, the CP oscillation is recorded through the whole measurement process. However, only part of the data, which is obtained when CP is between the patient's supra-SP and slightly under DP, are used for analysis. Within the above CP range, most vessels are closed during the measurement process except for the brachial artery. Thus only the brachial artery is simulated and all of the other vessels are ignored in this model.
- VI. As the arm tissue and the artery materials contain around 75% water, they are assumed nearly incompressible with Poisson's ratio $\gamma = 0.45$ [54].
- VII. The brachial artery wall consists mainly of three components: collagen, elastin, and smooth muscle. All of these components contain tissue fibres in different directions, which imply that the artery tissue has no preferred direction. Although the artery wall is anisotropic in nature, the literature lacks sufficient

information about the anisotropic properties. Thus for simplicity of modelling, the assumption of “isotropic” is widely used which has been proven to give satisfactory outcomes [36]. Therefore, the artery tissue is assumed as an isotropic material.

VIII. Although various individuals have different artery mechanical properties which may indicate nonlinearity, the arterial wall reveals minimum stiffness when the transmural pressure across the arterial wall is zero, which is defined as BP minus CP in BP measurement [54, 58]. This is attributed to the fact that the elasticity of collagen and smooth muscle approach their lowest values when the artery is minimally distended, while the elastin remains unchanged regardless of loading [54].

Implementing the above assumptions leads to the fact that the artery parameter which needs to be determined is the modulus of elasticity. Currently, measuring simultaneous BP, diameter (cross section area), and wall thickness of the artery in vivo is the most reliable way to determine the arterial elasticity [79]. By inflating a cuff surrounding the underlying brachial artery, the transmural arterial pressure is reduced. Under normal condition, which is also called baseline condition [80], the mean in vivo transmural pressure vs. area curve for eight normal human subjects measured by intravascular ultrasound over a wide transmural pressure range as shown Figure 4.1 [81]. In order to change the artery stiffness, the measurement after the administration of intra-arterial nitroglycerin (NTG) which relaxes artery smooth muscle and decrease artery stiffness and norepinephrine (NE) which increases vascular tone and artery stiffness are also presented in Figure 4.1.

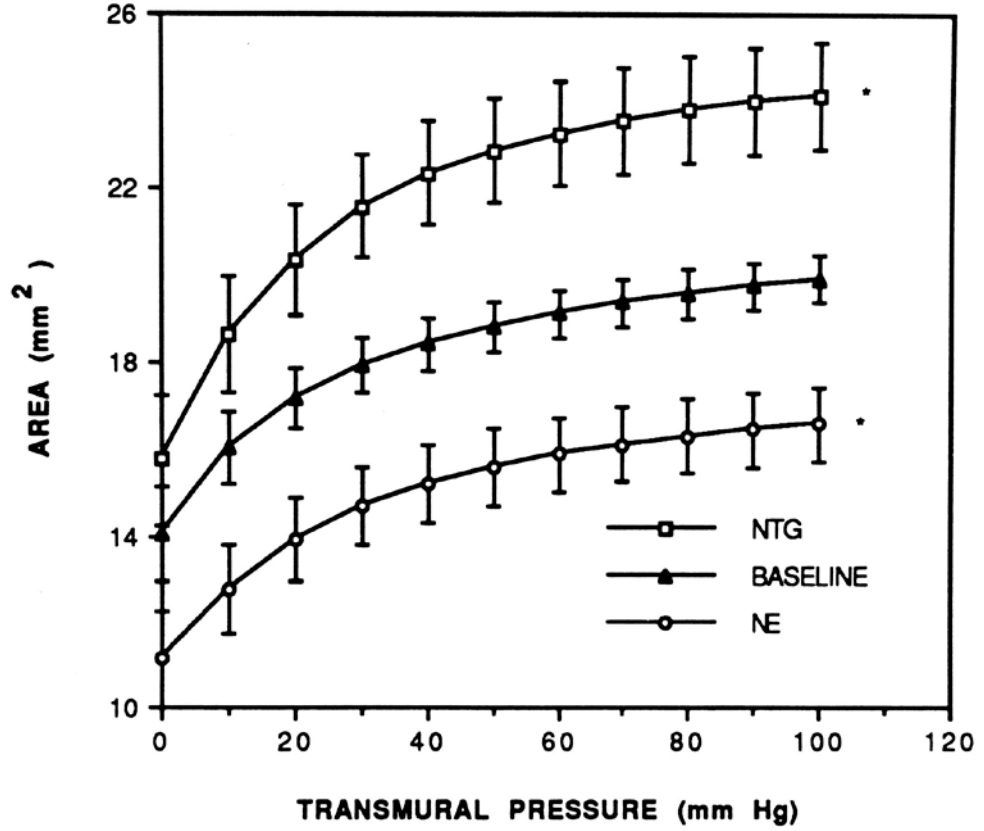


Figure 4.1 Brachial artery pressure vs. area under three experimental conditions: baseline, norepinephrine (NE, 1.2 µg), and nitroglycerin (NTG, 100 µg). [82]

To represent the transmural pressure – area relationship as shown in Figure 4.1, the experimental data are fitted to Langewouters' arctangent model,

$$A = a \times \left(0.5 + \frac{1}{\pi} \times \tan^{-1} \left(\frac{TP}{c} - \frac{b}{c} \right) \right) \quad (4.1)$$

where TP is transmural pressure, A is the cross section area of brachial artery and a , b , c are constant parameters describing the curve. By applying the data shown in Figure 4.1, the constant parameters in Equation (4.1) are obtained by fitting with different numbers with coefficient R^2 values over 0.97: (1) under baseline condition, $a = 21.55$, $b = -16$, $c = 28$; (2) after using NE, $a = 18$, $b = -12$, $c = 29$; (3) after using NTG, $a = 25.95$, $b = -10$, $c = 24.5$.

The measured area A includes wall cross sectional area (WCSA),

$$WCSA = \pi(R_{out}^2 - R_{in}^2) \quad (4.2)$$

$$A = \pi R_{out}^2 \quad (4.3)$$

where R_{out} is the outer radius, R_{in} is the inner radius. Since the artery wall is nearly incompressible, WCSA of the brachial artery under CP is assumed constant [83]. In this study, WCSA is assigned to be 4.37 mm^2 [80].

Since the ratio of brachial artery thickness and radius is 0.6:2.5 is higher than 1:10, the brachial artery was considered as a thick-wall cylinder in this study. For a thick-wall cylinder under uniform internal pressure, the modulus of elasticity of the vessel can be calculated by the following equations [81].

$$\Delta R_{out} = \frac{TP}{E} \frac{2R_{out}R_{in}^2}{R_{out}^2 - R_{in}^2} \quad (4.4)$$

Rearrange this equation to get

$$\therefore E = \frac{TP}{\Delta R_{out}} \frac{2R_{out}R_{in}^2}{R_{out}^2 - R_{in}^2} \quad (4.5)$$

Using Equation (4.2)(4.3) into Equation (4.5) leads to

$$E = \frac{2TP \cdot A(A - WCSA)}{dA} \quad (4.6)$$

where E is the modulus of elasticity. By substituting Equation (4.1) into Equation (4.6), the elasticity of the artery under different transmural pressure can be obtained. Using the clinical data shown in Figure 4.1, the TP-Elasticity relationships of the normal

(baseline), the hard (after using NTG) and the soft (after using NE) are calculated by Equation (4.6) is shown in Figure 4.2. Therefore, the stress-strain relationships of these three types of artery are obtained and shown in Figure 4.3.

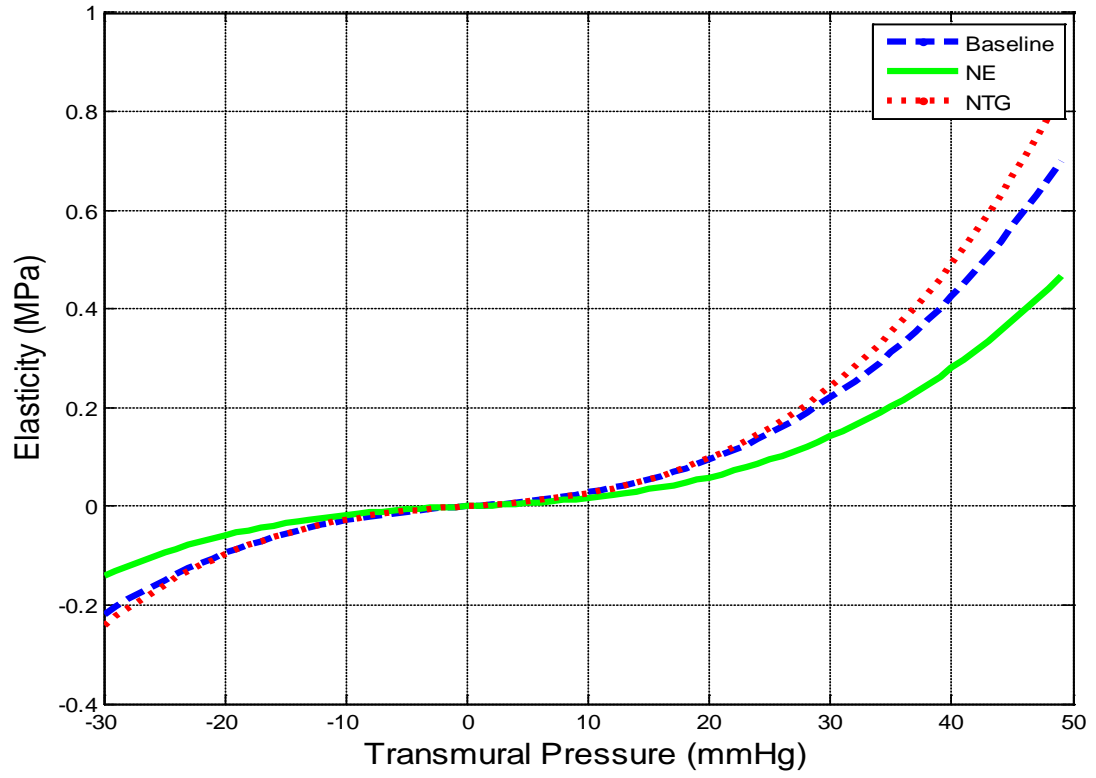


Figure 4.2 The stress-strain relationship of the artery wall used in the finite element model

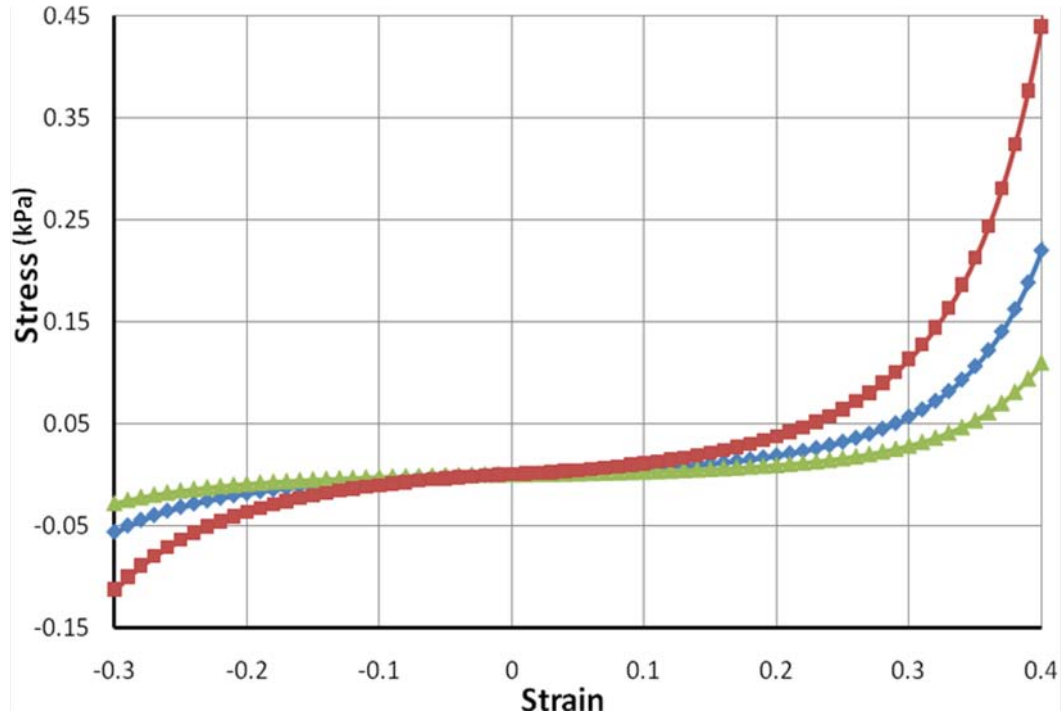


Figure 4.3 The stress-strain relationship of the artery wall is calculated from experimental results [81]. — normal artery, — soft artery, — hard artery

4.2.2 Geometry

From material properties aspect, the upper arm consists of three parts: bone, artery and soft tissue. Anatomically, the diaphysis of humerus is similar to a cylinder and the brachial artery is comparable to a tube. During BP measurement, the upper arm is surrounded by uniform external pressure. The arm tissue deforms and changes to the more stable geometry – cylinder. Therefore, the soft tissue part which includes the skin, fat and muscle is also assumed to be cylindrical.

By analysing cross-sectional images of the upper arm from the VHB Dataset [75], the humerus is simulated as an axisymmetric cylinder of radius 1.2 cm at the centre of the upper arm model; the brachial artery is simulated as a compliant tube of internal radius 2.5 mm and wall thickness 0.6 mm embedded in the muscle tissue at a distance of 4.2

cm from the longitudinal axis; the skin, fat and the muscle tissues are amalgamated as a single contiguous annular element with internal and external radii of 1.2 cm and 5.2 cm, respectively. The length of the model is 24 cm. Figure 4.4 shows a transverse section of the arm model with the above dimensions. All of the used dimensions are typical values and have been previously validated [35, 36, 40].

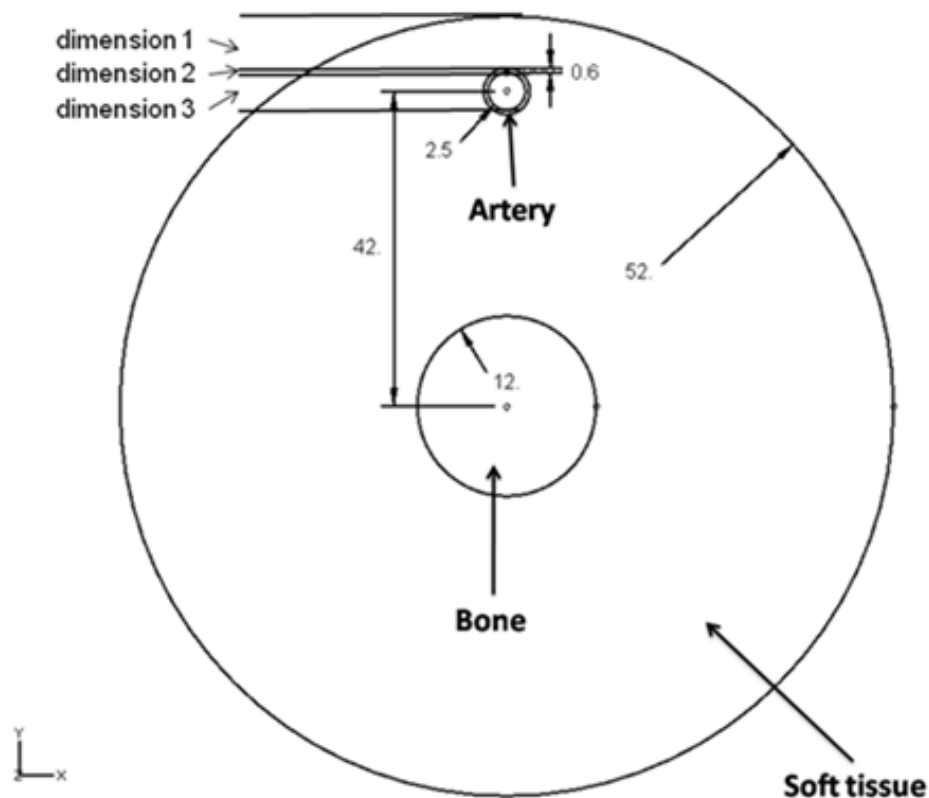


Figure 4.4 Transverse section of the arm model [36, 75]

4.2.3 Interactive properties

There are three pairs of interactive surfaces between the different parts in the simple model:

- **The surface between the bone part and the soft tissue part**

Since the muscles are attached to the bone, they are fixed to the bone and there is no relative motion between them at the points of contact.

- **The surface between the brachial artery part and the soft tissue part**

The brachial artery is connected with surrounding tissues through connective tissues. Thus, this pair of interactive surfaces is assumed to be rigidly fixed to each other. i.e. The interface between the artery and the tissue have the same property.

- **The internal surface of the brachial artery**

The internal surface of artery is smooth and there is no relative motion between the contacted surfaces during normal BP measurement. Therefore, frictionless self-contact interactive property is assigned on the internal surface of the brachial artery.

4.2.4 Boundary conditions

In context with the above assumptions, boundary conditions applied to the model are as following:

- 1) As the soft tissue is attached to the rigid bone, the boundary condition of the contacting surface is the same as the bone and the bone can be ignored in the simulation process. In normal BP measurement, the patient's arm is suitably supported to minimise any motion. So the bone is assumed fixed in 3D space at both ends. Consequently, fixed boundary conditions are applied on the internal surface of the soft tissue.
- 2) The cuff is assumed to perfectly adhere to the arm with no relative motion in between during the whole BP measurement. Since the cuff material is nearly unstretchable, the cuff stretch is very little during BP measurement. Therefore, the soft tissue surface under the cuff, which is the highlighted part in the mid of

the model as shown in Figure 4.5, can only move in radial direction. The degree of freedom in the longitudinal direction (Z direction) is set to zero.

- 3) The biceps, triceps and brachialis muscles terminate at or close to the elbow and shoulder. As the arm is fixed to minimize arm motion during normal BP measurement, the soft tissue at either end of the model is assumed no longitudinal movement and free to move in the cross section plane (X-Y plane). This boundary condition is applied to both of the end surfaces as shown in Figure 4.5.

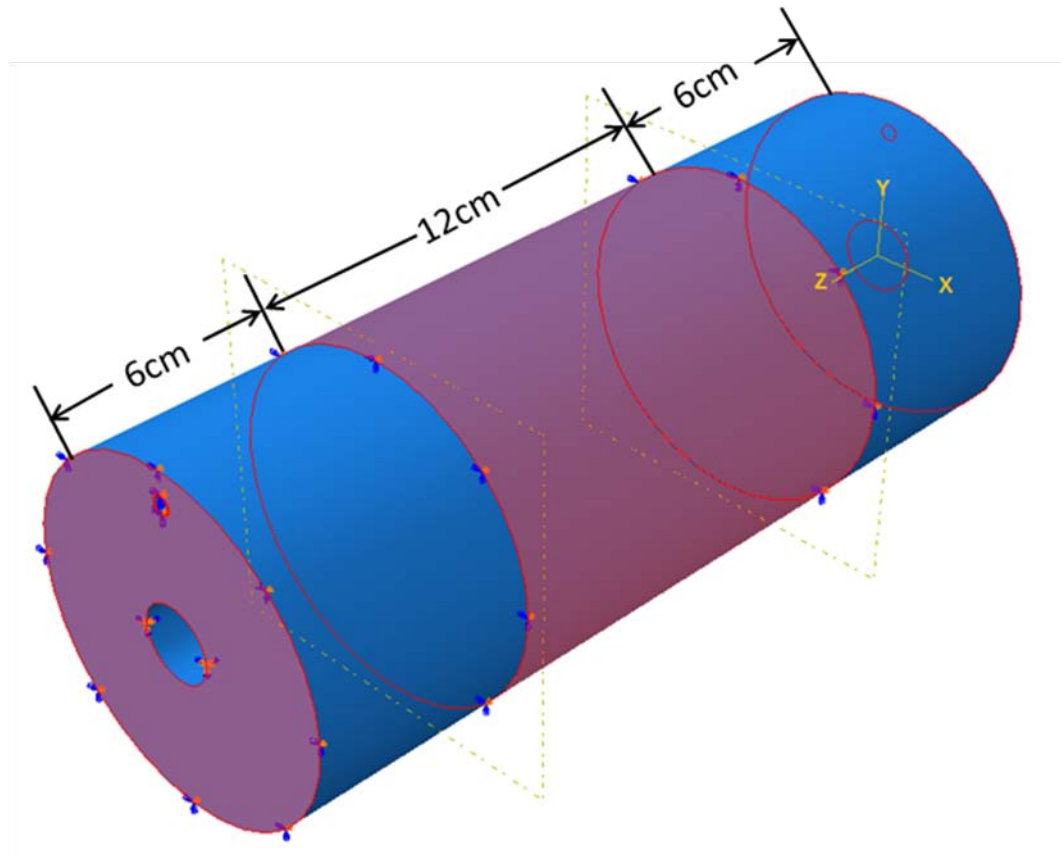


Figure 4.5 Boundary conditions of the simplified model

4.2.5 Model loading

Following the guideline from the British Hypertension Society, the proper size of the inflatable cuff is 12×35 cm (width \times length) for the chosen arm size [28]. To define the surface undergoing the external CP, the model is partitioned to three parts: 6 cm at both ends (outside of the cuff) and 12 cm in the middle (under the cuff) as shown in Figure 4.6.

In the normal cuff based BP measurement process, there are two loading: BP and CP which are applied at internal surface of the brachial artery and mid part of the soft tissue external surface as shown in Figure 4.6.

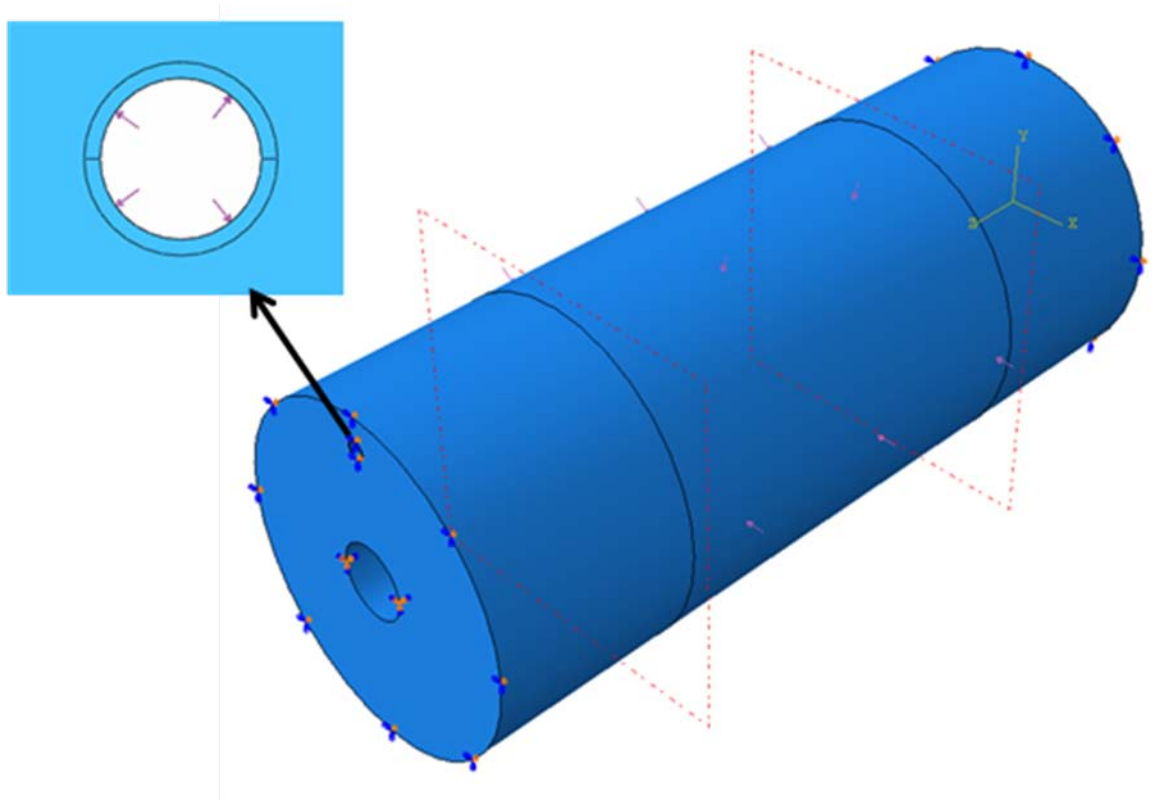


Figure 4.6 Load and boundary conditions of the simplified model

1. In previous research, it has been shown that the fluid interaction in the brachial artery has small influence on oscillometric BP measurement [36]. In this study, it is assumed that the acting pressure on the internal artery wall is not affected by the artery closure status. This assumption is validated by the following theoretical calculation.

Figure 4.7 shows a schematic diagram of the artery deformation under external CP in the BP measurement.

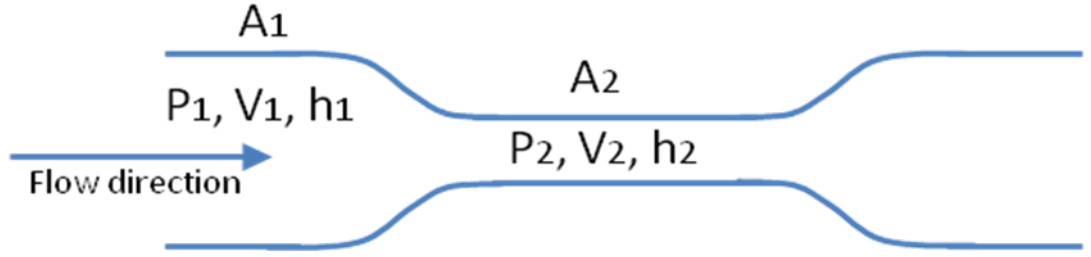


Figure 4.7 The artery is at normal open status at position 1 and compressed at position 2 by external CP.

As there is no blood leak in the brachial artery, the volume flow rate is constant along the artery and is expressed as,

$$Q = A_1 V_1 = A_2 V_2 \quad (4.7)$$

where, Q is the blood volume flow rate, V is the blood flow velocity, A is the cross section area of the brachial artery. The flow pressure in the artery before and under the cuff can be calculated by Bernoulli's equation,

$$P_1 + \frac{1}{2} \rho V_1^2 + \rho g h_1 = P_2 + \frac{1}{2} \rho V_2^2 + \rho g h_2 + P_{loss} \quad (4.8)$$

where, P is the flow pressure, h is the height. Since the blood flow in brachial artery was assumed laminar [84] and the artery internal surface is smooth [54], the friction between the blood and artery internal wall is very small and can be ignored. Therefore, the pressure loss is assumed zero in this study. Furthermore, the arm is placed almost horizontal in the normal BP measurement, h_1 and h_2 equal to each other. In an average sized adult, the normal blood flow in the entire human circulation is about 5 l/min at rest, and about 5% of the blood flow through brachial artery in each heart beat. Therefore, the average flow velocity in the brachial artery is 21.2 cm/s. In extreme conditions, when the artery is totally closed and there is no blood flowing through position 2, the pressure difference is $\Delta P = P_2 - P_1 = \frac{1}{2} \rho V_1^2 = 23.6 Pa$. Comparing with the normal blood pressure 110/70 mmHg (16000/10665 Pa), the pressure change due to artery closure status is less than 0.1%, and is ignored in this study. Hence, BP is assumed to be uniform along the artery.

2. To minimize the modelling and calculation expense, BP is simulated by applying pressure directly onto the artery internal wall. In this simulation, constant BP is applied, which remains the same diastolic and SP and the same pressure waveform. As shown in Figure 4.8, periodic BP waves obtained from typical clinical data conducted in this work, which is 110/70 mmHg at the heart rate of 1 beat/s (60 beat/min), is applied on the internal surface of the brachial artery. As the cuff is assumed to be perfectly adhered to the arm with no relative motion in between, and CP is distributed uniformly on the arm surface, the cuff material is ignored in the model and the CP is applied on the external surface of the mid part directly.

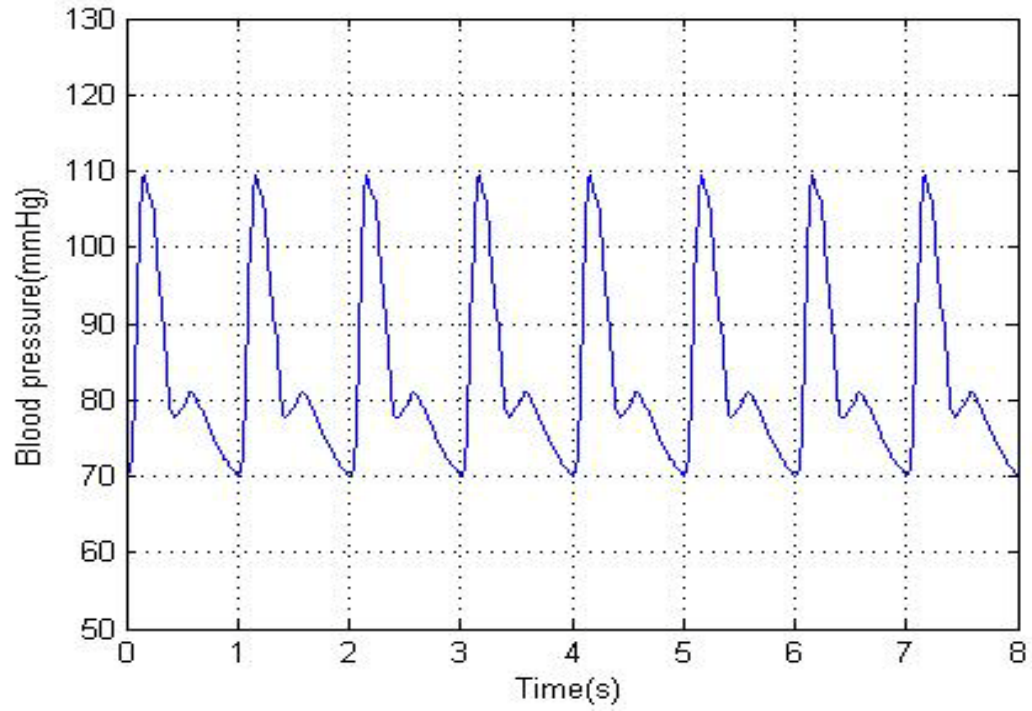


Figure 4.8 BP waveform obtained from clinical experiment.

Theoretically, CP need to be increased up to 30 mmHg over the patient's SP and then decrease to 0 mmHg at a rate of 2~5 mmHg/s. As shown in Figure 4.9, the simulated CP in this model is increased up to 150 mmHg at a high speed and then decreased to 0 mmHg linearly at 2.5 mmHg/s which is similar to the deflating speed in our BP monitoring device.

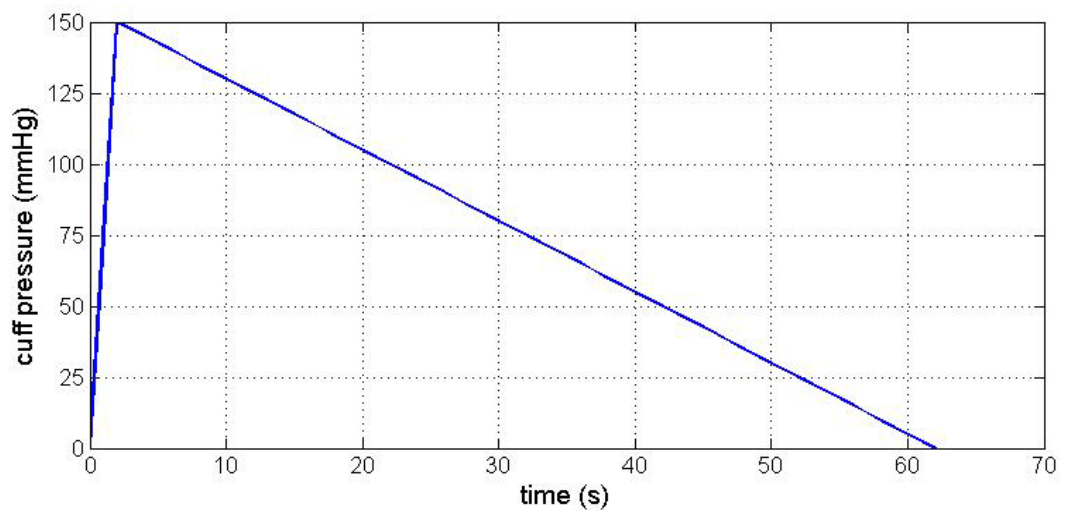


Figure 4.9 CP changes in the finite element model

4.2.6 Model mesh

Since this study was focused on the deformation of the brachial artery, the mesh process was initiated from the brachial artery. In finite element analysis, the thick wall tube was normal divided into 2-4 layers, and the element size was decided by the layer thickness. Since the brachial artery was the smallest part in the model, the entire model would be overly fine meshed if it was meshed using the same element size. Two different element sizes as shown in Figure 4.10 were tested in this study. In the test, both of the models had the same boundary conditions, material properties and pressure loading on the external surfaces. Both of the models showed the same artery closure process and achieve the most area change when the transmural pressure was 6 mmHg. The simulated results also matched the previous clinical experiment results which was conducted at 5 mmHg [41]. Therefore, the model mesh shown in Figure 4.10b is fine enough and used for determine the size of surrounding elements.

In order to minimize the element penetration between the brachial artery part and the soft tissue part, the coordinates of element nodes were shared by the contacting surface. Referring to the shared element nodes on the contacting surface, the soft tissue part was mesh using hex-dominated method with advancing front algorithm. This mesh method has the advantage of simplicity, robustness and handling capability of changes in the topology of the domain. Furthermore, the elements near the boundary can be controlled directly using advancing front methods. The whole meshed model is shown in Figure 4.11, which contains 104,544 nodes, 86,686 elements in the soft tissue and 1344 nodes 1296 elements in the artery.

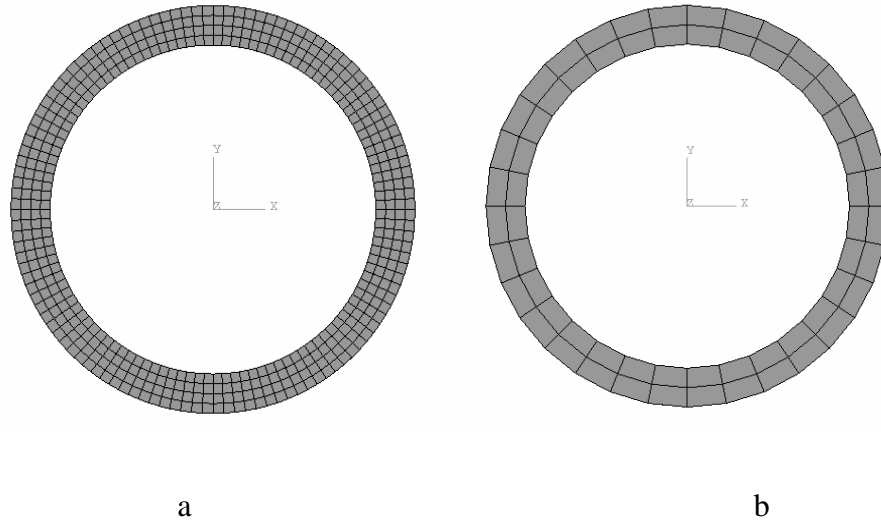


Figure 4.10 (a) the fine mesh with four layers; (b) the used mesh with two layers.

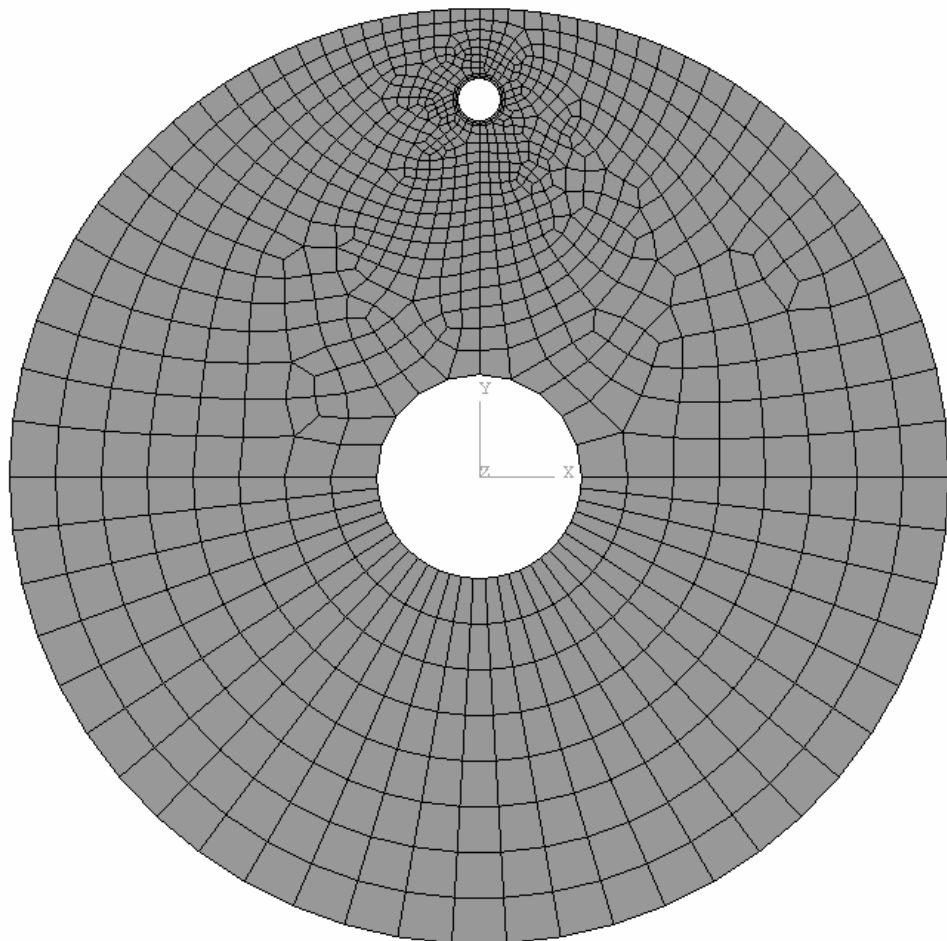


Figure 4.11 Cross section view of the meshed model

4.3 Refined model

Although the simplified model can simulate BP measurement process, it is very difficult to simulate arm motions using the model with simplified cylindrical geometry and a more accurate realistic model of the upper arm needs to be developed based on the geometry extracted from VHB Dataset [75]. This model will be used to study the artery closure process and surface strain distribution during BP measurement with arm motions.

4.3.1 Material properties

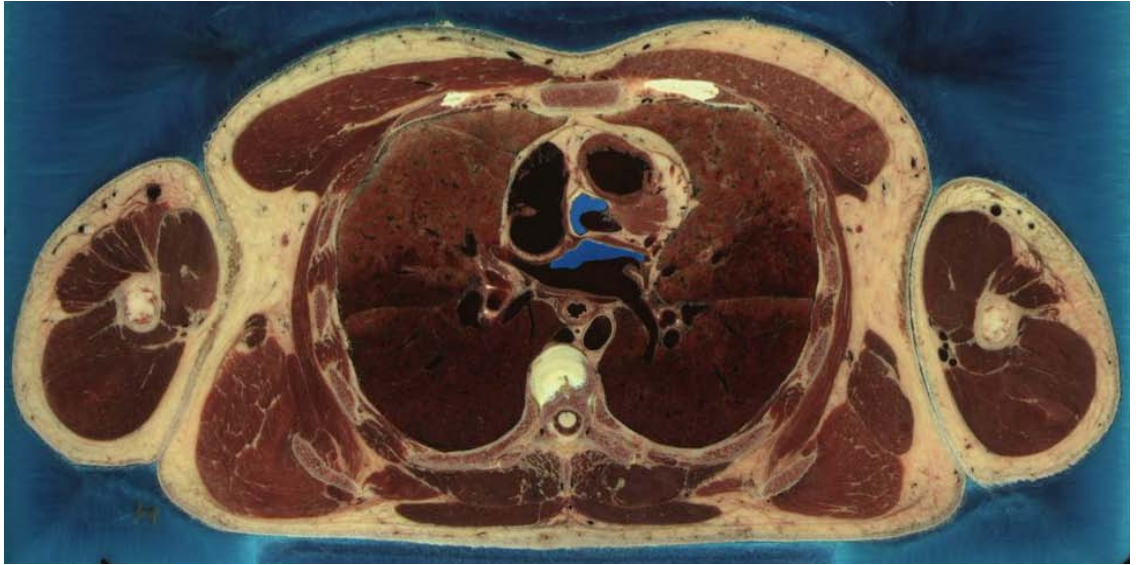
As shown in Figure 4.12a, the different tissues and organs can be identified by the colour, shape and texture. From the original image in VHB dataset shown in Figure 4.12b, the following tissues can be identified: skin, adipose fat, connective tissue, vessels, muscle, brachial artery and bone. In this model, the skin, adipose fat, connective tissue, vessels are integrated as one part named soft tissue for the following reasons:

- 1) The skin, adipose fat and connective tissue are connected to each other tightly and there are no clear boundaries between each other. Therefore, there is not interactive movement between these tissues.
- 2) Because adipose fat is another form of connective tissue and has similar properties, both are considered as one material – fat tissue.
- 3) As described in Section 4.2.1, the mechanical properties of skin, fat and connective tissues are the same.

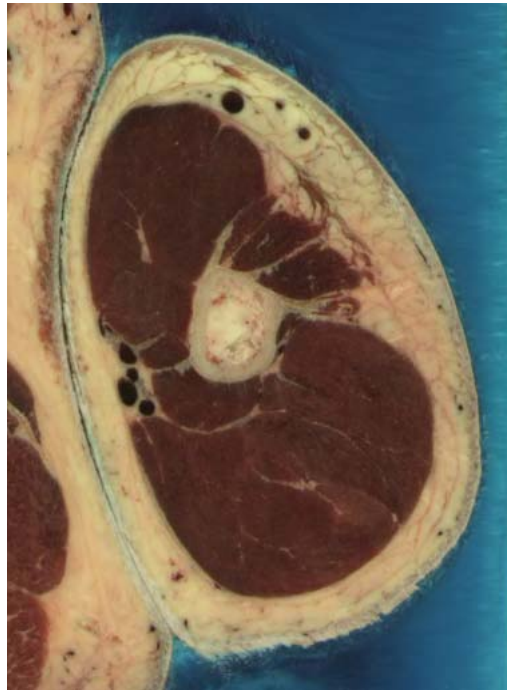
- 4) The vessels shown in Figure 4.12b will be closed and the space will be filled by fat tissue when the arm is compressed by external CP. Therefore, the vessels except brachial artery are replaced by the fat tissue.

Therefore, the anatomic accurate model includes four different types of material: soft tissue, bone, muscle and brachial artery.

As introduced in Section 4.2.1, the material properties of artery, bone, and soft tissue are already known. They are also used in this anatomic accurate model. Since some arm motion will be simulated in this model, the previously defined property of muscle tissues is no longer valid here. As the muscle tissues are almost incompressible which implies that the volume of the muscles is conserved during deformation, the hyperelastic material is used in this model to simulate the response of muscle tissue undergoing large deformation.



a



b

**Figure 4.12 (a) one sample (No.0417) of the selected images from VHB dataset [75]
(b) the image between pixel (1335, 530) and pixel (1713, 1033) of the original image is selected from the original image for further analysis.**

4.3.2 Geometry of the model

In anatomical usage, the upper arm is defined to be the segment between the shoulder and the elbow [85]. As shown in Figure 4.13, the upper arm is subdivided into two parts: the part above axilla and the part between axilla and elbow. Since the upper arm tissue and the body tissue join together above axilla, it is very difficult to isolate the upper arm from the body. Furthermore, the tissues and muscles in the shoulder are not involved in BP measurement. Therefore the part of the upper arm between axilla and elbow is selected for simulation in this study.

In the VHB dataset, the geometry of the proposed part is contained in the images between No.0402 and No.0557 as shown in Figure 4.13b. Figure 4.12a shows the original image including the cross section view of both arms and body. For simplification purpose, only the data containing the left upper arm, which are between pixel (1335, 530) and pixel (1713, 1033) of images are shown in Figure 4.12b. These data are selected and used in the next step. However, it is difficult to address the boundary edges between different anatomical structures in the original image. Therefore, the post-processing of these images is made to clarify the boundaries between the different tissues and muscles. As shown in Figure 4.14a, the contours of biceps, triceps and brachial artery are very easy to identify after image processing. Based on the colour threshold and the knowledge of anatomic structures, the simulated upper arm was segmented into the following parts: the muscles, the soft tissue, the brachial artery, and the bone. Referring to the functions of the arm muscles, the arm muscles are subdivided into three parts: the biceps, the triceps and other muscles. As shown in Figure 4.14b, the edges between each region are defined by smoothed spin lines in Solidworks®.

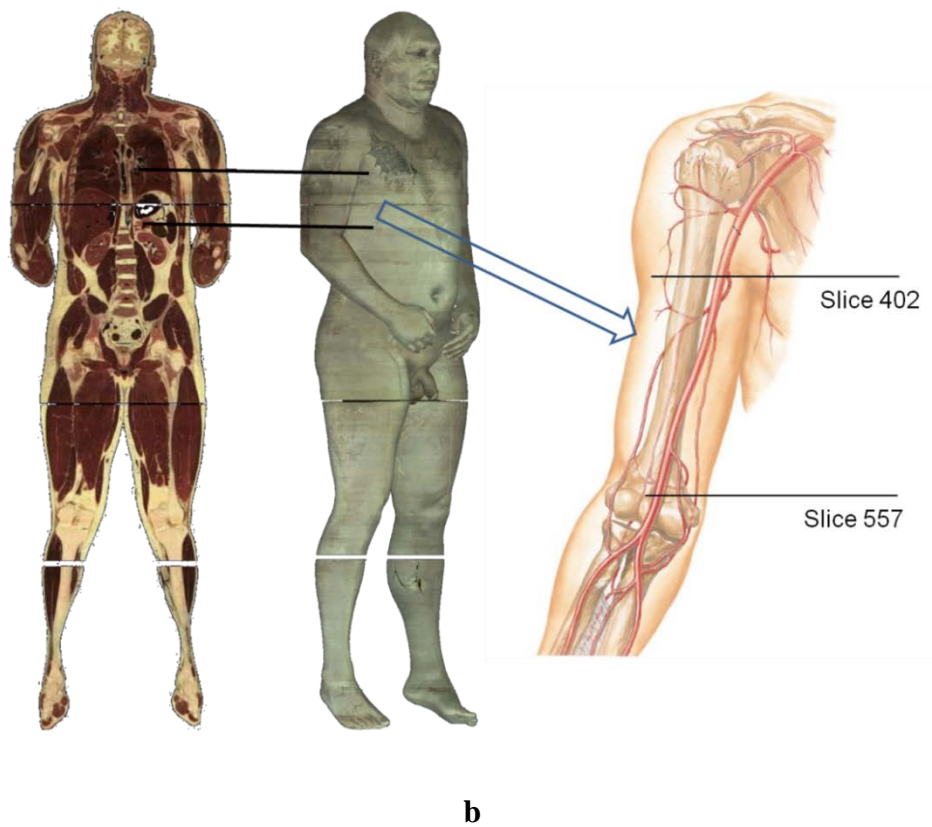
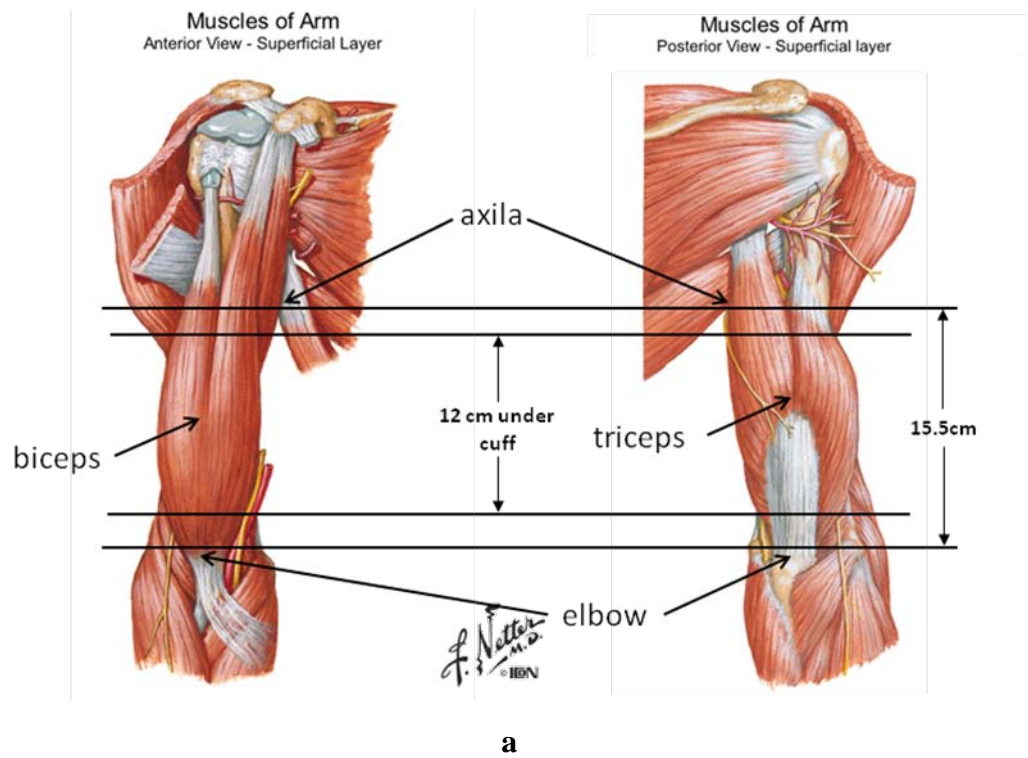
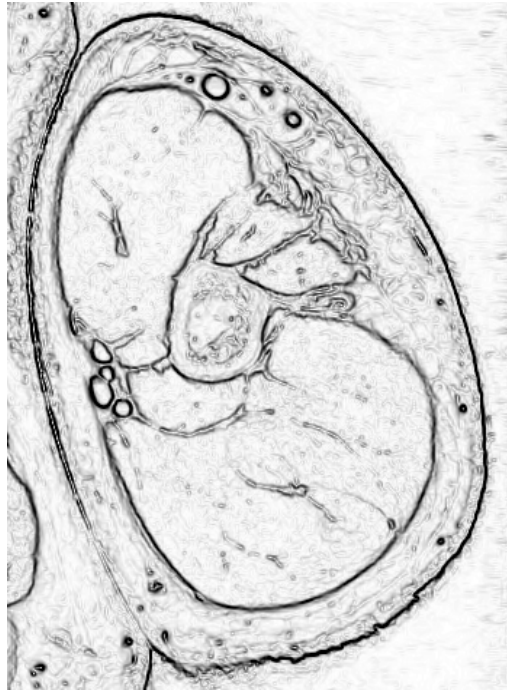
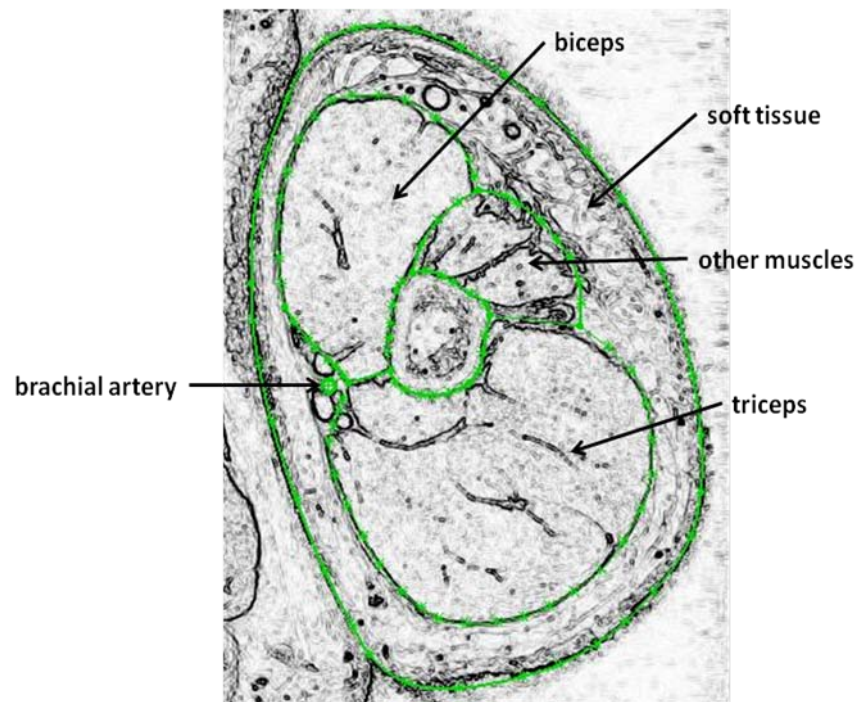


Figure 4.13 (a) Anterior and posterior view of upper arm muscles, (b) the positions of selected slices in VHB Dataset [75, 86]



a



b

Figure 4.14 (a) The edges between different materials are highlighted after colour processing. (b) The boundaries of different parts are defined by smoothed spin lines which are guided by the highlighted edges.

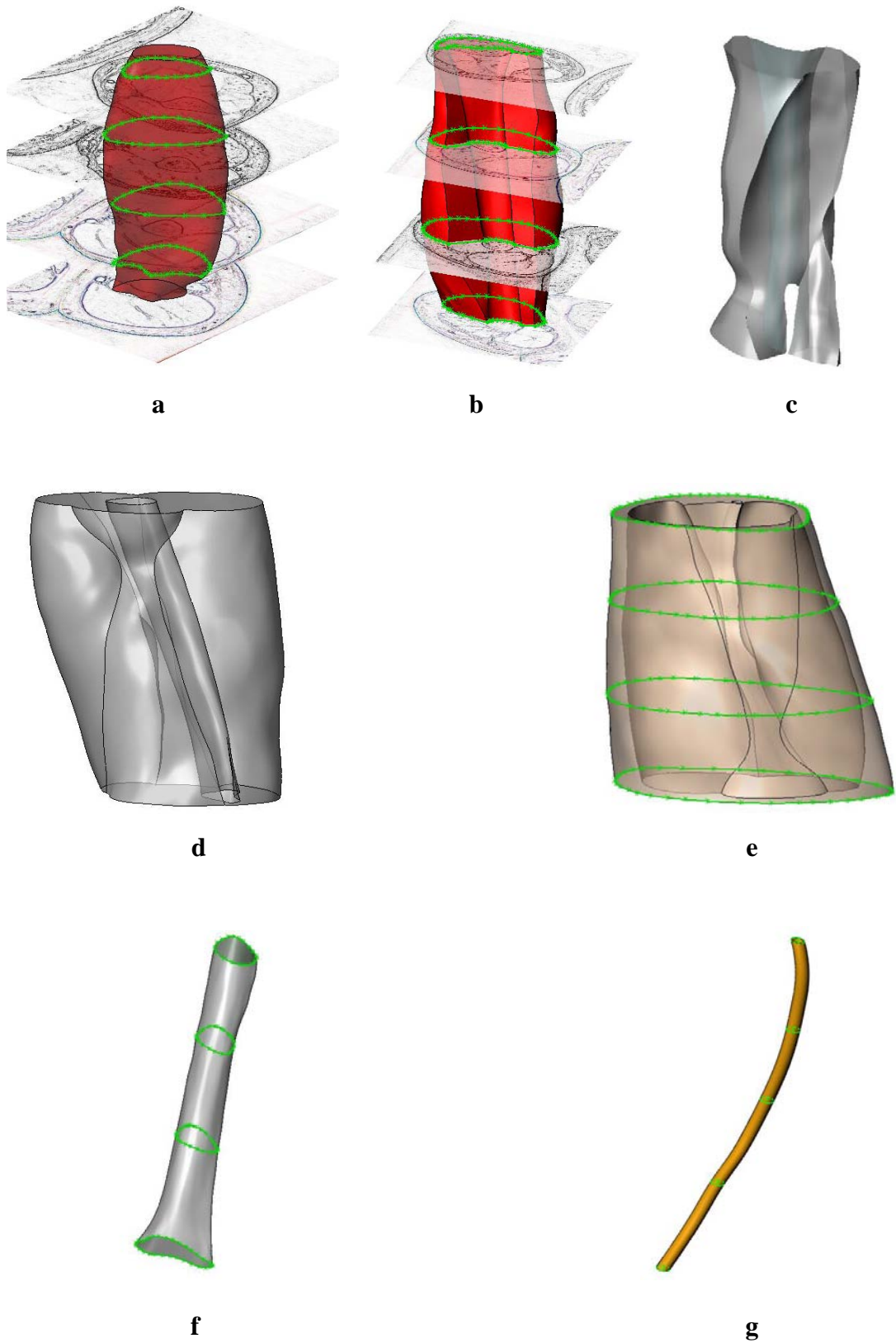


Figure 4.15 The 3D models of the simulated parts are shown above: (a) the biceps, (b) the triceps, (c) other muscles, (d) integrated muscles, (e) the soft tissue, (f) the bone, (g) the brachial artery.

The same process was done for all of the selected images from VHB dataset. Consequently, the contours of each part are defined in each image. As the interval between these images/slices is already known from the VHB dataset, the 3D models of these parts can be built up by connecting the contours together. Originally, the interval between each image is 1 mm. However, only a few of these images are shown in Figure 4.15 for demonstration purpose. In Figure 4.15, the 3D model contains: the biceps, the triceps, the other muscle, the brachial artery, the soft tissue and the bone.

In this study, all of the models were developed using Solidworks[®] software. Among the developed models, the biceps, the triceps, the bone and the brachial artery are built by connecting their contours together using loft function in Solidworks[®]. Since the loft function uses spline surface to connect the contours in each slice, there are some gaps or overlapped parts between the connected parts. In order to minimize the unmatched surfaces, the integrated muscles part is built by connecting the external edges of all of the muscles and cutting the bone part from the model as shown in Figure 4.15d. The part of other muscles, which is placed between the biceps and the triceps, is formed by cutting the biceps, and the triceps from the entire muscle as shown in Figure 4.15c. The soft tissue part is developed by cutting the integrated muscle and brachial artery from the entire arm model. Therefore, all of the contacted surfaces are formed by the same spline surfaces.

When assembling the developed models together, the 3D model of the upper arm is completed as shown in Figure 4.16. As the muscles are attached to the bone, the surfaces connecting to the bone are assumed to be fixed on the bone. Furthermore, the bone is rigid and indeformable in this model. Therefore, the internal surfaces of the muscles have the same boundary conditions as the bone, and the bone can be removed in the analysis as shown in Figure 4.16c.

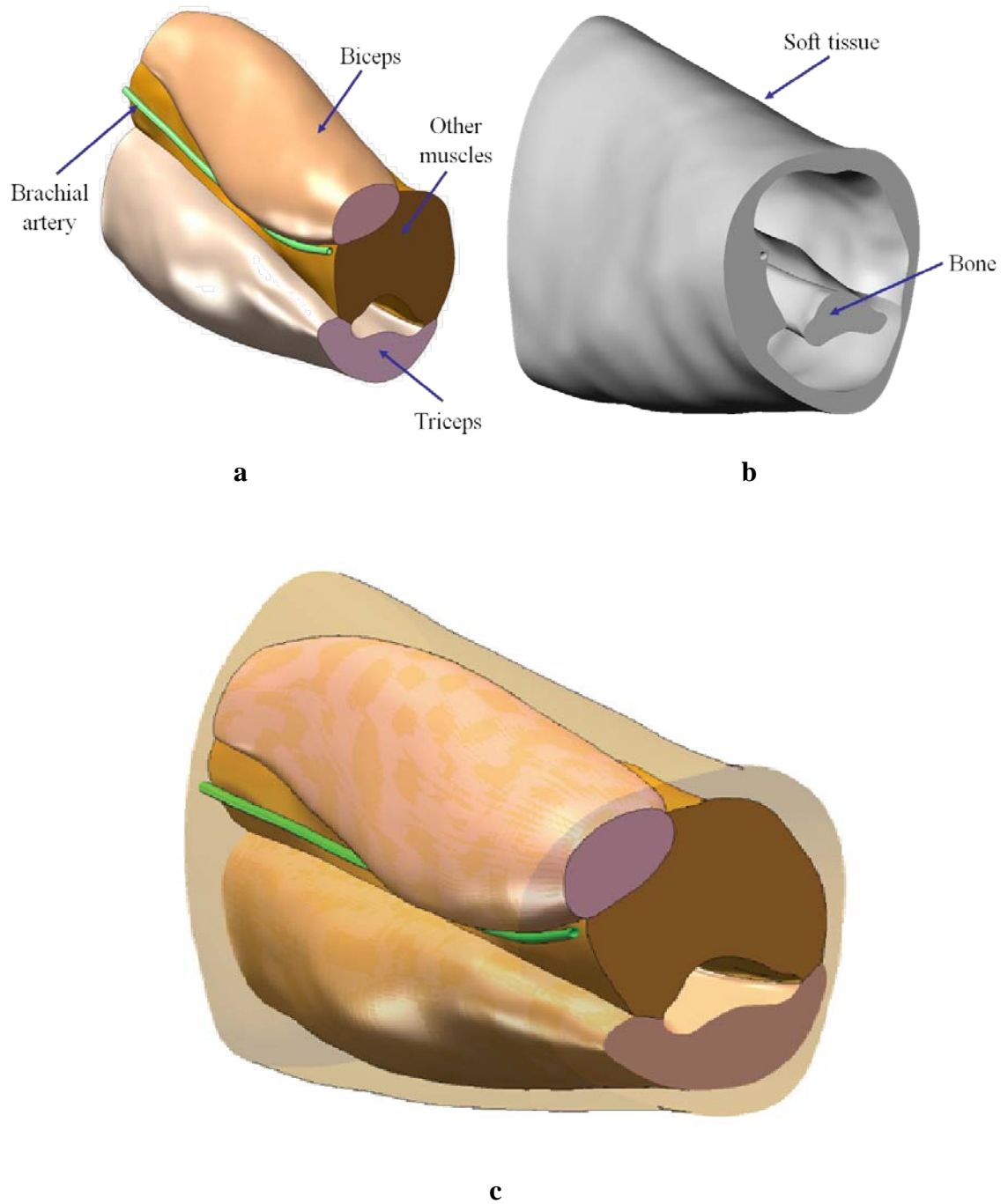


Figure 4.16 3D structure of the upper arm model: (a) biceps, triceps, other muscles and artery; (b) soft tissue and bone, (c) the assembled model.

4.3.3 Boundary conditions

In the principle coordinate system of this model, the X-Y plane is parallel to transverse plane and “Z” direction is from superior to inferior. However, the axis of humerus is not parallel to the axis of the whole body in VHB dataset. Since all arm deformations and arm motions are referred to the bone, a local co-ordinate system is set up as shown in Figure 4.17. The longitudinal direction “Z” starts from the central point of the biceps on the lower surface parallels to the axial direction of humerus, as shown in Figure 4.17.

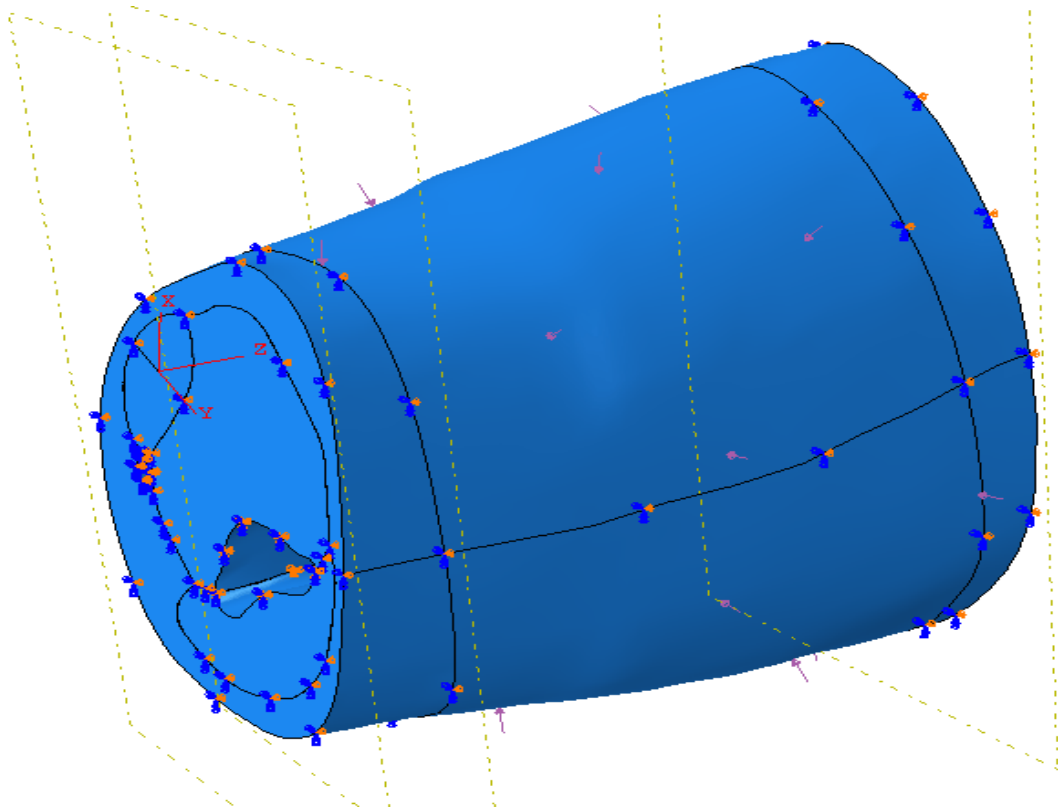


Figure 4.17 Boundary condition and loading in the 3D model

In the normal BP measurement, the cuff needs to be positioned about 2 cm above the elbow. Furthermore, the proper cuff size for the simulated arm size is 12×35 cm as stated in previous section. Therefore, the cuff covered surface is defined between two edges, which are 2 cm and 14 cm above the distal surface, as shown in Figure 4.17.

Boundary conditions are applied to the model as following:

- 1) Because the patient's arm is suitably supported to minimise any motion, the humerus is not moving during the BP measurement process. As the bone is removed from this model, the fixed boundary condition is applied on the internal surfaces of the muscles.
- 2) The cuff is assumed to perfectly adhere to the arm with no relative motion in between during the whole BP measurement. The soft tissue surface under the cuff is fixed in "Z" direction of the local coordinate system of the bone.
- 3) The biceps, triceps and brachialis muscles terminate at or close to the elbow and shoulder. When simulating normal BP measurement without any arm motion, the soft tissue and muscles at either end of the model are assumed fixed in local direction "Z".

4.3.4 Interactive properties

The interactive properties included in this model are:

- 1) The internal surface of the artery part is assigned self-contact interactive property with friction factor of 0.
- 2) Since the brachial artery connects to surrounding tissues by connective tissues, the surfaces between the brachial artery part and the soft tissue part are assumed fixed to each other.
- 3) There is a layer of fascia surrounding every muscle in the upper arm in order to isolate them from the other tissues. The interactive properties between different muscles and soft tissues are frictionless.

- 4) Although the artery and soft tissue parts share the same edges, there are some intersections or small gaps existing between the surfaces. In order to improve this problem, the interactive tolerance of artery external surface and soft tissue surface is 0.2 mm.
- 5) Since the shapes of the other surfaces are more complicated, the intersections and gaps are much larger. The interactive tolerance of the other contact pairs is 3 mm.

4.3.5 Model loading

Similar to the simplified model, there are two loadings applied on this model, which are BP and CP. The BP is applied on the internal surface of the artery. As shown in Figure 4.8, the periodic BP is 110/70 mmHg at the heart rate of 1 beat/s (60 beat/min). The CP is applied on the cuff covered region which is defined in the Section 2.3.3. As shown in Figure 4.9, CP is increased to 150 mmHg at a high speed and then decreased to 0 mmHg linearly at 2.5 mmHg/s.

4.3.6 Model mesh

Since the thickness of the brachial artery is uniform, hex element (C3D8) is used for this part. The geometries of the other parts are non-uniform and meshed by tetrahedral element (C3D4). For the artery and the surface contacting with the artery, the mesh size is 0.8 mm. For the other parts, the mesh size is 4 mm. In summary, brachial artery part contains 11088 nodes, 5520 elements; biceps part contains 8972 nodes, 42967 elements; soft tissue part contains 3683 nodes, 164952 elements; other muscles part contains 14692 nodes, 68270 elements; triceps part contains 7585 nodes, 36226 elements. Figure 4.18 shows the five parts after meshing.

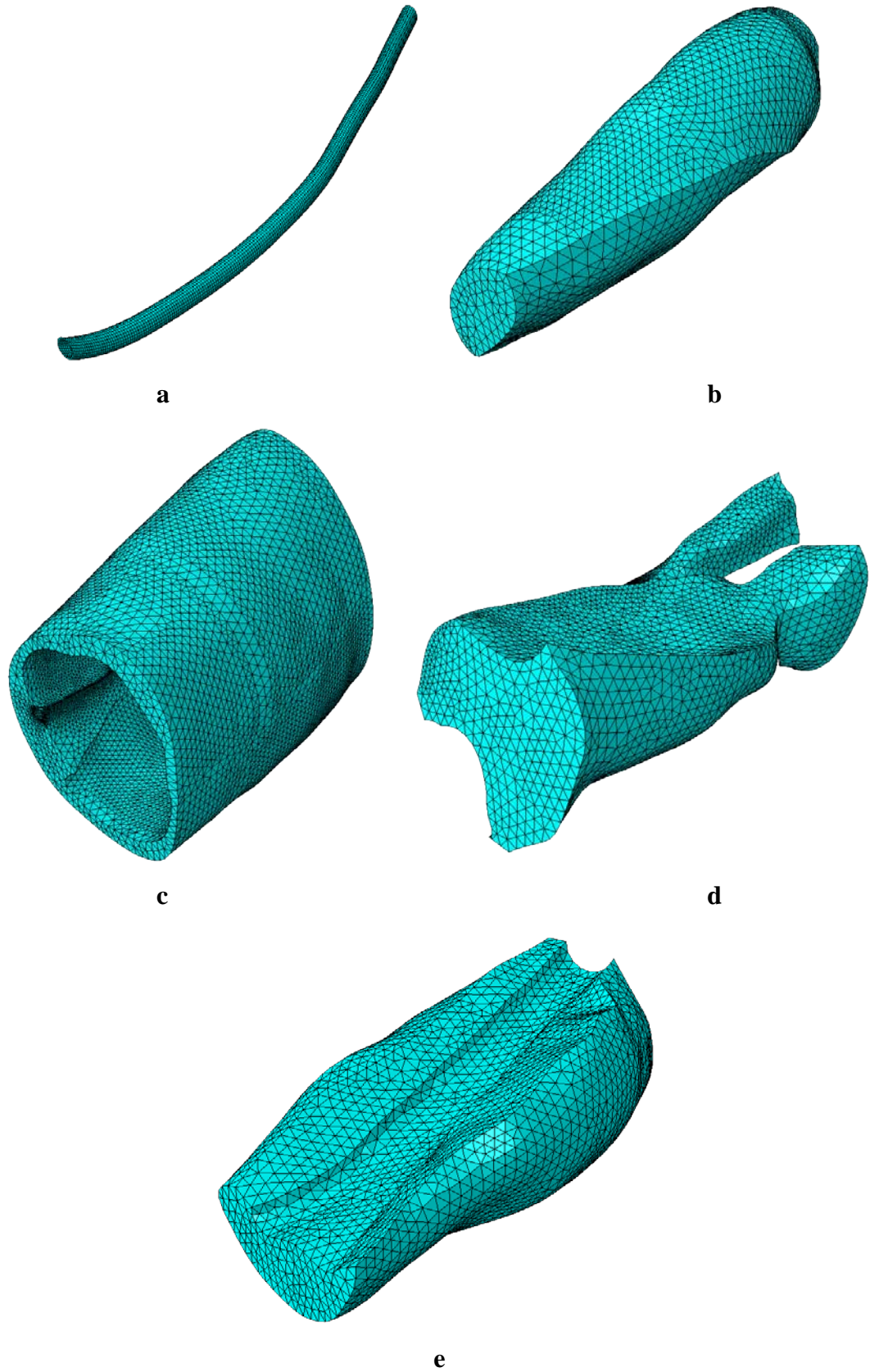


Figure 4.18 Mesh of different parts in the finite element model: (a) brachial artery, (b) biceps (c) soft tissue, (d) other muscles (e) triceps

The analyses were repeated by using a model with smaller mesh elements which were 0.4 mm in the artery part and 2 mm in the other parts. The difference of artery deformation between the two models is within 3%, which indicates that the current mesh is fine enough to achieve convergence of results.

4.4 Summary

The finite element models with both the simplified geometry and the anatomically accurate geometry were introduced in this chapter. The simplified model was designed to study the BP measurement in static status. Its geometry was mainly obtained from previous literature. With the improved artery location, the simulating results would be closer to reality. The anatomically accurate model was developed to study the BP measurement in both static and moving status. Its geometry was obtained from VHB Dataset. With the anatomically accurate geometry, some types of arm motion can be simulated.

Chapter 5 EXPERIMENT INVESTIGATION

5.1 Introduction

Since in vivo testing is very difficult to achieve with the condition of this work, an arm simulator is designed and manufactured to investigate the artery closure process during BP measurements and validate the FE model. It consists of two systems: the upper arm system and the circulation system. The structure of the upper arm system is referred to the simplified model introduced in Chapter 4. Two carefully selected silicone materials were used in this simulator, which have the most similar mechanical properties to human tissues [87]. The circulation system was set to generate blood pressure pulses in various cardiovascular conditions. It was driven by a DC pump and controlled by the customer designed Labview[®] program. The artery closure process was represented using the arm simulator and the artery deformation under external pressure was monitored and recorded by an ultrasound device. The clinical experimental protocol is also introduced in this chapter.

5.2 Arm simulator

The arm simulator is designed with three objectives in mind: (1) represent the BP measurement process, (2) investigate the relationship between the BP pulse in the artery and pressure oscillation in the inflatable cuff, and (3) validate the mathematic models. The simulator consists of two systems: the upper arm system and the circulation system.

5.2.1 Upper arm system

The upper arm system was designed and developed to simulate the upper arm. It was represented by silicone materials with simplified cylindrical geometry.

5.2.1.1 Model geometry

Since the simulator was designed to simulate the arm during normal BP measurement without any arm motion, the simplification made in Section 4.2 was applied. As described in Chapter 4, the simplified model includes three cylindrical segments: the soft tissue segment, the brachial artery segment and the bone segment. The geometrical details of the upper arm system were stated in Section 4.2.2. Furthermore, an additional artery was added in the arm simulator to study the artery closure process at different depth. The transverse section of the arm simulator is shown in Figure 5.1. The length of the arm simulator was 24 cm.

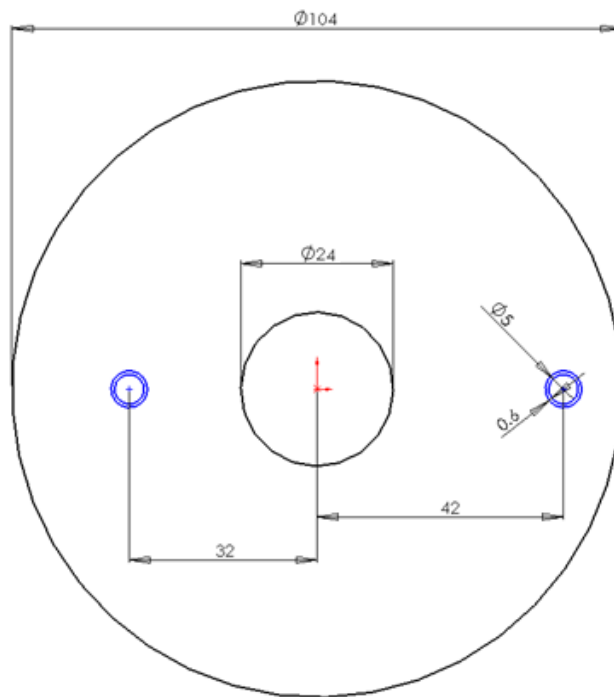


Figure 5.1 Transverse section of the arm simulator

5.2.1.2 Materials

Currently, silicone materials are most often used to simulate human tissues. This is mostly due to the fact that their mechanical properties are similar to human tissues, and they have low toxicity, high thermal stability, low chemical reactivity and long service life. Their mechanical properties can also be modified by adding additives to match the requirements. Since the bone is much stiffer than the soft tissue and assumed rigid in the model, an aluminium rod is used to simulate the bone segment.

As stated in Chapter 4, the skin, fat and muscles tissues were integrated together as the soft tissue segment. Since the muscle tissue is the major part of the arm tissues, the mechanical properties of the relaxed muscle were used as the criteria for choosing the proper material. Due to the multiple layers structure of the brachial artery, currently there is no available material which has the same non-linear elasticity as the brachial artery. Therefore, the mean elasticity of the published values was used to determine the desired material. Although the mechanical properties of human tissues vary among different people, previous studies have indicated the ranges of these tissues:

- Young's modulus of muscle tissue in the relaxed state is between 40 and 60 kPa [54].
- Densities of muscle, artery and skin are similar and approximately 1050 kg/m³ [54].
- Invasive measurements of brachial artery elasticity modulus are in the range of 400 to 600 kPa [81].

Among all types of silicone available in the market, two were chosen from their characteristics given by the suppliers. To mimic the brachial artery, the best fitting

silicone was Rhodorsil[®] RTV 3428 which was also used to build large arteries in previous studies [87]. The silicone to simulated soft tissue was Proskin[®], which was a two-part condensation cure (RTV-2) silicone rubber. Data sheets supplied by manufacturers are attached to the end of this thesis in Appendices A and B. However, the mechanical data given by the manufacture companies was not enough for research purpose. The tensile tests are required to obtain the strain-stress relationship of the selected materials.

For rubber-like soft silicone materials, the samples were tested as specified in ASTM standard D638. Because the chosen materials are very flexible, standard jigs cannot be used to hold the testing samples. As shown in Figure 5.2, specially designed jigs and fixtures were fabricated, where extremities of the sample were rolled up around axis to fix the sample.

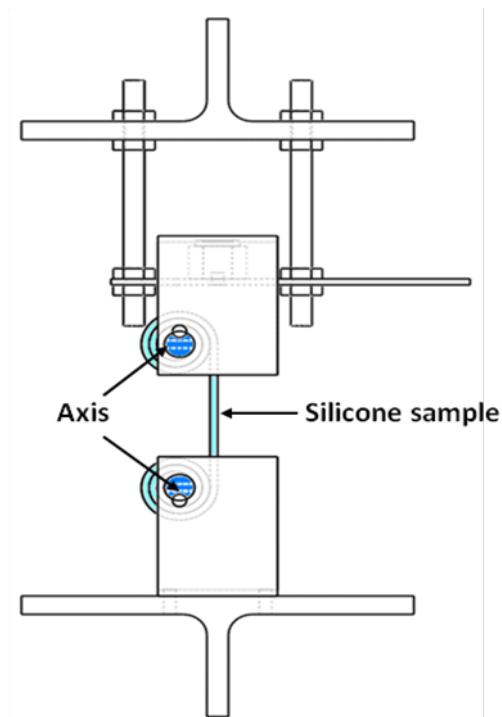


Figure 5.2 Custom designed jigs and fixtures for testing the elasticity of the selected silicone

From the tensile test, the calculated Young modulus of Rhodorsil[®] RTV 3428 was 441.7 kPa ($E_{RTV3428} = 441.7kPa$), which is within the range of brachial artery. However, the calculated elasticity of Proskin was 96 kPa, which was slightly above the required elasticity. Since the elasticity of Proskin can be reduced by adding silicone diluent, samples with different proportions of diluent were tested and shown in Table 5-1. Among the tested samples, Proskin with 15% of diluent was within the criteria and chosen to create the soft tissue segment for the arm simulator.

Table 5-1: Tensile test results of Proskin with different proportions of diluent.

| Silicone | Percentage of diluent | Elasticity |
|----------|-----------------------|------------|
| Proskin | 0% | 96 kPa |
| Proskin | 10% | 62 kPa |
| Proskin | 15% | 45 kPa |
| Proskin | 20% | 39 kPa |

5.2.1.3 Mould Development

Because of the characteristics of the selected silicone, moulding is the most suitable method to build the simulator. The custom designed mould consists of the following parts: 1×PVC pipe, 1×aluminium rod, 2×steel bar, 2×holding plate, 2×cap, 1×vacuum cover, 1×rubber stopper, and 1×glass tube. All of the parts were assembled together as shown in Figure 5.3.

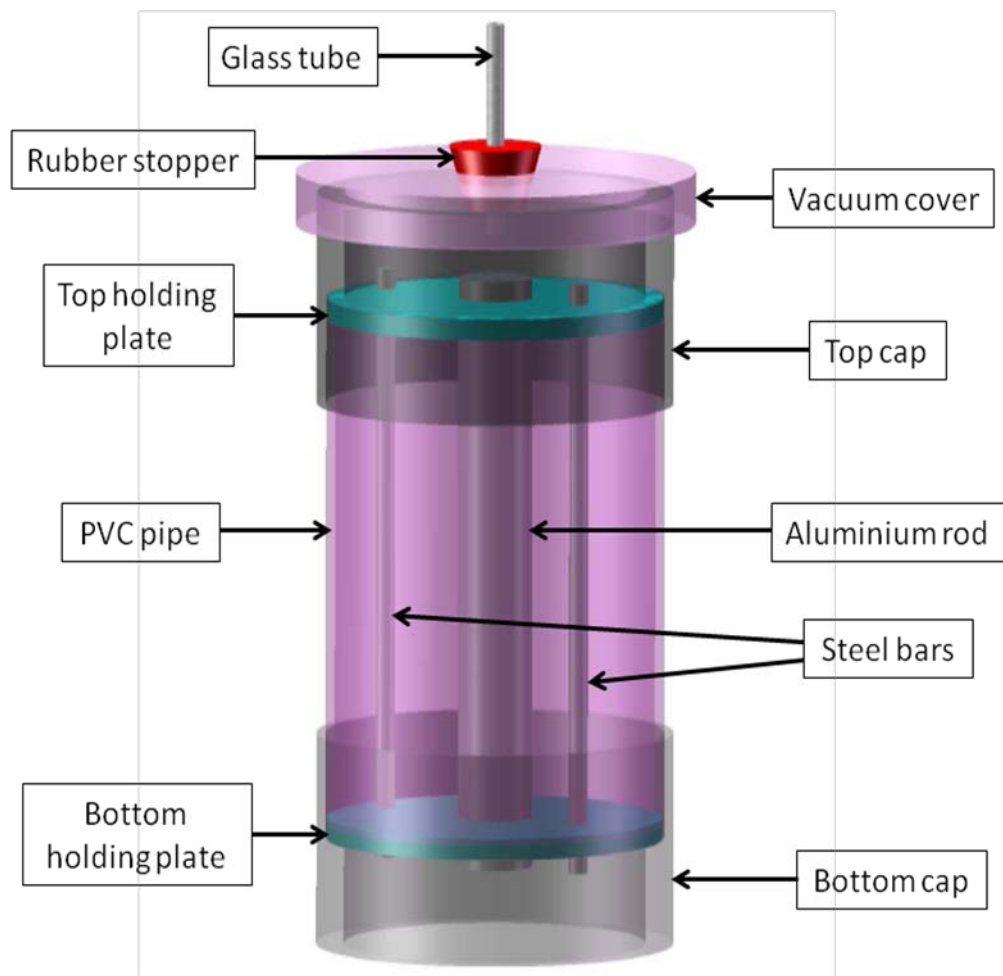


Figure 5.3 The assembled silicone mould

5.2.1.4 Model fabrication

For the selected two-part condensation cure silicone - Proskin, moulding is the best way to create the model. During the mixing process, many air bubbles were present into the silicone. As the viscosity of Proskin in liquid status is very high, the air bubble degassing process is very slow. Furthermore air bubbles significantly change the final silicone properties, silicone mixture must be degassed during the moulding process to remove air bubbles inside. In this experiment, the mould was connected to a vacuum device to accelerate the degassing process.

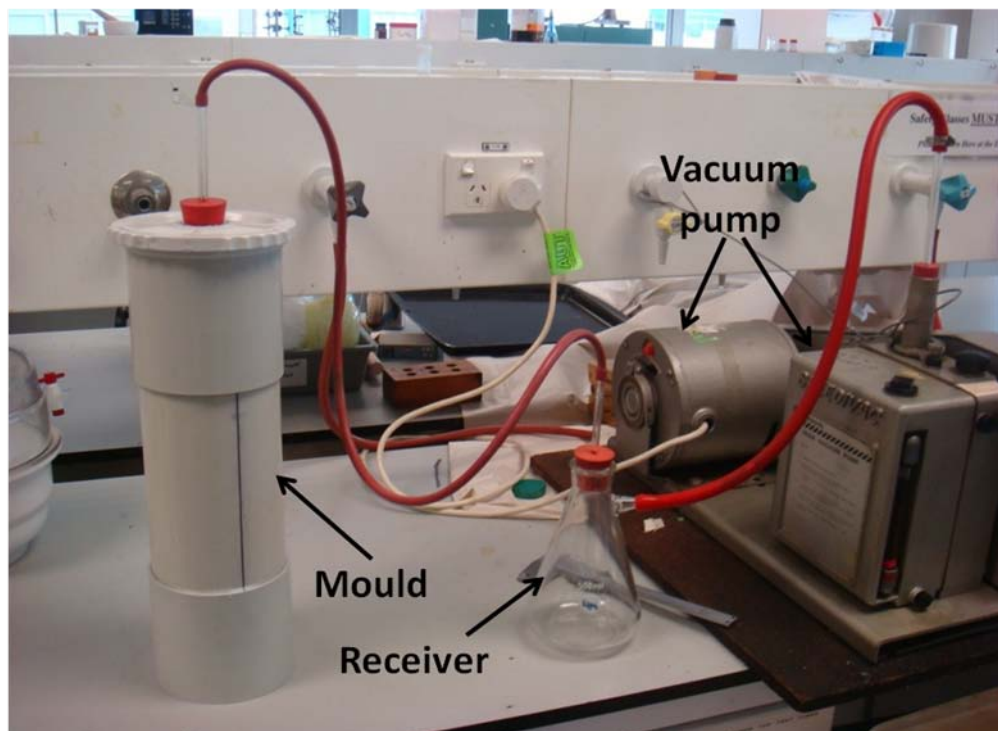
The moulding process is described as follow:

1. The bottom cap, bottom holding plate, PVC pipe, aluminium rod and steel bars were assembled together. To avoid leaking, the connecting surfaces were sealed.
2. The two-part condensation and diluent were mixed properly and placed in a vacuum charmer for 20 minutes, which included 820 ml Proskin Part A, 820 ml Proskin Part B and 290 ml diluent.
3. The degassed silicone mixture were poured into the mould as shown in Figure 5.4a;
4. The top holding plate, top cap and vacuum cover were connected to the mould.
5. The vacuum device was connected to the mould as shown in Figure 5.4b and operated in the entire curing process.

When the silicone was totally cured, the mould was removed and the soft tissue segment was fixed on wooden frame as shown in Figure 5.5. The aluminium rod was remained to simulate the bone. The top and bottom caps were fixed on the aluminium rod to limit the movement in axial directions.



a



b

Figure 5.4 Moulding process: a. the pouring process of moulding; b. the entire setup for simulator moulding

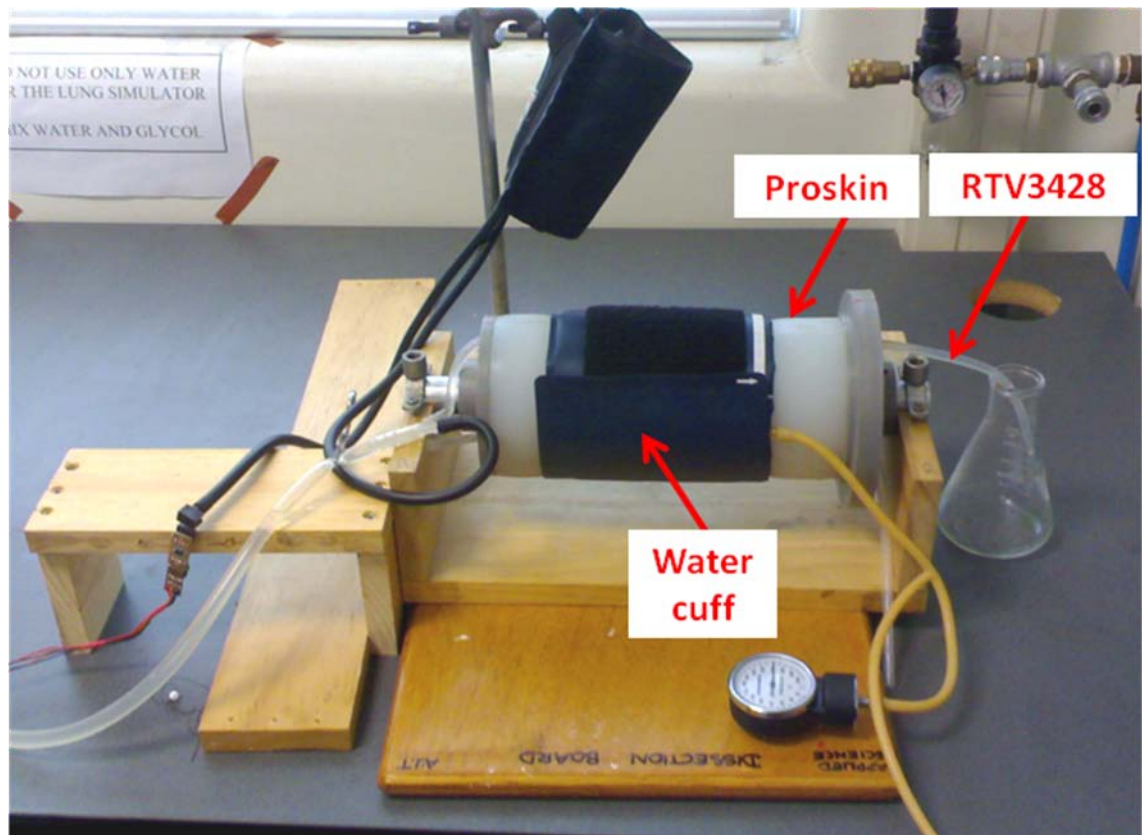


Figure 5.5 The assembled arm simulator.

In order to get the artery segment with accurate and uniform wall thickness, the improved spin coating technique was used in this study. The manufacturing process includes the following steps:

1. mixing RTV3428 Part A, Part B at the ratio of 10:1;
2. placing the mixture of RTV3428 in a vacuum chamber for 15 minutes to remove all air bubbles,
3. transferring the silicone mixture to a syringe,
4. fitting the steel bar (diameter is 5 mm) into the lathe as shown in Figure 5.6a,
5. applying a very thin layer of Vaseline on the bar to facilitate the removal of the cured silicone tube,

6. starting the lathe and setting the spinning speed at 45 rpm,
7. dripping the silicone at constant speed along the bar,
8. moving the parting tool along the steel bar to remove the extra silicone and control the tube thickness as shown in Figure 5.6b,
9. adjusting the parting tool's position and repeating step 8 until the silicone is cured.



a



b

Figure 5.6 (a) The silver steel bar is fitted into the lathe. (b) The parting tool is set to control the wall thickness.

Because the diameter of the fitted steel bar is just 5 mm and the length of the bar is over 40 cm, the normal steel bar will sag by gravity. Silver steel made bar was selected in this study, which has relatively high rigidity and good surface finish. When the tube was fully cured, it was removed from the spinning bar and inserted into the Proskin made soft tissue segment as shown in Figure 5.5.

5.2.2 Circulation System

The circulation system was designed to simulate the blood flow in the upper arm system. As shown in Figure 5.7, the circulation system consists of the following components: a DC operating pump to simulate the heart, the circulation pipes to simulate the arteries, pressure sensors, a computer controlling system, a field-programmable gate array (FPGA) pulse width modulation system, an H-bridge switch system and a fluid reservoir. In the circulation system, the operating pump is used to generate pressure and flow waves.

In this study, the circulation system contains two branches: the brachial artery branch and the other circulation branch. Since the experiment was designed to track the pressure wave in the brachial artery, most of the pressure sensors were placed in the brachial artery branch. As shown in Figure 5.7, four pressure sensors were connected to the circulation system to monitor the pressure in the circulation system, which are located after the operating pump (P1), before the silicone arm (P2), in the middle of the silicone arm (P3) and just after the silicone arm (P4).

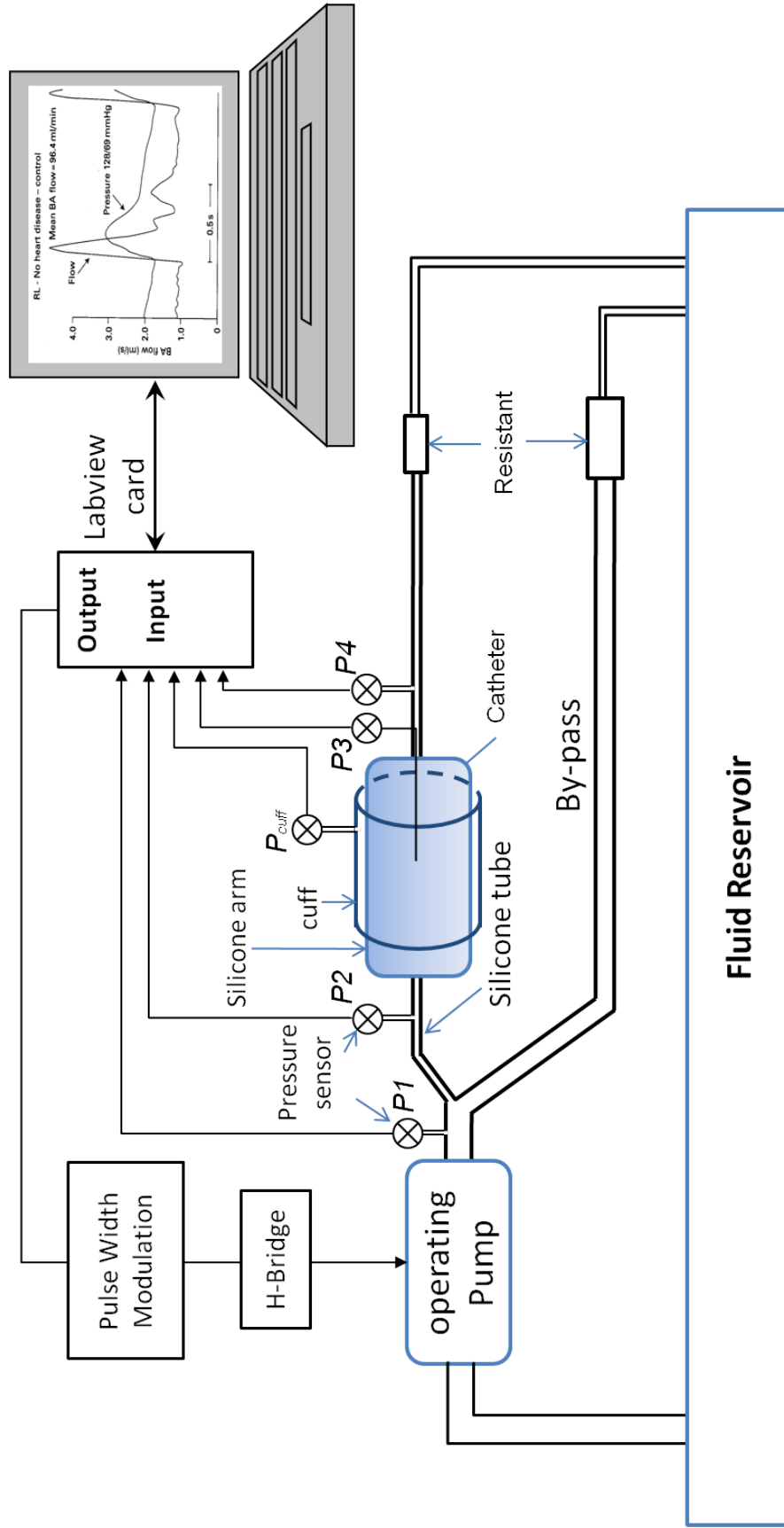


Figure 5.7 The schedule structure of the arm simulator

In the human circulations system, about 5% of the blood flow from the heart goes through the brachial artery in each heart beat [88], and the normal BP measurement has little effect on blood flow in human circulation system. In the arm simulator's circulation system, the sizes of the main and bypass branches in the circulation system are much larger than the brachial artery branch, and their diameters are 25 mm and 22 mm respectively. The diameter of the brachial artery branch is 5 mm as described previously in the model manufacturing section.

For an average sized adult, the normal blood flow in the entire human circulation is about 5 l/min at rest, but the value may be increased 5-6 times during heavy exercise [84]. Further, the maximum flow rate is about 3 times over the average flow rate. Therefore, the maximum flow rate occurring in the normal adult circulation system can achieve up to 90 l/min (1426.5 gallon/hr). Referring to the calculated value, the DC powered centrifugal pump (Rule[®] 1500), which can deliver up to 1500 gallon/hr was selected and used to simulate the heart in this study.

In order to perform the heart beat waveform as observed in human beings' circulation system, the pump was controlled by an open-loop control system as shown in

Figure 5.8. A customer designed Labview program sent the waveform to the on-chip FPGA which was set to Pulse Width Modulation (PWM) modulus. By adjusting the pulse width ratio of the supplied DC power, the programmed PWM provided variable voltage DC power to control the DC motor's running speed. The switches of the H-bridge are opened and closed to control the running directions of the DC motor.

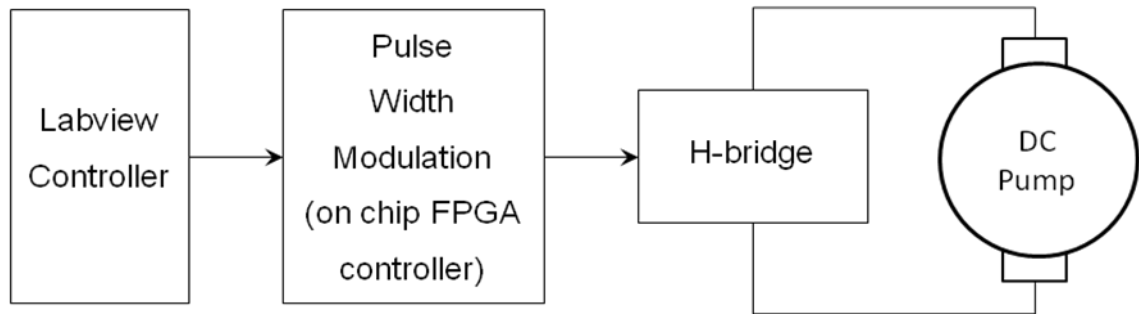
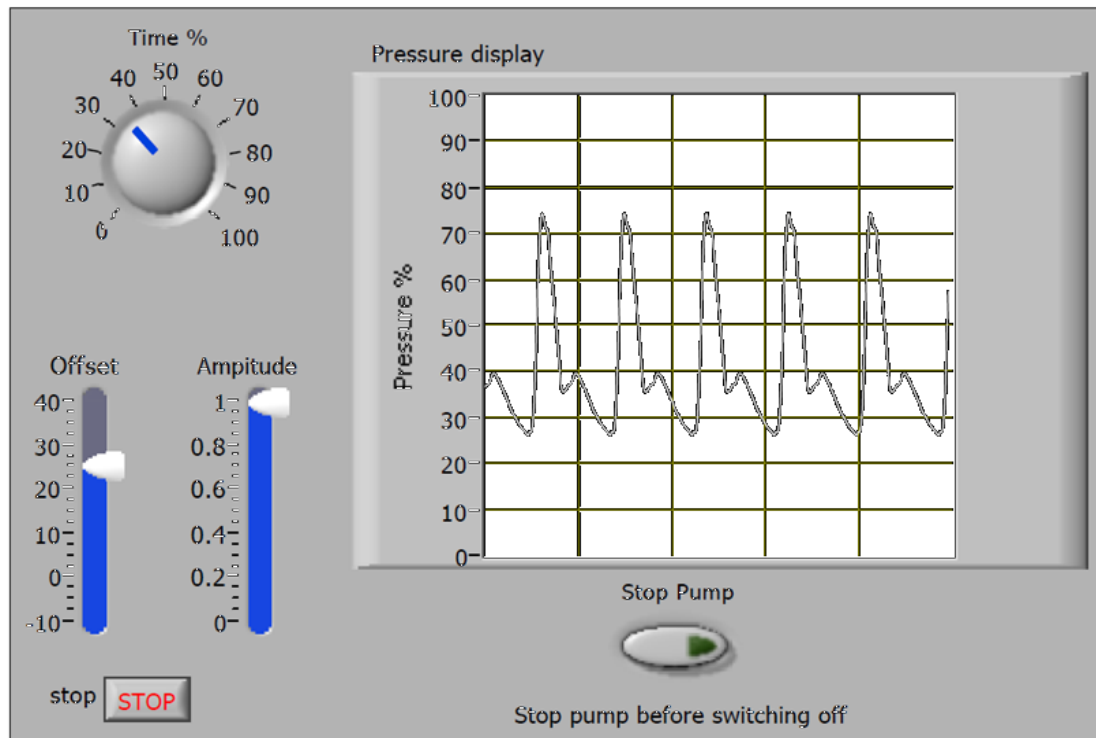


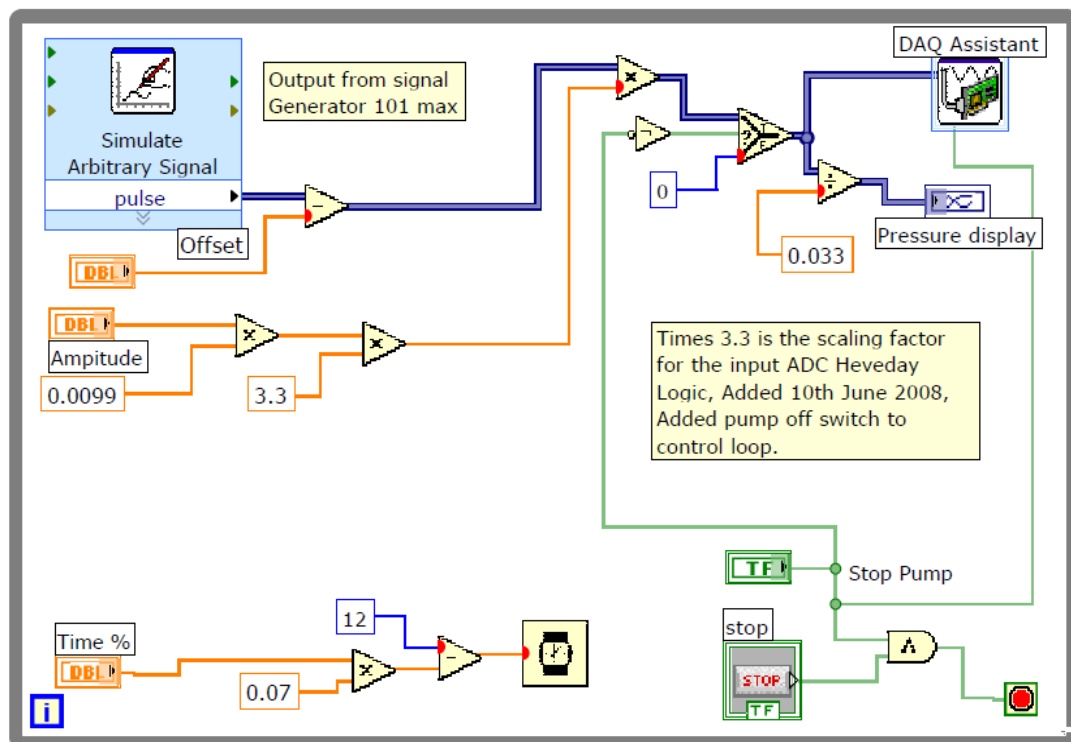
Figure 5.8 The open loop DC pump control system

Associated with the customer designed Labview[®] program as shown in Figure 5.9, the arm simulator can generate blood pressure pulses over a wide range: heart beats, 40 ~ 200 beat/min; blood pressure, 40 ~ 220 mmHg; blood pressure pulse amplitude, 20 ~ 100 mmHg.

Since the operating pump can generate the pressure up to 220 mmHg, 26PCB serials sensors (Honeywell Inc. Illinois, USA) were used in the system, which have linear performance and can measure pressure 0 ~ 5 psi (0 ~ 258 mmHg). In the circulation system, the pressure sensor $P1$ was connected to the main branch just after the operating pump to monitor the pump performance; the pressure sensor $P2$ and $P4$ was connected to the brachial artery branch through two side pressure tabs to measure fluid pressure at the proximal and distal ends of the arm simulator; the pressure sensor $P3$ was connected to a fluid filled catheter to measure the pressure in the arm simulator. Another sensor P_{cuff} was connected to the cuff to track the CP. The outputs of these sensors were connected to a data acquisition card CB-68LP and recorded by the Labview[®] program as shown in Figure 5.10.

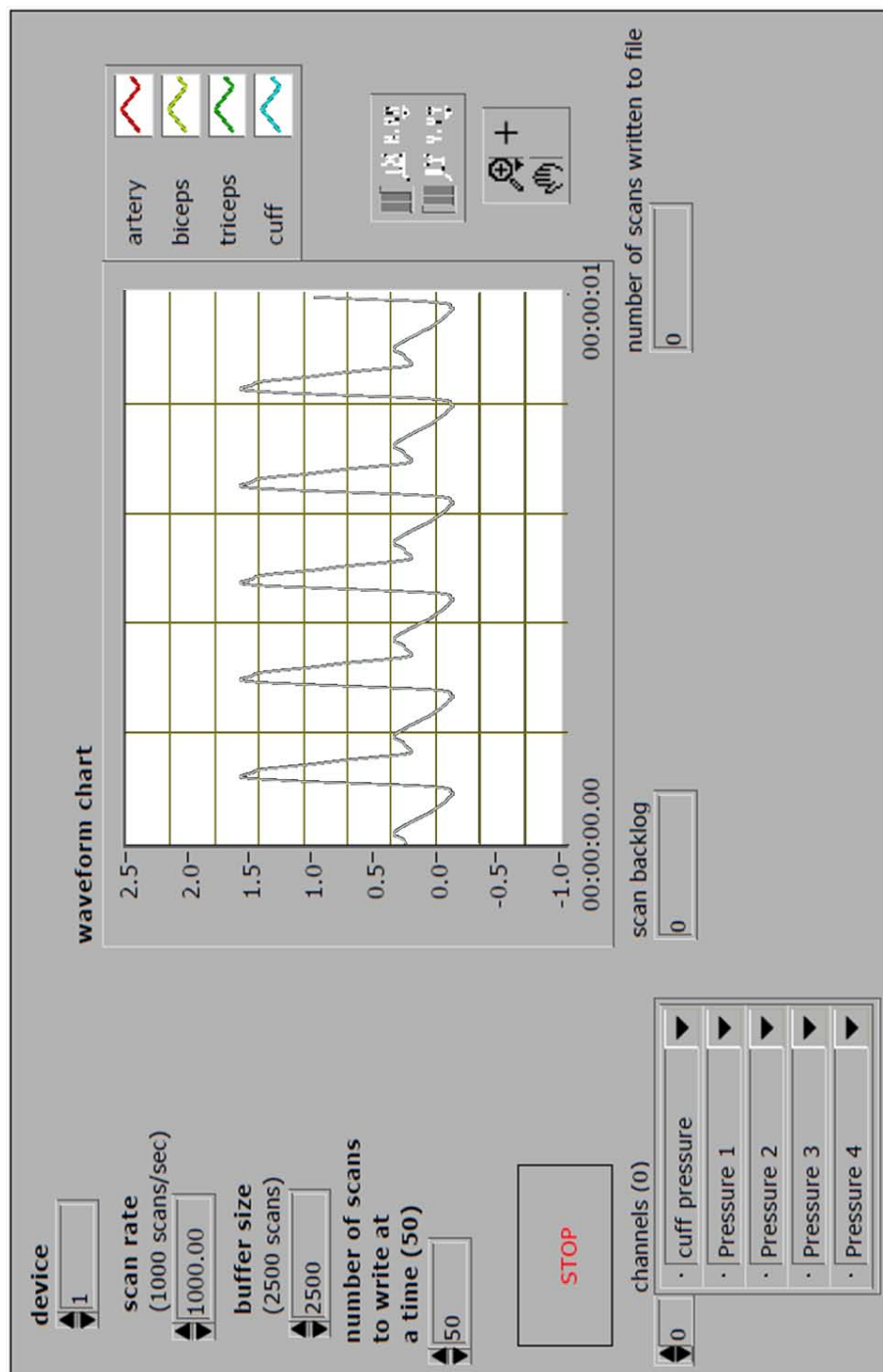


a

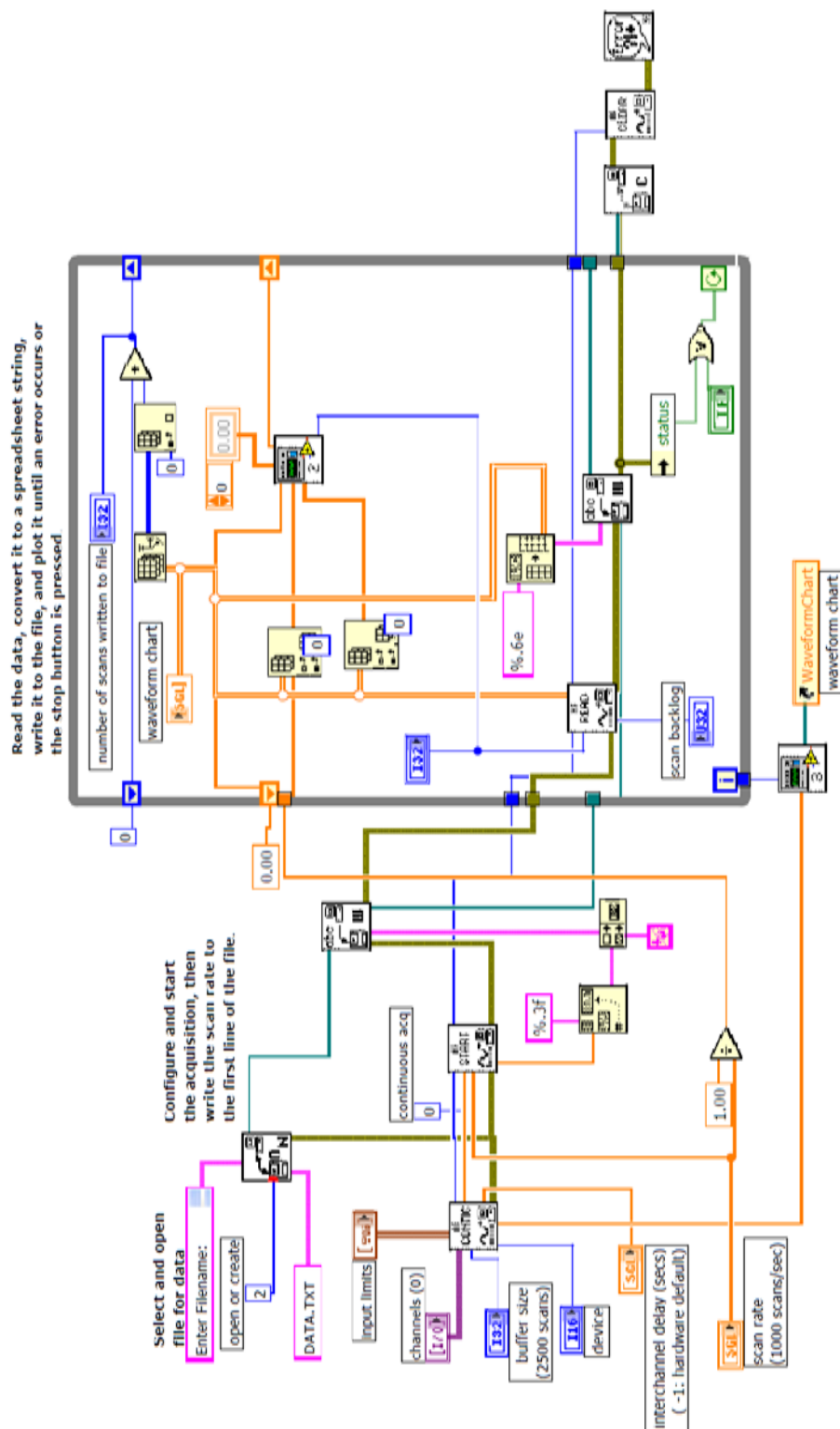


b

Figure 5.9 The Labview® program for generating pressure pulse waves: (a) front panel, (b) block diagram.



a



b

Figure 5.10 (a) Front panel of the Labview® program for recording pressure sensor readings (b) Block diagram of the Labview® program for recording pressure sensor readings

5.2.3 Ultrasound Measurement

In order to track the artery closure process under external pressure in the arm simulator, an ultrasound technique was used. Since the ultrasound signal cannot transfer through the air, the cuff and brachial artery branch were inflated with water. The deformation of the arm simulator under the water cuff was imaged and recorded by Philips® HD11 Ultrasound device (768 x 576 pixels) with a L12-5 MHz, 50mm broadband linear array transducer. The obtained data was initially post-processed on Phillips QLAB® software (Release 5.0, Da Best, The Netherlands) to create image files for further analysis. Because of the circular shape of the brachial artery branch, the reflected ultrasound wave was weak when the ultrasound sensor was placed in transverse plane. Furthermore, because the densities of the silicone and water are very close, the edge between the brachial artery branch and water is hard to be identified as shown in Figure 5.11. Therefore it is impractical to track the artery branch closure process using the image in transverse plane.

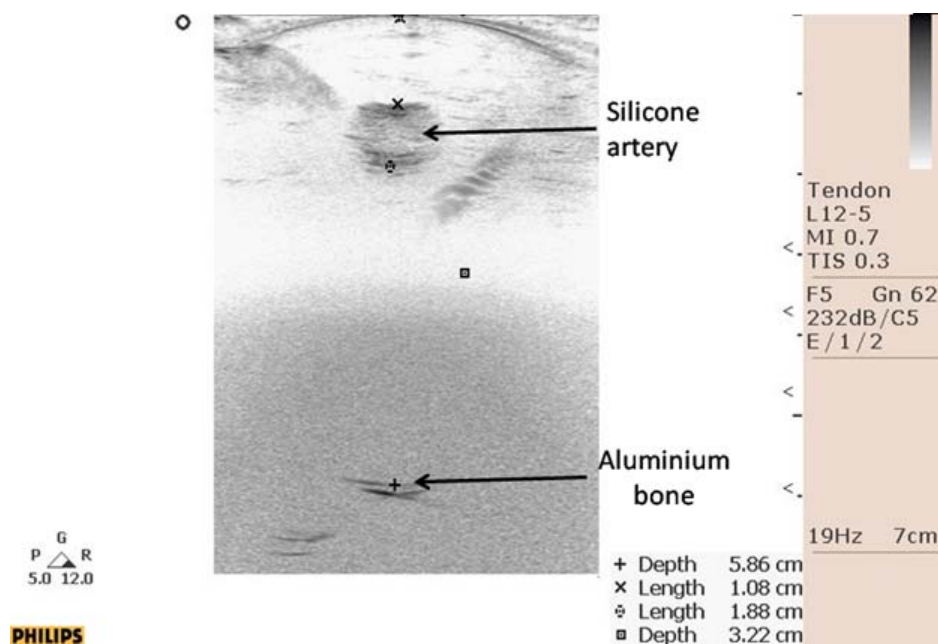


Figure 5.11 Ultrasound image in transverse plane

In this experiment, the ultrasound sensor was set parallel to the brachial artery branch in coronal plane as illustrated in Figure 5.12. From the obtained ultrasound image, the following subjects can be clearly identified: external and internal walls of the cuff, water in the cuff, the soft silicone (Proskin), internal walls of the brachial artery branch.

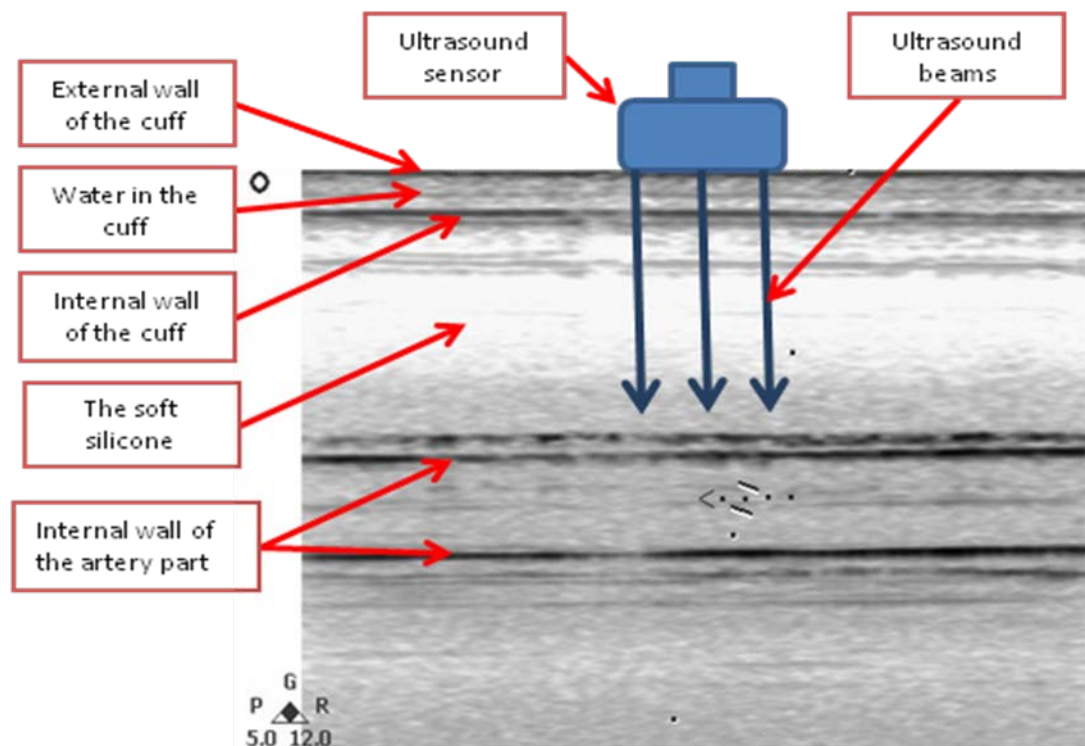


Figure 5.12 Ultrasound image in coronal plane

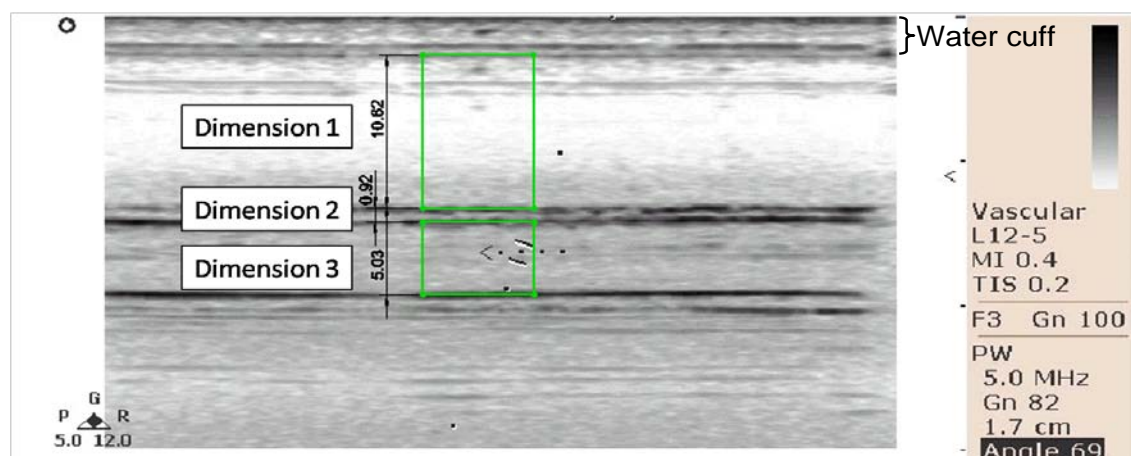


Figure 5.13 Ultrasound image of the silicone arm simulator

From the identified edges shown in Figure 5.12, the following dimensions were used in this study as shown in Figure 5.13: artery embedded depth (Dimension 1 – D1), artery wall thickness (Dimension 2 – D2) and the artery internal diameter (Dimension 3 – D3). These dimensions are also illustrated in cross-section view as shown in Figure 4.3.

During the measurement, the internal pressure in the brachial artery and water CP were set to zero. The obtained dimensions as shown in Figure 5.13 were 10.62 mm, 0.92 mm and 5.03 mm respectively which were measured by QLAB[®]. The results were quite different from the designed dimension 6.9 mm, 0.6 mm and 5 mm. This is attributed to the fact that the dimension distances shown in Figure 5.13 were originally calibrated for quantifying ultrasound data in human tissues. Therefore, the recalibration must be made for the silicone materials. The speed of ultrasound sound in human tissue is 1540 m/s [89], while that in silicone and water is 1000 m/s [89] and 1482 m/s [90] respectively. Consequently, the distance $D_{measured}$ shown in QLAB[®] program must be recalculated to the corresponding value in human tissue D_{cor} using the Equation (5.1),

$$D_{cor} = \frac{V_{testing}}{V_{tissue}} D_{measured} \quad (5.1)$$

where $V_{testing}$ and V_{tissue} are the speed of ultrasound in the tested materials and tissue respectively. Applying Equation (5.1) on the measured dimensions shown in Figure 5.13, the recalibrated results of D1, D2, and D3 are 6.896 mm, 0.597 mm, and 4.841 mm respectively. Comparing with the designed dimensions demonstrated in Figure 4.4, which are 6.9 mm, 0.6 mm and 5.0 mm, the measurement error is less than 3.2%. Therefore, the ultrasound technique associating with the amending equation is reliable and appropriate for this study.

5.3 FE Model Validation

The internal flow pressure at different positions in the brachial artery branch was tested to ensure the accurate measurement in the following experiments. In the tests, the flow pressure was kept at the mean pressure 90 mmHg; while the CP was set to 60 mmHg at the start. Then the CP was increased by 10 mmHg at each step until it achieved 190 mmHg. In each of these steps, the catheter was placed at different locations along the brachial artery branch. These measurements indicated that the internal flow pressure was almost constant with very small variation along the brachial artery segment when transmural pressure changed from 30 mmHg to -90 mmHg. These experimental results matched the assumption made in Section 4.2.5. The artery closure process was simulated using the arm simulator and used to compare with estimation from the finite element model. During the experiment, the artery opening status was tracked by ultrasound device.

Since the artery closure process is related to the transmural pressure rather than the external CP or internal flow pressure individually, the operating pump was set at a constant speed to maintain the flow pressure at 90 mmHg to make the experiment simpler. The cuff was inflated to 190 mmHg at first, then it was decreased from 190 mmHg to 90 mmHg at the rate of 5 mmHg/s. The catheter pressure sensor was placed in the middle portion of the arm simulator under the cuff. During the experiment, the data from the pressure sensors was synchronised in time with the image data to calculate the arm simulator deformation in the system at different transmural pressure levels. As shown in Figure 5.14, the relationship between the transmural pressure and artery diameter (D3) was plotted.

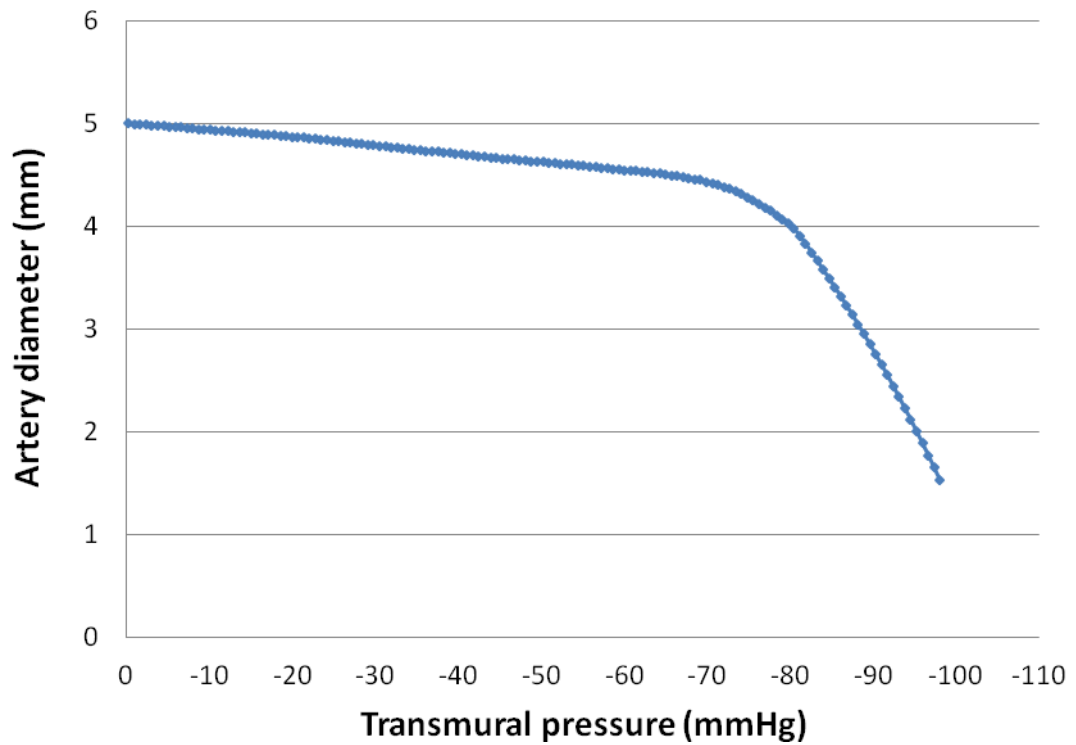


Figure 5.14 The relationship between transmural pressure and artery diameter obtained from arm simulator by ultrasound device.

5.4 Clinical Trial

All clinical trials were conducted with ethical approval (AUTEC 08/232). Clinical trials of normal BP measurement using oscillometric technique on 30 subjects were conducted in this study, which include 15 males and 15 females, age 20-80. CP oscillations during the measurement were recorded by a Pulsecor[®] R6.5 non-invasive monitor. Subjects' BP values were determined by the auscultatory method.

5.4.1 Oscillometric BP Measurement

Since it was cuff-based non-invasive BP measurement, BP pulses in the brachial artery are not able to be obtained and CP oscillations were recorded instead. Figure 5.15 shows the measurement result of one patient.

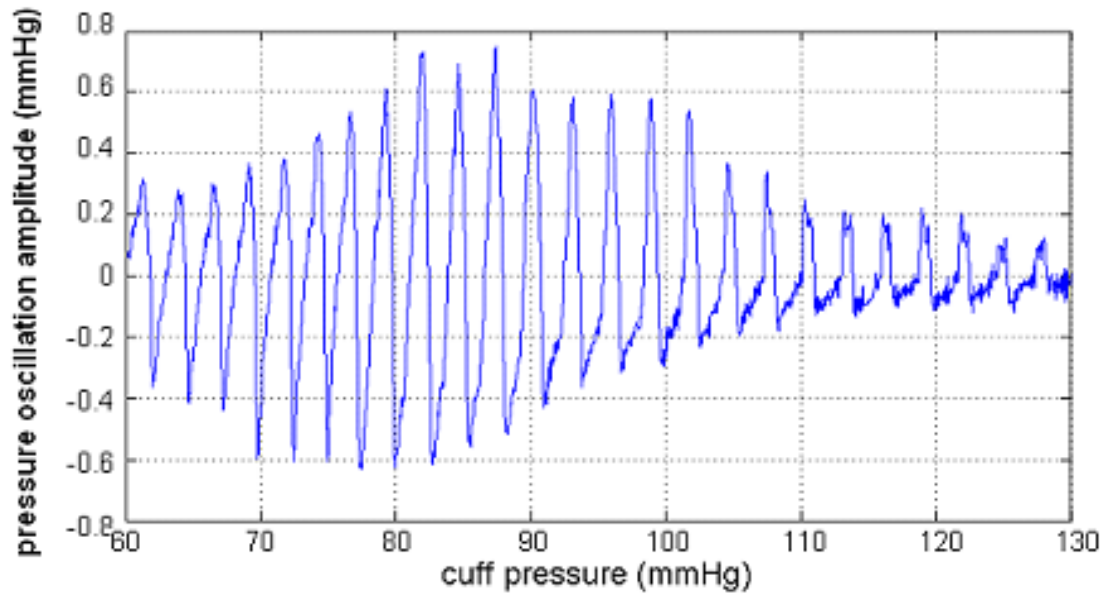


Figure 5.15 The CP oscillation measured in oscillometric BP measurement

5.4.2 Experimental Protocol

Other than CP oscillation, BP signals are also transferred to the arm skin by the form of surface strain. In the normal adult, the brachial artery lumen area change between systolic pressure and diastolic pressure is about 30% during each heart beat. When applying the upper arm size used in Chapter 4, the circumferential strain of the upper arm during each heart beat is about 0.35 millistrains.

Since the upper arm is soft and the shape is irregular, only the sensitive and flexible sensors are eligible for this study. Piezoelectric film sensors were selected among the strain sensors in the market. It is more sensitive, more flexible and easier to fit to the skin. In this study, Measurement Specialties FDT1-028K type piezoelectric film sensors were used. The properties of these sensors are attached in Appendix I-C. The electrical analog of the selected piezoelectric film sensor is a capacitor in series with a voltage source. As the impedance of FDT1-028K type sensor is normally over $10\text{ M}\Omega$, the normal measurement device such as the scope probe whose impedance is $1\text{ M}\Omega$ act

almost like a short-circuit when connects to the piezoelectric film sensor. With sensitivity of 12×10^{-3} v/millistrain, the sensor reading of in normal BP pulse is 4.2×10^{-3} v. Therefore, a differential charge amplifier is required. The advantages of connecting to a charge amplifier are: (1) the output of the amplifier is independent of cable capacitance and therefore the long cable can be used between the sensor and the charge amplifier; (2) since the feedback resistance of charge amplifier is very high resistant, the charge leakage of sensor is minimized. The designed circuit of the charge amplifier is shown in Figure 5.16.

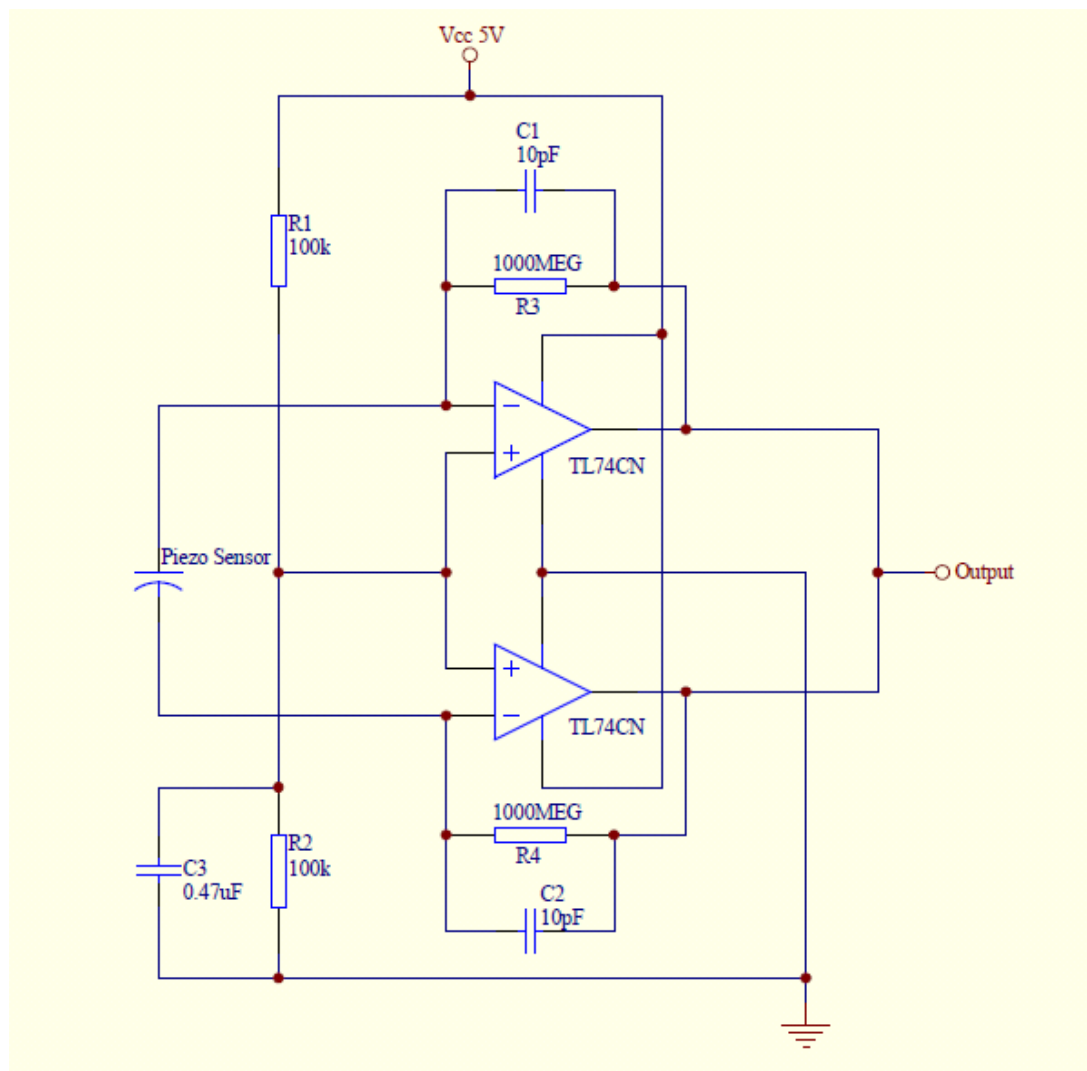


Figure 5.16 The differential charge amplifier is designed to connect the piezoelectric film sensor with data acquisition card.

R1, R2 and small bypass capacitor (C3) set the input common-mode voltage at the mid-supply level. Therefore, the output of the sensor varies between 0 V and 5 V. In the charge amplifier, the capacitance of the feedback capacitor is $C1 = C2 = 10\text{pF}$, and the voltage gain of the charge amplifier equals to $C_{\text{pie}}/C1$. As the capacitance of FDT1-028K piezoelectric sensor is 1.36 nF, the gain of the charge amplifier is 136. The charge amplifier also acts as a high pass filter and a low pass filter. The high-pass filter is determined by the capacitance of piezoelectric film sensor (C_{pie}) and feedback resistance (R3, R4); the low-pass filter is determined by the feedback capacitance (C1, C2) and feedback resistors (R3, R4) which are 1000 M Ω . Using Equation (5.2), the calculated cut-off frequencies of the designed charge amplifier are 0.12 Hz and 15.7 Hz respectively.

$$f = \frac{1}{2\pi RC} \quad (5.2)$$

Since normal people's heart rate is 30 ~ 180 beat per minute and most of BP features are contained in the first 5 harmonic frequencies, all of the useful signals are in the range between 0.5 Hz and 15 Hz. Therefore, the developed charge amplifier was suitable for the current study. Since the impedance of the piezoelectric film sensor is very high, the op amps are required to have high impedance to minimize the input current leakage. Therefore, low noise J-FET quad op amps TL074CN was selected, whose impedance is 1000 G Ω .

5.4.3 Experimental Procedures

Other than BP pulses, the muscle motions are also transferred to the skin in the form of surface strain. In this study the following arm motion are considered: bend and twist. From the model prediction and anatomic analysis, sensors will be placed at the

location(s) where the model predicts maximal strain in response to the arterial pulse and at location(s) where the model predicts minimal strain in response to the arterial pulse. Based on analyses carried out by the developed models, the piezoelectric film sensors were placed above brachial artery, bicep, and triceps respectively. The details of this sensor array will be demonstrated in Chapter 6.

5.5 Summary

The silicone made arm simulator was designed and manufactured to simulate the oscillometric BP measurement process. The artery closure process under external CP was tracked and recorded by an ultrasound device. The finite element model was validated and used to simulate brachial artery closure process during BP measurement. The piezo film sensors were selected to measure the surface strain on the arm.

Chapter 6 FE Model Results and Discussion

6.1 Introduction

This chapter first explains how the FE model of the upper arm is validated by the arm simulator experiments and clinical data respectively. The experimental silicone material properties are then simulated in the FE model for validation purpose. Then the arm tissues with various mechanical properties were implemented in the FE model. The effects of mechanical properties of the arm tissue material on the oscillometric BP measurement are also investigated. Thirdly, the FE model with anatomically accurate geometry was analysed in this chapter. The loadings, which included BP, muscle movement and CP, were simulated respectively in the anatomically accurate model. The surface strain distribution with different loadings was presented and utilized to determine the proper locations for piezoelectric film sensors which were attached to the arm skin to detect the arm motion and BP pulses.

6.2 FE model with cylindrical geometry

The FE model with simplified cylindrical geometry was validated using the simulator discussed in Chapter 4. CP oscillations and the artery closure process were simulated and compared with the clinical results. The models with different material properties were simulated to determine the effects of arm tissue mechanical properties in oscillometric BP measurement.

6.2.1 Validation of simplified cylindrical FE model

The FE model was validated by comparison with experimental results and clinical data. The first test looked at the artery closure process under external CP and compared with experimental results conducted on arm simulator. The second test looked at artery volume changing trend in the BP measurement process and compared with CP oscillations in the clinical measurements.

6.2.1.1 Artery closure process

In previous literature, it was reported that the artery closure status plays an important role in oscillometric BP measurement [30]. The artery closure processes under different CPs were reproduced by the FE model and the arm simulator respectively and their results were compared for validation.

As described in Section 4.2.3, the artery deformation under the central part of the cuff was recorded by the ultrasound device, in the TP range of 0 ~ 100 mmHg. To compare with the obtained results, the same process was simulated using the FE model with material properties of the same value as the arm simulator. Figure 6.1 shows artery diameter vs. TP obtained from the FE model. This figure shows an excellent agreement with the experimental data obtained from the arm simulator with coefficient R^2 value of 0.988. This kind of accuracy for the ABAQUS model provides a good justification for using the model to predict other conditions of the artery closure process.

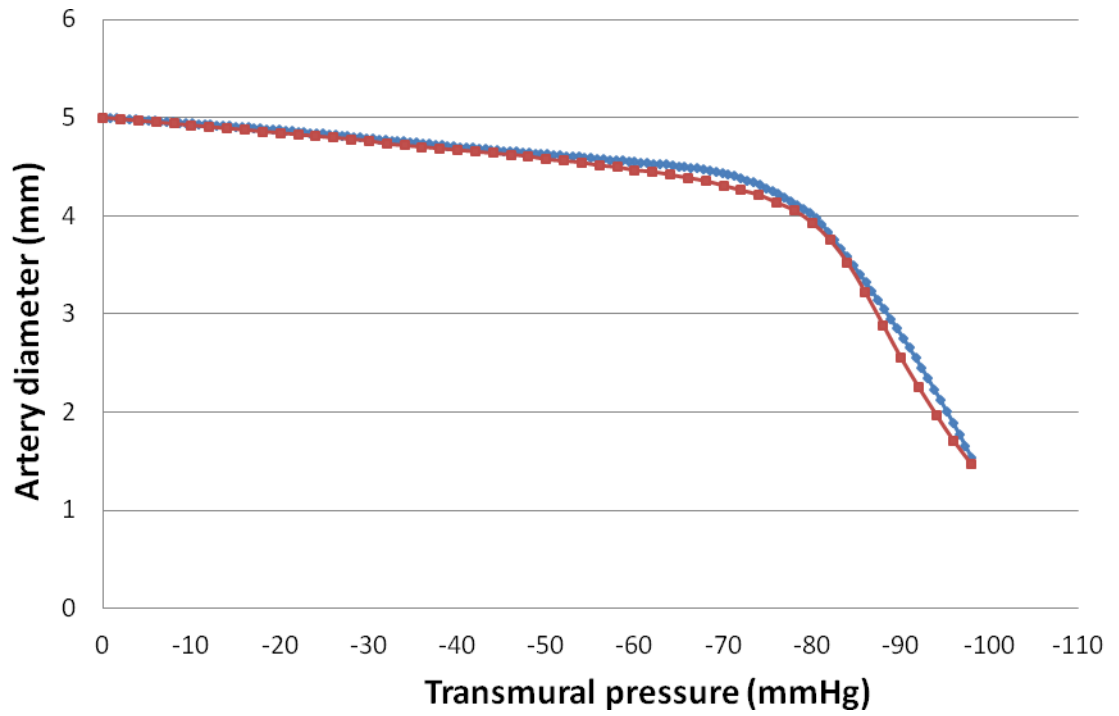


Figure 6.1 The relationship between TP and artery diameter obtained from arm simulator and FE model respectively. —■— FE model results; —◆— Ultrasound measurement

To validate the simplified cylindrical geometry, the model results were compared with those of the clinical data. To do that, the silicone material properties in the FE model were replaced by the soft tissue and brachial artery material properties as described in Chapter 4. In previous clinical experiments, Bank et al [81] reported changes of 71% for *in vivo* intravascular ultrasound measurement of the lumen area when TP changes from 100 to 0 mmHg, which was achieved by increasing the CP from 0 to 100 mmHg. Using a similar procedure in the present work, the initial BP value was set to 100 mmHg and the CP increased from 0 to 100 mmHg. The change in the predicted value of the lumen area is 69%, which is just 2% lower than the *in vivo* intravascular results. Therefore, the developed model accurately describes the artery deformation when TP is in the range of 1 ~ 100 mmHg. Since the brachial artery might collapse when TP is under 0 mmHg, the

lumen area of the brachial artery cannot be measured directly by the intravascular ultrasound device. Therefore, to compare with the FE model, further validation and modification to the experiment was carried out as introduced in the next section.

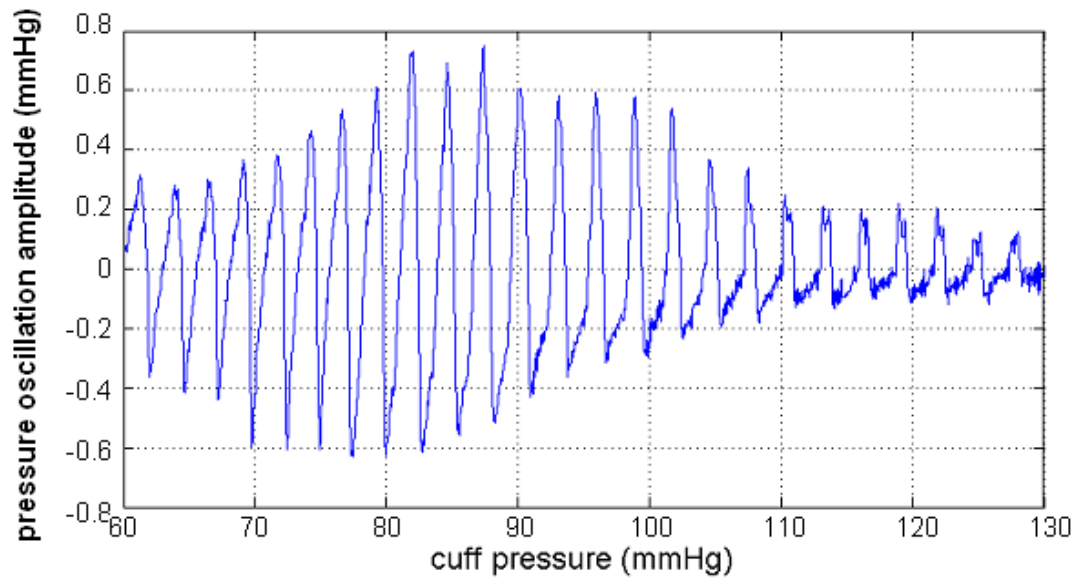
6.2.1.2 CP oscillation during BP measuring process

The oscillometric BP measuring process was simulated using the simplified cylindrical FE model developed in this work and the results were compared with clinical data. All clinical trials were conducted with ethical approval (AUTEC 08/232). In this study, clinical trials of normal BP measurement were conducted on 30 subjects, 15 males and 15 females, age 20-80. Each one of these trials generated a figure similar to Figure 6.2a (for brevity only one case is given). The CP deflation processes were controlled by a Pulsecor[®] R6.5 non-invasive monitor and subjects' BP values were determined by the auscultatory BP measurement method which was considered. At the same time, CP oscillations during the entire BP measurement process were recorded by the Pulsecor[®] R6.5 non-invasive monitor and the signals obtained were filtered by the inbuilt filters for further analysis. For the clinical experimental results shown in Figure 6.2a, the subject's BP reading was 110/70 mmHg by both auscultatory method and oscillometric method. To check against clinical trials, the simplified cylindrical FE model was simulated under the same loading as the clinical experiment, as follows:

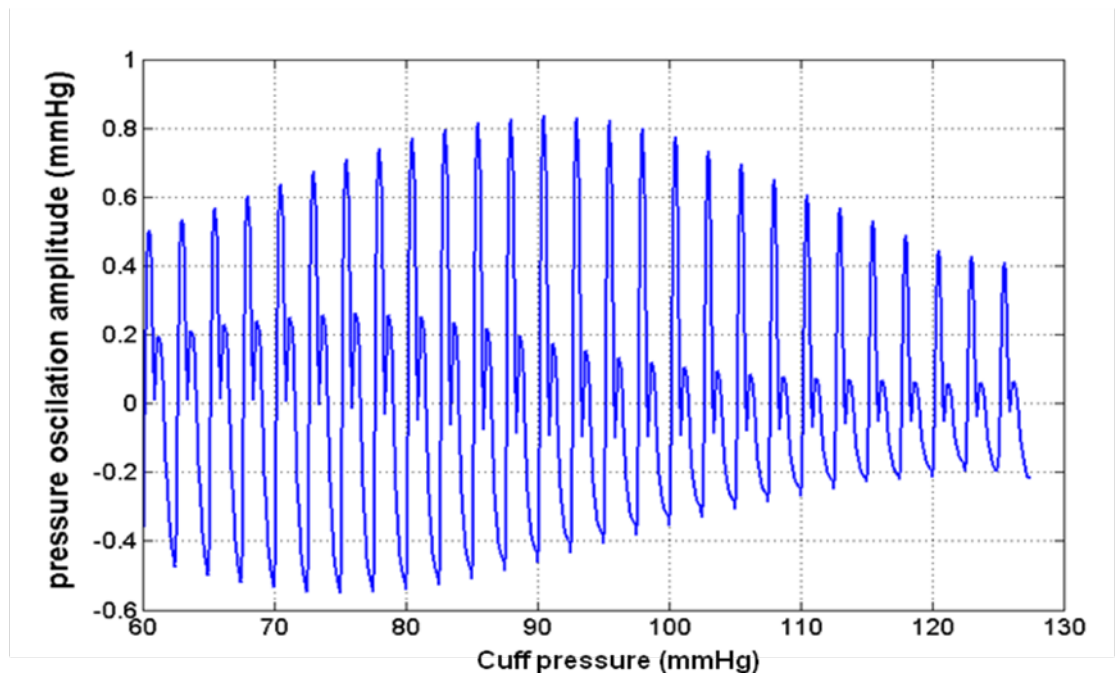
1. distributed CP was linearly decreased from 130 mmHg to 60 mmHg at a speed of 3 mmHg per second;
2. BP was 110/70 mmHg with the heart rate at 72 beats/min.

Since invasive BP measurement in the brachial artery is very difficult to achieve and brings a high associated risk, the BP waveform in the brachial artery was replaced by

the clinical waveform shown in Figure 4.8 which was collected from the artery near the heart. In this simulation, the applied BP pressure was 110/70 mmHg with the mean BP of 85 mmHg.



a



b

Figure 6.2 Pressure oscillations vs. CP: (a) clinical result, (b) FE model results.

In oscillometric BP measurement, the obtained BP values were determined by the oscillation amplitude of CP in the cuff deflation process. As the cuff was excluded in the current FE model, the CP oscillation cannot be predicted by the FE model directly, and the results were required to be converted to CP oscillations to compare with clinical results. Therefore, CP oscillations were calculated using Boyle's Law with the following assumptions:

1. Since the CP was decreased at a low speed in the BP measurement process, the amount of air in the cuff was assumed constant during each heart beat.
2. Since the external layer of the cuff was very rigid, the total volume under the external layer of the cuff was also assumed constant during each heart beat.
3. The volume of soft tissue under the cuff was constant during each heart beat. Because the pressure change during each heart beat was very small and the human tissues were nearly incompressible.
4. As stated Chapter 4, most of the arteries other than brachial artery and veins were closed when the CP was above diastolic pressure in the normal cuff based BP measurement.

Therefore, the artery volume changes under the cuff transferred to the cuff entirely and equalled the cuff volume changes. Consequently, CP changes could be calculated by Boyle's law as shown in Equation 6.1. The relationship between the cuff volume and CP during each heart beat was described by the following equation:

$$P_1 V_1 = (P_1 + P_{osci})(V_1 - V_{osci}) \quad (6.1)$$

where P_1 and V_1 are the mean CP and cuff volume in each heart beat, and P_{osci} and V_{osci} are oscillating pressure and volume in each heart beat respectively. Figure 6.2b shows

the pressure oscillation when the cuff volume was set to a typical working volume of 200 ml. As the applied BP waveform in the brachial artery of the FE model was different from the waveform in the clinical experiment, only the oscillation amplitude and the changing trend of the oscillation amplitude were compared with the clinical results in this study. As shown in Figure 6.2, in the cuff deflation process in which CP decreased from supra-systolic to sub-diastolic pressure, the amplitude of CP oscillations increased gradually until achieving the maximum amplitude at the midpoint of the process and then decreased slowly. In this process, the maximum pressure oscillation occurred when $CP = 83 \text{ mmHg}$ which was very close to the mean value of the applied BP, 85 mmHg . The value of CP at maximum amplitude is an identical point in oscillometric BP measurement method and is used in determining the subjects' BP. Furthermore, the maximum oscillation amplitude was 1.4 mmHg which was within the clinical observation of $1 - 5 \text{ mmHg}$.

In the FE model, the diastolic pressure and systolic pressure of applied BP was 70 and 110 mmHg. From Figure 6.2b, the calculated diastolic and systolic characteristics ratios of the model were 0.85 and 0.61 respectively, which were calculated by dividing the oscillation amplitude at diastolic and systolic pressure by the maximum oscillation amplitude near the mean BP. In the developed FE model, both the diastolic and systolic characteristics ratios were within previously reported range of 0.69-0.86 for diastolic pressure and 0.43-0.73 for systolic pressure in clinic [38], as shown in Figure 6.3. Therefore, the developed cylindrical FE model with tissue material properties was eligible for simulating oscillometric BP measurement.

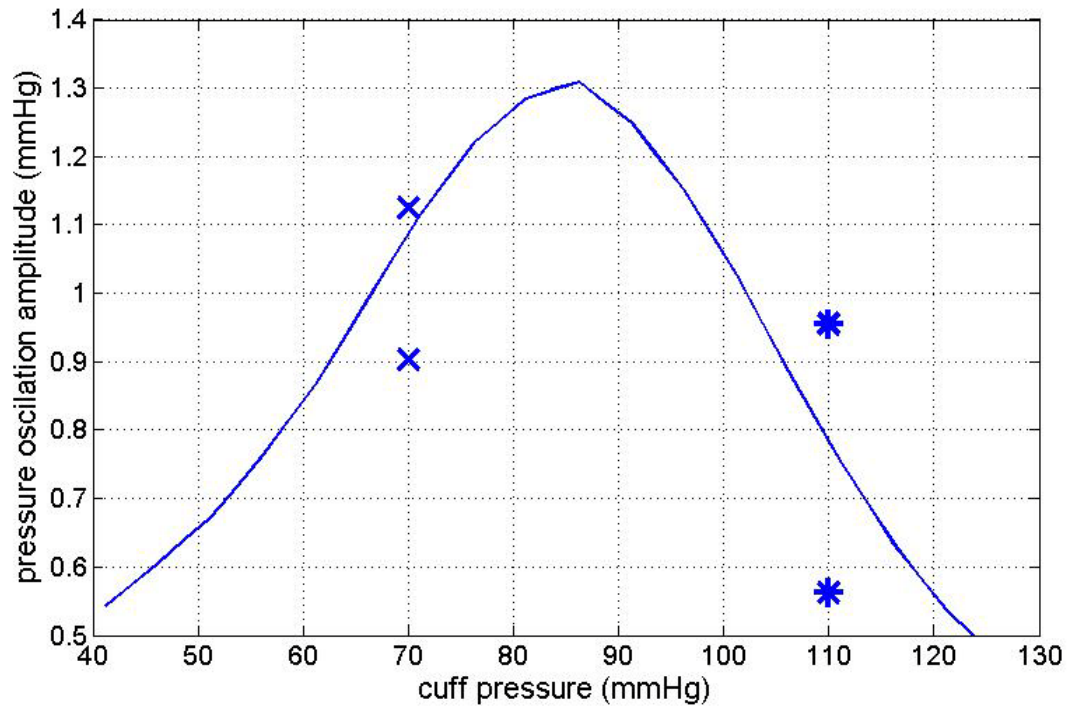


Figure 6.3 The relationship between CP oscillation amplitude and applied CP. × shows the characteristic ratios range of diastolic pressure and * shows the characteristic ratios range of the systolic pressure reported in the literature [38].

6.2.2 Variability of the arm tissue mechanical properties

As described above, CP oscillations in oscillometric BP measurement were dominated by the artery volume changes. The materials properties of the arm were considered to place an important role in artery closure process. The effects of soft tissue materials and brachial artery material are discussed respectively in this section.

6.2.2.1 Soft tissue materials

As the brachial artery was embedded in the soft tissue, its closure status is determined by the extra-vascular pressure in the soft tissue. As shown in Figure 6.4, the pressure

values around the brachial artery are calculated by the FE model and shown in the form of colour contour.

Since the pressure distribution is uniform along the arm axis and symmetrical about the cuff's mid-section, only half of the model along the longitudinal direction is shown in the figure. Furthermore, the displayed model is subdivided into two sections: Section 1 is the arm over the cuff and Section 2 is the arm under the cuff. As only the volume change in Section 2 would be transferred into the cuff, the contour colour gradients are determined by the maximum and minimum stress in Section 2 rather than the entire model. Therefore, some of the area in Section 1 is in black colour which means it is over the defined limit. From colour contour shown in Figure 6.4, the following factors were identified:

1. the extra-vascular pressure around the artery is different from the CP acting on the arm surface; and
2. the transferred pressure on brachial artery surface varies at different longitudinal locations in spite of the fact that the external pressure is uniformly applied on the arm surface.

As shown Figure 6.4, the pressure in the arm is uniform in both longitudinal and axial directions. In order to study the variation of pressure transmission in the longitudinal direction, fourteen equally spaced points along the external brachial artery surface were specified. Since the CP varied in most of the simulations, the pressure transmission ratio, which is defined as the pressure in the tissue divided by CP on the surface, is used in the study instead of the actual values of pressure in the surrounding tissues. As shown in Figure 6.5, only about half of the artery under the centre of the cuff experiences extra-vascular pressure close to CP, while the pressure transmission ratio drops gradually

down to 30% at the edge of the cuff. In previous studies, it is assumed that the CP transferred to the brachial artery uniformly [32, 61], or the extra-vascular pressure was equal to the CP [32, 36]. The results obtained in the work reflect the inaccuracy of these previous findings.

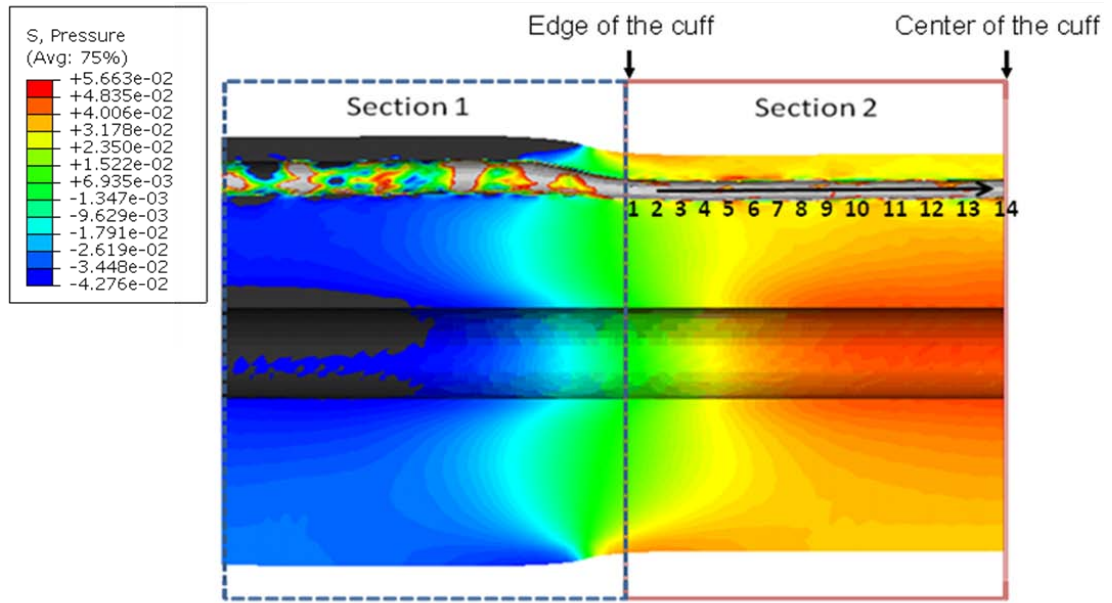


Figure 6.4 Pressure distribution of FE model under CP in longitudinal direction, when CP=100mmHg.

Other than the FE model's geometry, the pressure transmission ratio in the FE model might also be related to the mechanical properties of the tissues. Among the mechanical properties, compressibility and elasticity of the material were considered as the major factors. In previous studies, values were stated within a certain range. The Poisson's ratio of soft tissues was reported between 0.4 and 0.49 [36, 45, 54], and 0.45 was the most widely used value. The modulus of elasticity was reported between 30 kPa and 60 kPa [54] and 40 kPa was mostly used. For a modulus of elasticity $E = 40\text{kPa}$, three different Poisson's ratios 0.4, 0.45, 0.49 were tested in the FE model separately. As shown in Figure 6.5a, the pressure transmission ratio increases with Poisson's ratio of the surrounding tissues in most parts of the FE model. At the central half of the arm

under cuff, the obtained pressure transmission ratios are 93% to 97% and 101% corresponding to Poisson's ratios of 0.4, 0.45 and 0.49. With Poisson's ratio $\gamma = 0.45$, three tissues with different stiffness 30 kPa, 40 kPa, 60 kPa were tested in the FE model. As shown in Figure 6.5b, the obtained pressure transmission ratios are similar at the central half of the arm under the cuff. For the other half of the arm under the cuff, the pressure transmission ratio increases with the increase of the tissue's modulus of elasticity.

When the Poisson's ratio of the soft tissue changed between 0.4 and 0.49, the overall transmission ratio vary by up to 4% compared with a typical value of $\gamma = 0.45$. however, when the stiffness of the soft tissue changes between 30 kPa and 60 kPa, the overall transmission ratio varies by less than 1% compared with the value $E = 40$ kPa. To achieve the same extra-vascular pressure, the applied CP is varied up to 5% comparing with the standard value ($E = 40$ kPa, $\gamma = 0.45$). Therefore the BP measurement would be overestimated or underestimated by up to 5% because of the variation of the soft tissue properties. This finding quantifies the errors in BP measurements, in essence indicating that they are overestimated by about 5% in people with soft tissue that is softer and more compressible, which is normally observed in elderly and underestimated by about 5% in people with soft tissue which are less compressible, which is observed in children [9].

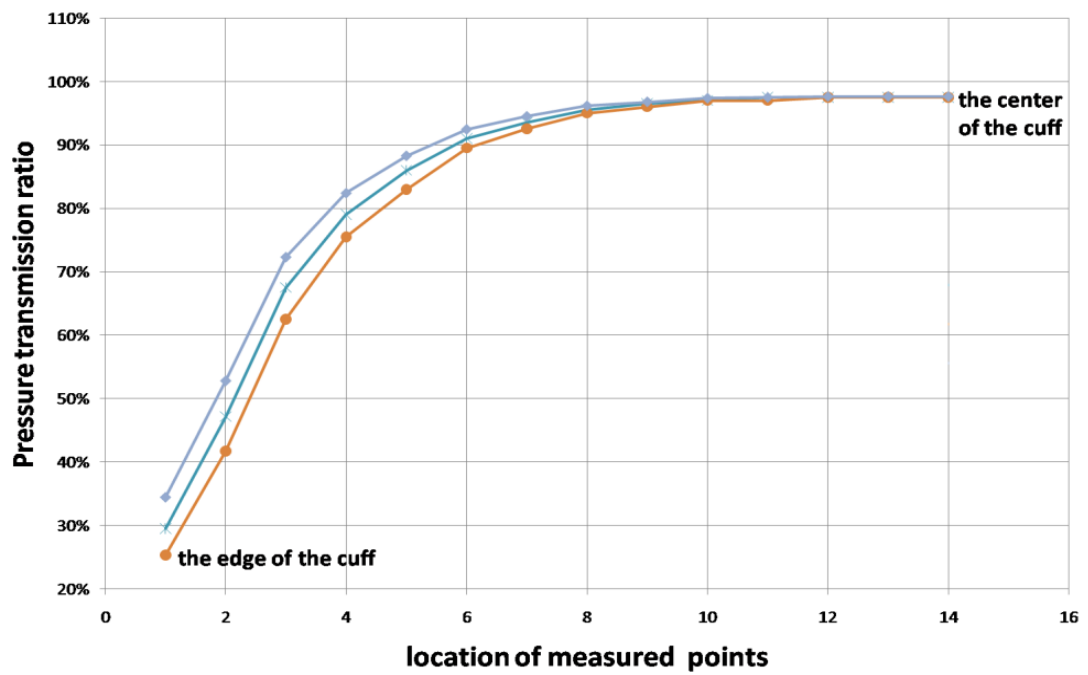
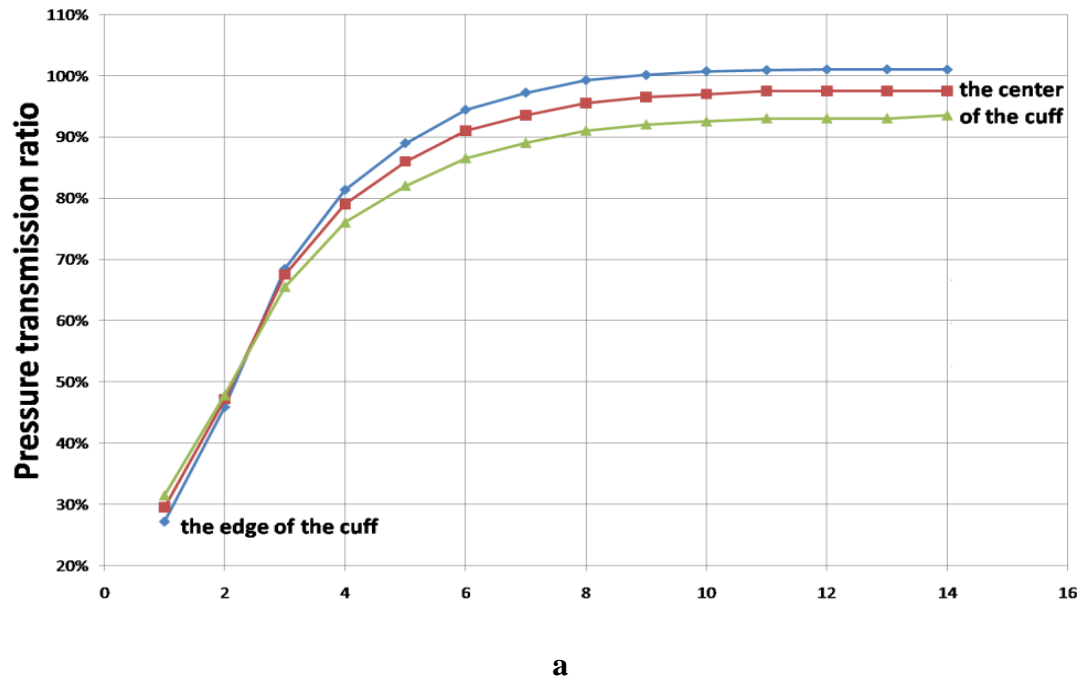


Figure 6.5 FE pressure transmission ratio for soft tissue material properties at CP= 100 mmHg; (a) $E = 40$ kPa, γ : \blacktriangle , 0.40; \blacksquare , 0.45; \blacklozenge 0.49. (b) $\gamma = 0.45$, E (kPa): \bullet , 30; \ast , 40; \blacklozenge , 60

6.2.2.2 Theory of oscillometric BP measurement method and brachial artery

In previous studies, it was explained that the maximum CP oscillations during BP measurement was due to buckling of the brachial artery under the cuff [30, 32, 36]. This conclusion was based on the observation that a brachial artery collapses at $TP = -7$ mmHg when the artery was isolated from the surrounding tissues. The same process was simulated by the FE model and the obtained artery buckling pressure was $TP = -5.6$ mmHg as shown in Figure 6.6. This result demonstrates that the used mechanical properties are similar to those of in vitro artery.

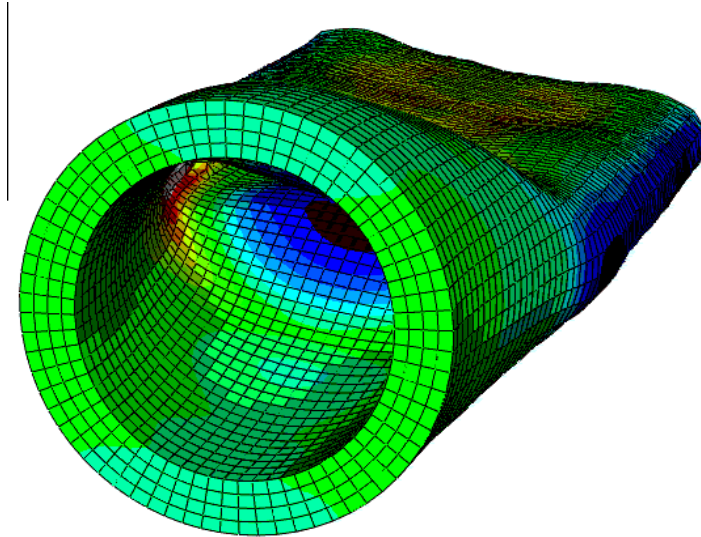
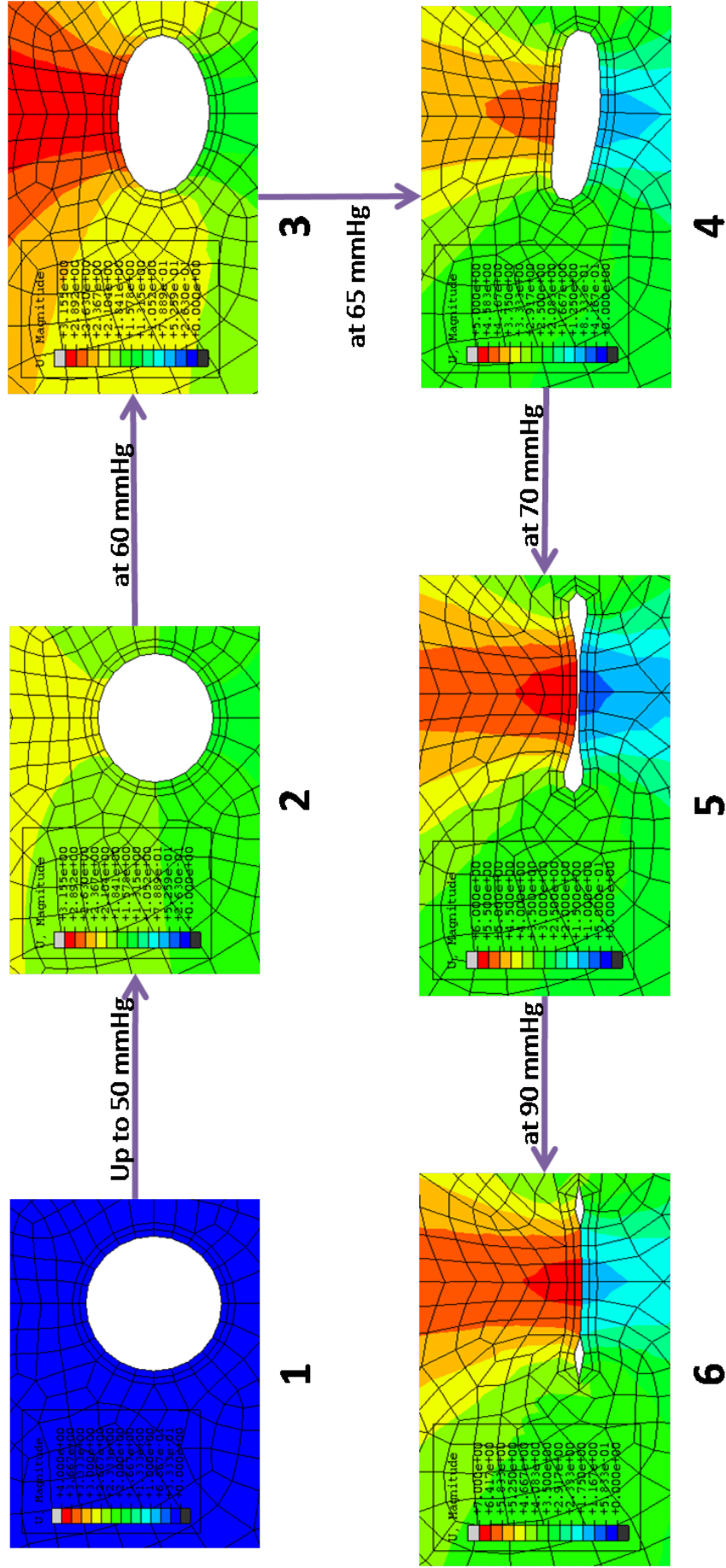


Figure 6.6 Brachial artery buckling pressure was $TP = -5.6$ mmHg when it was isolated from the surrounding tissues.

However, the brachial artery buckling pressure changes when it was surrounded by the soft tissues in the upper arm. A clinical experiment showed that the brachial artery buckled at $TP = -50$ mmHg [91]. As shown in Figure 6.7, the present FE model indicates that the brachial artery buckles at $TP = -70$ mmHg when it was in the arm. This result is closer to the clinical value than the value obtained for an artery in isolation.



Since the brachial artery was surrounded by the soft tissue, the stiffness of the soft tissue might affect the artery closure status significantly. As shown in Figure 6.8, the CP required to close the brachial artery increases in direct proportion to the elasticity of the surrounding tissue. A common practice is to use the collapse point as the point of mean BP [7]. The current work indicates that the required CP for closing the brachial artery is much higher than the measured BP and therefore this assumption is not valid and other approaches had to be sought.

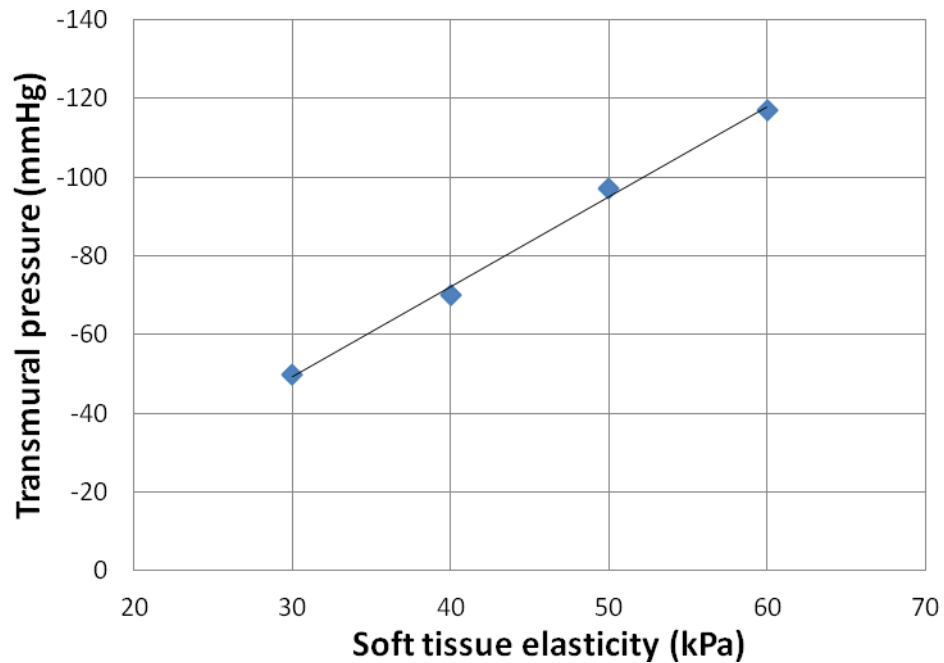


Figure 6.8 Relationship between artery buckling pressure and soft tissue elasticity
E

In the experiments on the arm simulator, both auscultatory method and oscillometric method were used to determine the applied pressure in the brachial artery. However, neither of these two methods could give a close reading of the applied pressure 110/70 mmHg. The CP oscillations change trend is calculated from the FE model with material of the same properties as the arm simulator. As shown in Figure 6.9, CP oscillations obtained from the simulator keep increasing in the whole deflating process. This result

is quite different from normal oscillometric BP measurement. This unique trend of CP oscillation explains the misreading of BP in the arm simulator. Since the major change between this model and previous model was the elasticity of the brachial artery, the nonlinearity of the brachial artery played an important role in BP measurement.

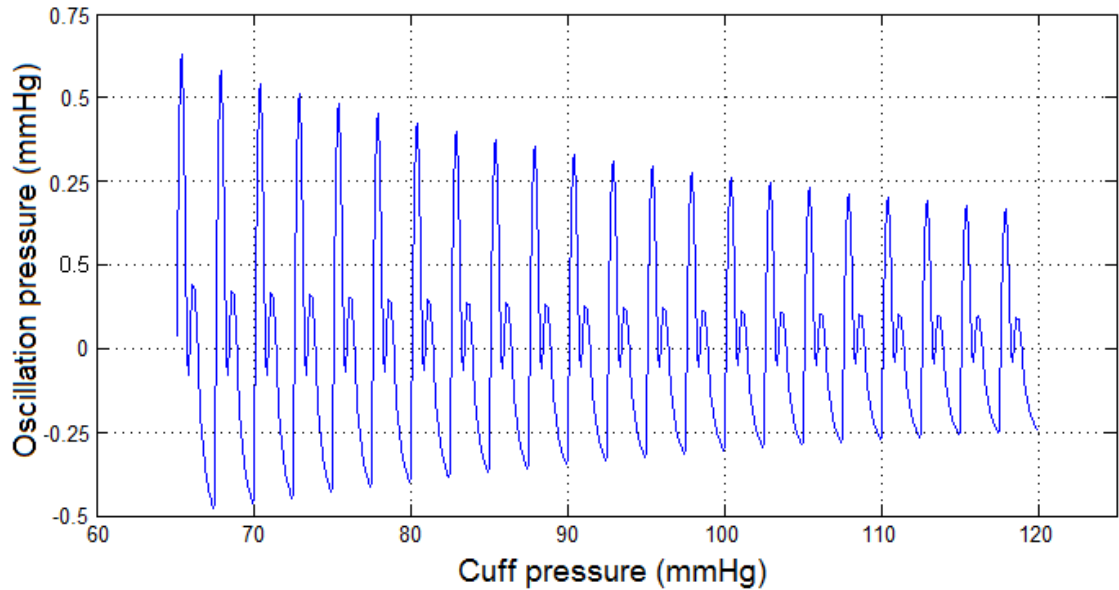


Figure 6.9 CP oscillations trend when linear elastic artery wall was used in the model

To study the effect of the artery properties on BP measurements, the data on the stiffness of the brachial artery wall shown in Figure 4.3 were applied in the model. In these simulations, the surrounding tissue properties were set to $E = 30$ kPa and $\gamma = 0.45$. Figure 6.10 shows the relationship between artery lumen area and CP at the mid section of the model. In these three simulations, which used normal, hard and soft artery materials, the results indicate that the trends generated in these simulations are identical to previous findings [14] that the oscillation amplitude increases initially until it reaches a maximum value and then gradually decreases to the end of the range. For the brachial arterial wall models with different stiffness data, their behaviours are qualitatively

similar, and the CP at which the maximum amplitude oscillations are obtained is approximately unchanged. However, the amplitude of the oscillations changed significantly. Since the oscillometric BP measurement is based on the location rather than the amplitude of the maximum oscillation, the difference in brachial artery wall stiffness would not affect the readings of the oscillometric BP measurements. As shown in Figure 6.10, the total brachial artery lumen area changes for each heart beat and achieve a maximal value when CP equals 70.6 mmHg, which is just above the diastolic pressure. Since the mechanical properties of the surrounding tissues are the same in these models, the pressure transmission ratios are equivalent in these models. The total artery volume changes under the cuff would give a similar trend. Therefore, the stiffness of the brachial artery would not affect the accuracy of non-invasive oscillometric BP measurement. In the measurement, the oscillation amplitude would be smaller with hard arteries and the measurement might be more sensitive to external noises.

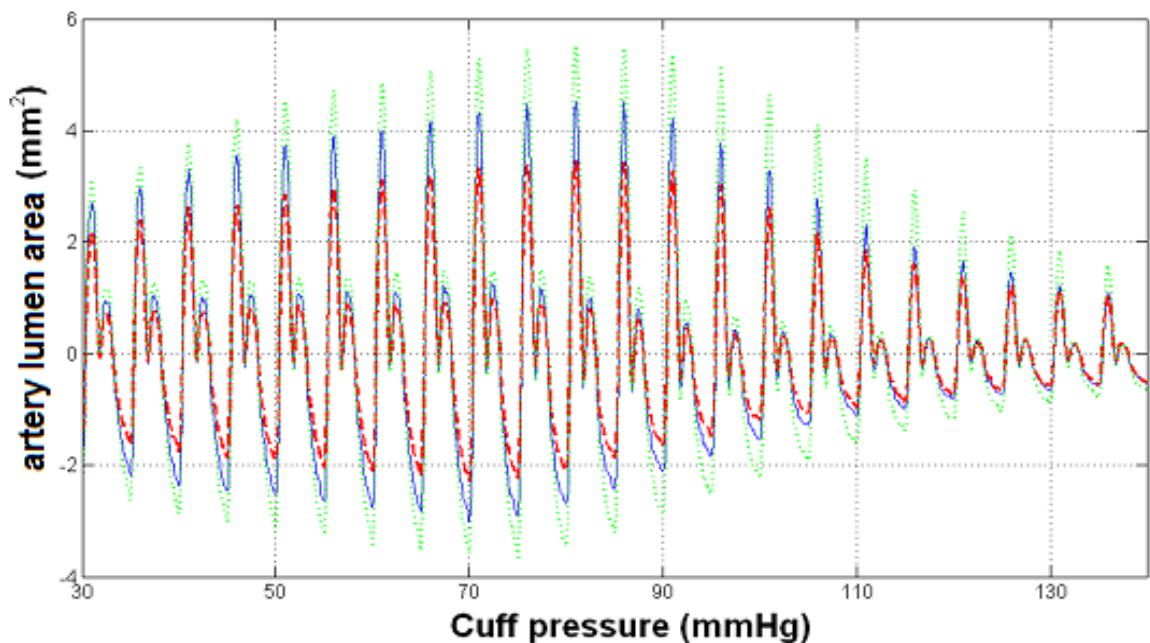


Figure 6.10 FE artery lumen area vs. CP of the mid section predicted: — normal artery; soft artery; - - - hard artery.

6.3 Realistic FE model

The FE model with anatomically accurate geometry was developed to simulate the BP measurement process in different situations. The arm deformations obtained and the surface strain distribution under the cuff are used to determine the best locations for the piezoelectric film sensors to detecting the arm motion and BP pulses. This section begins by considering BP loading and muscle movements individually. Then the best locations for piezoelectric film sensors are determined. Finally CP was introduced and compared with other loadings.

6.3.1 Piezoelectric film sensor array

The piezoelectric film sensors are small, flexible and very sensitive. The sensors attached on specified positions are sensitive to different signals. The sensor array was designed referring to positions determined by the FE model.

6.3.1.1 Strain distribution with BP

When the BP pulse passes through the brachial artery, the BP signal would be transferred to the skin surface in the form of strain change. In order to find the most sensitive location to pick up the BP pulses, a simulation with BP only was conducted. Since the minimum pressure in the brachial artery was diastolic pressure, it was applied as the initial loading in the simulation. The colour contour shown in Figure 6.11 is the strain distribution when the BP achieved systolic pressure and gave the maximum strain.

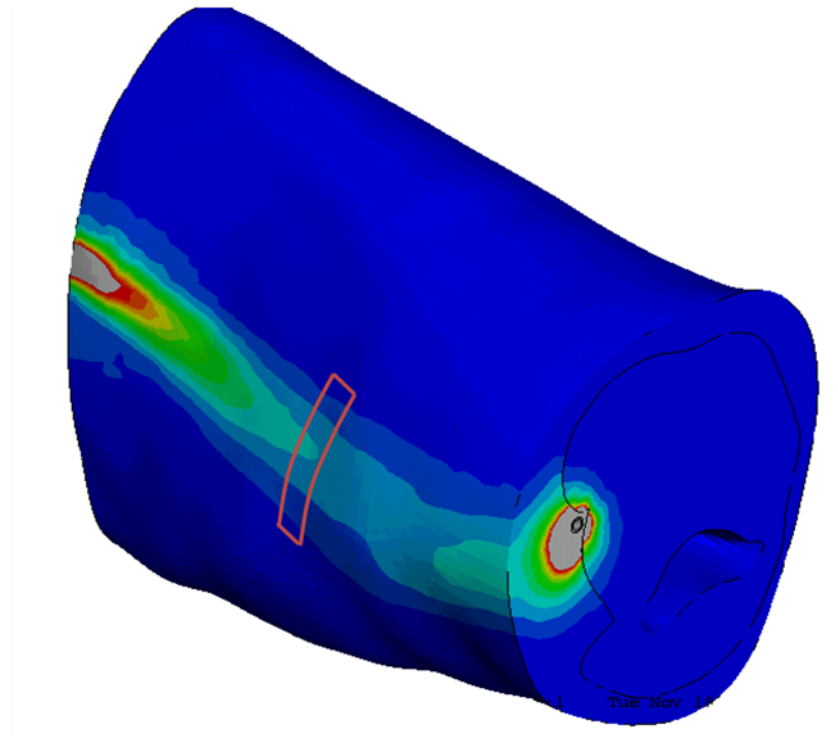


Figure 6.11 Arm surface strain distribution driven by the BP in the brachial artery without any external pressure

As shown in Figure 6.11, the strain changes are mainly on a 2.5 cm wide band area on the top of the brachial artery. If a 3 cm long piezoelectric film sensor was placed along the mid section as shown in Figure 6.11, the obtained strain changes are up to 0.0045 when the applied BP was 120/80 mmHg. Since the sensitivity of the selected piezoelectric film sensors are 0.00001, the proposed piezoelectric film sensor FDT1-028K was capable of capturing the BP pulse without CP.

In order to compare waveform of the applied intravascular pressure in the brachial artery and strain change on the arm surface easily, BP with sine waveform was applied in the simulation instead of the waveform obtained from clinical data. Furthermore, the BP waveform was scaled down to match the magnitude of strain changes. As shown in Figure 6.12, the surface strain change in the proposed 3 cm long area caught the similar waveform as the applied intravascular pressure. However, their relationship was

nonlinear and highly related to the mechanical properties of the brachial artery. Therefore the obtained strain signals would not be suitable to represent the intravascular pressure in the brachial artery.

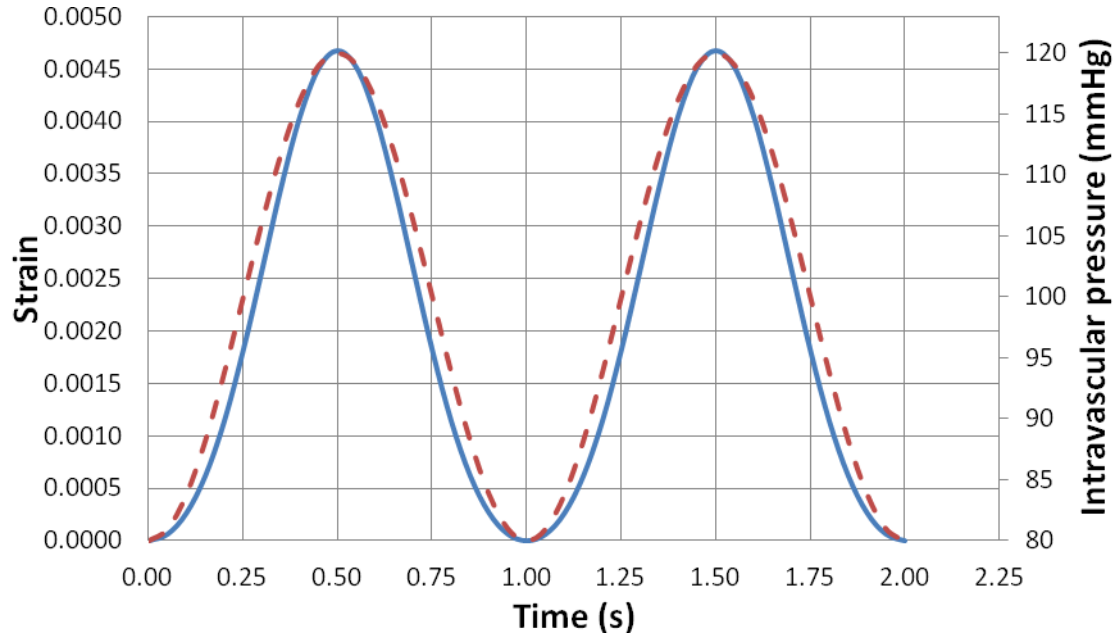


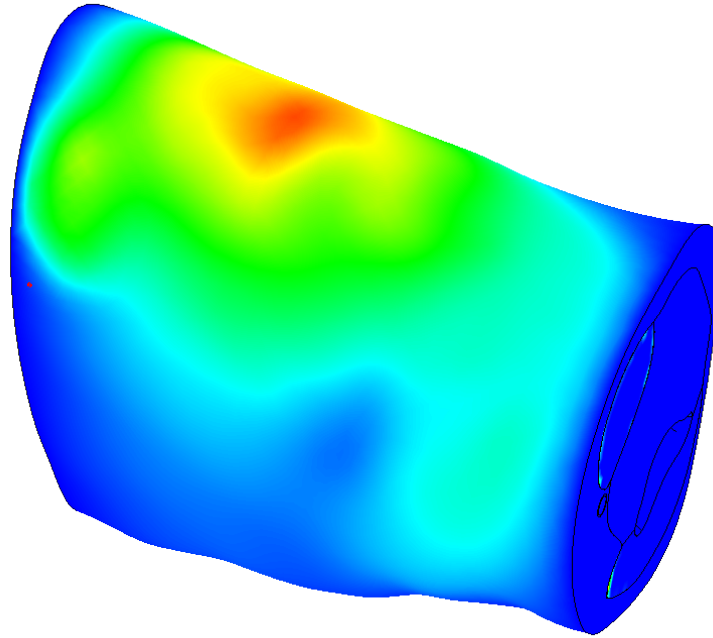
Figure 6.12 Comparison between the applied intravascular pressure and obtained surface strain changes. : — Surface strain change, - - intravascular pressure

6.3.1.2 Strain distribution with arm motion

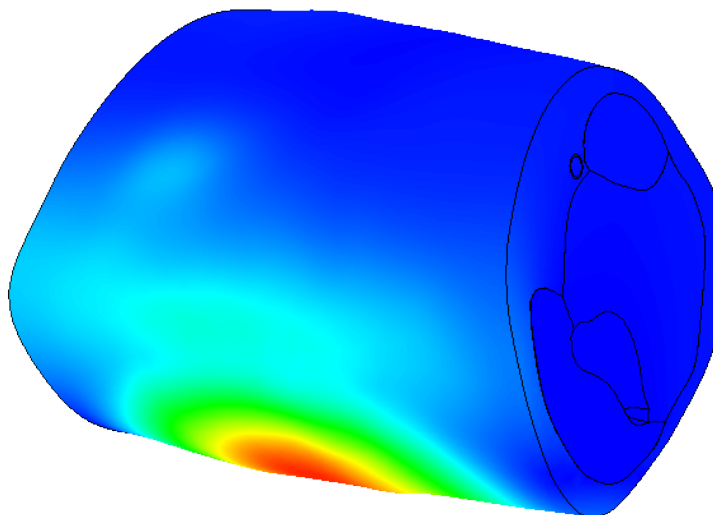
In the human body, any arm motion is controlled by the specific muscles. During muscle contraction or extension, their shapes change and their deformation transfers to the arm surface in the form of surface strain change.

In the upper arm, biceps and triceps dominate most of the arm motions and their moving directions are opposite in most of the arm motions. Since the muscle contraction generates more muscle deformation, this study was focused on finding out the arm surface areas which are most sensitive to individual muscle contractions. The contractions of the biceps and triceps are simulated separately using the developed FE

model. The colour contours in Figure 6.13 showed the strain distribution on the model's surface and indicated the best locations to reflex the muscle motions.



a



b

Figure 6.13 (a) Surface strain distribution during the biceps contraction; (b) Surface strain distribution during the triceps contraction

As shown in Figure 6.13a, the surface strain generated by the biceps contraction are mainly observed on the surface over the biceps. The maximum strain was just above the mid section of the model. On the area for detecting BP signals, the strain changes are very minor. Similar situation was also observed in Figure 6.13b. Referring to the strain distribution shown in Figure 6.11 and Figure 6.13, the three areas shown in Figure 6.14 are most sensitive to BP, biceps and triceps respectively, and insensitive to other signals. Therefore, the piezoelectric film sensors are better to be placed on the proposed locations in the clinical experiments. The sensors placed on locations 1, 2, 3 are named brachial artery sensor, biceps sensor and triceps sensor respectively.

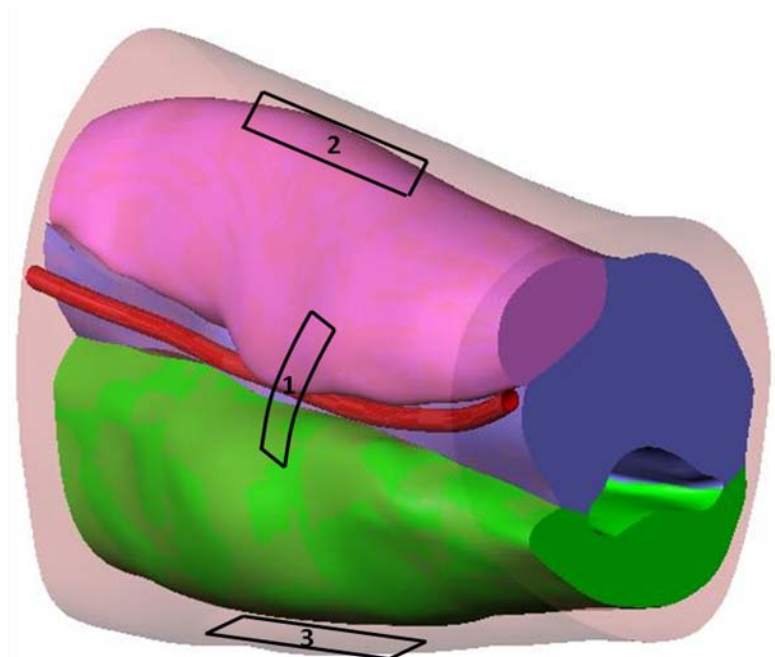


Figure 6.14 The locations for the piezoelectric sensors to detect arm motion and BP pulses. Location 1: on the mid section of the model and above brachial artery; Location 2: over the mid section of the model and above the biceps belly; Location 3: on the mid section of the model and above triceps.

From the above results, it was indicated that theoretically both arm motions and BP pulses in the brachial artery can be detected by piezoelectric film sensors on the arm surface in the designed array as shown in Figure 6.14.

6.3.2 Components of piezoelectric film sensor signals

Using the designed sensor array, piezoelectric film sensors would respond to both cuff compression and soft tissue stretches. In the normal cuff based BP measurement process, the cuff was tightened evenly over the upper arm before inflation to ensure CP was applied uniformly on the arm surface in the whole measurement process. Therefore, the compressive pressure on the piezoelectric film sensors was uniform and generated equivalent output in each sensor. With CP, the arm tissue would be compressed and deformed. As shown in Figure 6.15, the strain distribution in the upper arm surface was almost uniform under the cuff regardless of the irregular geometry of the upper arm. The outcomes of the piezoelectric film sensors would be equal to each other as well. Therefore, all of these three piezoelectric film sensors showed the same response to CP. Comparing the arm deformation shown in Figure 6.11 and Figure 6.15, CP created much more arm deformation than BP and muscle motions. Because CP rate of change was very slow in the BP measurement process, these signals could be recognized by the system. As shown in Figure 6.16, BP signal was still identical in the model.

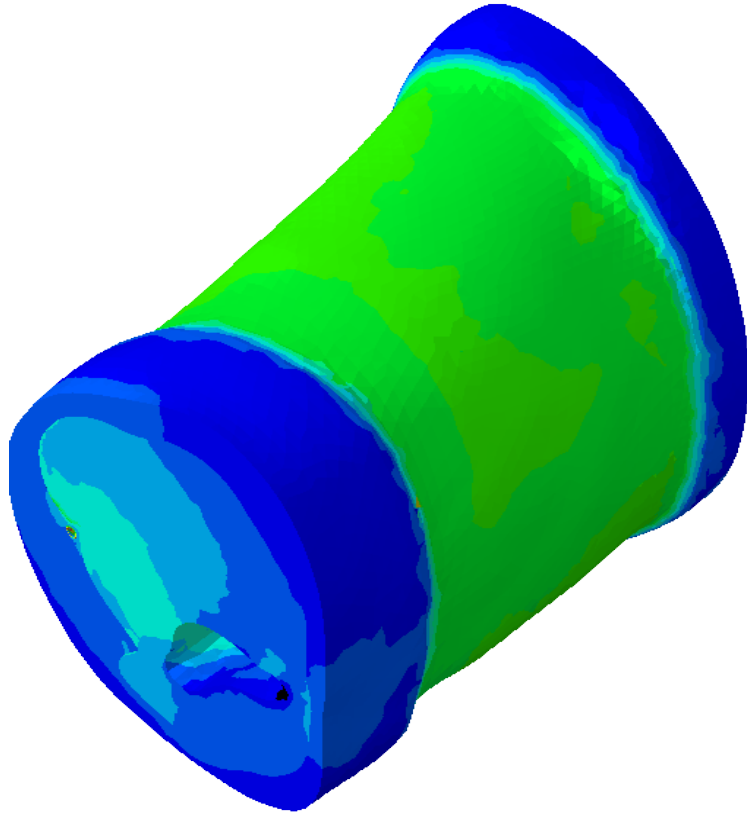


Figure 6.15 Pressure distribution under CP

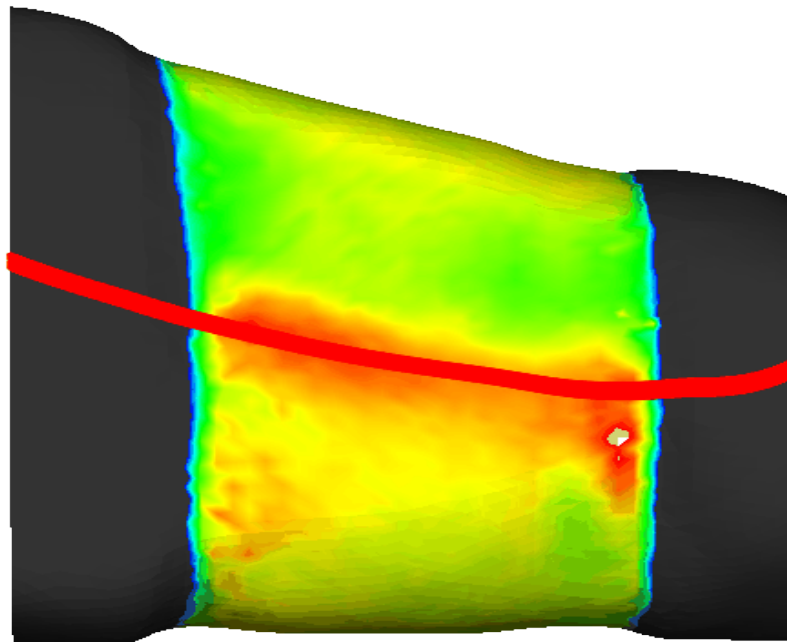


Figure 6.16 Strain distribution of the surface near the brachial artery

6.4 Summary

The FE model is compared with experimental data and validated in this chapter. The biomechanical basis of oscillometric BP measurements investigated using the model.

The analysis showed that:

1. The CP transmission through the arm was not uniform.
2. The measured CP oscillations are a reflection of the artery volume change under the cuff which was a mixture of arterial distension in different closure states during the entire BP measurement process.
3. The errors in BP measurements that it was overestimated in elderly people and underestimated in children are because of the difference of soft tissue compressibility.

A refined model whose geometry is extracted from VHB dataset is developed in this study. When BP pulses and some muscle movement were simulated in the model, the obtained arm surface strain distribution is shown in the form of colour contour. From the modelling results, a piezoelectric film sensor array was placed at the positions which are most sensitive to different muscle movements and BP pulses.

Chapter 7 Experimental results and Signal Post-Processing

7.1 Introduction

This chapter consists of clinical experiment results and signal post-processing. In all tests, CP was controlled and recorded by a Pulsecor[®] R6.5 non-invasive monitor and arm surface strain changes were measured by the piezoelectric film sensor array as demonstrated in Chapter 6. The tests were conducted in different conditions, including normal BP measurement process, constant CP and arm motions. The subjects' BP was monitored using the auscultatory method at the same time to get referring values. In the signal post-processing part, the input-output configuration of the designed measurement system was introduced. The transfer functions between different signals were obtained using empirical equations. By the developed method, the device is able to detect arm motions and determine the patient's BP in a way that is insensitive to arm motions.

7.2 Clinical experiment

In the normal oscillometric BP measurement without any arm motion, the biceps piezo sensor and triceps piezo sensor reflex CP changes, while the brachial artery sensor combined artery deformation signals and CP changes. As stated in Chapter 5, all of the piezoelectric film sensor signals are passed through a 0.12 ~ 15.7 Hz band-pass filter. The CP trend was obtained by using a 0.3 Hz low-pass filter. Since the signals were measured by different types of sensors, all of the signals shown in this section were

normalized before comparison in order to study oscillation waveforms and trends in amplitude changes.

7.2.1 Oscillometric BP measurement

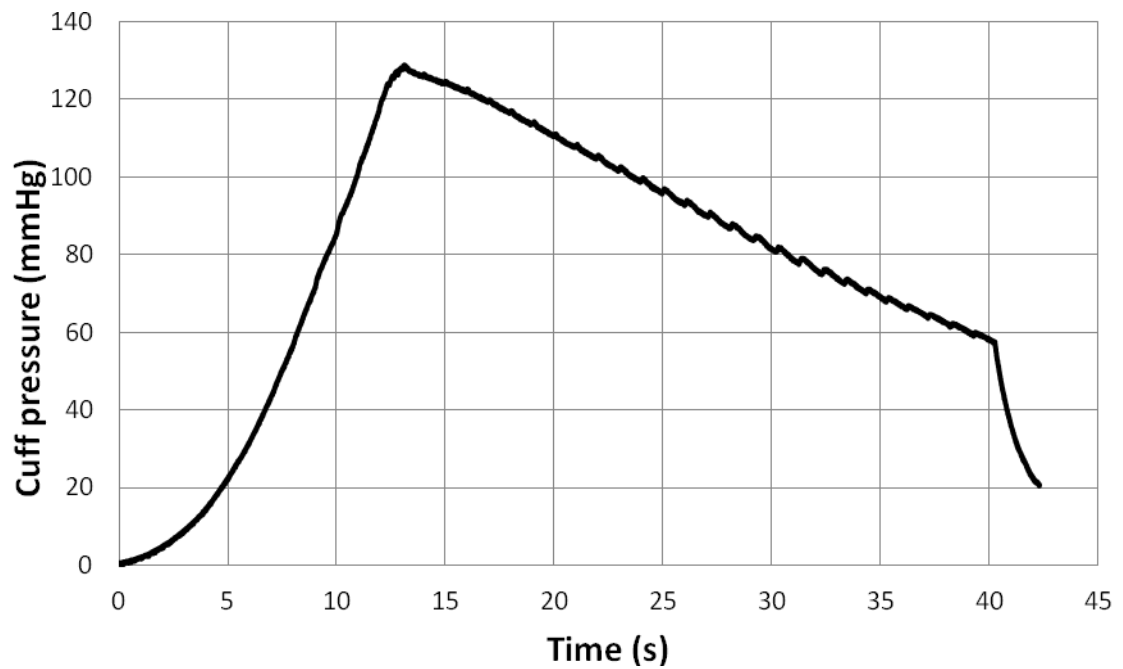
The data used in this section was collected from a subject whose BP was 110/77 mmHg. The whole measurement process was recorded as shown in Figure 7.1a. The data between 13 ~ 40 seconds in the deflating process was used in the oscillometric method and therefore analyzed in this study.

In the normal oscillometric BP measurement process, the arm muscles are at rest and the stiffness of arm soft tissues, such as skin, fat, connective tissues and muscles, is similar [54]. Therefore, the arm surface deformation under the cuff is nearly uniform. Since the applied CP is also considered to be uniform under the cuff, the readings from the biceps sensor and the triceps sensor are assumed to be similar to each other. As shown in Figure 7.1b, the readings from these two sensors prove the assumption and the trend in their amplitude changes is the same as for CP, especially when CP is in the measuring range between SP and DP.

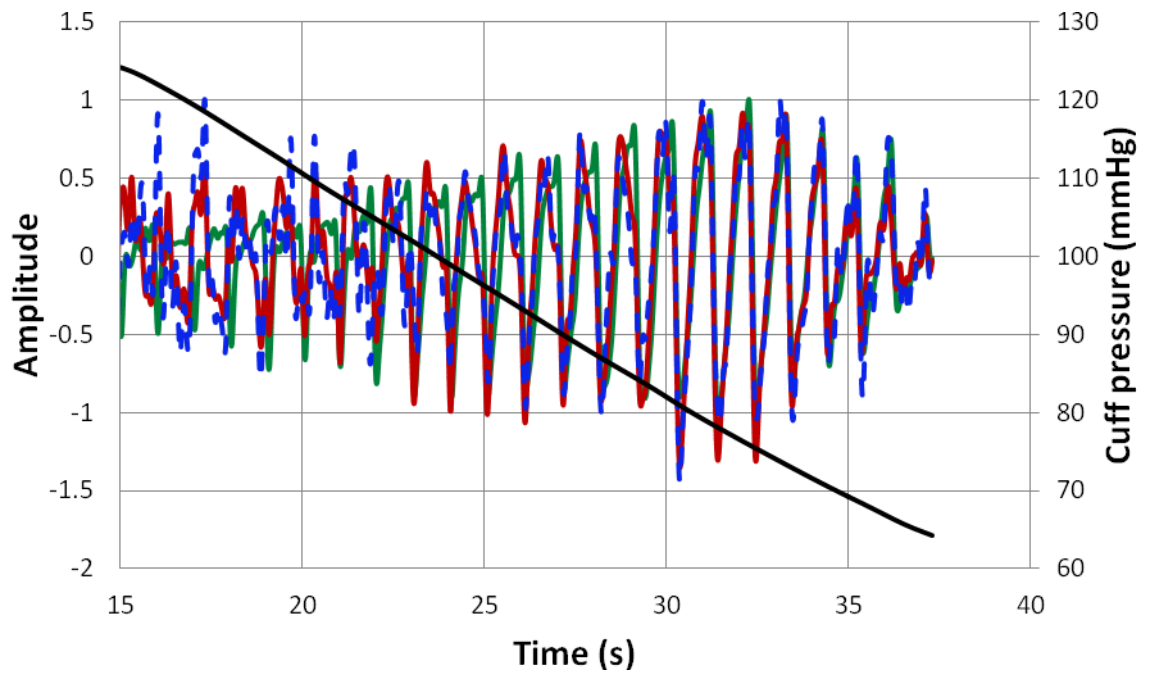
Since the artery sensor responded to both CP and arterial pulses, the readings are different from the other two sensors as shown in Figure 7.1c. When CP was greater than SP, the artery sensor was more sensitive to arterial pulses. The oscillation amplitude kept increasing and achieved the maximum value when CP was just above MP. Then it decreased slowly and dropped off dramatically when CP was lower than DP.

The Fast Fourier transform (FFT) analysis was also carried out on the obtained readings. Figure 7.1d shows the normalized FFT results. It is shown that all of these signals contain the same frequency components. However, the magnitude of each is slightly

different. This difference leads to the waveform distinction. In this measurement, the signals mainly consist of one fundamental frequency and three harmonic frequencies. The fundamental frequency illustrates the heart rate of the subject.



a



b

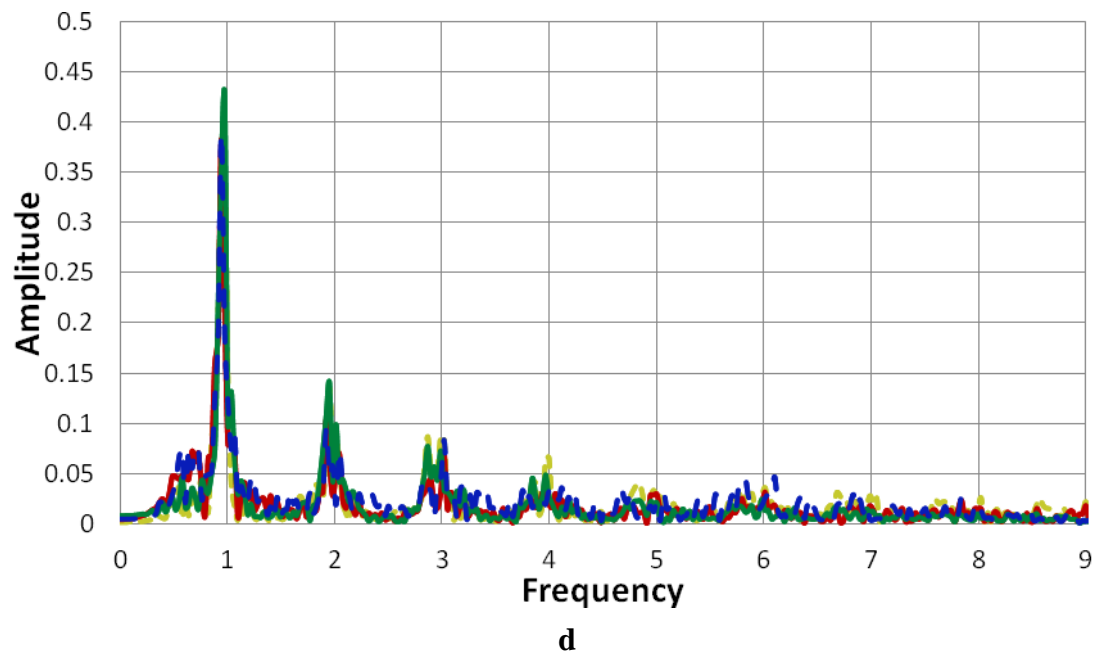
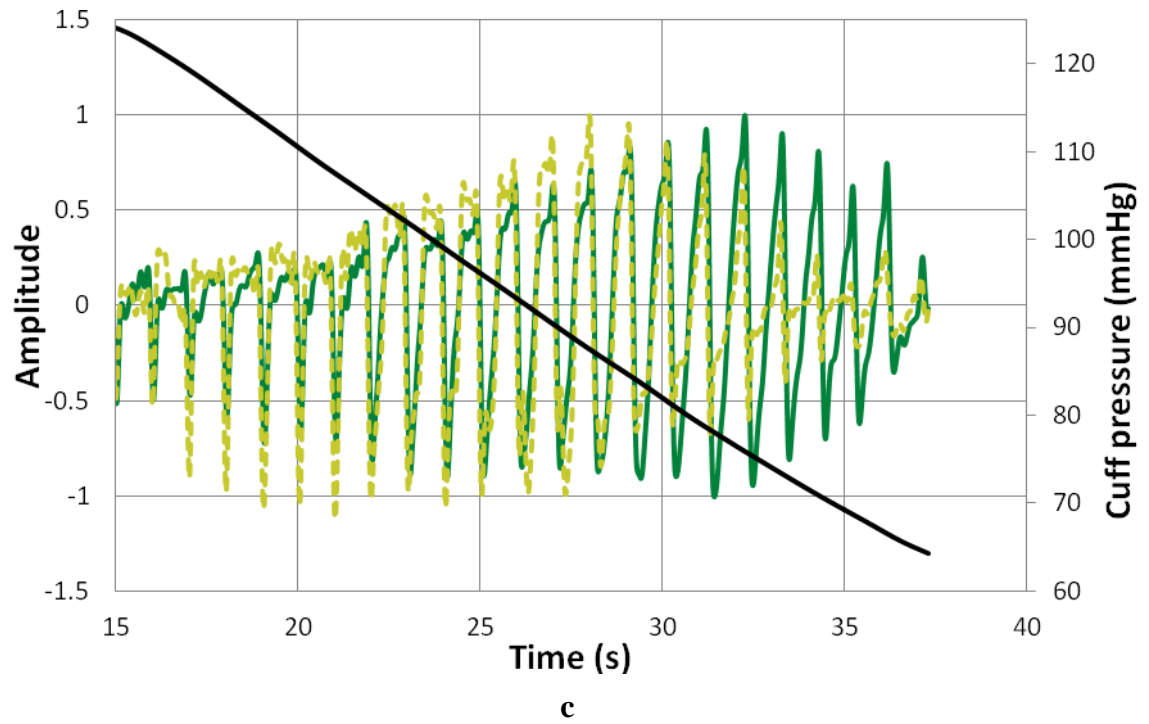


Figure 7.1 Sensor readings in the normal oscillometric BP measurement: (a) CP reading in the entire measuring process; (b) readings from the biceps sensor and the triceps sensor during normal oscillometric BP measurement; (c) artery CP reading during BP no motion; (d) FFT analysis of the obtained signals after normalizing: --- artery sensor, — biceps sensor, - - triceps sensor, — CP oscillation, — CP.

7.2.2 Constant CP

As shown in Figure 7.1, the measured waveforms and sensor response vary under different CP in the measurement process. Therefore, experiments at some critical CP were conducted in this study. In each trial, CP was pumped up to the target value and kept at that value for 15 seconds. Because of the cuff system leakage, CP was normally about 5mmHg lower than set values and decreased slowly in the measuring process. All of the presented results were conducted on the subject whose BP was 110/70 mmHg throughout the whole measuring process.

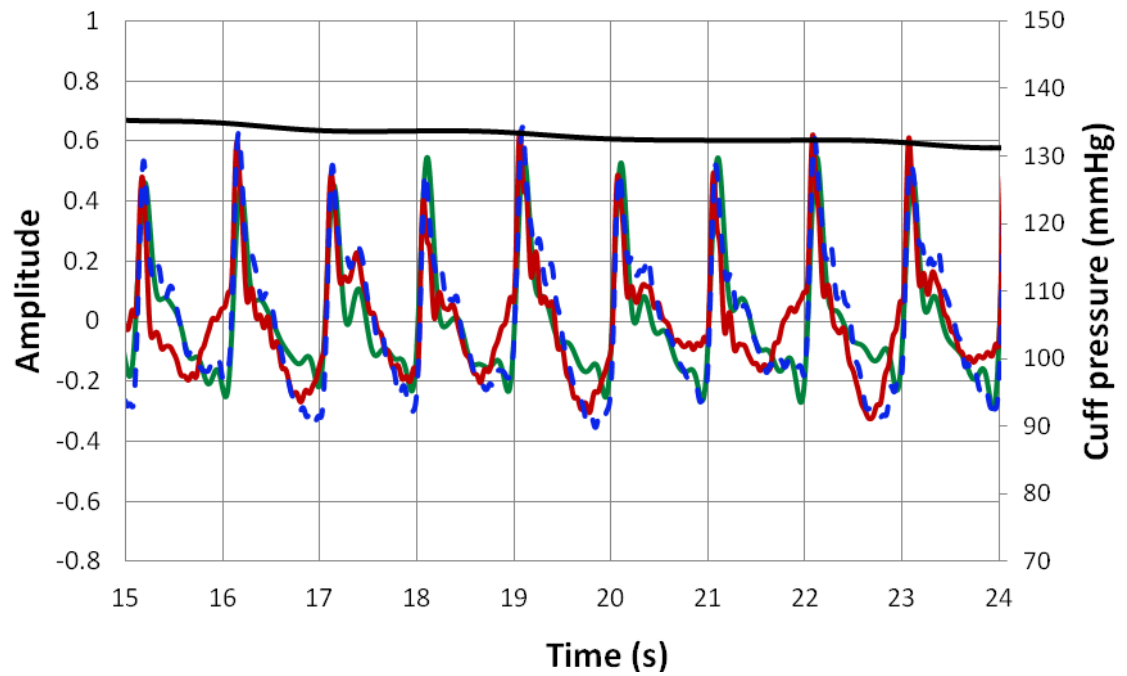
7.2.2.1 CP at supra-systolic pressure

The measurement was initiated from supra-systolic pressure. Figure 7.2 shows the readings when CP was set to 140 mmHg. The actual CP was between 136 mmHg and 130 mmHg. As shown in Figure 7.2a, readings from the biceps sensor and the triceps sensor are similar to each other and have comparable features of CP oscillation.

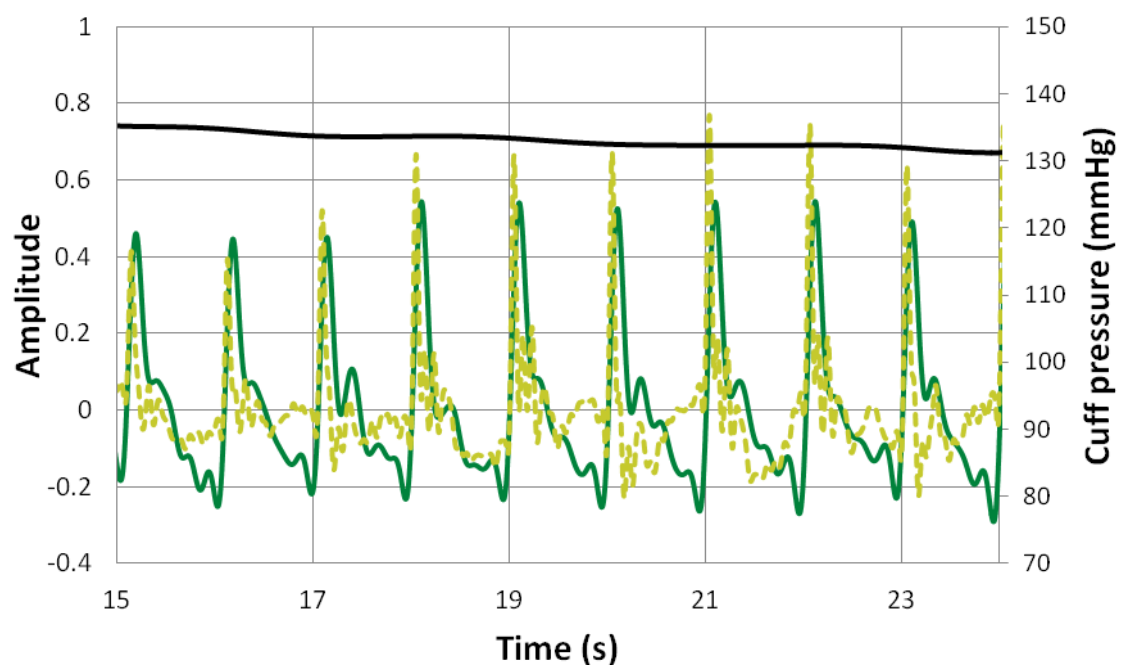
The artery sensor measures both CP oscillation and artery deformations. As shown in Figure 7.2b, the readings of the artery sensor show different features from CP oscillation. When the arm is highly compressed, the strain change due to artery deformation is comparable high. Therefore the artery sensor is more sensitive to artery deformation. Because the cuff is inflated with compressible air, the damping effect is observed in the cuff. The artery sensor is more sensitive to BP changes and the response time is shorter.

The FFT analysis also indicates the difference between the artery sensor readings and other signals. As shown in Figure 7.2c, the magnitudes of harmonic frequencies are

higher in the artery sensor readings. The damping factor of air inflated cuff also contributes to this difference.



a



b

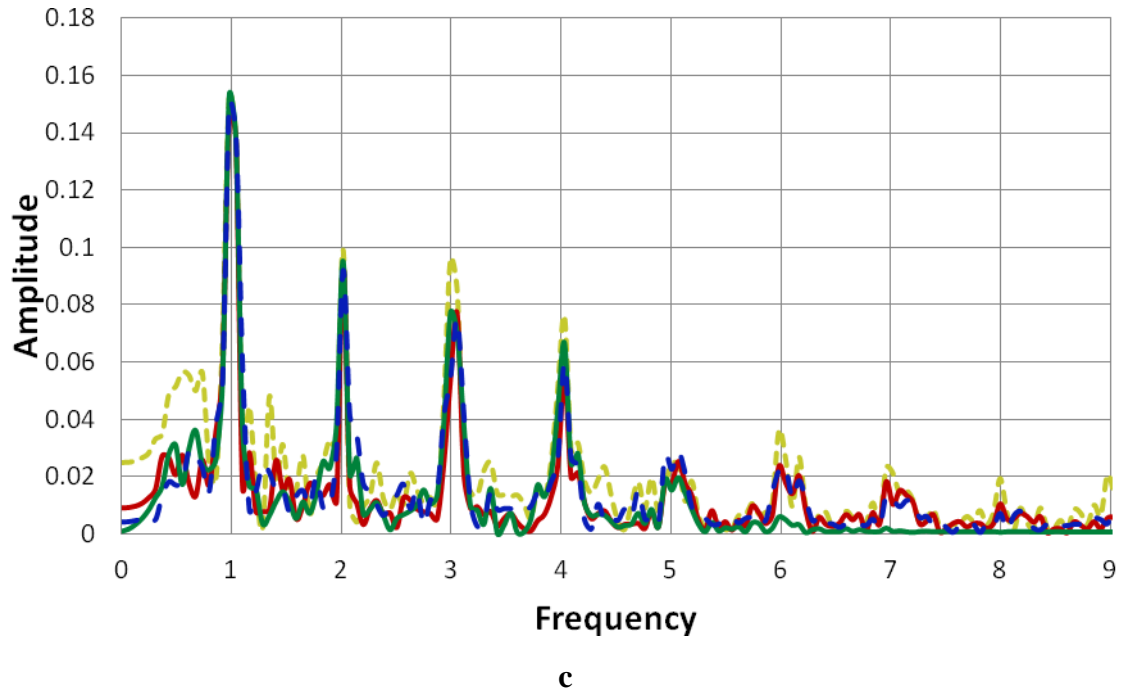


Figure 7.2 Experiment results when CP was at supra-systolic pressure: (a) readings from the biceps sensor and the triceps sensor during normal oscillometric BP measurement; (b) artery CP reading during BP no motion; (c) FFT analysis of the obtained signals after normalizing: ---- artery sensor, — biceps sensor, - - triceps sensor, — CP oscillation, — CP.

7.2.2.2 CP at SP

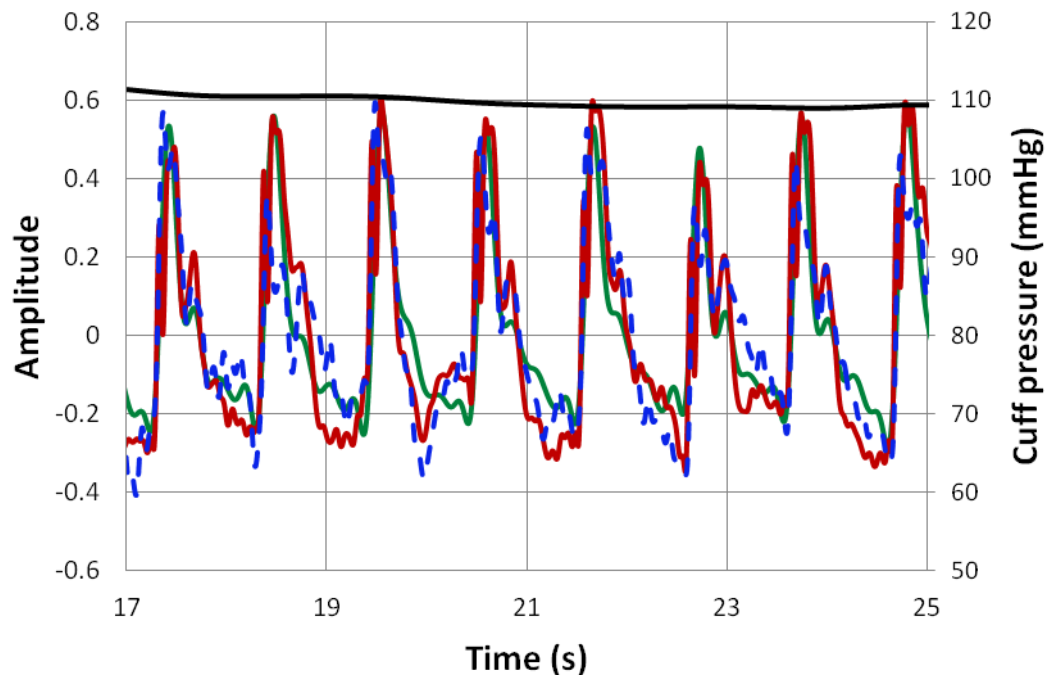
When CP was initially set to 115 mmHg, CP remained constant at 110 mmHg (± 2 mmHg) which was the SP of the subject.

The waveform of CP oscillations is similar to that shown in Figure 7.2 when CP was kept at supra-systolic pressure. Furthermore, the readings from the biceps sensor and the triceps sensor are still similar to CP oscillation, as shown in Figure 7.3a. However, the waveform measured from the artery sensor changes significantly, as shown Figure 7.3b. It is more sensitive to artery deformation when CP is near SP:

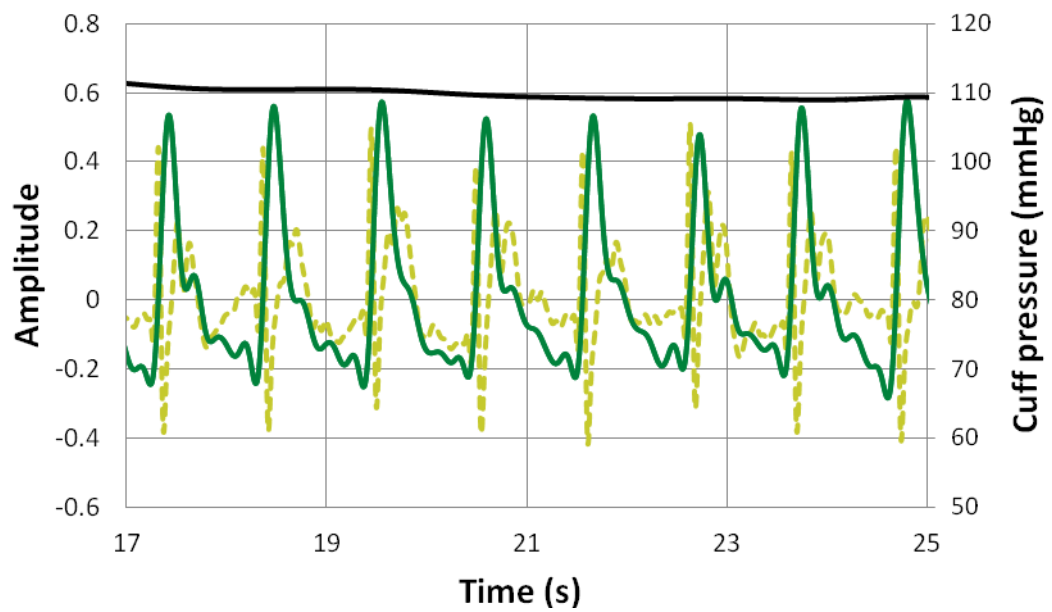
1. It responds to the artery deformation faster than CP oscillation.

2. There is an obvious second peak observed which is considered to be the combination of artery deformation and CP compression signals.

The FFT analysis was carried out and the results in Figure 7.3c show different frequency components.



a



b

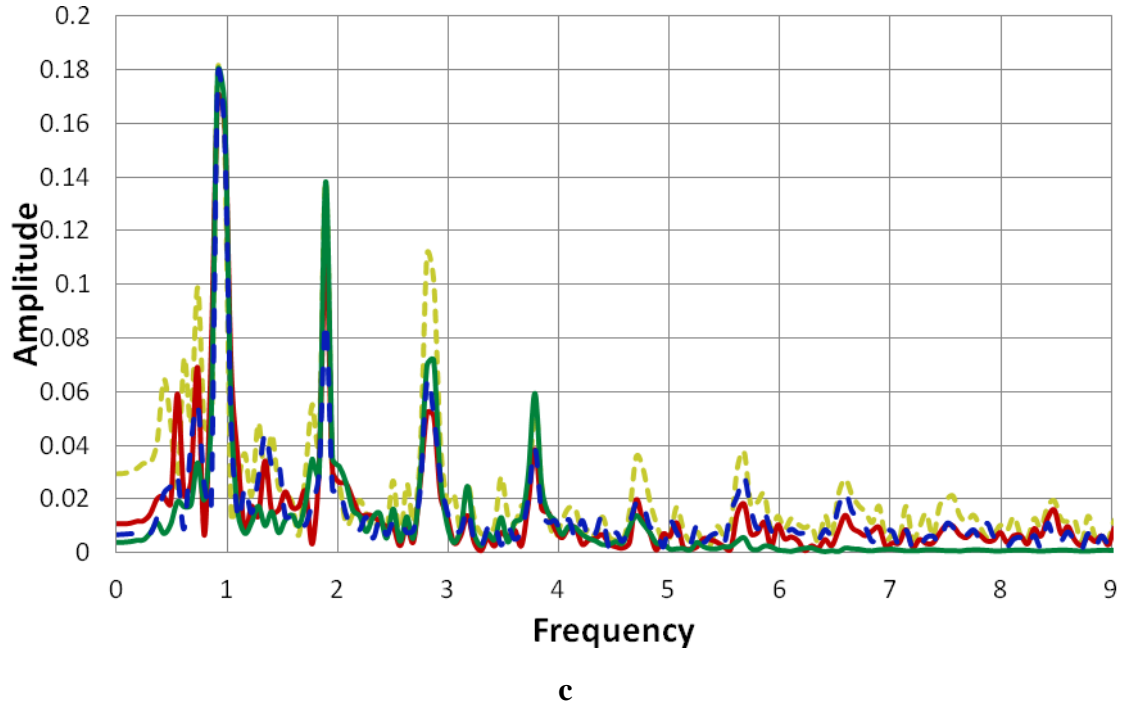
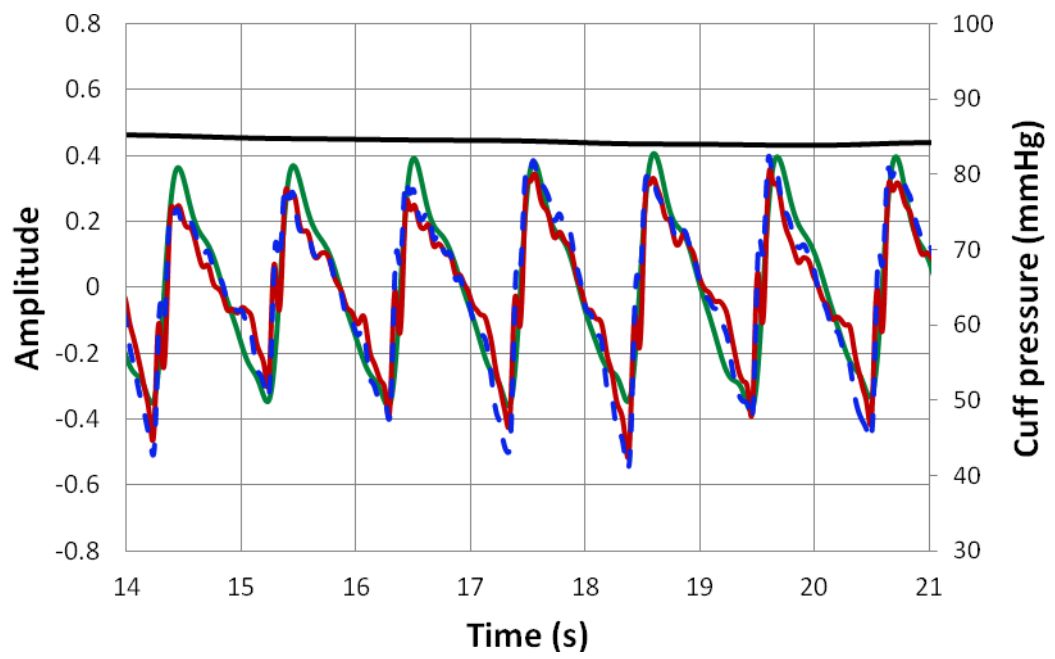


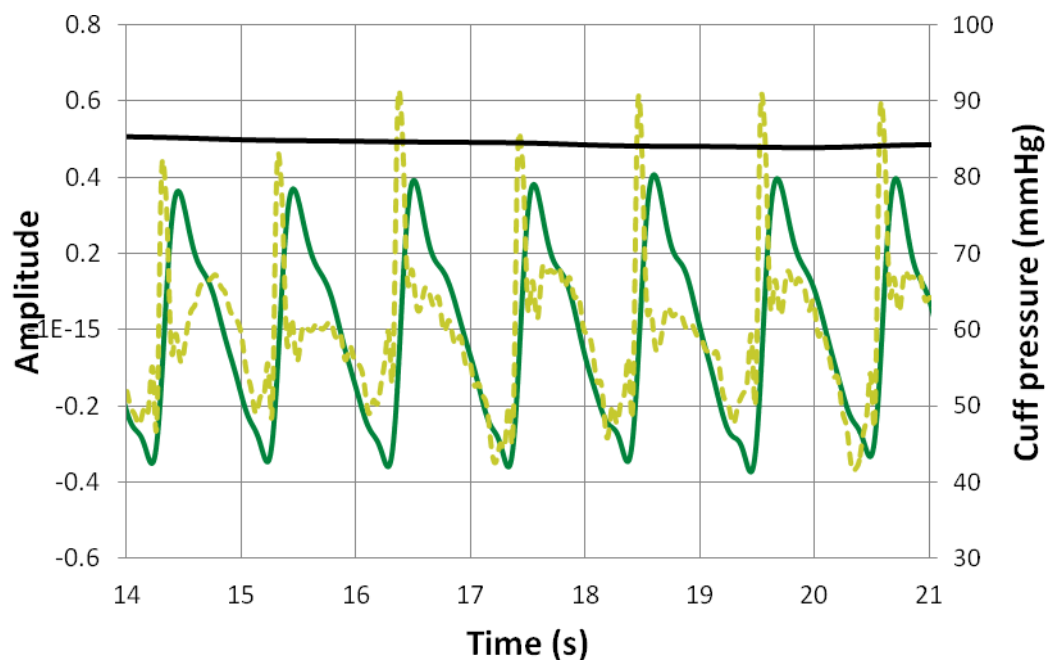
Figure 7.3 Experiment results when CP was at SP: (a) readings from the biceps sensor and the triceps sensor during normal oscillometric BP measurement; (b) artery CP reading during BP no motion; (c) FFT analysis of the obtained signals after normalizing: --- artery sensor, — biceps sensor, - - triceps sensor, — CP oscillation, — CP.

7.2.2.3 CP at MP

When CP was set to 90 mmHg in the device, CP remained around 85 mmHg which was close to the MP of the subject. As shown in Figure 7.4a, the outputs of the biceps sensor and the triceps are still dominated by CP. Figure 7.4b shows that the artery sensor is also sensitive to artery deformations and responds to BP impulses faster than CP when CP equals MP. The frequency analysis of all of the obtained signals is shown in Figure 7.4c.



a



b

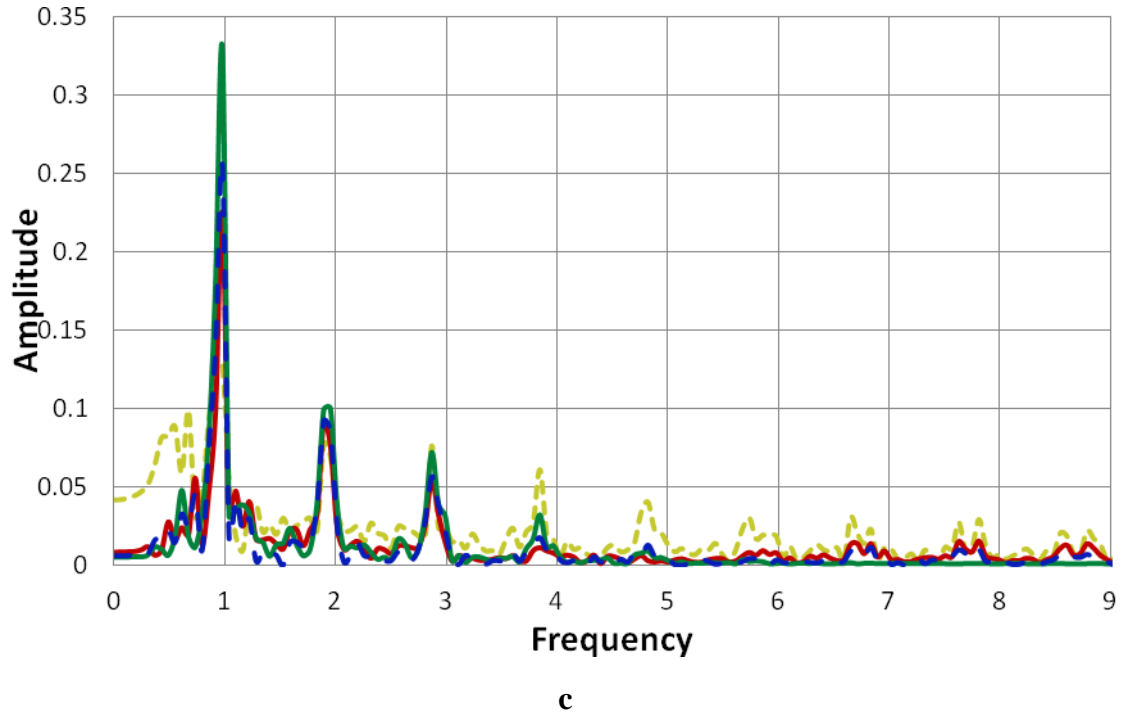
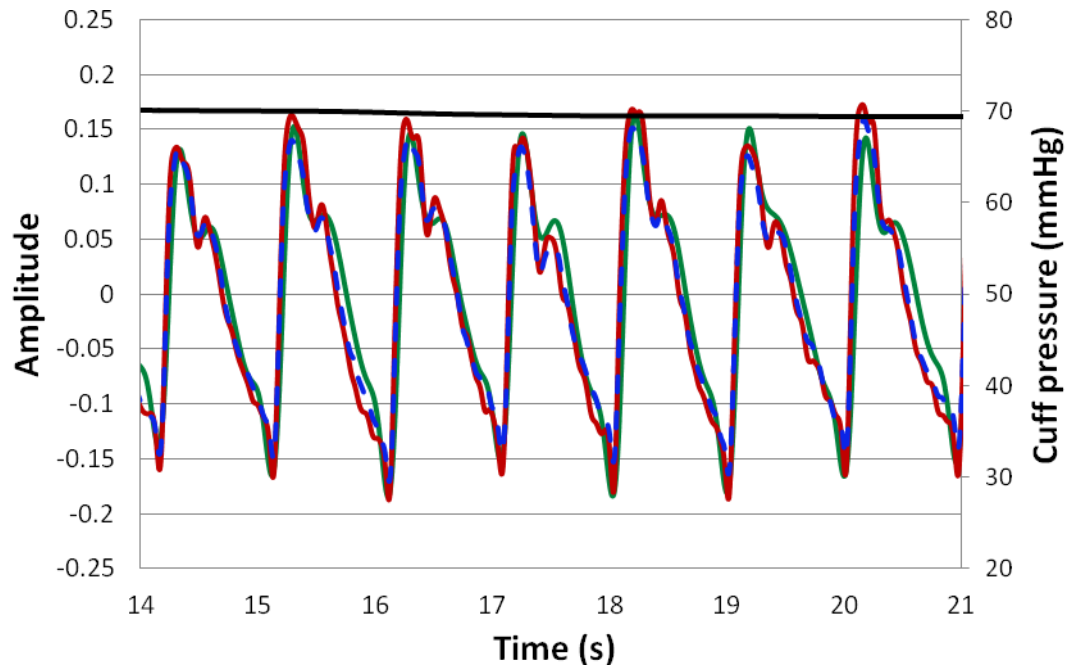


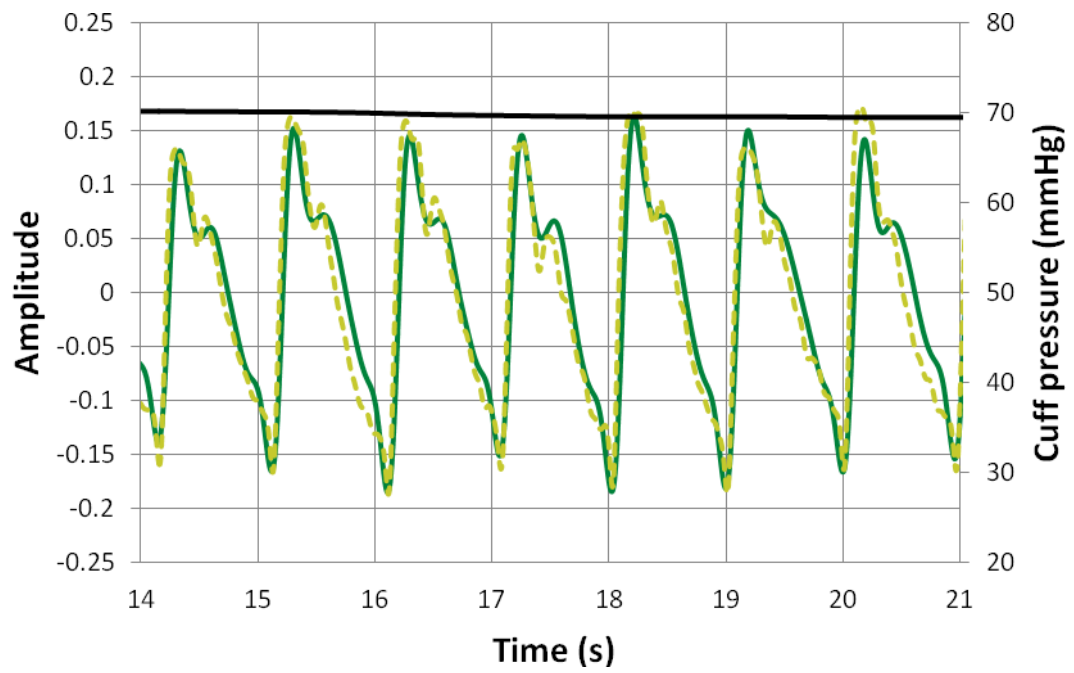
Figure 7.4 Experiment results when CP was at MP: (a) readings from the biceps sensor and the triceps sensor during normal oscillometric BP measurement; (b) artery CP reading during BP no motion; (c) FFT analysis of the obtained signals after normalizing: --- artery sensor, — biceps sensor, - - triceps sensor, — CP oscillation, — CP.

7.2.2.4 CP at DP

When CP was set to 75 mmHg in the device, CP was around the DP of the subject at 70 mmHg. Since the arm was less compressed under the cuff and artery deformation was small, the strain change transferred to the arm surface was low. The artery sensor mainly responded to CP oscillations. As shown in Figure 7.5a and Figure 7.5b, all of the attached piezoelectric film sensors give a waveform similar to CP oscillations.



a



b

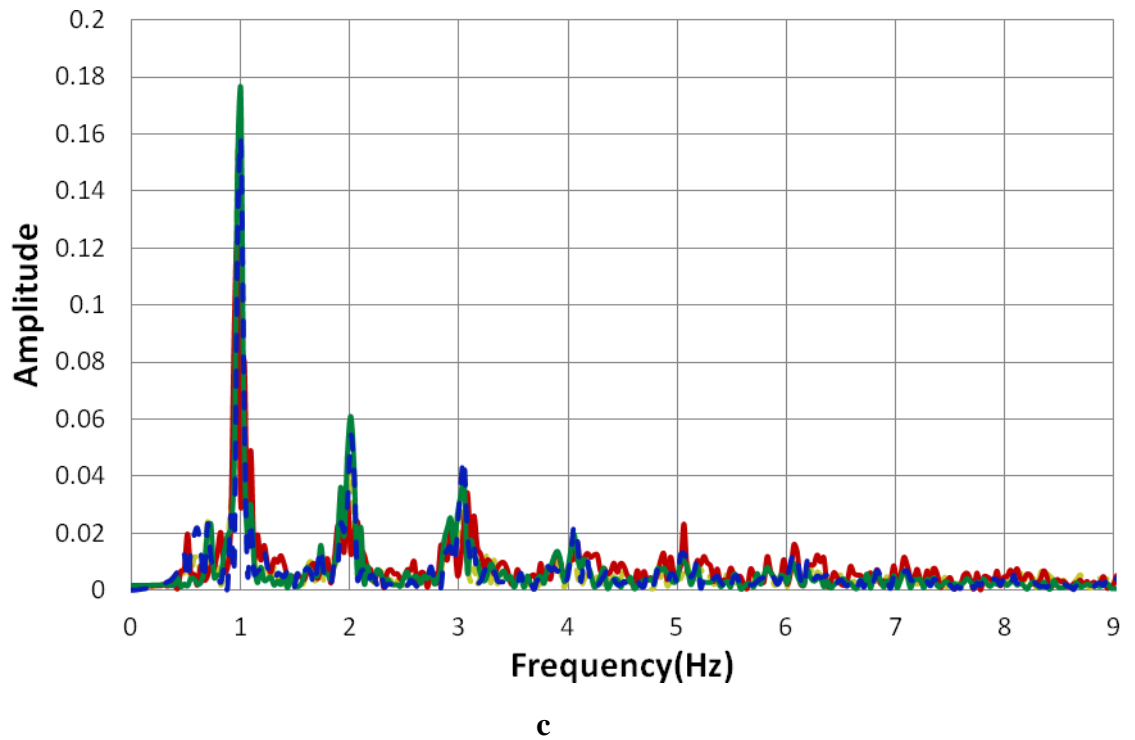
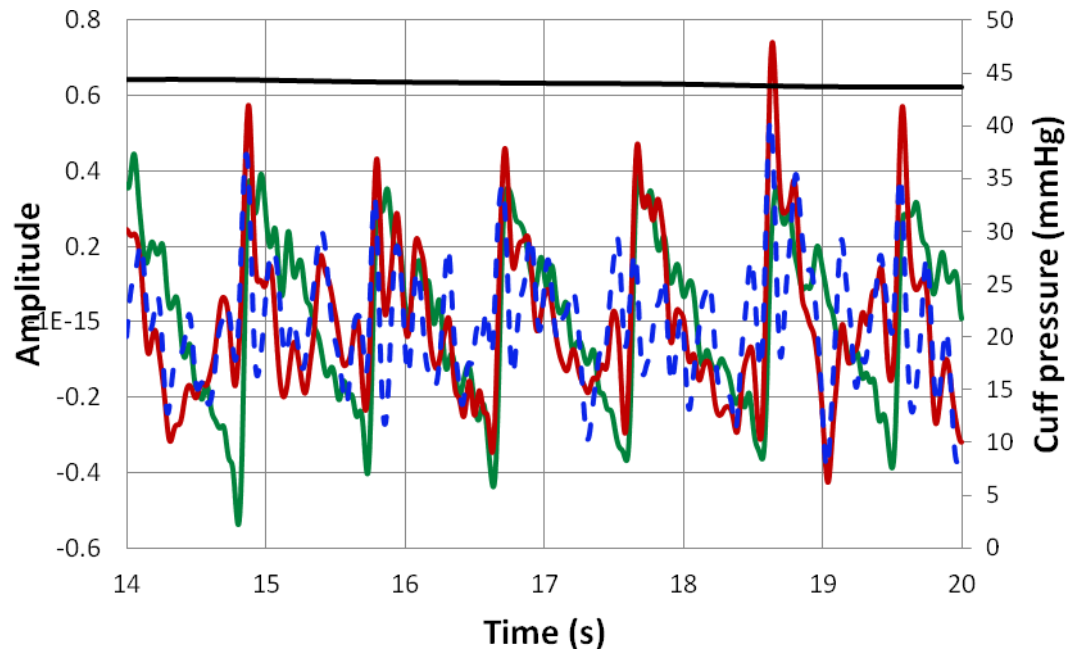


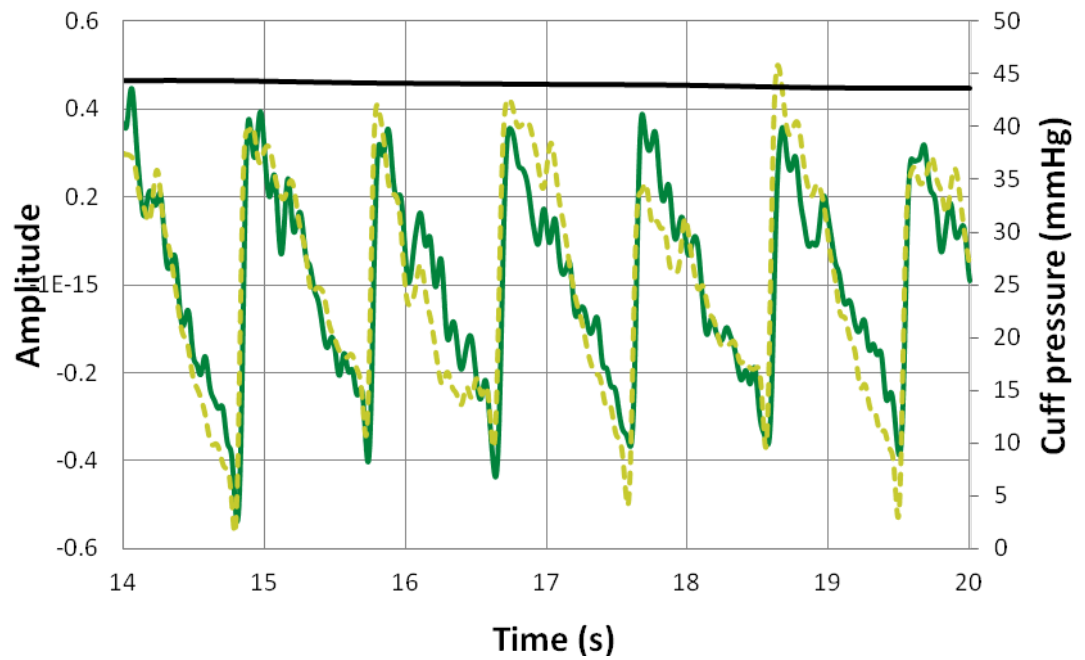
Figure 7.5 Experiment results when CP was at DP: (a) readings from the biceps sensor and the triceps sensor during normal oscillometric BP measurement; (b) artery CP reading during BP no motion; (c) FFT analysis of the obtained signals after normalizing: --- artery sensor, — biceps sensor, - - triceps sensor, — CP oscillation, — CP.

7.2.2.5 CP at sub-diastolic pressure

When CP was lower than DP, environmental noises become more obviously in piezoelectric film sensors signals. Although the obtained results still have features identical to CP oscillations, random noises are detected in the waveforms as shown in Figure 7.6. This is mainly because the arm tissue was more free to move when CP was low. Since the reading at sub-diastolic pressure is not used in oscillometric method, these results will not be used for further study.



a



b

Figure 7.6 Experiment results when CP was at sub-diastolic pressure: (a) readings from the biceps sensor and the triceps sensor during normal oscillometric BP measurement; (b) artery CP reading during BP no motion: --- artery sensor, — biceps sensor, - - triceps sensor, — CP oscillation, — CP.

7.2.3 Arm motion

In the human arm, any arm motion will lead to muscle movement and arm volume changes. Since the external layer of the cuff is very rigid, the arm volume change will transfer to the cuff in the form of volume and CP changes. When arm motions are introduced into the oscillometric BP measurement, the arm deformation led to unexpected pressure changes in the cuff. The CP reading is the combination of artery volume change and arm volume change. Since the artery is fairly small, the major component of the reading is derived from the arm motion. Therefore, the automated device can not figure out the subject's BP using the obtained CP readings, as shown in Figure 7.7.

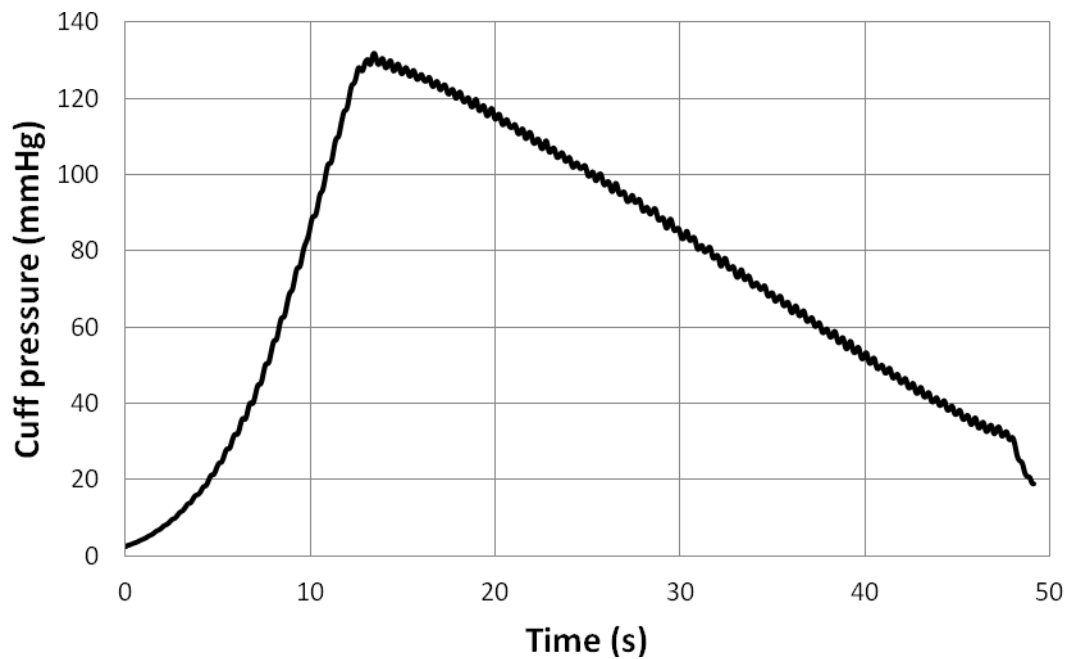


Figure 7.7 CP in the oscillometric BP measurement process when arm motion was involved in the BP measurement process.

7.3 Signal relationship

As demonstrated in Chapter 5, the designed measurement system consists of four sensors: one pressure sensor connected to the cuff and three piezoelectric film sensors on the skin of the arm. Since piezoelectric film sensors are placed on the arm surface under the cuff, they measured both arm skin strain changes and CP compression. Figure 7.8 shows the signal transmission for each piezoelectric film sensor in the designed system.

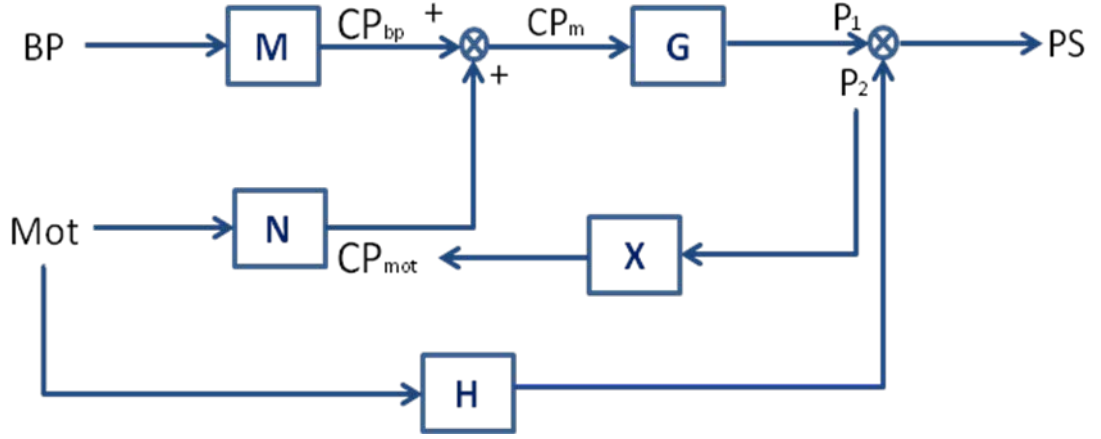


Figure 7.8 Generalized input-output configuration of the designed BP measurement system.

Where **G**, **H**, **M**, **N**, **X** are transfer functions in the system,

CP_{bp} = CP oscillation dominated by BP pulses,

CP_{mot} = CP changes generated by arm motions,

CP_m = the measured CP in the cuff by connected pressure sensor,

Mot = arm motion signal,

P_1, P_2 = strain signal generated by CP_m and arm motion respectively,

PS = output of the piezoelectric film sensor.

In this system, BP pulse signals transfer to the cuff in the form of CP oscillations (CP_{bp}) by changing artery volume under the cuff. The arm motions transfer to the cuff and create CP change (CP_{mot}). The measured CP value CP_m equals to $CP_{mot} + CP_{bp}$. When the piezoelectric film sensor is compressed by CP, it gives the reading P_1 . It is also sensitive to arm surface strain changes from the arm motions and its output is P_2 . The measured piezoelectric film sensor value PS equals to $P_1 + P_2$.

7.3.1 Without arm motion

As piezoelectric film sensors are placed on different locations, signal transmissions are different from each other, as shown in Figure 7.9. In the designed system, the biceps sensor and the triceps sensor are placed on top of biceps and triceps and proven non-sensitive to brachial artery movement in the FE model. Therefore the relationships between the obtained signals are

$$BP \cdot M = CP_{bp} = CP_m \quad (7.1)$$

$$CP_{bp} \cdot G = P_1 = PS \quad (7.2)$$

The artery sensor is place just above the brachial artery where it is also sensitive to artery movement. Therefore, the artery sensor measures both CP oscillations and brachial artery stretches. The relationships between the obtained signals are

$$BP \cdot M = CP_{bp} = CP_m \quad (7.3)$$

$$CP_{bp} \cdot G + BP \cdot N = P_1 + P_2 = PS \quad (7.4)$$

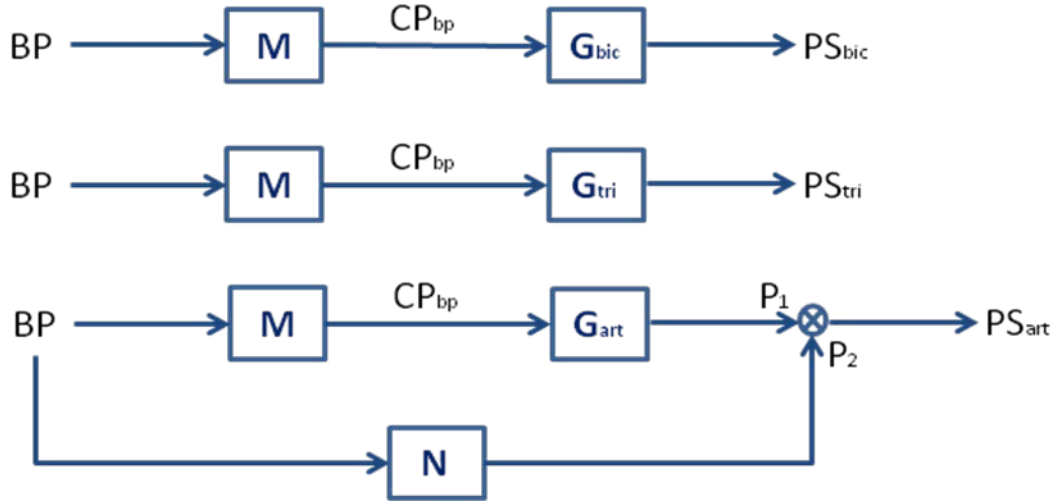


Figure 7.9 Generalized input-output configuration of the measurement without any arm motion.

Because of the lack of intravascular measurement in this study, it is impossible to work out the transfer function \mathbf{M} between BP pulse and CP oscillation. Using the measured results CP_m and PS , the transfer function \mathbf{G} is calculated through an empirical equation. The CP_m - PS relationships of the biceps sensor and triceps sensor (\mathbf{G}_{bic} and \mathbf{G}_{tri}) are very close to each other. Since the artery sensor has the same property as the other two sensors, the transfer function \mathbf{G}_{art} is also similar to \mathbf{G}_{bic} and \mathbf{G}_{tri} . In order to remove the artery stretch signals derived from BP pulses, a low-pass filter was applied to the artery sensor readings. As there is no muscle under the artery sensor, it is slightly different from the others. The relationship between the obtain signals are shown in Figure 7.10. Therefore, the brachial artery stretches (P_2 shown in Figure 7.9) can be isolated from the measured signals.

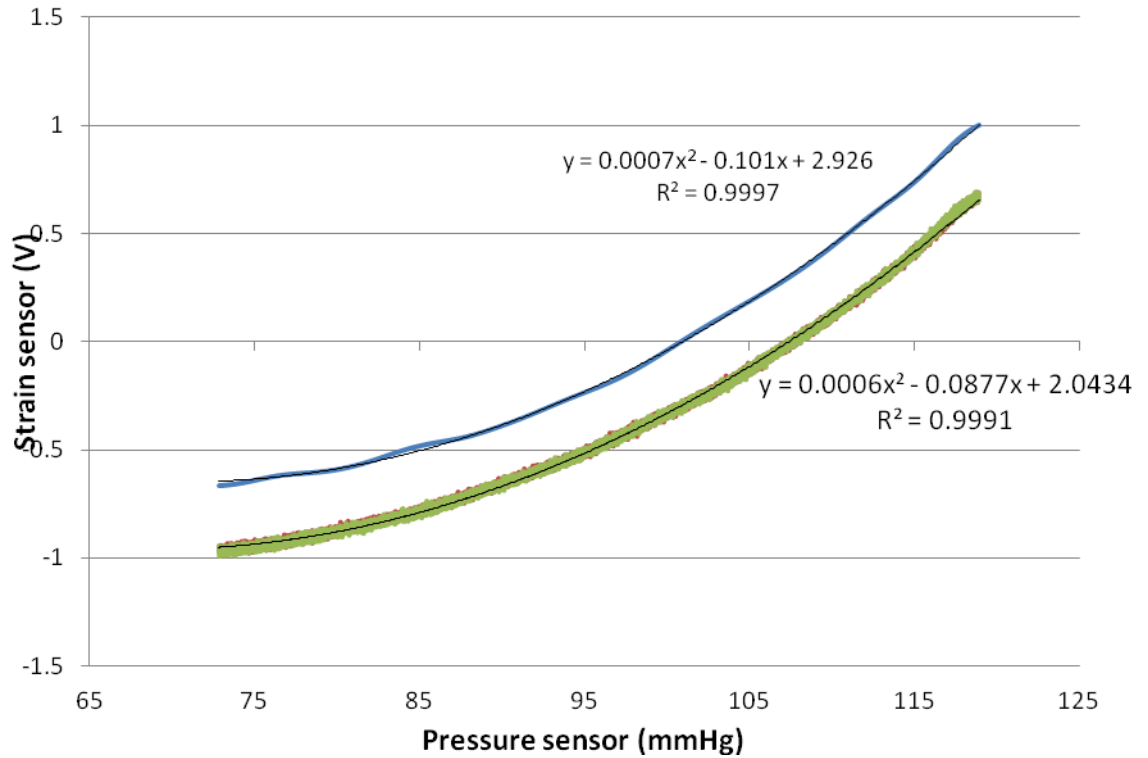


Figure 7.10 The relationship between CP and piezoelectric sensors. — G_{bic} — G_{tri} — G_{art}

7.3.2 With arm motion

When arm motions are introduced in the measurement, BP pulse transmission is the same as situation 1. However, there are too many unknown variables when arm motion is introduced into the system. In order to figure out the transfer functions in the designed system, the following experiments were done: (1) without BP, and with arm motion, (2) with BP and arm motion.

7.3.2.1 Without BP

In order to study the relationship between the motions and sensor readings, the experiments without BP pulses were conducted by placing an inflated cuff above the current cuff. When the blocking cuff was inflated 50 mmHg over the subject's supra-systolic pressure, the brachial artery was fully compressed and there was no blood

passing through. Therefore, CP_m readings were all derived from the arm motions. The input-output configuration of this test is as shown in Figure 7.11.

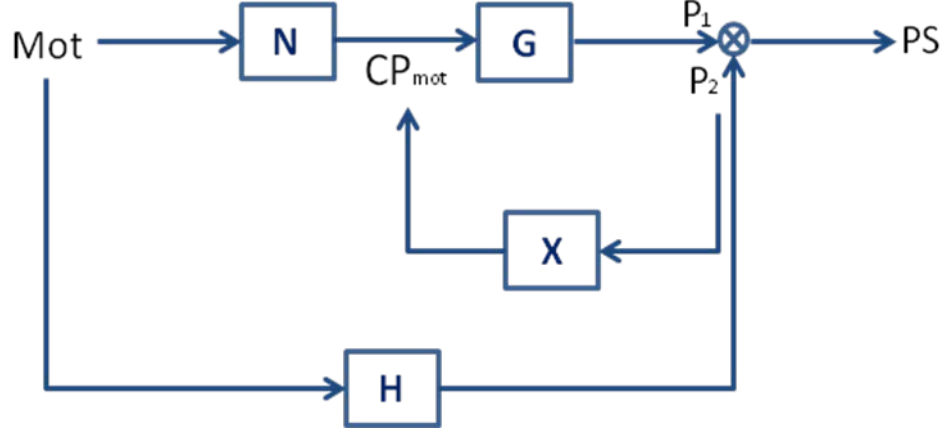


Figure 7.11 Generalized input-output configuration of the measurement without BP signals.

From in Figure 7.11, we get the following equations:

$$Mot \cdot N = CP_{mot} = CP_m \quad (7.5)$$

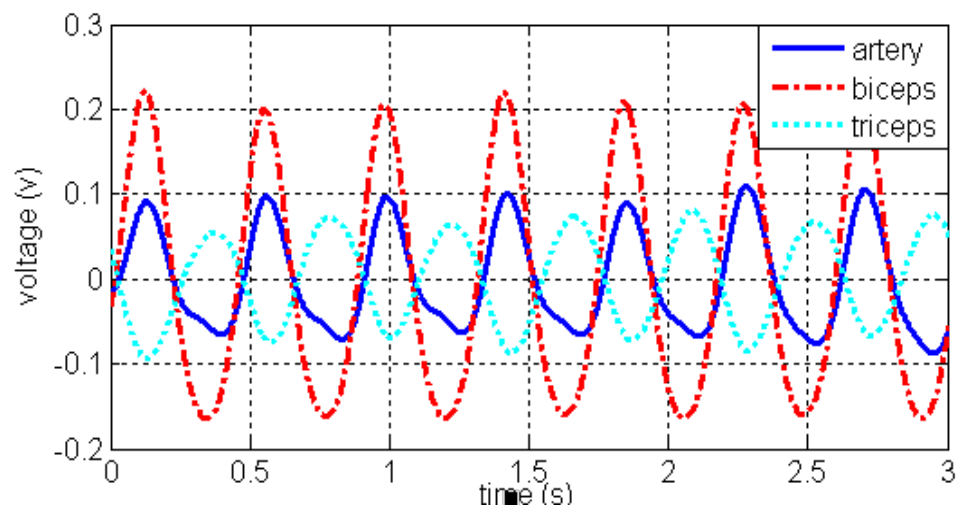
$$Mot \cdot H = P_2 = PS - CP_m \cdot G \quad (7.6)$$

Therefore, the transfer function **X** is

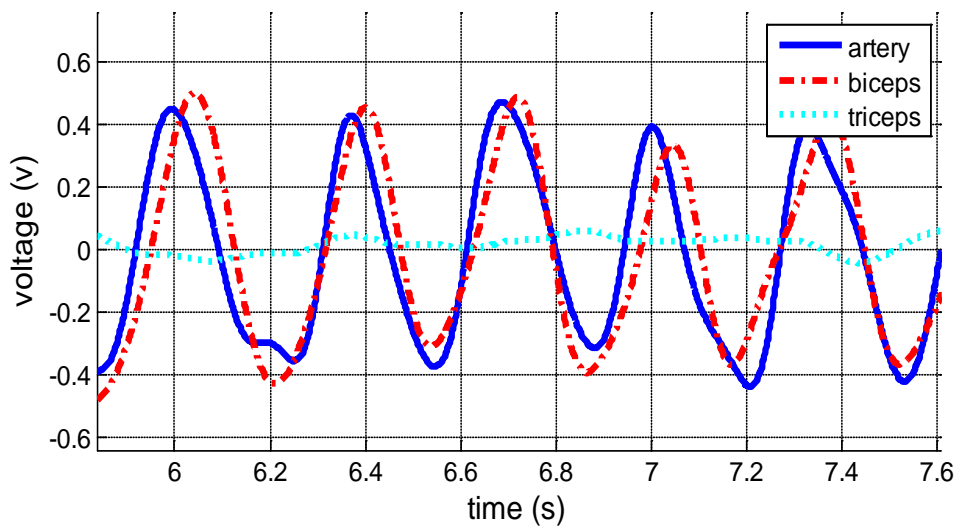
$$X = CP_{mot} / P_2 = CP_m / (PS - CP_m \cdot G) \quad (7.7)$$

Since CP_m and PS are directly measured by the devices in the experiment and **G** is already known from the previous test, the transfer function **X** is obtainable. However, the transfer function **X** for each sensor is unique, because piezoelectric film sensors are placed on different locations and they are sensitive to different muscle movements. Furthermore, the transfer function varies with different arm motions. In order to choose the proper transfer function, the system has to identify the arm motion beforehand.

An experiment was carried out without the surrounding cuff. Therefore, pure arm surface strain changes were measured. Two most common passive arm motions – lifting and twisting – were tested, and were controlled by a small motion control system to manage the moving frequency and amplitude. The results shown in Figure 7.12 indicate that the relationship between the arm motion and arm surface strain are repeatable and predictable. It is also shown that the sensor readings have a unique relationship for each arm motion which can be used to identify the arm motion.



a



b

Figure 7.12 (a) Readings from piezoelectric film sensors during passive lifting; (b) Readings from piezoelectric film sensors during passive twisting: — artery sensor - - - biceps sensor triceps sensor

As shown in Figure 7.12a, the biceps sensor is more sensitive to a lifting motion: the reading amplitude is about two times of the other two sensors. In the test, the biceps sensor is placed on the top the biceps belly where the maximum biceps deformation during biceps contraction and extension presents. The artery sensor gives a similar waveform to the biceps sensor but with lower amplitude. Because the artery sensor is placed on the inner side of the biceps, it also catches the biceps deformation signal but at lower sensitivity. Since the artery sensor will measure the signal from an artery deformation when BP is introduced in the brachial artery, the artery sensor will give different waveform from the biceps sensor during the BP measurement process. Because the triceps does the opposite movement as the biceps to create the lifting motion, the strain change in the triceps sensor is opposite to that in the biceps sensor. Furthermore, because the triceps deformation is more distributed over the entire muscle and the triceps sensor is placed above the medial head of the triceps, less strain change is produced in the triceps sensor area. From the results obtained, it is shown that the stretch of triceps sensor reading is close to half of that in the biceps sensor.

In Figure 7.12b, it is shown that the triceps sensor reading is less than 10% of the other two sensor readings in the twisting motion. The amplitude of the artery sensor and the biceps sensor readings is similar but there is a phase shift between the artery sensor and the biceps sensor readings which indicates the arm motion speed.

7.3.2.2 With BP and arm motion

In the designed system as shown in Figure 7.8, the signal transmission with both BP pulse and arm motion is described by the following equations

$$BP \cdot M + Mot \cdot N = CP_{bp} + CP_{mot} = CP_m \quad (7.8)$$

$$CP_m \cdot G + Mot \cdot H = P_1 + P_2 = PS \quad (7.9)$$

Therefore,

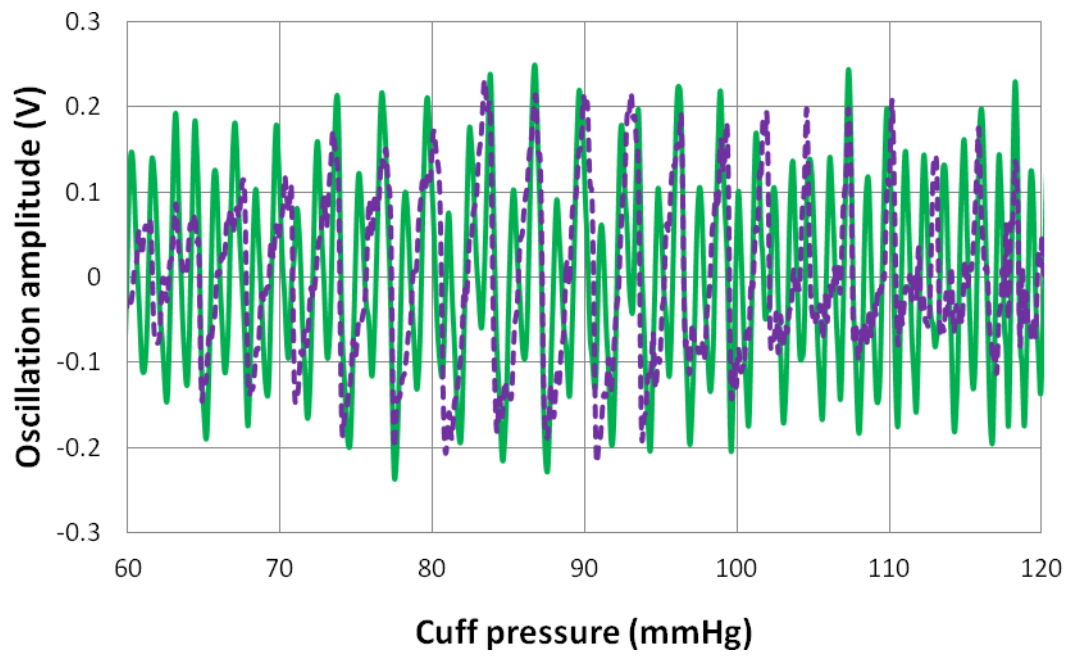
$$CP_{bp} = CP_m - CP_{mot} = CP_m - P_2 \cdot X = CP_m - (PS - CP_m \cdot G) \cdot X \quad (7.10)$$

Since CP_m and PS are measured by the device, and \mathbf{G} and \mathbf{X} are already determined, CP_{bp} can be calculated from the measured results CP_m and used to determine the patients' BP using the oscillometric method.

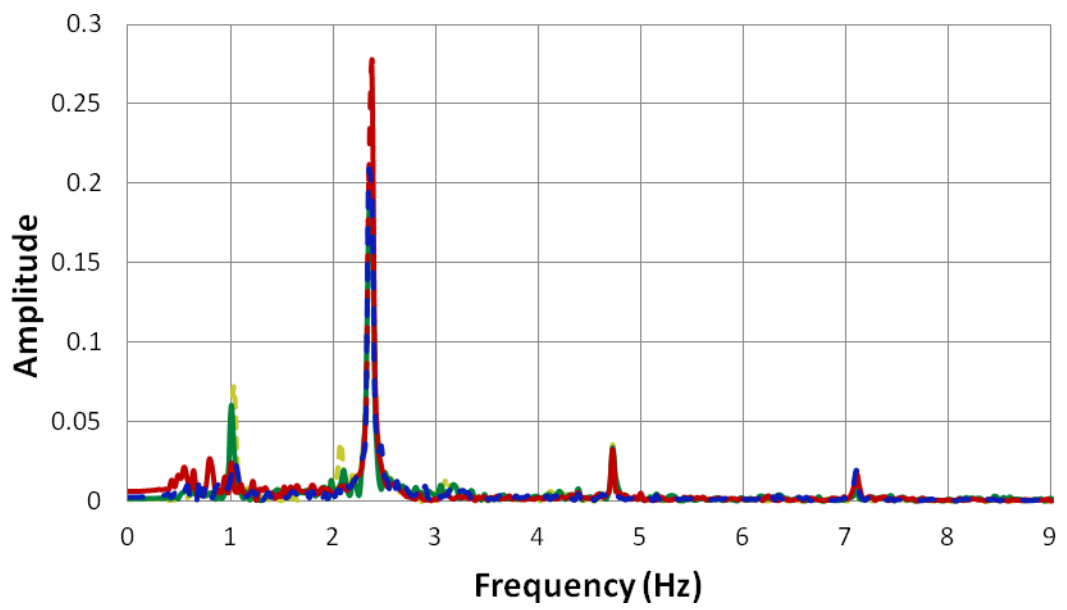
7.4 Waveform rebuild

An example of the CP waveform rebuilding process is shown in this section. Since the arm motion introduces a large CP oscillation in the BP measurement process, as shown in Figure 7.7 and Figure 7.13a, CP oscillations derived from the BP pulses cannot be identified by the normal device and therefore cannot give a subject's BP value. In order to display the arm motion more clearly, the arm motion was repeated at constant frequency (2.3Hz) instead of random motion in this study.

Because the biceps sensor and triceps sensor were each placed on the top of the muscles which dominate arm motions, they were more sensitive to arm motions. As shown in Figure 7.13b, their amplitudes of FFT analysis are comparably high at the motion frequency and can be ignored at BP frequency. In contrast, the artery sensor and cuff pressure sensor measured both arm motion signals and BP pulse signals.



a



b

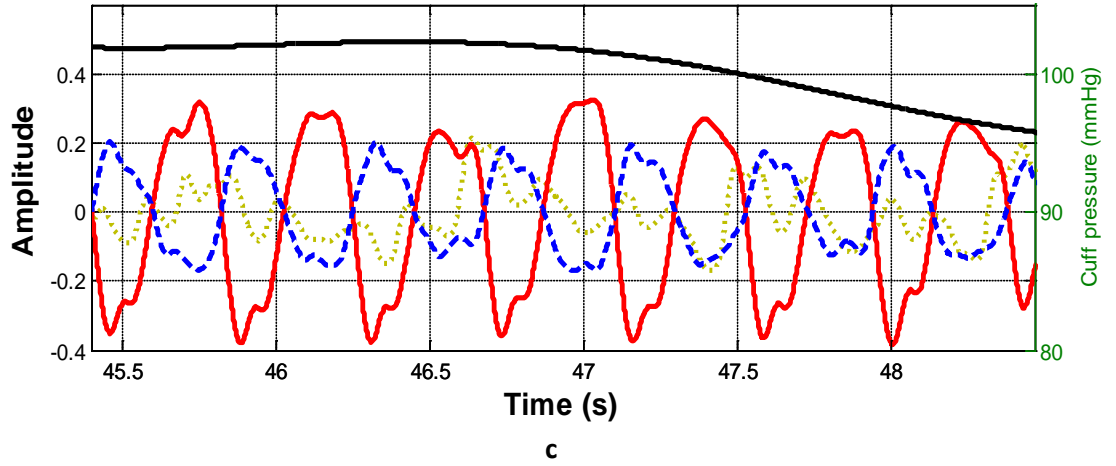


Figure 7.13 Experiment results when arm motion was involved in the BP measurement process: (a) rebuilt CP oscillations for BP analysis; (b) FFT analysis of the obtained signals after normalizing; (c) the measured oscillations signal from the artery sensor, the biceps sensor and the triceps sensor: --- artery sensor, — biceps sensor, - - triceps sensor, — measured CP oscillation, — CP, - - rebuilt CP oscillation.

The CP oscillations in the BP measurement process are rebuilt in the following steps:

1. Readings from the biceps sensor and the triceps sensor were used to identify arm motions.

As shown in Figure 7.13c, the biceps sensor and the triceps sensor oscillate at the same frequency; the relationship between their readings is close to lifting motion criteria $PS_{tri} \approx -0.5PS_{bi}$.

2. The subject's heart rate was determined by analyzing the artery stretch signals.

Since the normal heart rate is between 40 and 180 beat per minute, the frequency between 0.6 Hz and 3 Hz is analyzed. From the FFT analysis of the artery sensor, the identical peaks in the proposed range are 1.05 Hz, 2.1 Hz and 2.3 Hz. The

first peak at 1.05 Hz is determined as the heart rate for the following reasons: (a) the amplitude of the highest peak (2.3 Hz) is much higher than the other peaks and over the heart beat range, therefore it is considered to be arm motion frequency. (b) The second peak occurs at 2.1 Hz which is two times the first peak and its amplitude is about 30% of the first one. Both of these relationships are observed in the BP measurement.

3. Removing the noise from pressure sensor readings and using the result to calculating BP.

Using the transfer function for lifting motion, the noise is removed and CP oscillations are rebuilt as shown in Figure 7.13a. With the rebuild CP oscillations, the subject's BP value is determined by the Pulsecor[®] R6.5 non-invasive monitor and the result is equal to reference value measured by auscultatory method.

7.5 Summary

The relationships between the piezoelectric strain sensors under different conditions are studied in this chapter. The transfer functions between measured signals are determined separately through experiments conducted in different conditions. Using the method developed here, the designed system is able to detect the arm motions and rebuild CP oscillation for the automatic BP measurement device.

Chapter 8 Conclusion and Future work

8.1 Conclusion

This study has investigated two major issues related to ABPM technique: (1) the theory of oscillometric BP measurement method which is used in most of ABPM device; (2) the method to compensate the noises during the measurement.

8.1.1 Theory of oscillometric BP measurement method

The investigation of oscillometric BP measurement theory was carried out through a FE model. Although some simplifications were made to achieve the balance between computational cost and accuracy, the developed model was closer to reality and gave more accurate results than previous ones. It was validated by both experimental results on an arm simulator and clinical results on human body. The following findings were obtained from this investigation:

1. The CP transmission through the arm is not uniform and the artery closure status varies along the artery. Therefore, the measured CP oscillations are a reflection of the artery volume change under the cuff which is a mixture of arterial distension in different closure states.
2. The brachial artery did not collapse when CP equals to MP. Therefore, it denies the estimation that the maximum CP oscillation during oscillometric measurement is due to the buckling of the artery under the cuff.

3. The nonlinearity plays the key role in oscillometric BP measurement method.

The stiffness of the brachial artery does not have significant effect on the measurement accuracy using oscillometric BP measurement method.

4. The BP overestimation in the elderly and underestimation in the younger are mainly caused by the changes of compressibility of arm tissues.

8.1.2 Compensate the noises during the measurement

An anatomically accurate model was developed in this study, whose geometry was extracted from VHB dataset. The arm movements were achieved in the model by changing the boundary conditions of the simulated muscles. From the modelling results, a piezoelectric film sensor array was designed to detect the arm motions, which were placed above the brachial artery, biceps belly and the medial head of triceps respectively. The relationships between the piezoelectric strain sensors under different conditions were studied experimentally. The transfer functions between measured signals were determined separately by empirical equations through the experimental results. Using the developed method, the designed system was able to detect and determine simple arm motions, and then compensate the introduced noise. The CP oscillations were obtained by removing the noise from measured CP signals and then sent to the automatic BP measurement device to determine the subject's BP.

8.2 Future work

There are some suggestions for the future work on this study.

8.2.1 BP measurement technique

From the measurements at different CPs, it is shown that the oscillation waveforms vary with accompanying CP changes. Especially in the results from artery sensor, there are obviously impulses when CP is above MP. This phenomenon indicates that the practicality of getting the subject's BP by determining waveform features at different CP. This investigation can be carried out when the intravascular measurement is available.

8.2.2 Detecting BP waveform

As illustration from the developed model, the pressure sensor in the cuff measuring the mixture of arterial distension in different closure states, it is very difficult to represent the actual BP waveform in the brachial artery through obtained CP oscillation. The results from artery sensor are more suitable for working out the BP waveform for the following reasons:

1. The sensor is very narrow and just covers 1cm long artery.
2. The sensor is placed at the centre of the cuff range where the pressure transmission ratio is highest.

With intravascular experiments, the relationship between BP waveform and artery sensor readings can be solved and the obtained BP waveform will be used for diagnosing the subject's cardiovascular health conditions.

8.2.3 Noise compensation

In this study, the obtained transfer functions were valid for individuals only. The parameters of the transfer functions had to be recalculated in each time. Universal

transfer functions are required to be developed in the future. Furthermore, only lifting and twisting motions are investigated in this study. More arm motions can be developed in the future.

REFERENCES

1. Jordan, D. and J. Marshall, *Cardiovascular Regulation*. 1995, London, UK: Portland Press Ltd.
2. Pickering, T.G., et al., *Recommendations for Blood Pressure Measurement in Humans and Experimental Animals: Part 1: Blood Pressure Measurement in Humans: A Statement for Professionals From the Subcommittee of Professional and Public Education of the American Heart Association Council on High Blood Pressure Research*. Hypertension, 2005. **45**: p. 142-161.
3. Chobanian, A.V., et al., *Seventh Report of the Joint National Committee on Prevention, Detection, Evaluation, and Treatment of High Blood Pressure*. Hypertension, 2003. **42**(6): p. 1206-1252.
4. Ministry of Health, *A Portrait of Health: Key results of the 2002/03 New Zealand Health Survey*. 2004, Wellington, New Zealand: Ministry of Health.
5. Joffres, M.R., *Prevalence, control and awareness of high blood pressure among Canadian adults* Canadian Medical Association Journal, 1992. **146**(11): p. 1997-2005.
6. Jones, D.W., et al., *Measuring Blood Pressure Accurately: New and Persistent Challenges*. Journal of the American Medical Association, 2003. **289**(8): p. 1027-1030.
7. O'Brien, E. and K. O'Malley, *Blood pressure measurement*. Handbook of hypertension. 1991: Elsevier.
8. Geddes, L.A., *Handbook of Blood Pressure Measurement*. 1991: Humana Press.
9. Mangoni, A., *Radial artery compliance in young, obese, normotensive subjects*. . Hypertension 1995. **26**: p. 984-988.
10. O'Rourke, M.F., *From theory into practice: arterial haemodynamics in clinical hypertension*. Journal of Hypertens, 2002. **20**: p. 1901-1915.
11. Surawicz, B., *Heart Disease: A Textbook of Cardiovascular Medicine*. JAMA, 2001. **286**(7): p. 847-.
12. Pearson Education Inc. 2003 [cited 2008; Available from: http://home.comcast.net/~pegglestoncbbsd/MeasuringBloodPress_1.JPG.

13. Rose, G., *STANDARDISATION OF OBSERVERS IN BLOOD-PRESSURE MEASUREMENT*. The Lancet, 1965. **285**(7387): p. 673-674.
14. Van Montfrans, G.A., *Oscillometric blood pressure measurement: progress and problems*. Blood Pressure Monitoring, 2001. **6**: p. 287-290.
15. Amoores, J.N. and D.H. Scott, *Can simulators evaluate systematic differences between oscillometric non-invasive blood-pressure monitors?* . Blood Pressure Monitoring, 2000. **5**: p. 81-89.
16. Chung, I. and G.Y.H. Lip, *White coat hypertension: not so benign after all?* J Hum Hypertens, 2003. **17**(12): p. 807-809.
17. White, W.B., *Ambulatory Blood-Pressure Monitoring in Clinical Practice*. New England Journal of Medicine 2003. **348**(24): p. 2377-2378.
18. Marchiondo, R.J., et al., *Automated Ambulatory Blood Pressure Monitoring: Clinical Utility in the Family Practice Setting* American Family Physician 2003. **67**(11): p. 2343-50.
19. Hermida, R.C., et al., *Diagnosis of hypertension based on ambulatory blood pressure monitoring: are 24 hours of sampling enough?* American Journal of Hypertension, 2004. **17**(5).
20. Jones, D.W., et al., *Mercury Sphygmomanometers Should Not be Abandoned: An Advisory Statement From the Council for High Blood Pressure Research, American Heart Association*. Hypertension, 2001. **37**(2): p. 185-186.
21. Archibald, G.K., et al., *Non-invasive Blood Pressure Sensor With Motion Artifact Reduction*. 2000, Medwave, Inc.: US. p. 19.
22. Archibald, G.K., et al., *Non-invasive Blood Pressure Sensor With Motion Artifact Reduction and Constant Gain Adjustment during Pressure Pulses*. 2001, Medwave, Inc.: US. p. 22.
23. Donna R. Lunak, R.S.B., *Non-invasive Blood Pressure Monitor Having Automatic High Motion Tolerance*. 2006: US.
24. Imai, Y., et al., *Japanese Society of Hypertension (JSH) Guidelines for Self-Monitoring of Blood Pressure at Home*. Hypertension Res, 2003. **26**(10): p. 771-782.
25. Sims, A.J., et al., *Oscillometric blood pressure devices and simulators: measurements of repeatability and differences between models*. Journal of Medical Engineering & Technology, 2005. **29**(3): p. 112-118.
26. Colak, S. and C. Isik. *Evaluation of pulse features for oscillometry*. in *Bioengineering Conference, 2004. Proceedings of the IEEE 30th Annual Northeast*. 2004.

27. Stergiou, G.S., et al., *Home Self-Monitoring of Blood Pressure - Is Fully Automated Oscillometric Technique as Good as Conventional Stethoscopic Technique?* . American Journal of Hypertension, 1997. **10**(4): p. 428-433(6).
28. Williams, B., et al., *Guidelines for management of hypertension: report of the fourth working party of the British Hypertension Society, 2004—BHS IV.* Journal of Human Hypertension, 2004. **18**: p. 139-185.
29. Roger, J., S. Mark, and R. Shyam, *Blood Pressure Measurement*, in *The Measurement, Instrumentation and Sensors Handbook on CD-ROM*. 1999, CRC Press.
30. Drzewiecki, G., R. Hood, and H. Apple, *Theory of the oscillometric maximum and the systolic and diastolic detection ratios*. Annals of Biomedical Engineering, 1994. **22**(1): p. 88-96.
31. Drzewiecki, G., *Noninvasive assessment of arterial blood pressure and mechanics*. 1995: CRC Press.
32. Drzewiecki, G.M. and I.F. Moubarak. *Transmural pressure-area relation for veins and arteries*. in *Bioengineering Conference, 1988., Proceedings of the 1988 Fourteenth Annual Northeast*. 1988.
33. Baker, P., D. Westenskow, and K. Kück, *Theoretical analysis of non-invasive oscillometric maximum amplitude algorithm for estimating mean blood pressure*. Medical and Biological Engineering and Computing, 1997. **35**(3): p. 271-278.
34. Sang-hwa, Y., et al. *Simulation of Estimating the Blood Pressure Using an Arterial Pressure-Volume Model*. in *Convergence Information Technology, 2007. International Conference on*. 2007.
35. Ursino, M. and C. Cristalli, *Mathematical modeling of noninvasive blood pressure estimation techniques--Part I: Pressure transmission across the arm tissue*. Journal of biomechanical engineering, 1995. **117**(1): p. 107-16.
36. Ursino, M. and C. Cristalli, *A mathematical study of some biomechanical factors affecting the oscillometric blood pressure measurement*. Biomedical Engineering, IEEE Transactions on, 1996. **43**(8): p. 761-778.
37. Posey, J.A., et al., *The meaning of the point of maximum oscillations in cuff pressure in the indirect measurement of blood pressure. 1*. Cardiovasc Res Cent Bull, 1969 **8**(1).
38. Geddes, L., et al., *Characterization of the oscillometric method for measuring indirect blood pressure*. Annals of Biomedical Engineering, 1982. **10**(6): p. 271-280.
39. Forster, F.K. and D. Turney, *Oscillometric determination of diastolic, mean and systolic blood pressure--a numerical model*. Journal of biomechanical engineering, 1986. **108**(4): p. 359-364.

40. Drzewiecki, G. and J.J. Pilla, *Noninvasive Measurement of the Human Brachial Artery Pressure–Area Relation in Collapse and Hypertension*. Annals of Biomedical Engineering, 1998. **26**: p. 965-974.
41. Drzewiecki, G., et al., *Vessel growth and collapsible pressure-area relationship*. American Journal of Physiology - Heart and Circulatory Physiology, 1997. **273**(4): p. H2030-H2043.
42. Armentano, R., et al., *Mechanical pressure versus intrinsic effects of hypertension on large arteries in humans*. Hypertension, 1991. **18**(5): p. 657-664.
43. Hayoz, D., et al., *Conduit artery compliance and distensibility are not necessarily reduced in hypertension*. Hypertension, 1992. **20**(1): p. 1-6.
44. Heagerty, A.M., et al., *Small artery structure in hypertension. Dual processes of remodeling and growth*. Hypertension, 1993. **21**(4): p. 391-397.
45. Cristalli, C., P. Mancini, and M. Ursino, *An experimental and mathematical study of non-invasive blood pressure measurement*. Engineering in Medicine and Biology Society, 1992. **14**: p. 63-64.
46. Maurel, W., et al. *A biomechanical musculoskeletal model of human upper limb for dynamic simulation*. in *Biomedical Imaging, 2002. 5th IEEE EMBS International Summer School on*. 2002.
47. Fernandez, J.W., et al., *Anatomically based geometric modelling of the musculoskeletal system and other organs*. Biomechanics and Modeling in Mechanobiology, 2004. **2**(3): p. 139-155.
48. Teran, J., et al., *Creating and simulating skeletal muscle from the visible human data set*. Transactions on Visualization and Computer Graphics, 2005. **11**(3): p. 317-328.
49. Aritan, S., P. Dabnichki, and R. Bartlett, *Program for generation of three-dimensional finite element mesh from magnetic resonance imaging scans of human limbs*. Medical Engineering & Physics, 1997. **19**(8): p. 681-689.
50. Castleman, K.R., *Digital Image Processing*. 1979, New Jersey: Prentice-Hall.
51. Ackerman, M.J.P.I., *The visible human project*. Proceeding of the IEEE, 1998. **86**(3): p. 504-511.
52. Lu, W.M., et al., *Suitable location and optimum bladder width for the occluding cuff used for indirect arterial blood pressure measurements at the wrist*. Frontiers Med. Biol. Engng., 1999. **9**(1): p. 9-29.
53. Dong, F., et al., *An anatomy-based approach to human muscle modeling and defroamtion*. IEEE Transactions on visualization and computer graphics, 2002. **8**(2): p. 154-170.

54. Fung, Y.C., *Biomechanics: Mechanical Properties of Living Tissues*. 1993, New York: Springer-Verlag.
55. Shaltis, P.A., A.T. Reisner, and H.H. Asada. *A Finite Element Analysis of Local Oscillometric Blood Pressure Measurements*. in *Proceedings of the 29th Annual International Conference of the IEEE EMBS*. 2007. Lyon, France.
56. Johansson, T., P. Meier, and R. Blickhan, *A Finite-Element Model for the Mechanical Analysis of Skeletal Muscles*. *Journal of Theoretical Biology*, 2000. **206**(1): p. 131-149.
57. Bischoff, J.E., E.M. Arruda, and K. Grosh, *Finite element modeling of human skin using an isotropic, nonlinear elastic constitutive model*. *Journal of Biomechanics*, 2000. **33**(6): p. 645-652.
58. Kassab, G.S., *Biomechanics of the cardiovascular system: the aorta as an illustratory example*. *J. R. Soc. Interface* 2006. **3**: p. 719-740.
59. Tham, L.M., H.P. Lee, and C. Lu, *Cupping: From a biomechanical perspective*. *Journal of Biomechanics*, 2006. **39**(12): p. 2183-2193.
60. Oomens, C.W.J., et al., *Can Loaded Interface Characteristics Influence Strain Distributions in Muscle Adjacent to Bony Prominences?* *Computer Methods in Biomechanics and Biomedical Engineering*, 2003. **6**(3): p. 171 - 180.
61. Ursino, M. and C. Cristalli, *Mathematical analysis of the oscillometric technique for indirect blood pressure evaluation*. *IEEE TRANSACTIONS ON BIOMEDICAL ENGINEERING*, 1994. **41**(12): p. 1286-1287.
62. Blemker, S.S., P.M. Pinsky, and S.L. Delp, *A 3D model of muscle reveals the causes of nonuniform strains in the biceps brachii*. *Journal of Biomechanics*, 2005. **38**(4): p. 657-665.
63. Volokh, K.Y., *Prediction of arterial failure based on a microstructural bi-layer fiber-maxtrix model with softening*. *Journal of Biomechanics*, 2008. **41**: p. 447-453.
64. Lowery, M.M., et al., *Volume Conduction in an Anatomically Based Surface EMG Model*. *IEEE Transaction on biomedical engineering*, 2004. **51**(12): p. 2138-2147.
65. Zhang, M., et al., *Development of a non-linear finite element modelling of the below-knee prosthetic socket interface*. *Medical Engineering & Physics*, 1995. **17**(8): p. 559-566.
66. Lu, W.M., et al., *Indirect arterial blood pressure measurement at the wrist using a pad-type square cuff and volume-oscillometric*. *Frontiers Med. Biol. Engng*, 2001. **11**(3): p. 207-219.

67. Von Kinsky, B.R. and M.R. Zomlefer. *Interactive visualization of human arm structure and function*. in *Engineering in Medicine and Biology Society, 1994. Engineering Advances: New Opportunities for Biomedical Engineers. Proceedings of the 16th Annual International Conference of the IEEE*. 1994.
68. Lunak, D.R. and R.S. Bryngelson, *Non-invasive Blood Pressure Monitor Having Automatic High Motion Tolerance*. 2006: US.
69. Penrose, J.M.T., et al., *Development of An Accurate Three-dimensional Finite Element Knee Model*. *Computer Methods in Biomechanics and Biomedical Engineering*, 2002. **5**(4): p. 291-300.
70. Chung, T.J., *Applied continuum mechanics*. 1996, New York, USA: Cambridge University Press.
71. Strumpf, R.K., J.D. Humphrey, and F.C. Yin, *Biaxial mechanical properties of passive and tetanized canine diaphragm*. *American Journal of Physiology - Heart and Circulatory Physiology*, 1993. **265**(2): p. H469-H475.
72. Bovendeerd, P.H.M., et al., *Dependence of local left ventricular wall mechanics on myocardial fiber orientation: A model study*. *Journal of Biomechanics*, 1992. **25**(10): p. 1129-1140.
73. Herzog, W., *Skeletal muscle mechanics : from mechanisms to function / edited by W. Herzog*. 2000: New York : John Wiley, 2000.
74. Conrad, W., D. McQueen, and E. Yellin, *Steady pressure flow relations in compressed arteries: Possible origin of Korotkoff sounds*. *Medical and Biological Engineering and Computing*, 1980. **18**(4): p. 419-426.
75. Spitzer, V.M. and D.G. Whitlock, *The visible human dataset: The anatomical platform for human simulation*. *The Anatomical Record*, 1998. **253**(2): p. 49-57.
76. Ansari, M.Z., L. Sang-kyo, and C. Chongdu, *Hyperelastic Muscle Simulation*. *Key Engineering Materials*, 2007. **345-346**: p. 1241-1244.
77. Cristalli, C. and M. Ursino, *Influence of arm soft tissue on non-invasive blood pressure measurements: An experimental and mathematical study*. *Measurement*, 1995. **14**: p. 229-240.
78. Martin R.B., Burr D.B., and Sharkey N.A., *Skeletal Tissue Mechanics*. Vol. 33. 1998, New York: Springer. 392.
79. *Panvascular Medicine: Integrated Clinical Management*, ed. P.T. Lanzer, Eric J. . 2002: Springer.
80. Bank, A.J., et al., *Contribution of Collagen, Elastin, and Smooth Muscle to In Vivo Human Brachial Artery Wall Stress and Elastic Modulus Circulation*, 1996. **94**(3263-3270).


81. Bank, A.J., et al., *In Vivo Human Brachial Artery Elastic Mechanics Effects of Smooth Muscle Relaxation*. Circulation, 1999. **100**: p. 41-47.
82. Bank, A.J., et al., *Direct effects of smooth muscle relaxation and contraction on in vivo human brachial artery elastic properties*. Circ Res., 1995 **77**(5): p. 1008-16.
83. Carew, T.E., R. Vaishnav, and D.J. Patel, *Compressibility of the Arterial Wall*. Circ. Res., 1968. **23**: p. 61-68.
84. Wilmer W. Nichols, M.F.O.R., *McDonald's blood flow in arteries :theoretic, experimental, and clinical principles*. 2005, London :New York :: Hodder Arnold ;Distributed in the U.S.A. by Oxford University Press,.
85. Dorland, W.A.N., *Dorland's illustrated medical dictionary* 30th ed. ed. 2003, London Saunders.
86. Netter, F., *Interactive Atlas of Human Anatomy 3.0*. 2002.
87. Zannoli, R., I. Corazza, and A. Branzi, *Mechanical simulator of the cardiovascular system*. Physica Medica, 2009. **25**(2): p. 94-100.
88. Fung, Y.C., *Biomechanics: Circulation*. 1996, New York: Springer-Verlag.
89. Lopez, H. and K.M. Harris, *Ultrasound interactions with free silicone in a tissue-mimicking phantom*. J Ultrasound Med, 1998. **17**(3): p. 163-170.
90. Ng, Y.-k. and S.-y. Mak, *Measurement of the speed of sound in water*. Journal of Physics Education, 2001. **1**: p. 65.
91. Bassez, S., P. Flaud, and M. Chauveau, *Modeling of the deformation of flexible tubes using a single law: application to veins of the lower limb in man*. Journal of Biomechanical Engineering, 2001. **123**: p. 58-65.

APPENDIX

| | |
|--------------|------------------|
| APPENDIX I | Material data |
| APPENDIX II | ABAQUS codes |
| APPENDIX III | Matlab codes |
| APPENDIX IV | Ethical approval |

APPENDIX I

A- DATA SHEET OF RHODORSIL RTV 3428

| S I L I C O N E S | | | | | | | | | | | | | | | | | |
|---|--|---|--|----------------------|----------------------|---------------------|----------------|----------------|-------------|-------------|--------------------------|---------------------------------------|-----|-----|---------------------------------------|--------|------|
| RHODORSIL[®] RTV 3428 A and B | | | | | | | | | | | | | | | | | |
| August 2002 | | TECHNICAL DATA SHEET Cancels and replaces SIL 99 060 3 | | | | | | | | | | | | | | | |
| Description | <p>RHODORSIL RTV 3428 A and B is a two-component silicone elastomer which crosslinks at room temperature by a polyaddition reaction. This reaction can be accelerated by heat.</p> <p>RHODORSIL RTV 3428 A and B is a viscous liquid which, after curing, becomes a strong elastic material.</p> | | | | | | | | | | | | | | | | |
| Advantages | <ul style="list-style-type: none"> PART B : different colours available (see characteristics) EASE OF PROCESSING since components A and B to be mixed (100 parts and 10 parts) are both free-flowing. EASY CURING : RHODORSIL RTV 3428 A and B crosslinks at temperatures above 20°C even in the complete absence of air or humidity. Consequently, neither the thickness of the part nor the degree of confinement affect the rate and uniformity with which the elastomer crosslinks. The reaction can be accelerated by heating to 150°C. HIGH TEAR STRENGTH, compared to conventional RHODORSIL RTV. LOW SHRINKAGE when crosslinked at normal temperatures. GOOD TEMPERATURE RESISTANCE : it can be used for very long periods up to 150°C and for short periods up to 180°C. | | | | | | | | | | | | | | | | |
| Applications | <ul style="list-style-type: none"> Production of flexible moulds to be kept for long periods or where particularly accurate reproduction is required (ceramics, figurines, modelmakers, etc.) Production of thermal expansion formers for composite materials (the aeronautic industry, boat-building, etc.). | | | | | | | | | | | | | | | | |
| Characteristics | <p>1. Components of RHODORSIL RTV 3428 A and B</p> <table border="1"> <thead> <tr> <th></th> <th>RHODORSIL RTV 3428 A</th> <th>RHODORSIL RTV 3428 B</th> </tr> </thead> <tbody> <tr> <td>Appearance (1).....</td> <td>viscous liquid</td> <td>Viscous liquid</td> </tr> <tr> <td>Colour.....</td> <td>translucent</td> <td>pink , white, trans. (2)</td> </tr> <tr> <td>Specific gravity at 23°C, approx.....</td> <td>1.1</td> <td>1.1</td> </tr> <tr> <td>Viscosity at 23°C, mPa.s, approx.....</td> <td>25 000</td> <td>1000</td> </tr> </tbody> </table> <p>(1) Part A can become slightly thixotropic ; this is quickly corrected by agitation. (2) RHODORSIL RTV 3428 B is available in pink, translucent or white colours.</p> | | | RHODORSIL RTV 3428 A | RHODORSIL RTV 3428 B | Appearance (1)..... | viscous liquid | Viscous liquid | Colour..... | translucent | pink , white, trans. (2) | Specific gravity at 23°C, approx..... | 1.1 | 1.1 | Viscosity at 23°C, mPa.s, approx..... | 25 000 | 1000 |
| | RHODORSIL RTV 3428 A | RHODORSIL RTV 3428 B | | | | | | | | | | | | | | | |
| Appearance (1)..... | viscous liquid | Viscous liquid | | | | | | | | | | | | | | | |
| Colour..... | translucent | pink , white, trans. (2) | | | | | | | | | | | | | | | |
| Specific gravity at 23°C, approx..... | 1.1 | 1.1 | | | | | | | | | | | | | | | |
| Viscosity at 23°C, mPa.s, approx..... | 25 000 | 1000 | | | | | | | | | | | | | | | |
|  | | | | | | | | | | | | | | | | | |

Characteristics (cont'd)**2. Mixing of the two components****RHODORSIL RTV 3428 A** 100 parts**RHODORSIL RTV 3428 B** 10 parts

Pot life of catalyzed mixture at 23°C, h, approx. 1

Time after which article can be handled
(or removed from mould), at 23°C, h, approx. 16**3. Polymerized product****3.1 Crosslinked properties**

Measured taken after 24 hours polymerization at 23°C

3.1.1. On a 6-mm thick pieceShore A hardness, approx. 28
(ASTM D2240 standard)**3.1.2. On a 2-mm thick film**Secant modulus at 100% elongation, MPa, approx. 1.2
(AFNOR NFT 46 002)Tensile strength, MPa, approx. 7.5
(AFNOR NF T 46002 - H₂ specimen)Ultimate elongation, %, approx. 600
(AFNOR NF T 46002 standard, H₂ specimen)Tear strength, kN/m, approx. 20
(ASTL D 624, notched A specimen)**3.2 Physical properties**Linear shrinkage, %, approx. 0.1
(polymerized at 23°C)Volume expansion coefficient, K⁻¹, approx. 9×10^{-4}

Thermal conductivity, W.(m.K) approx. 0.23

Brittle temperature, °C, approx. - 70
(ASTM D 746)

Peak heat stability, °C, approx. + 180

***Note** : Crosslinking by heating does not affect the properties of **RHODORSIL RTV 3428 A and B**. However, dimensional changes do occur during of the elastomer and must be allowed for.

Processing**Re-mixing of the two components (parts A and B) before each use****1. Mixing the two components**Add 10 parts of **RHODORSIL RTV 3428 B** to 100 parts of **RHODORSIL RTV 3428 A**.

The two components may be intimately mixed either by hand or using a low-speed electric or pneumatic mixer to minimize the introduction of air into the mixture.

Note : it is also to use a special metering-mixing machine for two-component elastomers. Please consult us.

Processing (cont)

The viscosity of **RHODORSIL RTV 3428 A and B** can be reduced using RHODORSIL THINNER FOR RTV 2030, add 5 to 10% of the quantity of **RHODORSIL RTV 3428 A**. This will make no significant change to the mechanical properties after polymerization. Up to 40% of RHODORSIL THINNER FOR RTV 2030 can be added without causing exudation.

2. Degassing

The mixture of parts A and B should preferably be degassed to eliminate any air. If a special machine is used, the two components are degassed separately and no air is introduced.

Degas RTV 3428 under a 30 to 50 mbar vacuum.

When the vacuum is applied, the product expands to 4 to 5 times its initial volume and bubbles form at the surface. These progressively disappear and the mixture returns to its initial volume. Wait a few minutes to ensure complete degassing and then release the vacuum : the product is ready for use.

For example, to degas 5 kg of **RHODORSIL RTV 3428 A and B**, apply the vacuum for roughly 10 minutes : releasing the vacuum once or twice during the operation facilitates and improves degassing.

A container with a high diameter/height ratio will accelerate degassing.

3. Pouring

The product can be poured by gravity or under pressure. **RHODORSIL RTV 3428 A and B** is easier to use than normal RTV because the viscosity of the two components increases only relatively slowly.

4. Crosslinking

RHODORSIL RTV 3428 A and B crosslinks in approx 24 hours at 23°C, regardless of the thickness of the mould.

At temperature below 23°C, polymerization is much slower ; for example, 36 hours may be necessary at 20°C. Conversely, heating accelerates polymerization.

Recommended curing temperatures :

| | |
|------------------------|----------------------------|
| 2 hours at 60°C | these periods start at the |
| or 30 minutes at 100°C | time the RTV reaches the |
| or 15 minutes at 150°C | temperature required |

Notes :

Contacts with certain materials can inhibit crosslinking in this RTV :

- Natural rubbers vulcanized with sulphur,
- RTV elastomers catalyzed with metal salts,
- PVC stabilizing agents,
- Epoxy catalysts

*If doubts exist, it is advisable to do a test by pouring the mixture of the two components onto a limited area of the item. In addition, it is advisable to only use the degassing equipment for this type of RTV since the chamber can be contaminated when other products are degassed in it and thus inhibit crosslinking in **RHODORSIL RTV 3428 A and B**.*

Processing
(con't)

When making a moulding, the pattern must frequently be prepared to prevent the RTV adhering : apply a very fine film (with a spraygun or brush) of a carefully-selected mould-release agent (petrolatum, cellulose vamish or white soap). This release agent can reduce the inhibiting effect of the pattern.

Ensure that the packaging is hermetically sealed again each time it is used.

Packaging

RHODORSIL RTV 3428 A and B is delivered in kits of :

- 1 kg A + 0.100 kg B
- 5 kg A + 0.500 kg B

RHODORSIL RTV 3428 A is also available in 25 and 200 kg drums accompanied by the corresponding 2.5 and 20 kg of **RHODORSIL RTV 3428 B**.

Storage and shelf life

When stored in its original unopened packaging, at a temperature of between - 5°C and + 30°C, **RHODORSIL RTV 3428 A and B** may be stored for up to 20 months, from the date of manufacture marked clearly on the packaging.

Beyond this date, Rhodia Silicones no longer guarantees that the product meets sales specifications.

Safety

Consult the SAFETY DATA SHEET for **RHODORSIL RTV 3428 A and B**.

Warning to users

The information contained in this document is given in good faith based on our current knowledge. It is only an indication and is in no way binding, particularly as regards infringement of or prejudice to third party rights through the use of our products.

RHODIA SILICONES GUARANTEES THAT ITS PRODUCTS COMPLY WITH ITS SALES SPECIFICATIONS.

This information must on no account be used as a substitute for necessary prior tests which alone can ensure that a product is suitable for a given use.

Users are responsible for ensuring compliance with local legislation and for obtaining the necessary certifications and authorisations.

Users are requested to check that they are in possession of the latest version of this document and **RHODIA SILICONES** is at their disposal to supply any additional information.

**Silicones Europe**

55, avenue des Frères Perret - BP 60 - F-69192 SAINT-FONS CEDEX

Tél. (33) 4 72 73 66 26 - Fax (33) 4 72 73 66 28

Rhodia Chimie - Société Anonyme au capital de 2 883 675 200 F - RCS Nanterre B 642 014 526

| | | | |
|-----|----|-----|---|
| SIL | 02 | 120 | 3 |
|-----|----|-----|---|

B- DATA SHEET OF PROSKIN



ProSkin

PROSTHETIC SKIN SAFE SILICONE

RTV-2 SILICONE RUBBER

PRODUCT DESCRIPTION

ProSkin is a two-component silicone elastomer that cures at room temperature by a polyaddition reaction that may be accelerated by heating. It is designed as a 12 Shore A high tear strength rubber providing excellent physical properties for prosthetic and orthopaedic applications. It also displays good translucency and high elongation. ProSkin is easy to process with a 100:100 ratio by weight or volume and has an extremely low viscosity when mixed.

TYPICAL PRODUCT USES

Orthopaedic applications
Prosthetics devices & appliances
Anywhere a soft skin like feel is required
SFX Skins
Cushioning applications

TYPICAL CATALYSED PROPERTIES

Mixed @ 23°C and 50% RH.

| | |
|------------------------|------------|
| Mix Ratio A:B: | 100:100 |
| Mixed Viscosity mPa s: | 2500 |
| Potlife Life: | 60 minutes |
| Cure/Demould Time: | Variable |

TYPICAL CURED PROPERTIES

| | |
|--|-------------|
| Colour: | Translucent |
| Specific Gravity: | 1.08 |
| Hardness (Shore A): | 12 |
| (Shore 00): | 60 |
| Tensile Strength (N/mm ²): | 3.7 |
| Elongation (%): | 700 |
| Tear Strength (N/mm): | 15 |

Head Office
6 Portacella Road
Bankstown NSW 2200
Australia
T: (612) 9793 7555
F: (612) 9793 7091

Retail Showroom
53 King Street
Newtown NSW 2042
Australia
T: (612) 9557 9058
F: (612) 9557 9246

info@barnes.com.au
www.barnes.com.au

The following studies were performed in order to determine the biocompatibility of the test item to ISO 10993-1:

CYTOTOXICITY

SKIN SENSITISATION

INTRACUTANEOUS IRRITATION

The product did not show any adverse effects in the studies performed.

Issue: 1

Date: 21st July 2006

The data presented in this bulletin are in accordance with the present state of our knowledge, and does not absolve the user from carefully checking all supplies immediately on receipt. We reserve the right to alter product constants within the scope of technical progress or new developments. The recommendations made in this leaflet should be checked by preliminary trials because of conditions during processing over which we have no control, especially where other companies' raw materials are also being used. Recommendations for use do not constitute a warranty, either expressed or implied, of the fitness or suitability of the product for a particular purpose.

C- DATA SHEET OF PIEZOELECTRIC SENSOR

Table 1. Typical properties of piezo film

| Symbol | Parameter | | PVDF | Copolymer | Units |
|--------------------|-----------------------------------|------------------------|-------------------|-------------------|---|
| t | Thickness | | 9, 28, 52, 110 | <1 to 1200 | μm (micron, 10 ⁻⁶) |
| d ₃₁ | Piezo Strain Constant | | 23 | 11 | 10 ⁻¹² $\frac{\text{m/m}}{\text{V/m}}$ <i>or</i> $\frac{\text{C/m}^2}{\text{N/m}^2}$ |
| d ₃₃ | | | -33 | -38 | |
| g ₃₁ | Piezo Stress constant | | 216 | 162 | 10 ⁻³ $\frac{\text{V/m}}{\text{N/m}^2}$ <i>or</i> $\frac{\text{m/m}}{\text{C/m}^2}$ |
| g ₃₃ | | | -330 | -542 | |
| k ₃₁ | Electromechanical Coupling Factor | | 12% | 20% | |
| k _t | | | 14% | 25-29% | |
| C | Capacitance | | 380 for 28μm | 68 for 100μm | pF/cm ² @ 1KHz |
| Y | Young's Modulus | | 2-4 | 3-5 | 10 ⁹ N/m ² |
| V ₀ | Speed of Sound | stretch: thickness: | 1.5 2.2 | 2.3 2.4 | 10 ³ m/s |
| p | Pyroelectric Coefficient | | 30 | 40 | 10 ⁻⁶ C/m ² °K |
| ε | Permittivity | | 106-113 | 65-75 | 10 ⁻¹² F/m |
| ε/ε ₀ | Relative Permittivity | | 12-13 | 7-8 | |
| ρ _m | Mass Density | | 1.78 | 1.82 | 10 ³ kg/m |
| ρ _e | Volume Resistivity | | >10 ¹³ | >10 ¹⁴ | Ohm meters |
| R _□ | Surface Metallization Resistivity | | <3.0 | <3.0 | Ohms/square for NiAl |
| R _□ | | | 0.1 | 0.1 | Ohms/square for Ag Ink |
| tan δ _e | Loss Tangent | | 0.02 | 0.015 | @ 1KHz |
| | Yield Strength | | 45-55 | 20-30 | 10 ⁶ N/m ² (stretch axis) |
| | Temperature Range | | -40 to 80...100 | -40 to 115...145 | °C |
| | Water Absorption | | <0.02 | <0.02 | % H ₂ O |
| | Maximum Operating Voltage | | 750 (30) | 750 (30) | V/mil(V/μm), DC, @ 25°C |
| | Breakdown Voltage | | 2000 (80) | 2000 (80) | V/mil(V/μm), DC, @ 25°C |

FDT Series Elements with Lead Attachment

Piezo Film Technology
Flexible Leads
High Strain Output
Film Thickness Options
Lamination Options
Solderable Connection Pins

The “F” in FDT Series stands for “Flexible Leads.” These are rectangle elements of Piezo film with silver ink screen printed electrodes. Rather than making the lead attachment near the sensor, the Piezo polymer tail extends from the active sensor area as flex circuit material with offset traces. This gives a very flat, flexible lead with a connector at the end.

The FDT elements are available in a variety of different sizes and thicknesses. They are available without a laminate (FDT), with a laminated (0.005” mylar) on ones side (FLDT) or with tape release layer adhesive (FDT with adh) in the sensor area.



FEATURES

- Thin piezo film sensor
- Flexible leads give flat profile to the sensor
- Dynamic strain sensing with a high output
- Typical interface to a 1 or 10 M Ω input impedance
- Output Voltage dependant on Force applied 10 mV to 100V

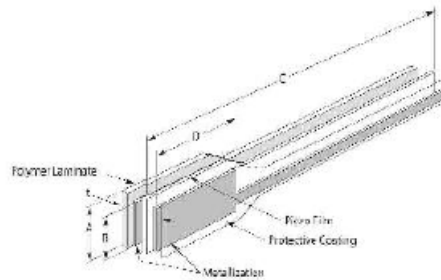
APPLICATIONS

- Sensing Direct Contact Force
- Recording Time of an Event
- Counting Number of Impact Events
- Measuring Impact Related Events
- Sensing Vibration using Cantilevered Beam
- Wakeup Switch
- Motion Detection

FDT Series Elements with Lead Attachment



dimensions



DIMENSION in INCHES (mm)

| Model Number | Part Number | Film thickness | A Film | B Electrode | C Film | D Electrode | t (μ m) | Cap (nF) |
|-----------------------|-------------|----------------|--------------|----------------|---------------|----------------|-----------------|-------------|
| FDT1-028K | 1-1002785-1 | 28 μ m | .620 (16) | .485 (12) | 9.25 [235] | 1.16 (30) | 55 | 1.37 |
| FDT1-052K | 2-1002785-1 | 52 μ m | .620 (16) | .485 (12) | 9.25 [235] | 1.16 (30) | 85 | .740 |
| FLDT1-028K | 1-1002786-1 | 28 μ m | .620 (16) | .485 (12) | 9.25 [235] | 1.16 (30) | 205 | 1.37 |
| FLDT1-052K | 2-1002786-1 | 52 μ m | .620 (16) | .485 (12) | 9.25 [235] | 1.16 (30) | 230 | .740 |
| FLDT1-028K w/adh-F | 1001777 | 28 μ m | .650 (17) | .485 (12) | 5.51 [140] | 1.18 (30) | 125 | 1.37 |

The connector pins on the FDT sensors can be directly soldered to a PCB with a reasonable level of care. This component cannot withstand high temperatures (>80°C) and therefore soldering of the pins to a PCB must be done quickly. A heat sink clamped to the interface area between the film and the crimps will take the heat away from the film. Pre-tin the pins and then quickly solder them to the board. Do not allow the soldering iron to touch the film and do not use a dwell time of over 5 seconds on the pins. Low temperature solder can also be used.

The information in this sheet has been carefully reviewed and is believed to be accurate; however, no responsibility is assumed for inaccuracies. Furthermore, this information does not convey to the purchaser of such devices any license under the patent rights to the manufacturer. Measurement Specialties, Inc. reserves the right to make changes without further notice to any product herein. Measurement Specialties, Inc. makes no warranty, representation or guarantee regarding the suitability of its product for any particular purpose, nor does Measurement Specialties, Inc. assume any liability arising out of the application or use of any product or circuit and specifically disclaims any and all liability, including without limitation consequential or incidental damages. Typical parameters can and do vary in different applications. All operating parameters must be validated for each customer application by customer's technical experts. Measurement Specialties, Inc. does not convey any license under its patent rights nor the rights of others.

ordering information

North America

Measurement Specialties, Inc.
1000 Lucas Way
Hampton, VA 23666
Sales and Customer Service
Tel: +1-800-745-8008 or
+1-757-766-1500
Fax: +1-757-766-4297
Technical Support
Email: piezo@meas-spec.com

Europe

MEAS Deutschland GmbH
Hauert 13
44227 Dortmund
Germany
Sales and Customer Service
Tel: +49 (0)231 9740 21
Technical Support
Tel: +49 (0)8074 862822
Email: piezo@meas-spec.com

Asia

Measurement Specialties (China), Ltd.
No. 26 Langshan Road
Shenzhen High-Tech Park (North)
Nanshan District
Shenzhen, China 518107
Sales and Customer Service
Tel: +86 755 3330 5088
Technical Support
Email: piezo@meas-spec.com

APPENDIX II

```

*Heading
** Job name: long-nolinear-BP80-CP200-st Model name: long-
nonlinear-cir
*Preprint, echo=NO, model=NO, history=NO, contact=NO
**
** PARTS
**
*Part, name=PART-1-1
*Node
1,          54.,          0.,          70.
.
.
.

*Element, type=C3D8R
1,  267,  4152, 23884,  3284,    1,   61,  2230,   156
.
.
.

*Element, type=C3D6
38341, 11539, 11393, 11432, 57019, 56873, 56912
.
.
.

*Element, type=C3D8RH
94289,   41,   1825,  21659,  1624,   1969,  22434, 103165,
.
.
.

*Nset, nset=_PICKEDSET6, internal
1,    2,    3,    4,    5,    6,    7,    8,
.
.
.

*Elset, elset=_PICKEDSET6, internal, generate
1,  94288,    1
.
.
.

*Nset, nset=_PICKEDSET7, internal
37,   38,   39,   40,   41,   42,   43,   44,
.
.
.

```

```

*Elset, elset=_PICKEDSET7, internal, generate
  94289,  97696,      1
.
.
.
** Region: (Section-1-_PICKEDSET6:Picked)
*Elset, elset=_I1, internal, generate
  1,  94288,      1
.
.
.

** Section: Section-1-_PICKEDSET6
*Solid Section, elset=_I1, material=PROSKIN
1.,
.
.
.

** Region: (Section-2-_PICKEDSET7:Picked)
*Elset, elset=_I2, internal, generate
  94289,  97696,      1
.
.
.

** Section: Section-2-_PICKEDSET7
*Solid Section, elset=_I2, material=NONLINEAR-EQUATION
1.,
*End Part
**
**
** ASSEMBLY
**
*Assembly, name=Assembly
**
*Instance, name=PART-1-1, part=PART-1-1
*End Instance
**
*Nset, nset=_PICKEDSET6, internal, instance=PART-1-1
5,      6,      7,      8,      11,      12,      13,      14,      17,      23,
.
.
.
*Elset, elset=_PICKEDSET6, internal, instance=PART-1-1
8065,  8066,  8067,  8068,  8069,  8070,  8071,  8072,  8073,
.

```

```

.
.
*Nset, nset=_PICKEDSET46, internal, instance=PART-1-1
3,    4,    10,    13,    14,    15,    16,    17,    18,    24,
.
.
.
*Elset, elset=_PICKEDSET46, internal, instance=PART-1-1
559,  560,  561,  562,  563,  564,  565,  566,  567,
.
.
.
*Elset, elset=__PICKEDSURF4_S2, internal, instance=PART-1-1
94523, 94524, 94525, 94526, 94527, 94528, 94529, 94530, 94531,
.
.
.
*Elset, elset=__PICKEDSURF23_S5, internal, instance=PART-1-1
65332, 65333, 65335, 65339, 65340, 65342, 65346, 65348, 65360,
.
.
.
*Elset, elset=__PICKEDSURF23_S3, internal, instance=PART-1-1
65344, 65357, 65359, 65367, 65397, 65400, 65679, 65692, 65694,
.
.
.
*Elset, elset=__PICKEDSURF23_S6, internal, instance=PART-1-1
65354, 65689, 66024, 66359, 66694, 67029, 67364, 67699, 68034,
.
.
.
*Elset, elset=__PICKEDSURF23_S4, internal, instance=PART-1-1,
generate
76225, 86982,    347
.
.
.
*Elset, elset=__PICKEDSURF23_S2, internal, instance=PART-1-1
1,    2,    3,    4,    5,    6,    7,    8,    9,    10,    11,
.
.

```

```

.

*Elset, elset=__PICKEDSURF4_S2, internal, instance=PART-1-1
  94523, 94524, 94525, 94526, 94527, 94528, 94529, 94530, 94531,
.
.
.

*Surface, type=ELEMENT, name=_PICKEDSURF4, internal
__PICKEDSURF4_S2, S2
*Elset, elset=__PICKEDSURF23_S5, internal, instance=PART-1-1
  65332, 65333, 65335, 65339, 65340, 65342, 65346, 65348, 65360,
.
.
.

*Elset, elset=__PICKEDSURF23_S6, internal, instance=PART-1-1
  65354, 65689, 66024, 66359, 66694, 67029, 67364, 67699, 68034,
.
.
.

*Elset, elset=__PICKEDSURF23_S4, internal, instance=PART-1-1,
generate
  76225, 86982, 347
.
.
.

*Elset, elset=__PICKEDSURF23_S2, internal, instance=PART-1-1
  1, 2, 3, 4, 5, 6, 7, 8, 9, 10, 11,
.
.
.

*Surface, type=ELEMENT, name=_PICKEDSURF23, internal
__PICKEDSURF23_S5, S5
.
.
.

*Elset, elset=__PickedSurf16_S2, internal, instance=PART-1-1
  94523, 94524, 94525, 94526, 94527, 94528, 94529, 94530, 94531,
.
.
.

*Surface, type=ELEMENT, name=_PickedSurf16, internal
__PickedSurf16_S2, S2

```

```

*End Assembly
*Amplitude, name=BP, time=TOTAL TIME
0., 0., 0.8, 80., 3., 80.
*Amplitude, name=CP, time=TOTAL TIME
0., 0., 0.8, 0., 3., 220.
**
** MATERIALS
**
*Material, name=MUSCLE
*Density
1.05e-09,
*Elastic
0.04, 0.499
*Material, name=NONLINEAR-EQUATION
*Density
1.05e-09,
*Hyperelastic, neo hooke, test data input, poisson=0.499
*Uniaxial Test Data
0.00032054, 0.01
0.000682848, 0.02
0.00108824, 0.03
0.00153841, 0.04
.
.
.
*Material, name=PROSKIN
*Density
1.05e-09,
*Elastic
0.03, 0.45
** INTERACTION PROPERTIES
**
*Surface Interaction, name=IntProp-1
1.,
*Friction
0.,
**
** BOUNDARY CONDITIONS
**
** Name: Disp-BC-1 Type: Symmetry/Antisymmetry/Enastre
*Boundary
_PICKEDSET46, ZSYMM
** Name: Disp-BC-2 Type: Symmetry/Antisymmetry/Enastre
*Boundary
_PICKEDSET6, ENCASTRE
**
** INTERACTIONS
**

```

```

** Interaction: Int-1
*Contact Pair, interaction=IntProp-1, type=SURFACE TO SURFACE
_PickedSurf16,
**
** STEP: bp
**
*Step, name=bp, nlgeom=YES
*Static
0.8, 0.8, 8e-06, 0.8
**
** LOADS
**
** Name: SURFFORCE-1    Type: Pressure
*Dload, amplitude=BP
_PICKEDSURF4, P, 0.000133322
** Name: SURFFORCE-2    Type: Pressure
*Dload, amplitude=CP
_PICKEDSURF23, P, 0.000133322
**
** OUTPUT REQUESTS
**
*Restart, write, frequency=0
**
** FIELD OUTPUT: F-Output-1
**
*Output, field, variable=PRESELECT, time interval=0.1, time
marks=NO
**
** HISTORY OUTPUT: H-Output-1
**
*Output, history
*Energy Output
ALLAE,
*End Step
**
** STEP: Step-1
**
*Step, name=Step-1, nlgeom=YES, inc=1000000
*Static
0.02, 2., 2e-05, 0.02
**
** OUTPUT REQUESTS
**
*Restart, write, number interval=1, time marks=NO
**
** FIELD OUTPUT: F-Output-1
**

```



```
*Output, field, variable=PRESELECT, time interval=0.02, time
marks=NO
**
** HISTORY OUTPUT: H-Output-1
**
*Output, history
*Energy Output
ALLAE,
*End Step
```

APPENDIX III

```

clc
clear all
format long
cuff=xlsread('M:\bp-large-3.xlsx'); % read excel file
biceps=cuff(100:(length(cuff)-1000),2); % input 1,2,3,4 are
artery,biceps,triceps,CP
triceps=cuff(100:(length(cuff)-1000),3);
artery=cuff(100:(length(cuff)-1000),1);
CP=cuff(100:(length(cuff)-1000),4);
[b1,a1]=butter(5,[5]/500); % low pass filter: 20 Hz
CPphg=(filtfilt(b1,a1,CP)*72.2+0.7274);
CPhgx=CPphg(1:5:end);
CPP=CPphg(1:5:end);
ttt=(1:5:length(CPphg))/1000;
ttt=ttt';
[b1,a1]=butter(5,0.5/500); % sample frequency 1000, low pass
filter 0.5Hz
CPllp=filtfilt(b1,a1,CP); % CP without oscillation
x=find(CPllp(:,1)==max(CPllp(:,1))+1000); % find the pump stop point
dCPllp=diff(CPllp); % find maximum CP change point (valve or motor
action)
y=find(dCPllp(:,1)==min(dCPllp(:,1))-1000); % find the measurement
stop point
CPhg=CPllp(x:y)*72.2+0.7274; % convert to mmHg
t=[x:y]*0.001;
t=t';

bicepschop=biceps(x:y)/(max(biceps(x:y))-min(biceps(x:y)));
tricepschop=triceps(x:y)/(max(triceps(x:y))-min(triceps(x:y)));
arterychop=artery(x:y)/(max(artery(x:y))-min(artery(x:y)));
CPchop=CP(x:y)/(max(CP(x:y))-min(CP(x:y))); % low pass
[b1,a1]=butter(5,[15]/500); % low pass filter: 15 Hz
bicepslp=filtfilt(b1,a1,bicepschop);
tricepslp=filtfilt(b1,a1,tricepschop); %filter signal
arterylp=filtfilt(b1,a1,arterychop);
CPlp=filtfilt(b1,a1,CPchop);
% high pass
[b,a]=butter(5,[0.5]/500,'high'); % filter
bicepsbp=filtfilt(b,a,bicepslp);
tricepsbp=filtfilt(b,a,tricepslp); % filter signal
arterybp=filtfilt(b,a,arterylp);
CPhp=filtfilt(b,a,CPchop); % band pass
bicepsbp=filtfilt(b,a,bicepslp);
bicepsbpb=(bicepsbp/(max(bicepsbp(2000:end))-min(bicepsbp(2000:end))));
% normalization for FFT analysis
tricepsbp=filtfilt(b,a,tricepslp);
tricepsbpb=(tricepsbp/(max(tricepsbp(2000:end))-
min(tricepsbp(2000:end))));
arterybpb=(arterybp/(max(arterybp(2000:end))-min(arterybp(2000:end))));
CPbp=filtfilt(b,a,CPlp);
CPbpb=(CPbp/(max(CPbp(1000:end))-min(CPbp(1000:end))));
tt=(1:length(CPphg))/1000;
tt=tttt(x:y)';

%%
figure(1)

```

```

plot(ttt, CPP, 'DisplayName', 'CPphg', 'YDataSource', 'CPphg');
figure(1)
hold off
[tt, CPc, CPh]=plotyy((1:length(CP)), CP, (1:length(CP)), CPphg);
set(CPc, 'displayname', 'CP')
set(CPh, 'displayname', 'CPtrend')
hold on;
plot(artery, '--b', 'LineWidth', 2.5, 'displayName', 'artery', 'YDataSource',
'artery');
plot(biceps, '-.r', 'LineWidth', 2.5, 'displayName', 'biceps')
plot(triceps, ':c', 'LineWidth', 2.5, 'displayName', 'triceps')
plot(CP, 'g', 'LineWidth', 2.5, 'displayName', 'CP')
scatter(x, CP(x)); scatter(y, CP(y))
legend('show')
hold off

%% fft
figure(2)
subplot(2,1,1)
[tt, CP1, CP2]=plotyy(t, CPbpp, t, CPhg);
set(CP1, 'displayname', 'CP-osc', 'LineWidth', 2.5, 'color', 'g');
set(CP2, 'displayname', 'CPtrend', 'LineWidth', 2.5, 'color', 'k');
hold on
plot(t, arterybpp, '--b', 'LineWidth', 2.5, 'DisplayName', 'artery',
'YDataSource', 'artery')
plot(t, bicepsbpp, '-.r', 'LineWidth', 2.5, 'DisplayName', 'biceps',
'YDataSource', 'biceps')
plot(t, tricepsbpp, ':c', 'LineWidth', 2.5, 'DisplayName', 'triceps',
'YDataSource', 'triceps')
legend('show')
grid on
hold off
xlabel('Time (s)')
ylabel('applitude (V)')
set(get(tt(2), 'Ylabel'), 'String', 'Cuff pressure (mmHg)')
Fs = 1000; % Sampling frequency
z=bicepsbp;
L = length(z); % Length of signal
NFFT = 2^nextpow2(L); % Next power of 2 from length of z
Z = fft(z, NFFT)/L;
bicepsfft=fft(bicepsbpp, NFFT)/L;
tricepsfft=fft(tricepsbpp, NFFT)/L;
arteryfft=fft(arterybpp, NFFT)/L;
CPfft=fft(CPbpp, NFFT)/L;
f = Fs/2*linspace(0,1,NFFT/2+1);
fftartery=2*abs(arteryfft(1:300));
fftbiceps=2*abs(bicepsfft(1:300));
ffttriceps=2*abs(tricepsfft(1:300));
fftCP=2*abs(CPfft(1:300));
% find the frequency of the max amplitude
mfartery=f(fftartery==max(fftartery));
mfbiceps=f(fftbiceps==max(fftbiceps));
mftriceps=f(ffttriceps==max(ffttriceps));
mfCP=f(fftCP==max(fftCP));
mf=[mfartery, mfbiceps, mftriceps, mfCP];
maxf=max(mf);
%%
subplot(2,1,2)
Bfft=2*abs(bicepsfft(1:300));
Afft=2*abs(arteryfft(1:300));
Cfft=2*abs(CPfft(1:300));

```

```

Tfft=2*abs(tricepsfft(1:300));
Ffft=f(1:300);
Ffft=Ffft';
hold off
plot(f(1:300),2*abs(bicepsfft(1:300)),'-
.r','LineWidth',2.5,'DisplayName','mbiceps','YDataSource','mbiceps')
hold on
plot(f(1:300),2*abs(tricepsfft(1:300)),':c','LineWidth',2.5,'DisplayNa
me','triceps','YDataSource','triceps')
plot(f(1:300),2*abs(arteryfft(1:300)),'--
b','LineWidth',2.5,'DisplayName','artery','YDataSource','artery')
plot(f(1:300),2*abs(CPfft(1:300)),'g','LineWidth',2.5,'DisplayName',
'CP','YDataSource','CP')
legend('show')
hold off
grid on
legend show
title('FFT')
xlabel('Frequency (Hz)')
ylabel('|Y(f)|')

%%
figure(3)
subplot(4,1,1)
plot(t,arterybp,'--b','LineWidth',2.5,'DisplayName','artery',
'YDataSource','artery')
legend('show')
grid on
subplot(4,1,2)
plot(t,bicepsbp,'-.r','LineWidth',2.5,'DisplayName','biceps',
'YDataSource','biceps')
legend('show')
grid on
subplot(4,1,3)
plot(t,tricepsbp,':c','LineWidth',2.5,'DisplayName','triceps',
'YDataSource','triceps')
legend('show')
grid on
subplot(4,1,4)
plotyy(t,CPbp,t,CPhg)
grid on
hold off

%%
[b1,a1]=butter(5,[mficeps+0.5]/500); %filter
bicepsid=filtfilt(b1,a1,bicepsbp);
bicepsiddiff=diff(bicepsid);
k=0;
n=0;
for i=2:length(bicepsiddiff)
    if bicepsiddiff(i)/bicepsiddiff(i-1)<0
        if bicepsiddiff(i)>bicepsiddiff(i-1)
            k=k+1;
            lidx(k)=i;
        else
            n=n+1;
            hidb(n)=i;
        end
    end
end
if length(hidb)<=length(lidx)

```

```

        n=length(hidb);
    else
        n=length(lidb);
    end
    for i=1:(n-1)
        minbi(i)=find(bicepsbp==min(bicepsbp(hidb(i):hidb(i+1)))));
    end
    for i=1:(n-1)
        maxbi(i)=find(bicepsbp==max(bicepsbp(lidb(i):lidb(i+1)))));
    end
    if maxbi(1)<minbi(1)
        maxbi=maxbi(2:end);
    end
    if length(maxbi)<length(minbi)
        minbi=minbi(1:(end-1));
    end
    % individual normalize
    for i=1:(length(maxbi)-1)
        bicepsn(minbi(i):maxbi(i))=(bicepsbp(minbi(i):maxbi(i))-
        bicepsbp(minbi(i)))/(bicepsbp(maxbi(i))-bicepsbp(minbi(i)));
        bicepsn(maxbi(i):minbi(i+1))=(bicepsbp(maxbi(i):minbi(i+1))-
        bicepsbp(minbi(i+1)))/(bicepsbp(maxbi(i))-bicepsbp(minbi(i+1)));
    end
    %%
    [b1,a1]=butter(5,[mftriceps+0.5]/500); %filter
    tricepsid=filtfilt(b1,a1,tricepsbp);
    tricepsiddiff=diff(tricepsid);
    k=0;
    n=0;
    for i=2:length(tricepsiddiff)
        if tricepsiddiff(i)/tricepsiddiff(i-1)<0
            if tricepsiddiff(i)>tricepsiddiff(i-1)
                k=k+1;
                tricepsidl(k)=i;
            else
                n=n+1;
                tricepsidh(n)=i;
            end
        end
    end
    if length(tricepsidh)<=length(tricepsidl)
        n=length(tricepsidh);
    else
        n=length(tricepsidl);
    end
    for i=1:(n-1)

        mintri(i)=find(tricepsbp==min(tricepsbp(tricepsidh(i):tricepsidh(i+1))
        ));
    end
    for i=1:(n-1)

        maxtri(i)=find(tricepsbp==max(tricepsbp(tricepsidl(i):tricepsidl(i+1))
        ));
    end
    if maxtri(1)<mintri(1)
        maxtri=maxtri(2:end);
    end
    if length(maxtri)<length(mintri)
        mintri=mintri(1:(end-1));
    end
end

```

```

% individual normalize
for i=1:(length(maxtri)-1)
    tricepsn(mintri(i):maxtri(i))=(tricepsbp(mintri(i):maxtri(i))-
    tricepsbp(mintri(i)))/(tricepsbp(maxtri(i))-tricepsbp(mintri(i)));
    tricepsn(maxtri(i):mintri(i+1))=(tricepsbp(maxtri(i):mintri(i+1))-
    tricepsbp(mintri(i+1)))/(tricepsbp(maxtri(i))-tricepsbp(mintri(i+1)));
end
%
[b1,a1]=butter(1,[mfartery+0.5]/500); %filter
arteryid=filtfilt(b1,a1,arterybp);
arteryiddiff=diff(arteryid);
%
k=0;
n=0;
for i=2:length(arteryiddiff)
    if arteryiddiff(i)/arteryiddiff(i-1)<0
        if arteryiddiff(i)>arteryiddiff(i-1)
            k=k+1;
            larteryid(k)=i;
        else
            n=n+1;
            harteryid(n)=i;
        end
    end
end
if length(harteryid)<=length(larteryid)
    n=length(harteryid);
else
    n=length(larteryid);
end
for i=1:(n-1)

minart(i)=find(arterybp==min(arterybp(harteryid(i):harteryid(i+1))));
end
for i=1:(n-1)

maxart(i)=find(arterybp==max(arterybp(larteryid(i):larteryid(i+1))));
end
if maxart(1)<minart(1)
    maxart=maxart(2:end);
end
if length(maxart)<length(minart)
    minart=minart(1:(end-1));
end
% individual normalize
for i=1:(length(maxart)-1)
    arteryyn(minart(i):maxart(i))=(arterybp(minart(i):maxart(i))-
    arterybp(minart(i)))/(arterybp(maxart(i))-arterybp(minart(i)));
    arteryyn(maxart(i):minart(i+1))=(arterybp(maxart(i):minart(i+1))-
    arterybp(minart(i+1)))/(arterybp(maxart(i))-arterybp(minart(i+1)));
end
%%
[b1,a1]=butter(5,[mfCP+0.5]/500); %filter
CPid=filtfilt(b1,a1,CPbp);
CPiddiff=diff(CPid);
%%
k=0;
n=0;
for i=2:length(CPiddiff)
    if CPiddiff(i)/CPiddiff(i-1)<0
        if CPiddiff(i)>CPiddiff(i-1)

```

```

        k=k+1;
        CPidl(k)=i;
    else
        n=n+1;
        CPidh(n)=i;
    end
end
end
if length(CPidh)<=length(CPidl)
    n=length(CPidh);
else
    n=length(CPidl);
end
for i=1:(n-1)
    miCPn(i)=find(CPbp==min(CPbp(CPidh(i):CPidh(i+1))));
end
for i=1:(n-1)
    maxCP(i)=find(CPbp==max(CPbp(CPidl(i):CPidl(i+1))));
end
if maxCP(1)<miCPn(1)
    maxCP=maxCP(2:end);
end
if length(maxCP)<length(miCPn)
    miCPn=miCPn(1:(end-1));
end
% individual normalize
for i=1:(length(maxCP)-1)
    CPn(miCPn(i):maxCP(i))=(CPbp(miCPn(i):maxCP(i))-
    CPbp(miCPn(i)))/(CPbp(maxCP(i))-CPbp(miCPn(i)));
    CPn(maxCP(i):miCPn(i+1))=(CPbp(maxCP(i):miCPn(i+1))-
    CPbp(miCPn(i+1)))/(CPbp(maxCP(i))-CPbp(miCPn(i+1)));
end

%%
figure(4)
t=[1:length(arteryn)]*0.001;
hold off
plot(t,arteryn,'--b','LineWidth',2.5,'DisplayName','artery',
'YDataSource','artery')
hold on
t=[1:length(bicepsn)]*0.001;
plot(t,bicepsn,'-.r','LineWidth',2.5,'DisplayName','biceps',
'YDataSource','biceps')
t=[1:length(tricepsn)]*0.001;
plot(t,tricepsn,':c','LineWidth',2.5,'DisplayName','triceps',
'YDataSource','triceps')
t=[1:length(CPn)]*0.001;
plot(t,1-CPn,'g','LineWidth',2.5,'DisplayName','CP','YDataSource',
'CP')
ctricepsn=1-tricepsn;
t=[1:length(ctricepsn)]*0.001;
plot(t,ctricepsn,'k','LineWidth',2.5,'displayname','tricepsinv')

legend show
hold off
%%
peak=find(ffttriceps==max(ffttriceps));
CPofft=CPfft;%(1:(length(CPfft)/2));
for i=(peak-3):(peak+3)
    CPofft(i)=CPfft(peak+3);
    CPofft(i)=0;
end

```

```

end
for i=(length(CPofft)-peak-6):(length(CPofft)-peak+6)
    CPofft(i)=CPfft(peak+6);
    CPofft(i)=0;
end
for i=(2*peak-6):(2*peak+6);
    CPofft(i)=CPfft(2*peak+6);
    CPofft(i)=0;
end
for i=(length(CPofft)-2*peak-5):(length(CPofft)-2*peak+5);
    CPofft(i)=CPfft(peak+6);
    CPofft(i)=0;
end
CPo=ifft(CPofft);
magCPo=real(CPo);
%%
t=(CPhg(1)-CPhg(end))/(y-x)*((y-x):-1:0)+CPhg(end);
t=CPhg;
%%
load m:\matlab\identpolydata.mat % load experimental results and
transfer function Gart, Gbi, Gtri, Xart, Xbi, Xtri,
artcal=sim(Gart,CPbp); % artery sensor reading generated from CP
artmot=artbp-artcal;
bical=sim(Gbi,CPbp); % biceps sensor reading generated from CP
bimot=bicepsbp-bical;
trical=sim(Gtri,CPbp); % triceps sensor reading generated from CP
trimot=tricepsbp-trical;
CPart=CPbp-sim(Xart,(arterybp-sim(Gart,CPbp)));
CPbi=CPbp-sim(Xbi,(bicepsbp-sim(Gbi,CPbp)));
CPtri=CPbp-sim(Xart,(bicepsbp-sim(Gart,CPbp)));
%%
figure(11)
subplot(2,1,1)
hold off
plot(trical,'--b','LineWidth',2.5,'displayName','trical','YDataSource',
'trical');
hold on
plot(tricepsbp,'-
.r','LineWidth',2.5,'displayName','triceps','YDataSource','triceps');
plot(trimot,'k','LineWidth',1,'displayName','triceps-
trical','YDataSource','triceps');
legend('show')
% motion FFT analysis
NFFT = 2^nextpow2(L); % Next power of 2 from length of z
Z = fft(z,NFFT)/L;
trimotfft=fft(trimot(2000:end),NFFT)/L;
f = Fs/2*linspace(0,1,NFFT/2+1);
ffttrimot=2*abs(trimotfft(1:300));
subplot(2,1,2)
hold off
plot(f(1:150),ffttrimot(1:150),'-.r','LineWidth',2.5,'DisplayName',
'trimotion','YDataSource','trimotion')
legend('show')
%%
figure(12)
subplot(2,1,1)
hold off
plot(bical,'--b','LineWidth',2.5,'displayName','bical','YDataSource',
'bical');
hold on

```



```

plot(bicepsbp, '-
.r', 'LineWidth', 2.5, 'displayName', 'biceps', 'YDataSource', 'biceps');
plot(bimot, 'k', 'LineWidth', 1, 'displayName', 'biceps-
bical', 'YDataSource', 'biceps');
legend('show')
% motion FFT analysis
NFFT = 2^nextpow2(L); % Next power of 2 from length of z
Z = fft(z,NFFT)/L;
bimotfft=fft(bimot(2000:end),NFFT)/L;
f = Fs/2*linspace(0,1,NFFT/2+1);
fftbimot=2*abs(bimotfft(1:300));
subplot(2,1,2)
hold off
plot(f(1:150),fftbimot(1:150),'-.r', 'LineWidth', 2.5, 'DisplayName',
'bimotion', 'YDataSource', 'bimotion')
legend('show')
%%
figure(13)
hold off
plot(CPart, '--b', 'LineWidth', 2.5, 'displayName', 'trical', 'YDataSource',
'trical');
hold on
plot(CPbi, '-.r', 'LineWidth', 2.5, 'displayName', 'triceps', 'YDataSource',
'triceps');
plot(CPtri, 'k', 'LineWidth', 1, 'displayName', 'triceps-
trical', 'YDataSource', 'triceps');
legend('show')

```

APPENDIX IV



MEMORANDUM

Auckland University of Technology Ethics Committee (AUTEC)

To: Ahmed Al-Jumaily
From: **Madeline Banda** Executive Secretary, AUTEC
Date: 18 November 2008
Subject: Ethics Application Number 08/232 **Creation of a database of blood pressure signals collected using Pulsecor's wideband external pulse (WEP) monitor.**

Dear Ahmed

Thank you for providing written evidence as requested. I am pleased to advise that it satisfies the points raised by the Auckland University of Technology Ethics Committee (AUTEC) at their meeting on 13 October 2008 and that I have approved your ethics application, including the requested amendments allowing an additional researcher and an extension to the storage time of data and consent forms. This delegated approval is made in accordance with section 5.3.2 of AUTEC's *Applying for Ethics Approval: Guidelines and Procedures* and is subject to endorsement at AUTEC's meeting on 8 December 2008.

Your ethics application is approved for a period of three years until 18 November 2011.

I advise that as part of the ethics approval process, you are required to submit the following to AUTEC:

- A brief annual progress report using form EA2, which is available online through <http://www.aut.ac.nz/about/ethics>. When necessary this form may also be used to request an extension of the approval at least one month prior to its expiry on 18 November 2011;
- A brief report on the status of the project using form EA3, which is available online through <http://www.aut.ac.nz/about/ethics>. This report is to be submitted either when the approval expires on 18 November 2011 or on completion of the project, whichever comes sooner;

It is a condition of approval that AUTEC is notified of any adverse events or if the research does not commence. AUTEC approval needs to be sought for any alteration to the research, including any alteration of or addition to any documents that are provided to participants. You are reminded that, as applicant, you are responsible for ensuring that research undertaken under this approval occurs within the parameters outlined in the approved application.

Please note that AUTEC grants ethical approval only. If you require management approval from an institution or organisation for your research, then you will need to make the arrangements necessary to obtain this.

When communicating with us about this application, we ask that you use the application number and study title to enable us to provide you with prompt service. Should you have any further enquiries regarding this matter, you are welcome to contact Charles Grinter, Ethics Coordinator, by email at charles.grinter@aut.ac.nz or by telephone on 921 9999 at extension 8860.

On behalf of the AUTEC and myself, I wish you success with your research and look forward to reading about it in your reports.

Yours sincerely

Madeline Banda

Executive Secretary

Auckland University of Technology Ethics Committee

Cc: Ashis Mookerjee Ashis.mookerjee@aut.ac.nz, Hai Lan, Wayne Hing